

# **Experimental Investigation of Shock-Shock Interactions over a 2-D Wedge at $M = 6$**

Michelle Lynne Jones

Thesis submitted to the faculty of the Virginia Polytechnic Institute and State University in  
partial fulfillment of the requirements for the degree of

Master of Science  
In  
Mechanical Engineering

Michael R. von Spakovsky, Chair  
Walter F. O'Brien  
Elaine P. Scott  
Scott A. Berry

May 3, 2013  
Hampton, Virginia

Keywords: shock-shock interaction, phosphor thermography, conduction, two-dimensional

Copyright 2013, Michelle Lynne Jones

# **Experimental Investigation of Shock-Shock Interactions over a 2-D Wedge at $M = 6$**

Michelle Lynne Jones

## **Abstract**

The effects of fin-leading-edge radius and sweep angle on peak heating rates due to shock-shock interactions were investigated in the NASA Langley Research Center 20-inch Mach 6 Air Tunnel. The fin model leading edges, which represent cylindrical leading edges or struts on hypersonic vehicles, were varied from 0.25 inches to 0.75 inches in radius. A  $9^\circ$  wedge generated a planar oblique shock at  $16.7^\circ$  to the flow that intersected the fin bow shock, producing a shock-shock interaction that impinged on the fin leading edge. The fin angle of attack was varied from  $0^\circ$  (normal to the free-stream) to  $15^\circ$  and  $25^\circ$  swept forward. Global temperature data was obtained from the surface of the fused silica fins through phosphor thermography. Metal oil flow models with the same geometries as the fused silica models were used to visualize the streamline patterns for each angle of attack. High-speed zoom-schlieren videos were recorded to show the features and temporal unsteadiness of the shock-shock interactions. The temperature data were analyzed using one-dimensional semi-infinite as well as one- and two-dimensional finite-volume methods to determine the proper heat transfer analysis approach to minimize errors from lateral heat conduction due to the presence of strong surface temperature gradients induced by the shock interactions. The general trends in the leading-edge heat transfer behavior were similar for the three shock-shock interactions, respectively, between the test articles with varying leading-edge radius. The dimensional peak heat transfer coefficient augmentation increased with decreasing leading-edge radius. The dimensional peak heat transfer output from the two-dimensional code was about 20% higher than the value from a standard, semi-infinite one-dimensional method.



## Acknowledgements

The researcher would like to acknowledge the following people for their contributions to this Master's thesis project. The researcher's NASA LaRC project adviser, Scott Berry, answered every question and shared his insight on investigating shock-shock interactions through thin-film and phosphor thermography wind tunnel tests. Scott Berry also provided several NASA drawings of the support hardware used in the wind tunnel experiment that are included in Appendix B. Next, the researcher would like to thank her Virginia Tech graduate committee members, Dr. Michael von Spakovsky, Dr. Walter O'Brien, and Dr. Elaine Scott for their guidance and support throughout the testing and the process of writing and defending this thesis.

Dr. Alireza Mazaheri provided advice on how to run the LAURA simulations, how to use Tecplot, and how to validate CFD predictions with experimental data. Dr. Kamran Daryabeigi taught the researcher how to write a finite-volume code to estimate both one and two-dimensional conduction through wind tunnel models, and provided extensive support during the development of these codes. Mike Powers and Mark Griffith made the fused silica wind tunnel test articles and prepared the metal, Macor® and Upilex® test articles for testing. Grace Gleason provided practical advice on how to run experiments in the wind tunnel; Grace, Johnnie Ellis and Paul Tucker ran the 20-Inch Mach 6 Air Tunnel during the study. Kevin Hollingsworth assisted the researcher with test set-up, thin-film-gage calibrations, taking pictures throughout the test, and phosphor data analysis. Richard Wheless generated the CAD models used to make the fused silica and metal models for the experimental test, and the Pointwise grids for the CFD simulations. Richard also generated several of the images and diagrams included in this paper.

Dr. Shann Rufer and Karen Berger provided advice on the phosphor thermography data acquisition and reduction systems during the development of the updated version of IHEAT and the wind tunnel testing in this study. Dr. Rufer also edited this thesis extensively. Dr. Brian Hollis answered questions concerning the operation of his 1DHEAT and Map3D codes. Steve Jones set up the zoom schlieren system to obtain the focused images of the shock-shock interactions in the thin-film-gage and oil flow wind tunnel runs. Sheila Wright helped set up the tunnel data reduction program (DRP) for each wind tunnel test.

The researcher would also like to thank Drs. Joseph Zalameda and Eric Burke for loaning a FLIR SC6000 camera to the Aerothermodynamics Branch for the duration of the October testing. Joseph Zalameda explained how to use ImageJ to view the IR videos and to obtain qualitative data. Eric Burke explained how to use the IR camera and how to modify the location of the view window. Paul Bagby also provided high-speed Phantom cameras to obtain schlieren and oil flow data during the August and October testing, as well as other essential hardware to make the IR and schlieren data acquisition possible.

A Dykem® chemist, Naresh Patel, explained the possible reasons for the movement of the blue ink fiducials on the fused silica ceramic test articles during the runs. Mark Roth made very small thermocouples and embedded these temperature sensors in the fused silica models. Margaret Holloman, Pete Veneris, Ronnie Deans and Kathy Kuykendoll measured the oil flow and fused silica models and marked these models with fiducials. Finally, Tony Robbins submitted the paperwork to complete the calibrations of the thin-film gages.

## Table of Contents

Acknowledgements .....	iii
List of Figures .....	vii
List of Tables .....	xvi
List of Symbols and Acronyms .....	xvii
1. Chapter 1: Introduction .....	1
1.1. Current study overview .....	1
1.1.1. Problem statement .....	2
1.1.2. Purpose statement .....	2
1.1.3. Hypotheses .....	3
1.1.4. Application to future aerothermodynamic tests .....	3
1.2. Comparison to a previous shock-shock interaction study (Test 6692) .....	4
1.3. Thesis objectives and goals .....	4
2. Chapter 2: Literature review .....	5
2.1. Background information .....	5
2.2. Edney types of shock-shock interactions .....	5
2.3. Effect of shock-shock interaction heating on hypersonic vehicles .....	7
2.4. Previous shock-shock interaction wind tunnel studies .....	14
2.5. Previous evaluation of 1D and 2D heat transfer analyses .....	32
3. Chapter 3: Wind tunnel experiments for this study .....	40
3.1. Facility (20-Inch Mach 6 Air Tunnel) .....	40
3.2. Experimental set up .....	43
3.3. Test articles .....	49
3.3.1. Thin-film test articles (Tests 6692/6976) .....	49
3.3.1.1. Fabrication of test article with standard thin-film gages (Painted 1, 2) .....	50
3.3.1.2. Fabrication of test article with etched gages on polyimide film (Upilex®) .....	50
3.3.1.3. Calibrations of thin-film test articles .....	50
3.3.2. Oil flow test articles (Test 6983) .....	53
3.3.2.1. Metal test article fabrication .....	54
3.3.2.2. Fiducial mark application .....	54
3.3.2.3. Quality Assurance analysis of oil flow test articles .....	55
3.3.3. Fused silica test articles instrumented with a phosphor coating (Test 6983) .....	57

3.3.3.1. Fabrication of fused silica test articles .....	57
3.3.3.2. Fiducial mark application .....	60
3.3.3.3. Calibrations of phosphor system.....	62
3.3.3.4. Quality Assurance analysis of fused silica test articles .....	62
3.4. Experimental run matrix (Tests 6976 and 6983) .....	63
3.4.1. Test 6976 run matrix .....	64
3.4.2. Test 6983, Phase 1 run matrix.....	65
3.4.3. Test 6983, Phase 2 run matrix.....	66
3.5. Wind tunnel data acquisition .....	67
3.5.1. Oil flow test articles .....	67
3.5.2. Fused silica test articles instrumented with a phosphor coating .....	69
3.5.2.1. Phosphor and thermocouple temperature data .....	70
3.5.2.2. Infrared (IR) temperature data .....	71
3.5.3. Zoom schlieren cases .....	72
4. Chapter 4: Numerical analysis .....	77
4.1. Temperature data (IHEAT).....	77
4.2. Heat transfer analyses .....	77
4.2.1. One-dimensional semi-infinite code (IHEAT) .....	77
4.2.2. Finite-volume conduction calculations .....	78
4.2.2.1. One-dimensional FV code .....	81
4.2.2.2. Two-dimensional FV code.....	85
5. Chapter 5: Experimental measurements and results .....	92
5.1. Visual shock-shock interactions .....	92
5.1.1. SG angle of 9° (Test 6976) .....	93
5.1.1.1. Fin sweep of 0° .....	93
5.1.1.2. Fin sweep of -15° .....	94
5.1.1.3. Fin sweep of -25° .....	97
5.1.2. SG angle of 9° (Test 6983) .....	98
5.1.2.1. Fin sweep of 0° .....	98
5.1.2.2. Fin sweep of -15° .....	106
5.1.2.3. Fin sweep of -25° .....	112
5.1.3. SG angle of 6° (Test 6976) .....	119
5.1.3.1. Fin sweep of 0° .....	120

5.1.3.2. Fin sweep of $-15^\circ$ .....	120
5.1.3.3. Fin sweep of $-25^\circ$ .....	121
5.2. Heat transfer analyses .....	122
5.2.1. Fin sweep of $0^\circ$ and a $Re = 2.1 \times 10^6/ft$ .....	128
5.2.1.1. Leading-edge radius of 0.25 in .....	128
5.2.1.2. Leading-edge radius of 0.50 in .....	131
5.2.1.3. Leading-edge radius of 0.75 in .....	134
5.2.2. Fin sweep of $-15^\circ$ and a $Re = 2.1 \times 10^6/ft$ .....	137
5.2.2.1. Leading-edge radius of 0.25 in .....	137
5.2.2.2. Leading-edge radius of 0.50 in .....	140
5.2.2.3. Leading-edge radius of 0.75 in .....	142
5.2.3. Fin sweep of $-25^\circ$ and a $Re = 2.1 \times 10^6/ft$ .....	144
5.2.3.1. Leading-edge radius of 0.25 in .....	144
5.2.3.2. Leading-edge radius of 0.50 in .....	147
5.2.3.3. Leading-edge radius of 0.75 in .....	149
5.2.4. Fin sweep of $-15^\circ$ and a $Re$ number sweep .....	151
5.3. Preliminary results from the LAURA CFD analysis .....	161
6. Chapter 6: Conclusions .....	168
6.1. Characterization of shock-shock interactions .....	168
6.2. Analysis of 1D and 2D heat transfer methods .....	169
6.3. Comparison of experimental and computational visualization techniques .....	169
6.4. Future work .....	170
References .....	171
A. Appendix A: Thermal properties .....	174
B. Appendix B: Test article measurements .....	176
C. Appendix C: IHEAT heat transfer results at $t = 3.4$ s .....	209

## List of Figures

Figure 2-1. Edney catalogued the shock interaction types in this diagram, IS = incident shock, BS = bow shock, RS = reflected shock, EF = expansion fan, TP = triple point, SL = shear layer (diagram used with Berry's permission [8]).	6
Figure 2-2. Hypersonic flight vehicle configuration (image used with Berry's permission [8]).	8
Figure 2-3. Dummy ramjet installed on the fuselage of the X-15-2 plane (image reproduced from a NASA report [9]).	9
Figure 2-4. Damaged dummy ramjet after impact on Edwards bombing range (image reproduced from a NASA report [9]).	10
Figure 2-5. Damaged X-15-2 pylon from Mach 6.7 shock interference heating (images reproduced from a NASA report [9]).	10
Figure 2-6. KSC Launch of Columbia STS 107. Reinforced carbon/carbon protects the wing leading edges on this vehicle. (CAIB photo by NASA, January 16, 2003 [16]).	12
Figure 2-7. Image from video of STS 107 launch, which showed shedding debris impacting the left Columbia wing. (CAIB photo by NASA, January 16, 2003 [17]).	12
Figure 2-8. Recovered Columbia debris after break-up during re-entry. (CAIB photo by NASA, March 18, 2003 [18]).	13
Figure 2-9. Shock-on-cowl and shock-on-fin types of shock-shock interactions (image used with Berry's permission, not previously published).	14
Figure 2-10. The effect of the coolant mass flux, $\lambda$ , with a fixed incident shock, on the peak heat flux and the angle $\Theta$ measured from the model centerline (image used with Nowak's permission [24]).	15
Figure 2-11. Heat flux distribution for a Type IV interaction on a hemisphere with either a non-dimensional coolant mass flux of $\lambda = 0$ (no coolant) or $\lambda = 0.31$ (image used with Nowak's permission [24]).	16
Figure 2-12. Mach 6.5 velocity vectors from the computational simulations of different types of shock-shock interactions (image reprinted with permission of the American Institute of Aeronautics and Astronautics [25]).	17
Figure 2-13. Structured and unstructured meshes combined into a single grid for the shock interference problem (image reprinted with permission of the American Institute of Aeronautics and Astronautics [26]).	18
Figure 2-14. A finite element solution of the heat flux distribution at the wall for the investigated shock interference case (image reprinted with permission of the American Institute of Aeronautics and Astronautics [26]).	19
Figure 2-15. Adaptive re-meshing technique for a Type IV interaction (image reprinted with permission of the American Institute of Aeronautics and Astronautics [25]).	20
Figure 2-16. Schlieren image and peak heat transfer augmentation plot for a Type IV interaction with a 0.25 in-radius test article at a $-15^\circ$ AoA (image used with Berry's permission [8]).	21
Figure 2-17. Schlieren image and peak heat transfer augmentation plot for a Type III interaction with a 0.25 in-radius test article at a $-25^\circ$ AoA (image used with Berry's permission [8]).	21
Figure 2-18. Sketch of a possible shock-shock interaction between the vehicle bow shock and a leading-edge shock in hypersonic flow (image used with Bushnell's permission [28]).	22
Figure 2-19. Diagram of the cylindrical models instrumented with either thermocouples or pressure orifices, with non-dimensional lengths based on the cylinder diameter (image used with Bushnell's permission [27]).	23

Figure 2-20. Sketch of a typical schlieren photograph that shows the inviscid flow-field phenomena associated with the intersection of two right running shocks (image used with Bushnell's permission [27]).	24
Figure 2-21. Increase in peak heating due to shock impingement as a function of the non-dimensional distance from the tip of the cylinder (image used with Bushnell's permission [28]).	25
Figure 2-22. Schlieren, pressure and heat transfer data for a Type IVa interaction on a fin at Mach 5.94 in air with a SG angle of $10^\circ$ (image reproduced from a NASA report [13]).	26
Figure 2-23. Image of the rocket and the attached unswept transverse cylinder used in a shock-shock interaction flight experiment (image reproduced from a NASA report [30]).	27
Figure 2-24. Ratios of experimental to theoretical laminar heat transfer coefficients as Mach number increases, with an arrow at the approximate location of the shock intersection (plots reproduced from a NASA report [30]).	28
Figure 2-25. Sketch of the SG and the test article (image reproduced from a NASA report [31]).	29
Figure 2-26. Stagnation line heat transfer rates for an unswept leading-edge test article with a SG angle of $10^\circ$ and divided by a Fay-Riddell reference heat transfer rate (plot reproduced from a NASA report [31]).	30
Figure 2-27. Leading-edge oil flow image for an unswept test article and a SG angle of $15^\circ$ (image reproduced from a NASA report [31]).	31
Figure 2-28. Peak surface pressure and heat flux due to laser energy deposition (used with Trumble's, now Zarchi's, permission [33]).	32
Figure 2-29. Comparison of one- and two-dimensional estimate for heat flux in Test 6692, Run 14 using the Macor® test article at 2 sec (image used with Walker's permission [34]).	34
Figure 2-30. Relative difference between one- and two-dimensional inverse finite-volume aeroheating rates for run with gas injection at $x/L_x$ for a) 0.25 and b) 0.50 (plots used with Daryabeigi's permission [37]).	35
Figure 2-31. Heat flux for Run 50, shown along with 2D and axisymmetric finite-volume conduction effects (plot used with Rufer's permission [38]).	36
Figure 2-32. Heat flux data on a double-cone configuration based on (a) estimated lateral heat flux and (b) calculated lateral heat flux in Run 2894 (plots used with Coblish's permission [39]).	37
Figure 2-33. Corrected heat flux data, considering calculated lateral heat flux, for Run 2894 (plot used with Coblish's permission [39]).	37
Figure 2-34. Images of a) experimental and b) computed schlieren data for the shock-shock interaction region on a 0.25 in-radius test article at a $-15^\circ$ AoA (left images) and at a $-25^\circ$ AoA (right images) in Mach 6 flow (images used with Wright's permission [3]).	39
Figure 3-1. LAL 20-Inch Mach 6 Air Tunnel.	41
Figure 3-2. 20-Inch Mach 6 Air Tunnel layout.	42
Figure 3-3. Side-view renderings of tunnel set-up with arc sector, I-beam, and strut.	44
Figure 3-4. Side-view rendering of 0.25 in-radius fused silica test article at $0^\circ$ AoA.	44
Figure 3-5. Side-view rendering of 0.5 in-radius fused silica test article at $-15^\circ$ AoA.	44
Figure 3-6. Side-view rendering of 0.75 in-radius fused silica test article at $-25^\circ$ AoA.	45
Figure 3-7. Top-view rendering of 0.5 in-radius fused silica test article at $0^\circ$ AoA.	45
Figure 3-8. Slanted top view of 0.25 in-radius fused silica test article at $0^\circ$ AoA.	45
Figure 3-9. Fused silica (0.25 in-radius) test article in support hardware without the SG.	47

Figure 3-10. Fused silica (0.75 in-radius) test article in support hardware with the 9° SG.....	47
Figure 3-11. Fused silica (0.50 in-radius) test article with thermocouple near the bottom. ....	48
Figure 3-12. Close-up of 0.50 in-radius fused silica test article showing thermocouple bead. ....	48
Figure 3-13. Fused silica, 15-5 stainless steel (painted black), and thin-film-gage test articles (image of thin-film test articles used with Berry's permission [8])......	49
Figure 3-14. Red high-temperature RTV silicone bonded Macor® rods into metal holders. ....	51
Figure 3-15. Painted 2 test article mounted on the sting in the support hardware and inserted in the tunnel.....	52
Figure 3-16. Damaged sensors on Painted 2 test article. ....	53
Figure 3-17. Damaged sensors (cut wires) on Upilex® test article. ....	53
Figure 3-18. Metal test article (0.75 in-radius) used in oil flow visualization runs.....	54
Figure 3-19. Practice enamel-paint fiducial marks on scrap metal (illuminated by UV light).....	55
Figure 3-20. Diagram of the dimensions measured with a CMM on the metal and the fused silica test articles (a 0.25 in-radius metal test article is shown for reference).....	56
Figure 3-21. A 0.02 in-diameter bead was welded onto 10 mil, Type K thermocouple (TC) wire using a UNITEK TC welder, and the bead and lead wires were flattened with crimping pliers.....	59
Figure 3-22. TC inserted into a groove in the surface of the fused silica test article with a 0.01 in depth beneath the bead and a width and depth of 0.075 in beneath the lead wires. ....	59
Figure 3-23. The 0.075 in wide by 0.075 in deep groove in the fused silica test article was filled in with alumina cement to secure the TC bead in place. ....	60
Figure 3-24. Primary and back-up fused silica test articles and metal oil flow test articles.....	61
Figure 3-25. Phantom 9 camera used to capture oil flow videos at 100 fps with UV lights to illuminate the fluorescent fiducial marks.....	67
Figure 3-26. Hitachi camera aimed at the leading edge of the oil-flow test articles through the top window.....	68
Figure 3-27. Example of a metal test article covered with white oil dots near the beginning of the run. ....	68
Figure 3-28. Example of a metal test article covered with a white oil layer near the beginning of the run. ....	69
Figure 3-29. 0.5 in-radius fused silica test article in the tunnel with 360 nm UV illumination. ..	71
Figure 3-30. FLIR SC6000 IR camera mounted above the wind tunnel test section. ....	72
Figure 3-31. Test 6976 zoom schlieren set-up (used with permission of Steve Jones, not previously published).....	73
Figure 3-32. Test 6983 zoom schlieren set-up (used with permission of Steve Jones, not previously published).....	74
Figure 3-33. Test 6983 zoom schlieren set-up on the front side of the tunnel with the newer light source. ....	75
Figure 3-34. Zoom schlieren set-up on the other side of the tunnel with the Phantom camera installed.....	75
Figure 3-35. Test 6983 zoom schlieren set-up with the light source turned on.....	76
Figure 3-36. Test 6983 zoom schlieren set-up with the shutter to block light until the end of the run. ....	76
Figure 4-1. Overall view of the boundary conditions of the cylindrical leading edge modeled in the 1D (neglecting curvature) and 2D (using cylindrical coordinates) FV codes.....	79
Figure 4-2. Diagram of the first few nodes below the test article surface in the 1D FV code. ....	82

Figure 4-3. Side view of the approximated cylindrical leading edge of the test articles used in the 2D FV code. ....	86
Figure 4-4. Top view of the approximated cylindrical leading edge of the test articles used in the 2D FV code. ....	86
Figure 5-1. Zoom schlieren image of Painted 2 test article (0.25 in-radius) at a 0° AoA with a 9° SG angle (recolored with saturation: 0%; brightness: +40%; contrast: +20%). ....	94
Figure 5-2. Zoom schlieren image of Painted 2 test article (0.25 in-radius) at a -15° AoA with a 9° SG angle (recolored with saturation: 0%; brightness: +40%; contrast: +20%). ....	95
Figure 5-3. Zoom schlieren image with test article retracted and no flow in the wind tunnel (recolored with saturation: 0%; brightness: +40%; contrast: +20%). ....	96
Figure 5-4. Shock-interaction image subtracted from the wind-tunnel window (no flow) image for the Painted 2 test article at a -15° AoA with a 9° SG angle (recolored with saturation: 0%; brightness: +40%; contrast: +20%). ....	96
Figure 5-5. Wind-tunnel window (no flow) image subtracted from the shock-interaction image for the Painted 2 test article at a -15° AoA with a 9° SG angle (recolored with saturation: 0%; brightness: +40%; contrast: +20%) ....	97
Figure 5-6. Two zoom schlieren images of a 0.25 in-radius Upilex® model angled at -25° (recolored with saturation: 0%; brightness: +40%; contrast: +20%). ....	98
Figure 5-7. Zoom schlieren (1000 fps) image of a Type IVa shock-interaction for the 0.25 in-radius test article angled at a 0° AoA. ....	99
Figure 5-8. Zoom schlieren (1600 fps) image of the 0.25 in-radius test article at a 0° AoA. ....	99
Figure 5-9. Zoom schlieren (1000 fps) image of a Type IVa shock-interaction for the 0.50 in-radius test article angled at a 0° AoA. ....	100
Figure 5-10. Zoom schlieren (1600 fps) image of the 0.50 in-radius test article at a 0° AoA. ..	101
Figure 5-11. Zoom schlieren (1000 fps) image of a Type IVa shock-interaction for the 0.75 in-radius test article angled at a 0° AoA. ....	102
Figure 5-12. Zoom schlieren (1600 fps) image of the 0.75 in-radius test article at a 0° AoA. ..	102
Figure 5-13. Phantom 12 (7900 fps) zoom schlieren image overlaid with fiducials for the 0.25 in-radius test article at a 0° AoA (recolored with brightness: +40%). ....	103
Figure 5-14. Leading-edge oil-flow images for the 0.75 in-radius metal test article at a 0° AoA (using the two oil-flow techniques: dots in the left image, full coating in the right image). ....	104
Figure 5-15. Side oil-flow images for the 0.75 in-radius metal test article at a 0° AoA (both images display streamlines produced with the oil flow dots technique). ....	105
Figure 5-16. Zoom schlieren (1000 fps) image of a Type IV shock-interaction for the 0.25 in-radius test article angled at a -15° AoA. ....	106
Figure 5-17. Zoom schlieren (1000 fps) image of a Type IV shock-interaction for the 0.50 in-radius test article angled at a -15° AoA. ....	107
Figure 5-18. Zoom schlieren (1600 fps) image of the 0.50 in-radius test article at a -15° AoA. ....	107
Figure 5-19. Zoom schlieren (1000 fps) image of a Type IV shock-interaction for the 0.75 in-radius test article angled at a -15° AoA. ....	108
Figure 5-20. Zoom schlieren (1600 fps) image of the 0.75 in-radius test article at a -15° AoA. ....	109
Figure 5-21. Phantom 12 (7900 fps) zoom schlieren image overlaid with fiducials for the 0.75 in-radius test article at a -15° AoA. ....	110
Figure 5-22. Leading-edge oil-flow images for the 0.75 in-radius metal test article at a -15° AoA (using the two oil-flow techniques: dots in the left image, full coating in the right image). ....	



.....	111
Figure 5-23. Side oil-flow images for the 0.75 in-radius metal test article at a $-15^\circ$ AoA (using the two oil-flow techniques: dots in the left image, full coating in the right image). .....	112
Figure 5-24. Zoom schlieren (1000 fps) image of a Type III shock-interaction for the 0.25 in-radius test article angled at a $-25^\circ$ AoA. ....	113
Figure 5-25. Zoom schlieren (1000 fps) image of a Type III shock-interaction for the 0.50 in-radius test article angled at a $-25^\circ$ AoA. ....	114
Figure 5-26. Zoom schlieren (1600 fps) image of the 0.50 in-radius test article at a $-25^\circ$ AoA. ....	114
Figure 5-27. Zoom schlieren (1000 fps) image of a Type III shock-interaction for the 0.75 in-radius test article angled at a $-25^\circ$ AoA. ....	115
Figure 5-28. Zoom schlieren (1000 fps) image of the 0.75 in-radius test article at a $-25^\circ$ AoA raised to a height 0.75 in above the flat plate SG. ....	116
Figure 5-29. Phantom 12 (7900 fps) zoom schlieren image overlaid with fiducials for the 0.5 in-radius test article at a $-25^\circ$ AoA. ....	117
Figure 5-30. Leading-edge oil-flow images for the 0.75 in-radius metal test article at a $-25^\circ$ AoA (using the two oil-flow techniques: dots in the left image, full coating in the right image). ....	118
Figure 5-31. Side oil-flow images for the 0.75 in-radius metal test article at a $-25^\circ$ AoA (using the two oil-flow techniques: dots in the left image, full coating in the right image). ....	119
Figure 5-32. Zoom schlieren image of the Upilex® test article at a $0^\circ$ AoA with a $6^\circ$ SG angle (recolored with saturation: 0%; brightness: +40%; contrast: +20%). ....	120
Figure 5-33. Zoom schlieren image of the Upilex® test article at a $-15^\circ$ AoA with a $6^\circ$ SG angle (recolored with saturation: 0%; brightness: +40%; contrast: +20%). ....	121
Figure 5-34. Zoom schlieren image of the Upilex® test article at a $-25^\circ$ AoA with a $6^\circ$ SG angle (recolored with saturation: 0%; brightness: +40%; contrast: +20%). ....	122
Figure 5-35. Temporal collapse of IHEAT ch/ch,FR for the 0.25 in-radius test article at a $-15^\circ$ AoA with a $Re = 1.1 \times 10^6/ft$ and using data from every sixth frame (every 0.2 s) during the run. ....	123
Figure 5-36. Enthalpy-based heat transfer coefficients from the 2D FV code at different locations (specified by the IHEAT pixel number) along the leading edge over time. ....	124
Figure 5-37. Grid convergence of the heat transfer coefficients along the leading edge of the 0.25 in-radius test article at a $-15^\circ$ AoA ( $Re = 1.1 \times 10^6/ft$ ) and $t = 4.6$ s for the 1D FV code....	125
Figure 5-38. Grid convergence of the heat transfer coefficients along the leading edge of the 0.25 in-radius test article at a $-15^\circ$ AoA ( $Re = 1.1 \times 10^6/ft$ ) at $t = 4.6$ s for the 2D FV code.....	126
Figure 5-39. Run 39: IHEAT ch/ch,FR contour map for the 0.25 in-radius test article at a $0^\circ$ AoA. ....	128
Figure 5-40. Run 47: IHEAT ch/ch,FR contour map for the 0.25 in-radius test article at a $0^\circ$ AoA (zoomed in). ....	129
Figure 5-41. Non-dimensional heat transfer coefficients from the IHEAT and 1D FV codes for the 0.25 in-radius test article at a $0^\circ$ AoA. ....	129
Figure 5-42. Non-dimensional heat transfer coefficients from the thin-film gages on the 0.25 in-radius Macor® Painted 1 and Upilex® test articles in Test 6692 at a $0^\circ$ AoA [8]. ....	130
Figure 5-43. Run 38: IHEAT ch/ch,FR contour map for the 0.50 in-radius test article at a $0^\circ$ AoA. ....	131
Figure 5-44. Run 53: IHEAT ch/ch,FR contour map for the 0.50 in-radius test article at a $0^\circ$ AoA (zoomed in). ....	132

Figure 5-45. Run 54: IHEAT ch/ch,FR contour map for the 0.50 in-radius test article at a 0° AoA (zoomed in, repeat run). .....	132
Figure 5-46. Non-dimensional heat transfer coefficients from the IHEAT and 1D FV codes for the 0.50 in-radius test article at a 0° AoA. ....	133
Figure 5-47. Non-dimensional heat transfer coefficients from the IHEAT and 1D FV codes for repeat runs zoomed in on the interaction region for the 0.50 in-radius test article at a 0° AoA. ....	134
Figure 5-48. Run 35: IHEAT ch/ch,FR contour map for the 0.75 in-radius test article at a 0° AoA. ....	135
Figure 5-49. Run 48: IHEAT ch/ch,FR contour map for the 0.75 in-radius test article at a 0° AoA (zoomed in). ....	135
Figure 5-50. Non-dimensional heat transfer coefficients from the IHEAT and 1D FV codes for the 0.75 in-radius test article at a 0° AoA. ....	136
Figure 5-51. Non-dimensional heat transfer coefficients at t = 4.6 s from the IHEAT and 2D FV codes for the 0.75 in-radius test article at a 0° AoA. ....	137
Figure 5-52. Run 40: IHEAT ch/ch,FR contour map for the 0.25 in-radius test article at a -15° AoA. ....	138
Figure 5-53. Run 45: IHEAT ch/ch,FR contour map for the 0.25 in-radius test article at a -15° AoA (zoomed in). ....	138
Figure 5-54. Non-dimensional heat transfer coefficients from the IHEAT and 1D FV codes for the 0.25 in-radius test article at a -15° AoA. ....	139
Figure 5-55. Non-dimensional heat transfer coefficients from the thin-film gages on the 0.25 in-radius Macor® Painted 1 and Upilex® test articles in Test 6692 at a -15° AoA [8]. ....	140
Figure 5-56. Run 37: IHEAT ch/ch,FR contour map for the 0.50 in-radius test article at a -15° AoA. ....	141
Figure 5-57. Run 52: IHEAT ch/ch,FR contour map for the 0.50 in-radius test article at a -15° AoA (zoomed in). ....	141
Figure 5-58. Non-dimensional heat transfer coefficients from the IHEAT and 1D FV codes for the 0.50 in-radius test article at a -15° AoA. ....	142
Figure 5-59. Run 34: IHEAT ch/ch,FR contour map for the 0.75 in-radius test article at a -15° AoA. ....	143
Figure 5-60. Run 49: IHEAT ch/ch,FR contour map for the 0.75 in-radius test article at a -15° AoA (zoomed in). ....	143
Figure 5-61. Non-dimensional heat transfer coefficients from the IHEAT and 1D FV codes for the 0.75 in-radius test article at a -15° AoA. ....	144
Figure 5-62. Run 41: IHEAT ch/ch,FR contour map for the 0.25 in-radius test article at a -25° AoA. ....	145
Figure 5-63. Run 46: IHEAT ch/ch,FR contour map for the 0.25 in-radius test article at a -25° AoA (zoomed in). ....	145
Figure 5-64. Non-dimensional heat transfer coefficients from the IHEAT and 1D FV codes for the 0.25 in-radius test article at a -25° AoA. ....	146
Figure 5-65. Non-dimensional heat transfer coefficients from the thin-film gages on the 0.25 in-radius Macor® Painted 1 and Upilex® test articles in Test 6692 at a -25° AoA [8]. ....	147
Figure 5-66. Run 36: IHEAT ch/ch,FR contour map for the 0.50 in-radius test article at a -25° AoA. ....	148
Figure 5-67. Run 51: IHEAT ch/ch,FR contour map for the 0.75 in-radius test article at a -25°	

AoA (zoomed in). .....	148
Figure 5-68. Non-dimensional heat transfer coefficients from the IHEAT and 1D FV codes for the 0.50 in-radius test article at a -25° AoA. ....	149
Figure 5-69. Run 33: IHEAT ch/ch,FR contour map for the 0.75 in-radius test article at a -25° AoA. ....	150
Figure 5-70. Run 50: IHEAT ch/ch,FR contour map for the 0.75 in-radius test article at a -25° AoA (zoomed in). ....	150
Figure 5-71. Non-dimensional heat transfer coefficients from the IHEAT and 1D FV codes for the 0.75 in-radius test article at a -25° AoA. ....	151
Figure 5-72. Non-dimensional heat transfer coefficients from the IHEAT code for the Re number sweep (considering Re = 1.1, 2.1 and 4.1 x106/ft) for a 0.25 in-radius test article at a -15° AoA. ....	152
Figure 5-73. Run 43: IHEAT ch/ch,FR contour map for the 0.25 in-radius test article at a -15° AoA and a Re = 1.1 x106/ft. ....	153
Figure 5-74. Run 44: IHEAT ch/ch,FR contour map for the 0.25 in-radius test article at a -15° AoA and a Re = 1.1x106/ft (zoomed in). ....	153
Figure 5-75. Enthalpy-based heat transfer coefficients at t = 3.4 s from the IHEAT, 1D, and 2D FV codes for the 0.25 in-radius test article at a -15° AoA and a Re = 1.1x106/ft. ....	154
Figure 5-76. Non-dimensional heat transfer coefficients at t = 3.4 s from the IHEAT, 1D, and 2D FV codes for the 0.25 in-radius test article at a -15° AoA and a Re = 1.1 x106/ft. ....	155
Figure 5-77. Heat transfer coefficients for the zoomed-in case at t = 4.6 s from the IHEAT code for the 0.25 in-radius test article at a -15° AoA and a Re = 1.1 x106/ft (using two different reference values). ....	156
Figure 5-78. Enthalpy-based heat transfer coefficients at t = 4.6 s from the IHEAT, 1D, and 2D FV codes for the 0.25 in-radius test article at a -15° AoA and a Re = 1.1 x106/ft. ....	157
Figure 5-79. Non-dimensional heat transfer coefficients at t = 4.6 s from the IHEAT, 1D, and 2D FV codes for the 0.25 in-radius test article at a -15° AoA and a Re = 1.1 x106/ft (zoomed-in and regular). ....	158
Figure 5-80. Spatial resolution of IHEAT zoomed-in versus zoomed-out non-dimensional peak heat transfer coefficients at t = 4.6 s for the 0.25 in-radius test article at a -15° AoA and a Re = 1.1 x106/ft. ....	159
Figure 5-81. Run 42: IHEAT ch/ch,FR contour map for the 0.25 in-radius test article at a -15° AoA and a Re = 4.1x106/ft. ....	160
Figure 5-82. Non-dimensional heat transfer coefficients from the IHEAT and 1D FV codes for the 0.25 in-radius test article at a -15° AoA and a Re = 4.1x106/ft. ....	160
Figure 5-83. Flat plate SG boundary layer thickness ( $\Delta$ ) with the leading edge at 0.43 m (17 in) upstream of the Mach 5.96 flow (LAURA simulation). ....	161
Figure 5-84. Contour map of the boundary layer thickness ( $\Delta$ ) over the flat plate SG in Mach 5.96 flow (LAURA simulation). ....	162
Figure 5-85. Numerical schlieren images for the 0.25 in-radius test article at a -15° AoA with a 9° SG (samples of non-consecutive frames in the time-accurate LAURA simulation). ....	164
Figure 5-86. Numerical schlieren images for the 0.25 in-radius test article at a -25° AoA with a 9° SG (samples of consecutive frames in the time-accurate LAURA simulation). ....	165
Figure 5-87. Heating patterns on the axisymmetric leading edge of the 0.25 in-radius test article at a -25° AoA (left image) and a -15° AoA (right image) early in the LAURA simulations. ....	166

Figure 5-88. Density and pressure contour maps with a few streamlines along an axisymmetric leading edge for the 0.25 in-radius test article at a $-15^\circ$ AoA (from the LAURA simulation).	167
Figure B-1. Dimensions of metal oil flow test article with a 0.25 in-radius leading edge, machined from 15-5 stainless steel.	177
Figure B-2. 15-5 stainless steel insert for 0.25 in-radius (leading edge) ceramic test article (used to attach test article with bolts).	178
Figure B-3. Dimensions of metal oil flow test article with 0.5 in-radius leading edge, machined from 15-5 stainless steel.	179
Figure B-4. 15-5 stainless steel insert for 0.5 in-radius (leading edge) fused silica test article (used to attach test article with bolts).	180
Figure B-5. Dimensions of metal oil flow test article with 0.75 in-radius leading edge, machined from 15-5 stainless steel.	181
Figure B-6. 15-5 stainless steel insert for 0.75 in-radius (leading edge) fused silica test article (used to attach test article with bolts).	182
Figure B-7. Diagram of the hardware used to adjust the vertical height of the sting (NASA drawing).	183
Figure B-8. Diagram of the flat plate with a sharp leading edge used to generate an incident shock (NASA drawing).	184
Figure B-9. Diagram of the strut head geometry used to angle the test article at either $6^\circ$ or $9^\circ$ (NASA drawing).	185
Figure B-10. Diagram of the strut used to support the test hardware during the wind tunnel runs (NASA drawing).	186
Figure B-11. Diagram of the test article angle of attack (fin) adjuster and the legacy test article (fin) holder (NASA drawing).	187
Figure B-12. Diagram of the legacy I-beam used to raise the test hardware during the wind tunnel runs (NASA drawing).	188
Figure B-13. Assembly of hardware components for wind tunnel experiment.	189
Figure B-14. Ghost view of assembly of hardware components for wind tunnel experiment.	189
Figure B-15. Fiducial mark arrangement for fused silica and metal 0.25 in-radius test articles.	190
Figure B-16. Fiducial mark arrangement for fused silica and metal 0.5 in-radius test articles.	190
Figure B-17. Fiducial mark arrangement for fused silica and metal 0.75 in-radius test articles.	191
Figure B-18. Sketched locations of the fiducial marks on the 0.25 in-radius and the 0.50 in-radius test articles based on the nominal test article dimensions.	192
Figure B-19. Sketched locations of the fiducial marks on the 0.75 in-radius test articles based on the nominal test article dimensions.	193
Figure B-20. Diagram of fiducial mark numbers for fused silica and metal test articles.	194
Figure C-1. Run 39: IHEAT ch/ch,FR contour map for the 0.25 in-radius test article at a $0^\circ$ AoA.	209
Figure C-2. Run 38: IHEAT ch/ch,FR contour map for the 0.50 in-radius test article at a $0^\circ$ AoA.	210
Figure C-3. Run 35: IHEAT ch/ch,FR contour map for the 0.75 in-radius test article at a $0^\circ$ AoA.	210
Figure C-4. Run 43: IHEAT ch/ch,FR contour map for the 0.25 in-radius test article at a $-15^\circ$	

AoA with a $Re = 1.1 \times 10^6/ft$ .....	211
Figure C-5. Run 40: IHEAT ch/ch,FR contour map for the 0.25 in-radius test article at a $-15^\circ$ AoA with a $Re = 2.1 \times 10^6/ft$ .....	211
Figure C-6. Run 42: IHEAT ch/ch,FR contour map for the 0.25 in-radius test article at a $0^\circ$ AoA with $Re = 4.1 \times 10^6/ft$ . ....	212
Figure C-7. Run 37: IHEAT ch/ch,FR contour map for the 0.50 in-radius test article at a $-15^\circ$ AoA.....	212
Figure C-8. Run 34: IHEAT ch/ch,FR contour map for the 0.75 in-radius test article at a $-15^\circ$ AoA.....	213
Figure C-9. Run 41: IHEAT ch/ch,FR contour map for the 0.25 in-radius test article at a $-25^\circ$ AoA.....	213
Figure C-10. Run 36: IHEAT ch/ch,FR contour map for the 0.50 in-radius test article at a $-25^\circ$ AoA.....	214
Figure C-11. Run 33: IHEAT ch/ch,FR contour map for the 0.75 in-radius test article at a $-25^\circ$ AoA.....	214

## List of Tables

Table 3-1. Tunnel entries in the current wind tunnel experiment.....	40
Table 3-2. Nominal flow conditions in the 20-Inch Mach 6 Air Tunnel.....	42
Table 3-3. Actual mean flow conditions in Tests 6976 and 6983 in 20-Inch Mach 6 Air Tunnel. .....	42
Table 3-4. Key dimensions of metal test articles. Unless otherwise specified, units are inches. .	57
Table 3-5. Key primary fused silica test article dimensions. Unless otherwise specified, units are inches. ....	63
Table 3-6. Thin-film-gage test articles run matrix.....	65
Table 3-7. Metal test articles for the oil-flow visualization run matrix. ....	65
Table 3-8. Fused silica test articles run matrix. ....	66
Table 5-1. Flow properties across the incident shock (IS) due to the SG angle [45]. ....	92
Table A-1. Thermal conductivity (k) and specific heat (cP) of Macor®.....	174
Table A-2. Fused silica thermal diffusivity versus temperature measurements [51]. ....	174
Table A-3. Fused silica thermal conductivity versus temperature measurements [51]. ....	175
Table B-1. Actual fiducial mark locations on the 0.25 in-radius fused silica test article (the primary test article with an embedded thermocouple).....	195
Table B-2. Actual fiducial mark locations on the 0.25 in-radius fused silica test article (the back- up test article without an embedded thermocouple). ....	197
Table B-3. Actual fiducial mark locations on the 0.50 in-radius fused silica test article (the primary test article with an embedded thermocouple).....	199
Table B-4. Actual fiducial mark locations on the 0.50 in-radius fused silica test article (the back- up test article without an embedded thermocouple). ....	200
Table B-5. Actual fiducial mark locations on the 0.75 in-radius fused silica test article (the primary test article with an embedded thermocouple).....	202
Table B-6. Actual fiducial mark locations on the 0.75 in-radius fused silica test article (the back- up test article without an embedded thermocouple). ....	204
Table B-7. Actual fiducial mark locations on the 0.25 in-radius metal test article (oil flow). ...	205
Table B-8. Actual fiducial mark locations on the 0.50 in-radius metal test article (oil flow). ...	207
Table B-9. Actual fiducial mark locations on the 0.75 in-radius metal test article (oil flow). ...	208

## List of Symbols and Acronyms

### Variables:

$c_h$  = convective heat transfer coefficient ( $\text{kg/m}^2\text{s}$ )  
 $c_{h,FR}$  = Fay-Riddell reference convective heat transfer coefficient ( $\text{kg/m}^2\text{s}$ )  
 $c_{h,ref}$  = Reference convective heat transfer coefficient from average baseline heating ( $\text{kg/m}^2\text{s}$ )  
 $h_{aw}$  = adiabatic wall enthalpy ( $\text{kJ/kg}$ )  
 $h_w$  = wall enthalpy ( $\text{kJ/kg}$ )  
 $M$  = Mach number  
 $P$  = pressure (psi or psia)  
 $r$  = radial direction in cylindrical coordinates  
 $Re$  = Reynolds number  
 $t$  = time (s)  
 $T$  = temperature ( $^{\circ}\text{F}$  or  $\text{K}$ )  
 $V$  = velocity ( $\text{ft/s}$ )  
 $x$  = distance into test article geometry from surface (m)  
 $z$  = lateral direction in cylindrical coordinates  
 $\alpha$  = angle of attack, degrees  
 $\alpha_d$  = thermal diffusivity,  $\text{m}^2/\text{s}$   
 $\beta$  = thermal product,  $\sqrt{\rho c_p k}$ ,  $\text{J}/(\text{m}^2\text{-K-s}^{0.5})$   
 $\epsilon_{fs}$  = emissivity of phosphor-coated fused silica models  
 $\rho$  = density ( $\text{slug/ft}^3$ )  
 $\phi$  = circumferential direction in cylindrical coordinates

### Subscripts:

$d$  = diffusivity  
 $eff$  = effective  
 $n$  = nose  
 $t,1$  = reservoir stagnation  
 $tw$  = tunnel wall  
 $\infty$  = free-stream conditions

### Acronyms

AEDC = Arnold Engineering Development Center  
AoA = angle of attack  
BL = boundary layer  
BS = bow shock  
CAD = Computer-Aided Design  
CFD = Computational Fluid Dynamics  
CMM = Coordinate Measuring Machine  
CUBRC = Calspan-University at Buffalo Research Center  
DPLR = Data Parallel Line Relaxation  
EDM = Wire Electrical Discharge Machine  
GASP = General Aerodynamic Simulation Program  
IHEAT = Imaging for Hypersonic Experimental Aeroheating Testing  
IR = Infrared

IS = incident shock  
KSC = John F. Kennedy Space Center  
LAL = Langley Aerothermodynamics Laboratory  
LaRC = Langley Research Center  
LAURA = Langley Aerothermodynamic Upwind Relaxation Algorithm  
NASA = National Aeronautics and Space Administration  
NASP = National Aero-Space Plane  
QA = Quality Assurance Branch  
RCC = Reinforced Carbon/Carbon  
RS = reflected shock  
RTF = Shuttle Return to Flight program  
RTV = Room-Temperature Vulcanized silicone rubber  
Scramjet = Supersonic combustion ramjet  
SG = shock generator  
SL = shear layer  
STS = Space Transportation System  
TP = triple point  
TPS = Thermal Protection System  
UV = ultra-violet (radiation)



# 1. Chapter 1: Introduction

Commercial, government and military applications rely on research into safe, reliable hypersonic technology. Access to space, planetary entry vehicles, and advanced long-range weapons are just a few of the areas in which hypersonic flight is a key topic of research [1]. Vehicles designed to fly at hypersonic speeds, such as the Space Shuttle Orbiter and planes with integrated ramjet or supersonic combustion ramjet (scramjet) engines, can be subjected to a phenomenon called shock-shock interactions that cause significant, localized surface temperature and pressure augmentations [2]. Interactions between the vehicle bow shock and the shock around a strut or a wing leading edge can compromise the vehicle's structural components in the absence of protective measures. Numerous experiments were conducted to better understand shock interaction behavior and heating effects that occur in the hypersonic flight regime to aid in the development of sufficient thermal protection systems. These studies helped classify shock interaction types and pointed to the need for improved spatial resolution data in the regions affected by the interactions. Measurement techniques have gradually improved to provide better spatial resolution in shock-interaction heat transfer analyses. The current study examines shock-shock interactions in Mach 6 flow using a global phosphor thermography technique.

This thesis is comprised of six chapters describing the current study and related research. This chapter provides an introduction to the problem, purpose and hypothesis addressed in the current study, as well as a brief comparison between the current work and a previous shock-shock interaction study conducted in the same wind tunnel with similar flow and shock conditions. Chapter 2 presents a review of pertinent shock-shock interaction literature and analyses of one-dimensional (1D) versus two- and three-dimensional (2D and 3D) heat transfer analysis methods. The wind tunnel facility, test set-up, test article configurations and run parameters in the current study are described in Chapter 3. Computer codes used to convert the experimental wind tunnel data to temperatures and heat transfer coefficients are discussed in Chapter 4. Chapter 5 outlines key results from the thin-film-gage, oil flow visualization, zoom schlieren, and phosphor thermography tests conducted as a part of this study. Finally, conclusions based on the results are listed in Chapter 6, followed by references and appendices.

## 1.1. Current study overview

The current study is primarily a wind tunnel experiment to obtain temperature versus time profiles along the cylindrical leading edge of blunt bodies (called test articles) with different diameters in the National Aeronautics and Space Administration (NASA) Langley Research Center (LaRC) 20-Inch Mach 6 Air Tunnel. The test articles were exposed to incident shocks from flow over a 2D wedge that interacted with the blunt body bow shock and caused increased heating in a localized region on the surface of the test article. These test articles are representative of leading edges of wings or struts on a hypersonic vehicle in which a planar shock around the bow of the vehicle bisects the bow shock around a cylindrical fin shape.

Multiple test techniques were utilized during this study. Oil flow techniques and high-speed schlieren were used to visualize the shock-shock interactions. Global surface temperature data was acquired using the phosphor thermography technique. For the cases with the most severe heating, the temperature-time data were reduced using 1D semi-infinite and finite-volume

techniques. These 1D codes only consider heat transfer from the surface into the test article. Additionally, a 2D finite-volume, direct-method conduction code was employed for a few of the cases with lower peak heating levels to investigate the need for a multi-dimensional conduction analysis for aeroheating tests that involve shock-shock interactions. The 2D code considered conduction through the thickness of the test article and along the leading edge. The third dimension was neglected because the temperature gradient close to the peak in the shock-shock interaction region was expected to be much smaller around the circumference of the leading edge ( $dT/d\phi$ ) than along the leading edge ( $dT/dz$ ). Wright et al. [3] found that circumferential heat flux gradients are an order of magnitude smaller than the longitudinal gradients (along the leading edge of the test article). A supplemental computational study was conducted using the Langley Aerothermodynamic Upwind Relaxation Algorithm (LAURA) code to provide further visualization of the shock interaction processes and surface heating patterns with time.

### **1.1.1. Problem statement**

Many tools are available to estimate reentry heating environments at hypersonic conditions. Discrete thin-film temperature gages and heat flux sensors, and global techniques, such as IR and temperature-sensitive paints are examples of experimental tools used in aeroheating measurements in wind tunnel tests. Compressible flow computational solvers are also available for heat transfer analysis. At NASA LaRC, a global phosphor thermography technique is utilized in wind tunnel experiments to measure aeroheating behavior [4]. The Imaging for Hypersonic Experimental Aerothermodynamic Testing (IHEAT) program is used to reduce phosphor thermography data to surface heat transfer coefficients for cast fused-silica ceramic wind tunnel models [5]. Another program called 1DHEAT is used to reduce thin-film gage data [6]. These two codes employ approximations to perform one-dimensional calculations from available test article surface temperature data.

The one-dimensional approximation used in the IHEAT analysis works well for short duration hypersonic wind tunnel tests that last no longer than a second [5]. For certain fused silica model geometries, the 1D approximation is assumed to be acceptable for phosphor thermography tests in the 20-inch Mach 6 facility that last between 5 and 10 seconds. For example, phosphor thermography data 3 seconds into a wind tunnel run was reduced using IHEAT in reference [7]. However, in some cases the heating profile and model geometry amplify the errors in the 1D heat transfer assumption. The current study briefly addresses the problem of whether the errors associated with neglecting lateral conduction in a 1D approximation of the heat transfer induced in a test article by a shock interaction are sufficiently large to necessitate a 2D or 3D analysis.

### **1.1.2. Purpose statement**

Thermal Protection Systems (TPS) are intended to protect space vehicles from the high thermal loads of reentry that could cause structural damage. Vehicles that travel at hypersonic speeds are subjected to shock waves that form around the nose of the vehicle, at the leading edges of wings and tails, and on control surfaces; these shocks can interact, augmenting the heat transfer to the vehicle's surface. Hypersonic aeroheating environments are modeled in ground-based testing and through computational methods to predict the heat flux to the vehicle surface. The heat flux and thermal load predictions are then used to design the TPS for the given flight trajectory.

The main purpose of this study is to characterize a subset of shock-shock interaction types for test articles with varying leading-edge radii. Knowledge of shock-interaction behavior relative to the geometry of a supersonic or hypersonic vehicle is necessary to balance the design considerations of drag and heating. A secondary purpose of this study is to investigate the effects of multi-dimensional conduction in test articles that represent the leading edges of hypersonic vehicles. The results of the 1D and 2D calculations were compared to determine which heat transfer analysis approach is required to minimize errors when strong temperature gradients are present on the test article surface, as in the current shock-shock interaction study. The experimental results were also compared to 3D computational simulations of the investigated shock-shock interactions.

### **1.1.3. Hypotheses**

In each wind tunnel run, the nose radius and angle of attack of the test article were specified as independent variables in the test matrix. The features of the three shock-shock interactions considered in this study were hypothesized to be similar for each test article leading-edge radius. Based on an earlier study in the 20-Inch Mach 6 Air Tunnel, the heating augmentation for wind tunnel runs in which the leading edge of the test article was perpendicular to the Mach 6 flow (a  $0^\circ$  angle of attack) was expected to be lower than the peak heating levels for the other two angles of attack considered in this study [8]. Another hypothesis is that as the diameter of the test article's leading edge increased, the effects of lateral conduction would decrease, assuming the thicker test article would behave more like the approximated semi-infinite solid during a short wind tunnel run. The applied heat was expected to diffuse more in the larger diameter models, yielding lower maximum temperatures at the surface of the model in the region of the shock-shock interaction region. In other words, a 1D approximation is more accurate as the model size increases, so a 2D conduction analysis was predicted to be less critical as the leading edge diameter of the test article was increased. Watts [9] mentioned the possibility of reducing heating due to a shock-shock interaction by increasing either the leading-edge radius or the sweep angle of a pylon on the X-15A-2 research plane.

Another hypothesis of this study is that a heat transfer analysis assuming 1D conduction through the test article thickness is insufficient in the presence of a large lateral temperature gradient produced by a shock-shock interaction. The 2D conduction analyses were expected to predict sharper and higher peak heat transfer coefficients than the 1D codes where the shock-shock interaction impinges on the test article. At surface locations with gradual temperature variations or uniform temperatures or in runs with no incident shock, the 1D and 2D heat transfer results were expected to be similar. Studies that support this hypothesis are discussed in section 2.5 of the literature review.

### **1.1.4. Application to future aerothermodynamic tests**

Although the specific cases considered in this study deal with increased heating due to shock-shock interactions, multi-dimensional heat transfer analysis may be required for many other aerothermodynamic problems. Test configurations with significant temperature variations include test articles with thin geometric features or sharp corners (for which an infinite thickness assumption is inaccurate) or, to a lesser extent, models with boundary layer (BL) trips that cause

early or rapid transition from laminar to turbulent flow [7]. Occasionally, vehicle designs are tested in which jets of hot air impinge on a vehicle, increasing the local heating rates, as is the case when reaction control system (RCS) jets impinge on the International Space Station during close-range maneuvers [10]. The 2D finite-volume code can be modified to apply to additional wind tunnel test article geometries and used to provide a more conservative estimate than the IHEAT heat transfer coefficients in regions of steep temperature gradients. The 1D finite-volume code can be used to check the 2D code assumptions in regions with smaller temperature gradients.

## **1.2. Comparison to a previous shock-shock interaction study (Test 6692)**

The present experiment utilized hardware that was previously developed in the early 90's for a shock-on-fin study during Test 6692 [8]. The previous study specifically examined the effect of the fin sweep angle on the heating augmentation due to a planar shock interaction. The present study focuses on the impact of a multi-dimensional analysis approach to the problem of shock impingement heating. The facility, hardware and approach are similar between the two studies. In the current study, similar test articles with cylindrical leading edges with a range of nose radii were tested to determine the importance of considering 2D conduction in regions of steep temperature gradients as the thickness of the test article increases. The current study focused on the peak heating caused by Type III and IV interactions [2] caused by a subset of the fin sweep angles examined in the Berry and Nowak study [8]. The main difference between the two studies is that the focus of the current study is a deeper investigation into the post-test analysis assumptions, specifically the effect of 1D versus 2D analysis of the temperature versus time data, and the effect of leading-edge radius.

## **1.3. Thesis objectives and goals**

The main objective of this thesis is to investigate shock-shock interactions experimentally that could affect the flight of supersonic and hypersonic vehicles. One goal of this thesis is to characterize the type of shock interactions produced for different relative angles between the incident shock and leading-edge bow shock using high-speed experimental zoom schlieren videos and images. This schlieren data was compared to numerical schlieren data obtained for selected test article configurations and used to verify the correlation between the increase in peak heating and the shock-shock interaction type. Another goal of this thesis is to analyze the flow streamlines over the test articles using oil flow visualization techniques. Oil flow videos and images were obtained to provide insight into the possible flow pattern near the surface of the model to help explain the shape of the heating profile for each type of shock-shock interaction on each of the three test article geometries.

Finally, a second objective of this thesis is to examine the error associated with assuming 1D conduction in a test article by comparison to a 2D analysis for a series of leading-edge diameters with strong heating gradients due to shock interactions. Therefore, the final goal of this thesis is to compare test article heating profiles calculated using a standard 1D code (IHEAT) to results from 1D and 2D finite-volume conduction codes.

## **2. Chapter 2: Literature review**

Several experiments and numerical studies have been conducted to better understand the impact of shock-shock interactions on flight programs. Previous experiments and computational studies that are related to the current study are described in this chapter. Normal and oblique shocks and shock-shock interactions are briefly defined in section 2.1. Different types of shock-shock interactions, including the Type III and Type IV interactions considered in the current study, are discussed in section 2.2. Examples of vehicles affected by shock-shock interactions are described in section 2.3. Section 2.4 presents the key conclusions of other tests involving shock-shock interactions on a blunt body. Finally, section 2.5 discusses computational and wind tunnel experiments that evaluate the difference between 1D and 2D heat transfer analysis methods for test articles with sharp surface temperature gradients.

### **2.1. Background information**

A shock is defined as a “mechanical wave of large amplitude” that propagates at a supersonic velocity, across which fluid properties such as the pressure, temperature and density change in a “nearly discontinuous manner” [11]. The velocity of a shock wave is amplitude dependent. Plane shocks can be normal (oriented perpendicular to the direction of the flow) or oblique (at a non-orthogonal angle to the flow) [12]. The pressure of a fluid increases and the velocity decreases when a shock is crossed. The fluid flow direction also changes if the shock is oblique. Shock-shock interactions in hypersonic flow, as described in this thesis, involve an oblique incident shock that intersects a bow shock around a blunt body.

### **2.2. Edney types of shock-shock interactions**

Edney [2] identified six types of interactions between bow shocks around blunt bodies and incident shocks. The relative angle between the incident shock and the bow shock, as well as the strengths of these two shocks, dictate the features of the resulting shock impingement, such as the angle of the reflected shock, the number of shear layers that form, or the presence of a supersonic jet. These shock-shock interactions are sketched in Figure 2-1 and more detailed sketches of these interactions are available in reference [2] and on page 54 in reference [13].

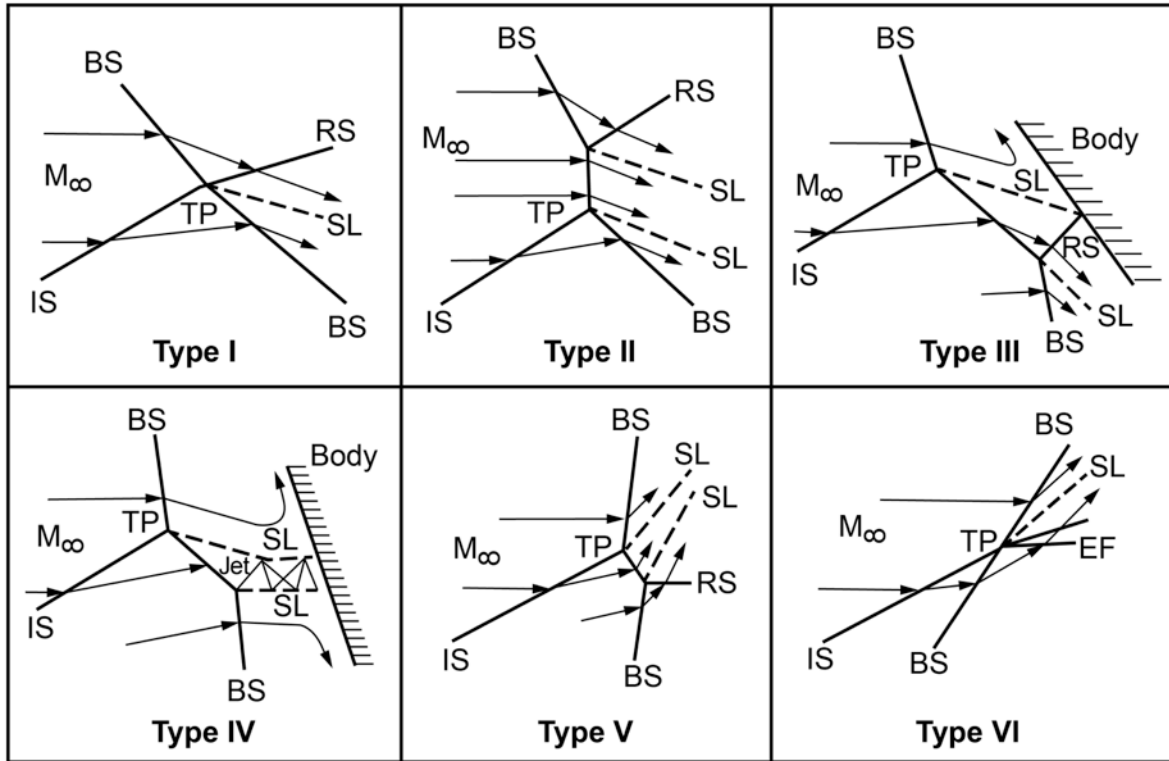


**Figure 2-1.** Edney catalogued the shock interaction types in this diagram, IS = incident shock, BS = bow shock, RS = reflected shock, EF = expansion fan, TP = triple point, SL = shear layer (diagram used with Berry's permission [8]).

Edney's shock impingement investigation was prompted by experiments with a Pyrex® hemisphere model with platinum thin-film gages. During wind tunnel runs, a spike in the heat transfer occurred over a narrow region on the hemisphere as the model passed through a "weak" extraneous shock generated by a splitter plate. Surprised by this observation, Edney conducted additional experiments in which the hemispherical glass model was positioned in multiple locations relative to an incident shock from a 2D wedge. In each case, Edney aimed for a separation of at least one model diameter between the extraneous shock and the boundary layer of the flat plate as was done in the current study. The heat transfer to the model was calculated using the temperature data from six thin-film gages as the model passed through the incident shock during a one-second long wind tunnel injection, neglecting conduction and radiation losses from the model during the short time the shock-shock interaction existed.

Edney ran similar tests using models with pressure manometers and one model with a single pressure transducer to measure the pressure distributions due to a shock-shock interaction. The results of those tests indicate a pressure peak or discontinuity typically occurs where a shear layer, supersonic jet, shock or expansion fan generated in the shock-shock interaction impinges on the model surface. To visualize the flow, Edney took pictures of the density gradients in the interactions using an 80 frame per second (fps) schlieren system. Based on these tests, Edney used graphical and numerical techniques to estimate the type and shape of a shock interaction. The location of the shock impingement impacts the type of interaction that occurs. For example, if the shock impinges within the subsonic region, the interaction is either Type III or IV.

In the current study, Type III and Type IV (both direct and glancing) shock-shock interactions were investigated. Edney stated that the peak heating associated with a Type III interference is attributed to a free shear layer attaching to the body, much like in separated flows. The shear layer can be either turbulent or laminar, depending on the Mach number of the free-stream flow ahead of the shock interaction. The flow between the bow shock and shear layer is supersonic in this type of interaction for a blunt body. A detailed sketch of this interaction in Figure 6.10 on page 33 in reference [2] shows the locations where the flow is either subsonic or supersonic, including triangular regions between the bow shock and the reflected shock and between the reflected shock and the model of the vehicle. The Type IV interaction yielded the highest peak heating augmentation in Edney's study. In this interaction, a supersonic jet either curls upward (as in a Type IVa interaction) or impinges directly on the blunt body. Reflected shocks between two shear layers in this supersonic jet produce shock triangles that are also referred to as a shock train. The direct impinging Type IV interaction is shown in Figure 2-1. As the shock impingement point moves up the body, the width of the supersonic jet decreases and the jet turns further upward. From an oil flow test with an unswept cylinder, Edney found the flow was only 2D directly on the model leading edge, and a "dead-air region" existed below the jet impingement point for the Type IV interaction. Oil flow images in Chapter 5 display similar behavior for this type of interaction.

### **2.3. Effect of shock-shock interaction heating on hypersonic vehicles**

When a vehicle flies at supersonic or hypersonic speeds through the atmosphere, the vehicle heats up as the air in front of the vehicle is compressed. Heating profiles observed on scaled test articles during wind tunnel experiments are used to develop thermal protection systems for use on aeronautical and space vehicles flying at high speeds through an atmosphere (on Earth or on Mars, for example). Shock-shock interactions are important phenomena in supersonic and hypersonic aviation because the location on a flight vehicle where a shock-shock interaction impinges experiences increased heating and pressure levels that can damage the vehicle's structural components. The necessity of considering heating augmentation due to shock-shock interactions is evident in real flight scenarios.

Edney described three general cases in which shock-shock interactions could occur in flight (refer to Figure 1.4 in reference [2] for a diagram of these cases). One possible case is the interaction between a planar extraneous shock and the shock around a cowl lip on a vehicle with either a ramjet or a scramjet engine. During the flight of a missile, the bow shock that originates at the nose of the missile can interact with the shock around a fuel tank or a booster attached to the missile. The interaction simulated by the test set-up in the current work is the intersection between a bow shock around an aircraft fuselage and the shock around a strut (fin) leading edge. The cowl and struts for a hypersonic vehicle are shown for reference in Figure 2-2. The difference between a "shock-on-cowl" and a "shock-on-fin" interaction is described further in section 2.4.

## Shock Interaction on Hypersonic Flight Vehicles

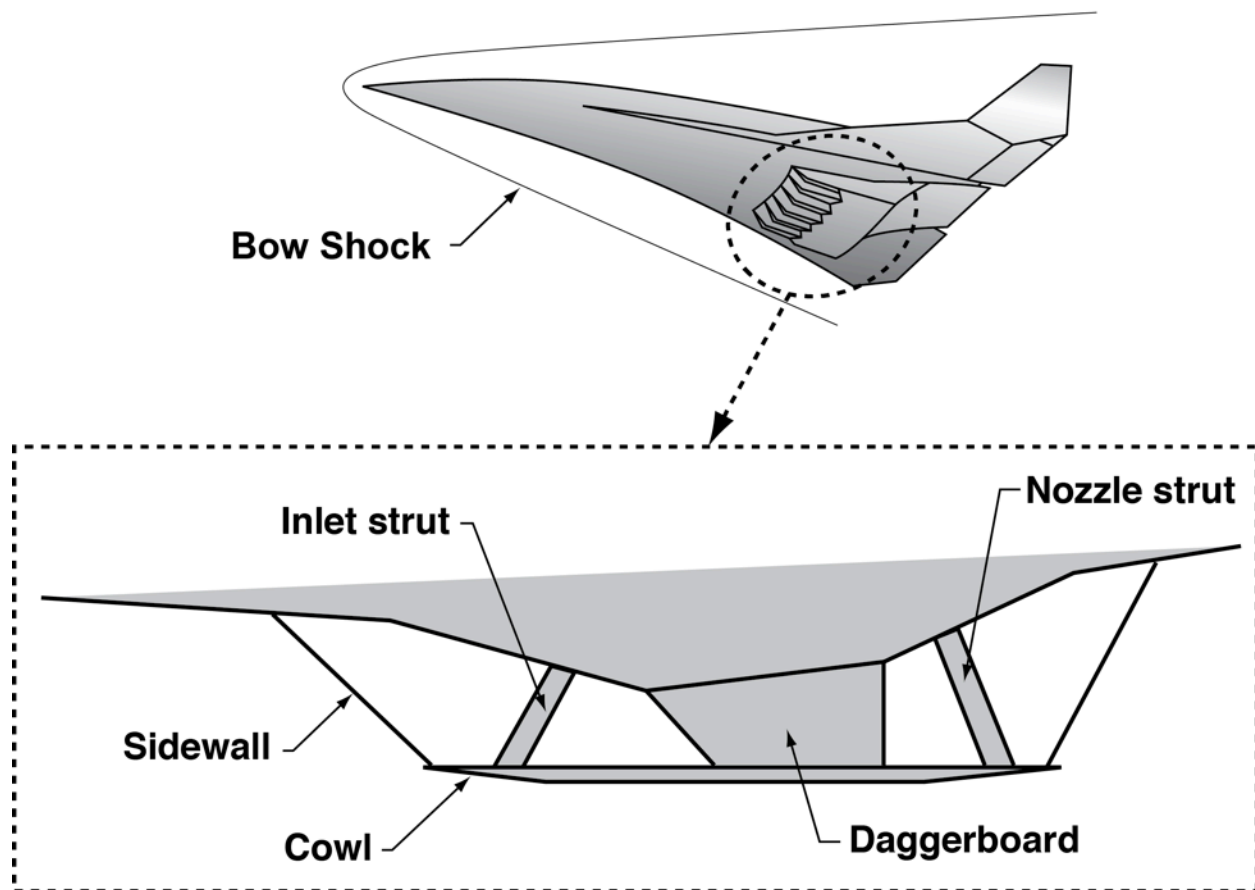


**Figure 2-2.** Hypersonic flight vehicle configuration (image used with Berry's permission [8]).

Edney also mentioned the record-setting flight of the NASA X-15A-2 plane that demonstrated the damage that increased heating due to shock-shock interactions can cause [2]. The X-15A-2 (or X-15-2) research plane was structurally modified to include a longer fuselage than a regular X-15 airplane and flew in several test flights with a dummy ramjet attached to the fuselage as shown Figure 2-3 [9]. The goals of this flight program were to assess an ablative thermal protection system on both the vehicle and the ramjet engine and to understand how installing a ramjet engine would change the flight behavior of the X-15-2 as the vehicle flew at increasingly faster speeds [14].



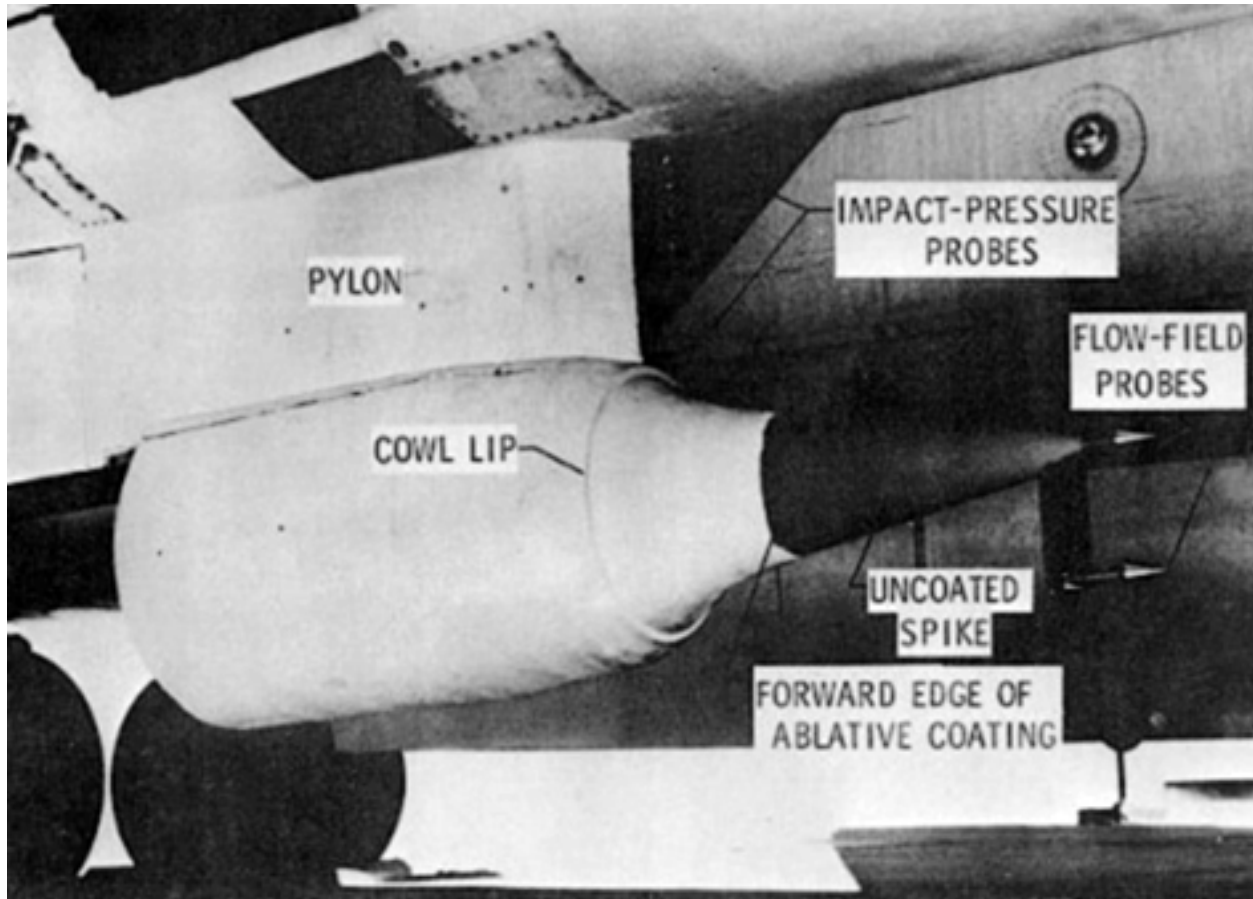


**Figure 2-3.** Dummy ramjet installed on the fuselage of the X-15-2 plane (image reproduced from a NASA report [9]).

During one test flight with the dummy ramjet, the X-15-2 plane reached a speed of Mach 6.7 [9]. While the vehicle flew at hypersonic speeds, the fuselage of the X-15-2 acted as a flat plate that generated a shock that impinged on the shock around a cylindrical leading edge of the pylon attached to the dummy ramjet engine. Additional shocks around the uncoated spike and the impact pressure probes also may have intersected the shock around the pylon, contributing to the heat transferred to the pylon by the shock-shock interaction. The pylon suffered heating damage as the rocket engines on the X-15-2 shut down (just as the vehicle reached the peak speed), but the dummy engine did not separate from the vehicle until the plane had slowed down to approximately Mach 1. The dummy ramjet crashed on the Edwards bombing range as the plane approached Edwards Air Force Base, and the remains of the engine are shown in Figure 2-4.



**Figure 2-4.** Damaged dummy ramjet after impact on Edwards bombing range (image reproduced from a NASA report [9]).

The ablator around the pylon leading edge at the bottom of the fuselage was completely eroded during the flight, which led to permanent deformation of the underlying skin of the vehicle. Based on recorded and calculated temperature time histories, the substrate material reached high enough temperatures (about 1400°F) to permanently buckle the Inconel X in the shock-shock interaction region on the fuselage as shown in Figure 2-5. Also, the 4130 steel at the ramjet cowl lip melted when temperatures (2795°F) briefly exceeded the melting point, as shown in Figure 2-4, and parts of the pylon that held the ramjet melted as shown in Figure 2-5.



**Figure 2-5.** Damaged X-15-2 pylon from Mach 6.7 shock interference heating (images reproduced from a NASA report [9]).

Watts reiterates the requirement to exercise caution when designing hypersonic vehicles exposed to shock impingement and shock-interference heating, as the X-15A-2 example demonstrates. Watts states that shock impingement could raise vehicle temperatures beyond the maximum allowable temperatures of “high-performance metals” unless the structural geometry is “designed to minimize aerodynamic heating” [9]. The metals mentioned in this paper are columbium, tantalum and tungsten, with melting points of 4474°F (2468°C), 5425°F (2996°C) and 6100°F (3370°C), respectively.

The Space Shuttle Orbiter is another example of a vehicle that is susceptible to shock-shock interaction heating at supersonic and hypersonic speeds. As the Space Shuttle accelerates during ascent in a mated configuration with rocket boosters, the six Edney interactions develop from intersections between shock waves around the nose, fuel tank, or wings of the Orbiter and the attached rockets [13]. On re-entry, shock waves around the same surfaces of the Orbiter interact as the vehicle decelerates, again producing shock interference heating [15].

The sweep of the Shuttle wings influences the types of interactions that form. Keyes and Hains [13] pointed out that “sweeping back wings and control surfaces” can eliminate regions of increased heating due to shock-shock interactions. Bertin and Cummings [16] reiterate this concept, stating that the interaction between the vehicle bow shock and wing leading-edge shock transitioned from a Type V interaction for a proposed straight-wing Orbiter to a Type VI interaction for delta-winged Orbiters. Space Shuttle Orbiter wings were covered with reinforced carbon/carbon (RCC) tiles to protect the wing from the expected extreme temperatures (above 1530K or 2294°F). Bertin and Cummings explain that the radii of the nose cap (also protected with RCC) and the wing leading edges are sufficiently large to mitigate the effects of shock interference heating on the Shuttle provided the RCC thermal protection system remains intact. Changing the wing geometry is not feasible with all supersonic or hypersonic vehicles, since designers must balance the tradeoff between increased drag and reduced heating due to an increase in wing leading-edge radius.

The “Columbia” Space Shuttle Orbiter shown in Figure 2-6 was launched from John F. Kennedy Space Center (KSC) on January 16, 2003 for a 16-day research mission labeled Space Transportation System (STS) mission 107 [15]. During the launch, a piece of insulation foam dislodged from the rocket boosters and struck the thermal protection system on the Shuttle’s left wing. Video footage that shows the foam impacting the Shuttle is represented by the images included in Figure 2-7. This problem of “shedding foam” was not uncommon for a Shuttle launch. The day after the launch, radar showed an object approximately the size of a carrier panel, which interfaces between the Shuttle and an RCC panel, detached and fell from the spacecraft. The mission continued without Shuttle repairs, and the Earth landing was scheduled for February 1, 2003.

During re-entry, Columbia was subjected to “unusual aerodynamic forces” on the left wing soon after the vehicle entered the atmosphere. Temperature sensors on the vehicle failed, and debris was shed from the descending Shuttle until Columbia broke apart 200,000 feet above Texas. Damage from the impact of the insulation foam may have led to an RCC panel detaching from the Shuttle, which in turn may have contributed to further damage during re-entry.





**Figure 2-6.** KSC Launch of Columbia STS 107. Reinforced carbon/carbon protects the wing leading edges on this vehicle. (CAIB photo by NASA, January 16, 2003 [17])

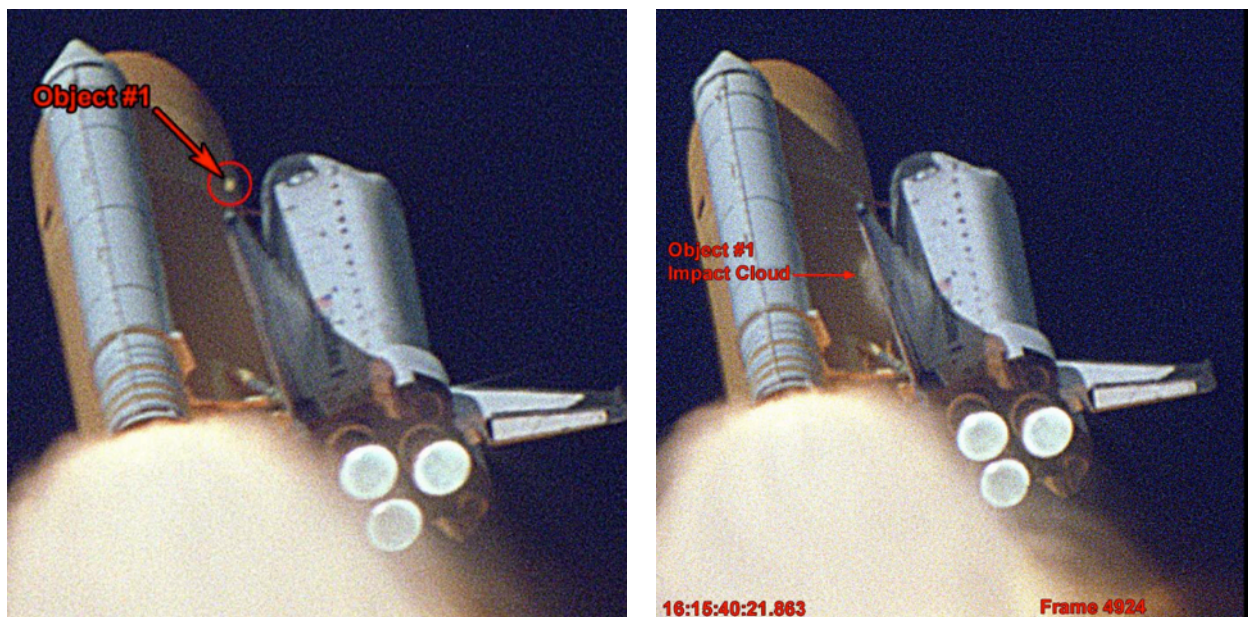


**Figure 2-7.** Image from video of STS 107 launch, which showed shedding debris impacting the left Columbia wing. (CAIB photo by NASA, January 16, 2003 [18])

After the accident, several computational and wind tunnel investigations were carried out during the Shuttle Return to Flight (RTF) program to determine the likely cause and whether future accidents could be avoided. The general conclusion is that heated air was ingested into a small breach in the leading edge of the Shuttle's left wing, yielding elevated temperatures, burning through instrumentation wiring, and finally causing the structural failure of Columbia. Recovered remains of the Space Shuttle used in the accident investigation are shown in Figure 2-8. Analysis of the damaged components suggests the breach in the wing began at, or close to, RCC panels 6 and 9. Bertin surmised that if additional RCC panels were missing, in effect negating the wing sweep in that region, then the breach would be exposed to "strong interactions and very large heating" since two hypersonic shock waves intersect near panel 9 in a Shuttle descent trajectory [15]. The Columbia accident highlights the potential for shock-interaction damage on any hypersonic vehicle if the designed thermal protection system is compromised.



**Figure 2-8.** Recovered Columbia debris after break-up during re-entry. (CAIB photo by NASA, March 18, 2003 [19])

Strong Type III and IV shock-shock interactions are possible during hypersonic flight on forward swept leading edges inside scramjet engines [3]. Potential applications for scramjet vehicles include cruise missiles, long-range aircraft, and single-stage-to-orbit (SSTO) space vehicles [1]. Notable experiments include the X-43A and the X-51A. The X-43A burned hydrogen fuel to accelerate the vehicle to speeds of either Mach 7 (briefly) or Mach 10 (for about 10 seconds) in separate flight tests, as described in references [20] and [21]. The X-51A "WaveRider" burned JP-7 hydrocarbon fuel for 200 seconds to accelerate the vehicle to Mach 5 [22]. Another major scramjet project was the development of the National Aero-Space Plane (NASP), also known as the X-30. The goal for this aircraft was to design a vehicle to fly in subsonic to hypersonic flight regimes with a combined low-speed accelerator, ramjet and scramjet propulsion system [1].

The Hypersonic International Flight Research Experimentation (HIFiRE) Program and other research groups are still investigating this method of propulsion with wind tunnel and flight

experiments [7]. If this technology is implemented in a military, government or commercial aircraft or space vehicle, the heating augmentation due to shock-shock interactions will be a fundamental consideration in the vehicle design process, especially if speeds at or above Mach 6 are sustained for longer periods of time. Engine or structural failure is unacceptable in either hypersonic missiles used to quickly strike long-range targets or in manned hypersonic vehicles.

## 2.4. Previous shock-shock interaction wind tunnel studies

Numerous shock-shock interaction studies have focused on the 2D shock-on-cowl interaction in which a planar incident shock intersects the bow shock around a cowl leading edge that is parallel to the plane of the incident shock [3]. The current study investigates 3D shock-on-fin interactions due to a planar incident shock impinging on a bow shock of a leading edge that is nearly perpendicular to the plane of the incident shock. These two shock interaction types are shown in an unclassified chart developed during the NASP program in Figure 2-9. The following four studies describe the effects of a Type III or IV interaction on the cowl lip of a hypersonic vehicle (represented by a hemisphere or a cylinder parallel to the plane of the incident shock). These studies are followed by references to previous shock-on-fin cases.

## SHOCK/SHOCK INTERFERENCE ON ENGINE LEADING EDGES

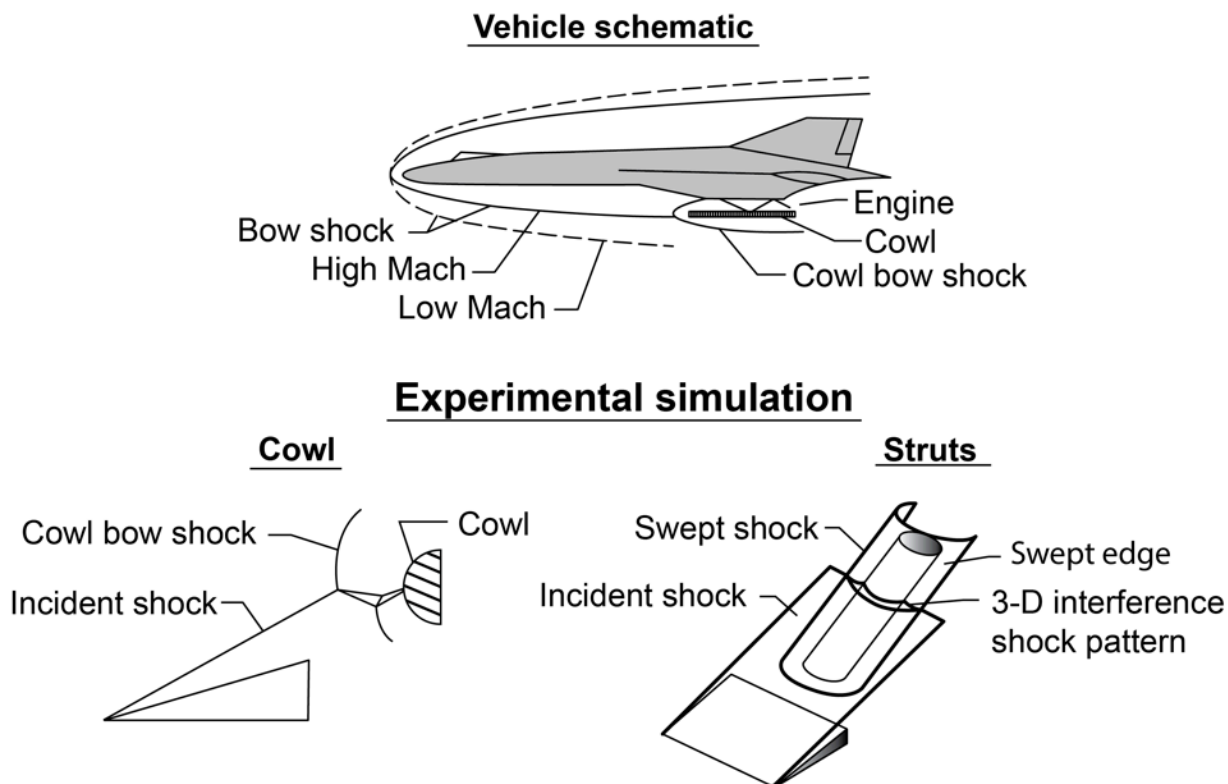


**Figure 2-9.** Shock-on-cowl and shock-on-fin types of shock-shock interactions (image used with Berry's permission, not previously published)



Wieting [23] summarizes computational and experimental studies conducted during the NASP program to model “shock interference heating in scramjet engines”. According to Wieting, the areas of scramjet engines that experience the highest heating loads are leading edges, such as the “cowl leading edge, inlet axial compression corners and the combustor.” Wieting describes a shock-on-cowl study in which a wedge with a sharp leading edge was angled at  $10^\circ$  to  $15^\circ$  to the free-stream flow to produce an incident shock on a 3.0 in-diameter cylinder that was axially aligned with the planar shock. The summary of shock-shock interaction experiments in this report describes the heating loads expected on surfaces of the NASP engine, including the cowl lip represented by the cylinder.

Wieting references a study in which Nowak et al. [24] investigated the use of a coolant to reduce the peak heat load caused by a shock impinging on a bow shock of a 12.0 in-diameter hemispherical model. A blunt, flat plate, inclined at  $10^\circ$  to the free-stream flow produced the incident shock waves. The purpose of this study was to determine if transpiration cooling could reduce peak heat loads for a similar shock-shock interaction on the cowl lip of the NASP. The use of the coolant reduced the heat flux caused by a shock-shock interaction on a hemisphere as the plot in Figure 2-10 shows. The heat flux distributions in Figure 2-11 show an 8.3% decrease in the peak heat flux when coolant flows through the hemisphere compared to a case with no coolant. The Wieting and Nowak et al. studies reported the local heat flux in the interaction region increased by a maximum of 30 times the stagnation point heat flux in undisturbed flow (with no shock-shock interaction).

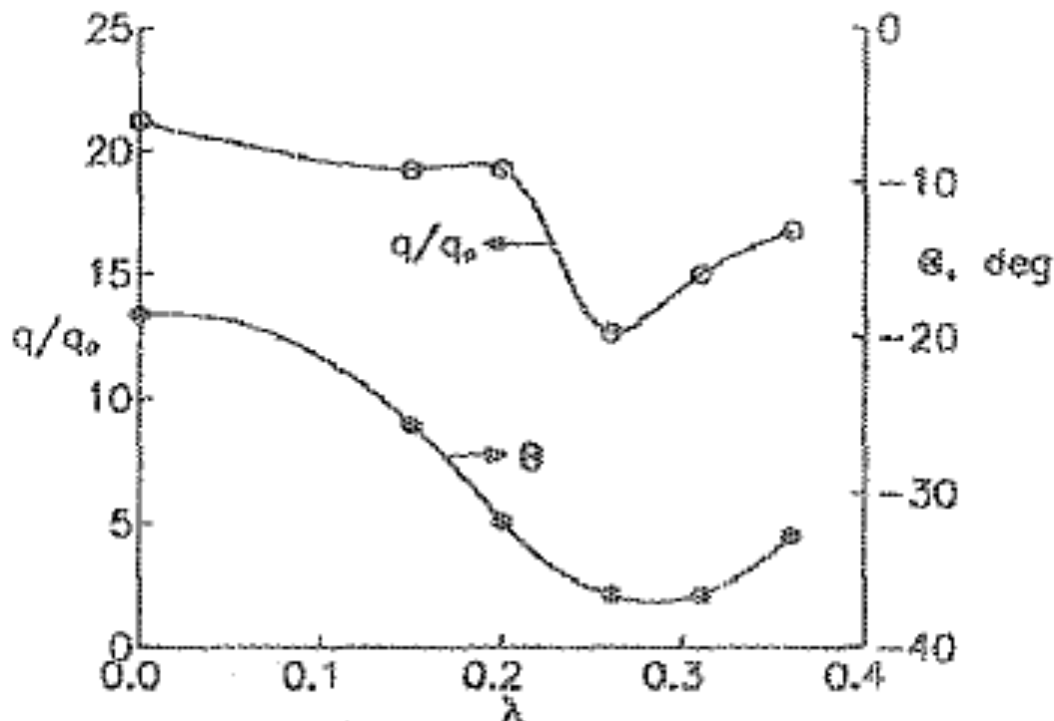


**Figure 2-10.** The effect of the coolant mass flux,  $\lambda$ , with a fixed incident shock, on the peak heat flux and the angle  $\Theta$  measured from the model centerline (image used with Nowak’s permission [24]).

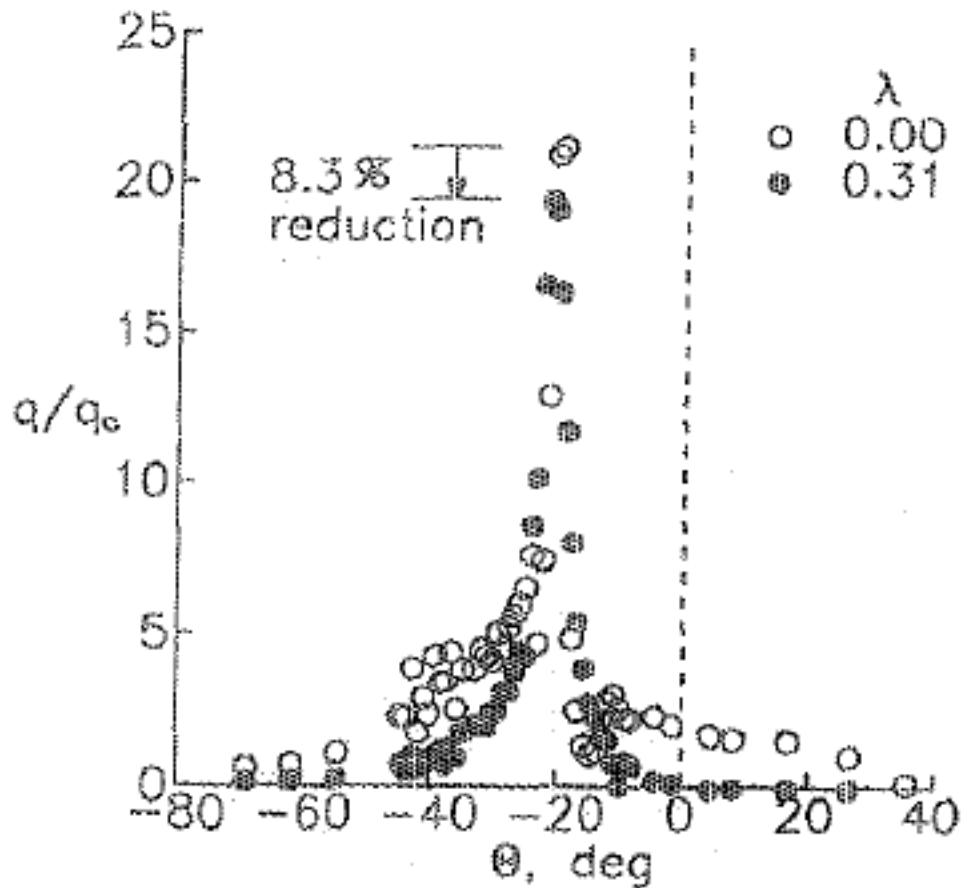


**Figure 2-11.** Heat flux distribution for a Type IV interaction on a hemisphere with either a non-dimensional coolant mass flux of  $\lambda = 0$  (no coolant) or  $\lambda = 0.31$  (image used with Nowak's permission [24]).

Stewart et al. [25] investigated the effects of oblique shock impingement (generated by a  $10^\circ$  or  $12.5^\circ$  wedge) on a leading edge that represented an engine cowl lip in inviscid hypersonic flow. Stewart, et al. used the Galerkin-Runge-Kutta time-stepping method with finite elements to discretize the compressible Euler equations. When the flow is at a high velocity (up to Mach 16) the shock standoff distances are small, so the air was assumed to be in a non-equilibrium state. Non-equilibrium states are difficult to model, so two data sets were considered in this study: solutions obtained with a calorically perfect gas model and air in chemical equilibrium, since these two models "bracket the non-equilibrium state." The LAURA simulations in the current study used the perfect gas model to mimic the conditions in the wind tunnel experiments.

Stewart et al. discovered the location of the sonic point on a vehicle changes based on the shape of the bow shock due to the intersection with an incident shock in a shock-shock interaction. Thus, simulations in which the flow conditions behind an oblique shock are set in certain regions of the flow based on the undisturbed bow shock shape may yield different interactions than the predicted types. In one case at Mach 6.5 in which a Type V interaction was expected, Stewart et al. instead observed a Type IVa interaction in which the supersonic jet curled upward away from the axially horizontal cylinder, as shown in image a in Figure 2-12. Stewart et al. described the supersonic jet that passes through a nearly normal shock in a regular Type IV interaction as



likely unsteady and moving back and forth within a small area. The Type III and Type IV interactions also display unsteady behavior in the shock-on-fin cases of the current study.

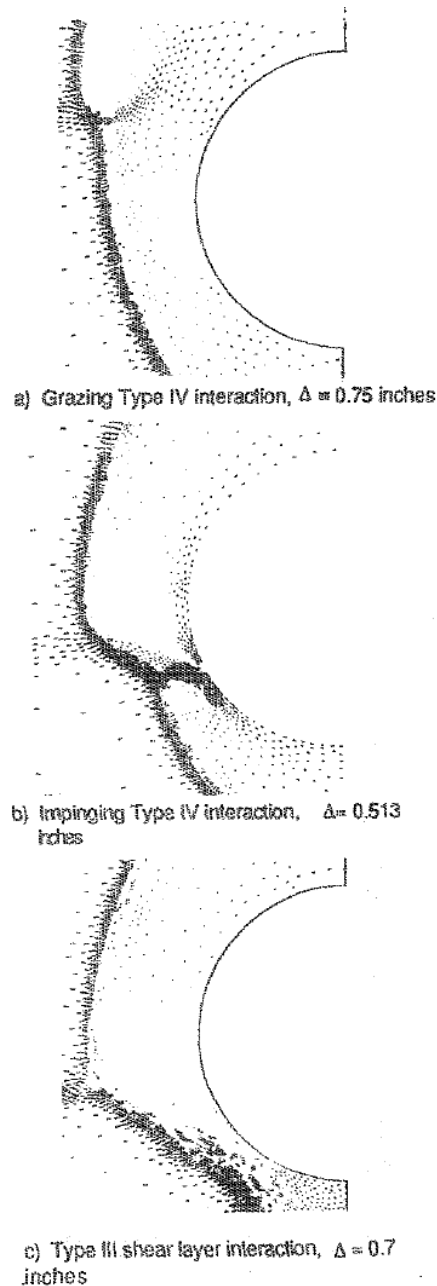


**Figure 2-12.** Mach 6.5 velocity vectors from the computational simulations of different types of shock-shock interactions (image reprinted with permission of the American Institute of Aeronautics and Astronautics [25]).

Vemaganti and Wieting [26] conducted similar computational simulations to study viscous flows using finite element methods to discretize the Navier-Stokes equations. Vemaganti and Wieting state that unstructured meshes are better suited for complicated geometries and adapting the grid relative to the physics of the flow, but structured meshes are better able to “predict aerodynamic

heating” in boundary layers. Grids that were structured in the boundary layer and unstructured in the remaining elements were used to obtain information about a shock-shock interaction in Mach 8 flow over a 3.0 in-diameter cylinder that represented a cowl leading edge. The diagram in Figure 2-13 shows this combination of structured and unstructured meshes. These computational fluid dynamics (CFD) simulations were conducted using the Streamline Upwinding Petrov-Galerkin/least squares (SUPG) method and the results, which agreed well with data from another numerical simulation, were compared to experimental data. Vemaganti and Wieting assumed laminar flow in the simulations, because SUPG did not model turbulence, and attributed the difference between the numerical and experimental non-dimensional heat transfer ( $q$ ) results in Figure 2-14 to this required assumption.

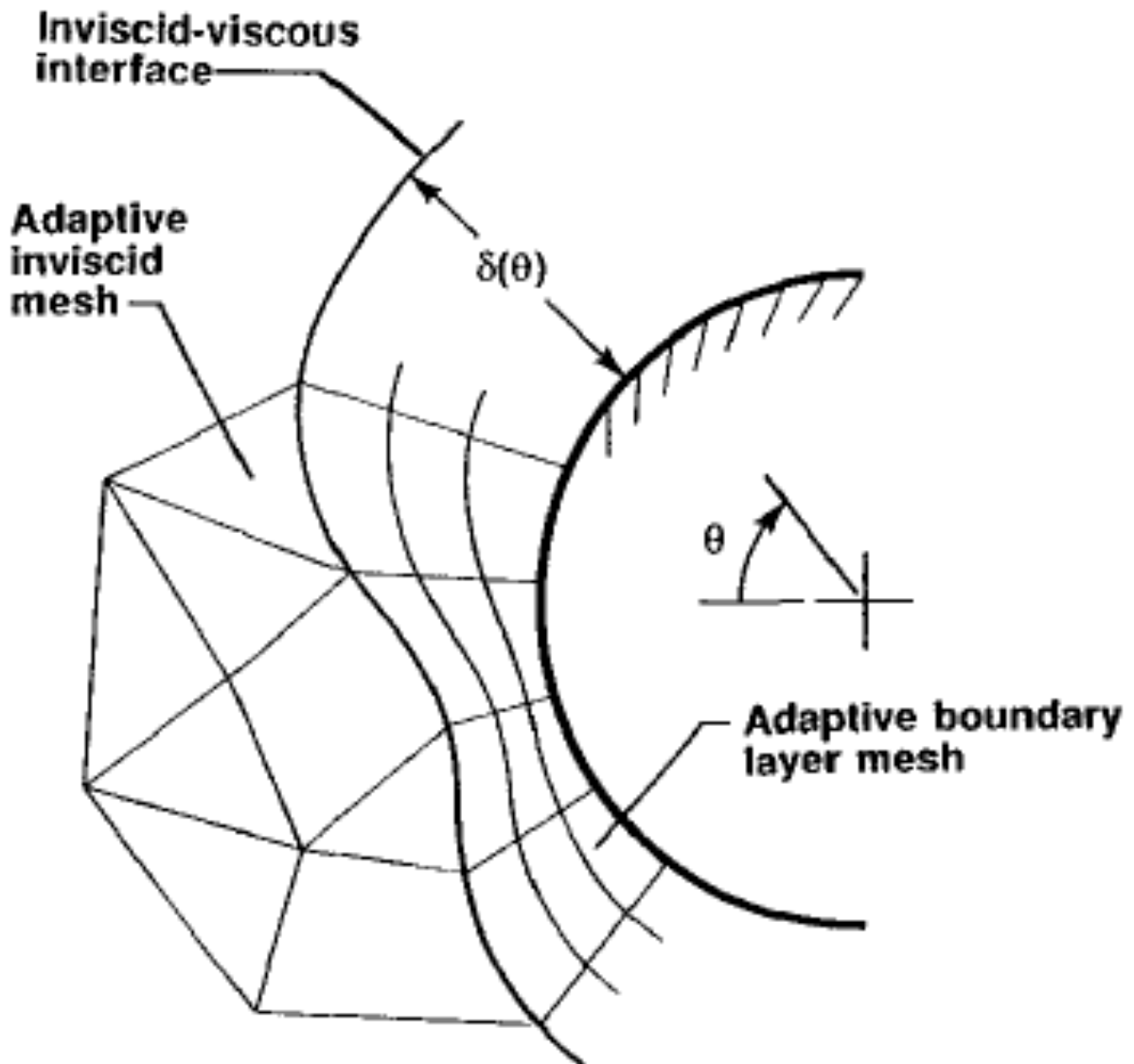


**Figure 2-13.** Structured and unstructured meshes combined into a single grid for the shock interference problem (image reprinted with permission of the American Institute of Aeronautics and Astronautics [26]).

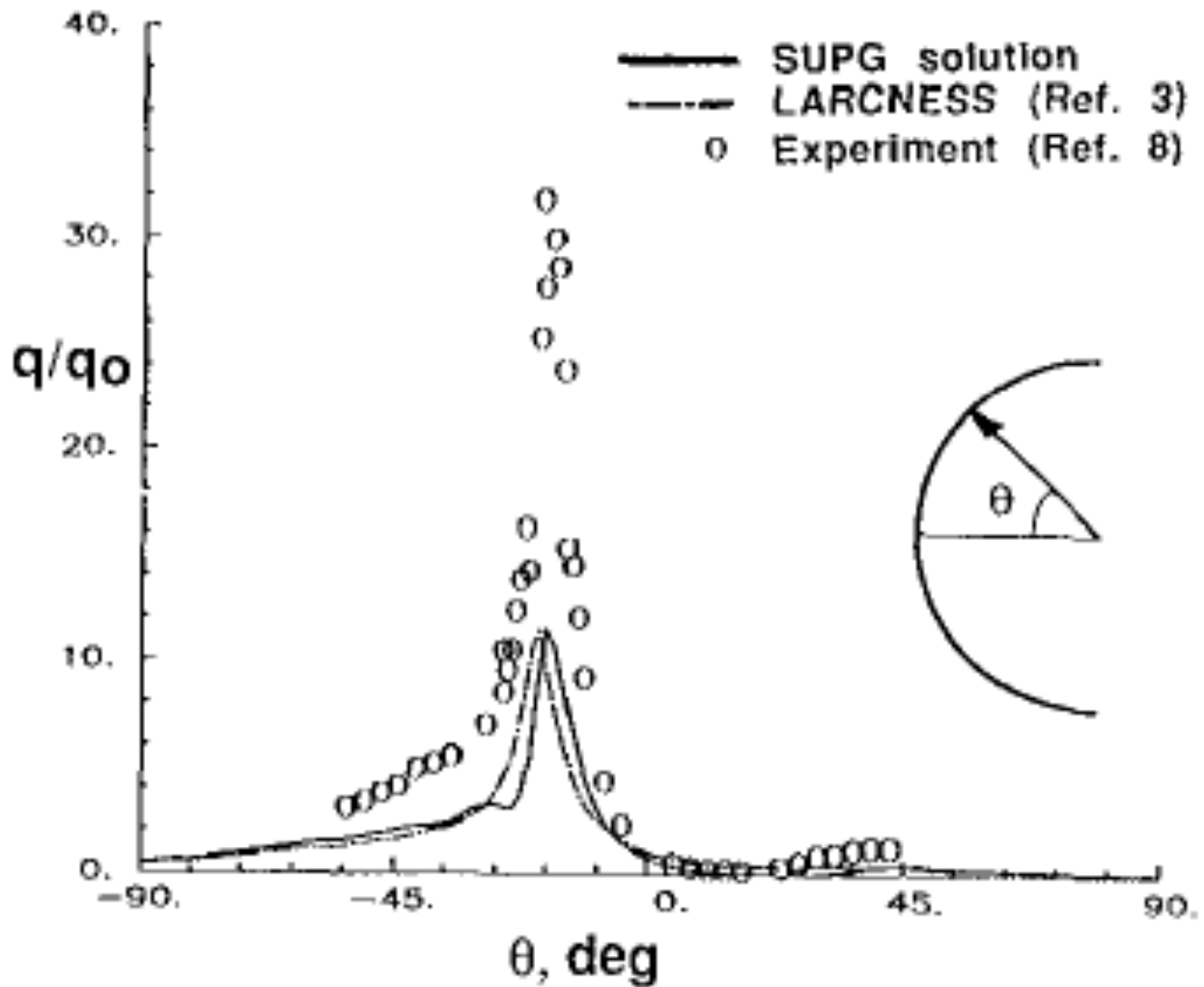


**Figure 2-14.** A finite element solution of the heat flux distribution at the wall for the investigated shock interference case (image reprinted with permission of the American Institute of Aeronautics and Astronautics [26]).

Both Stewart et al. and Vemaganti and Wieting used adaptive re-meshing techniques to cluster the grid elements in locations with large gradients in the flow parameters as the successively adapted grids from Stewart et al. in Figure 2-15 demonstrate. Structured grids and a laminar flow assumption were used in the LAURA simulations in the current study. Due to time constraints, cells were clustered in the shock interaction region manually, but these grids were not adapted to match the shape of the converged bow shock solution for the test article. This additional step will be performed in future work.

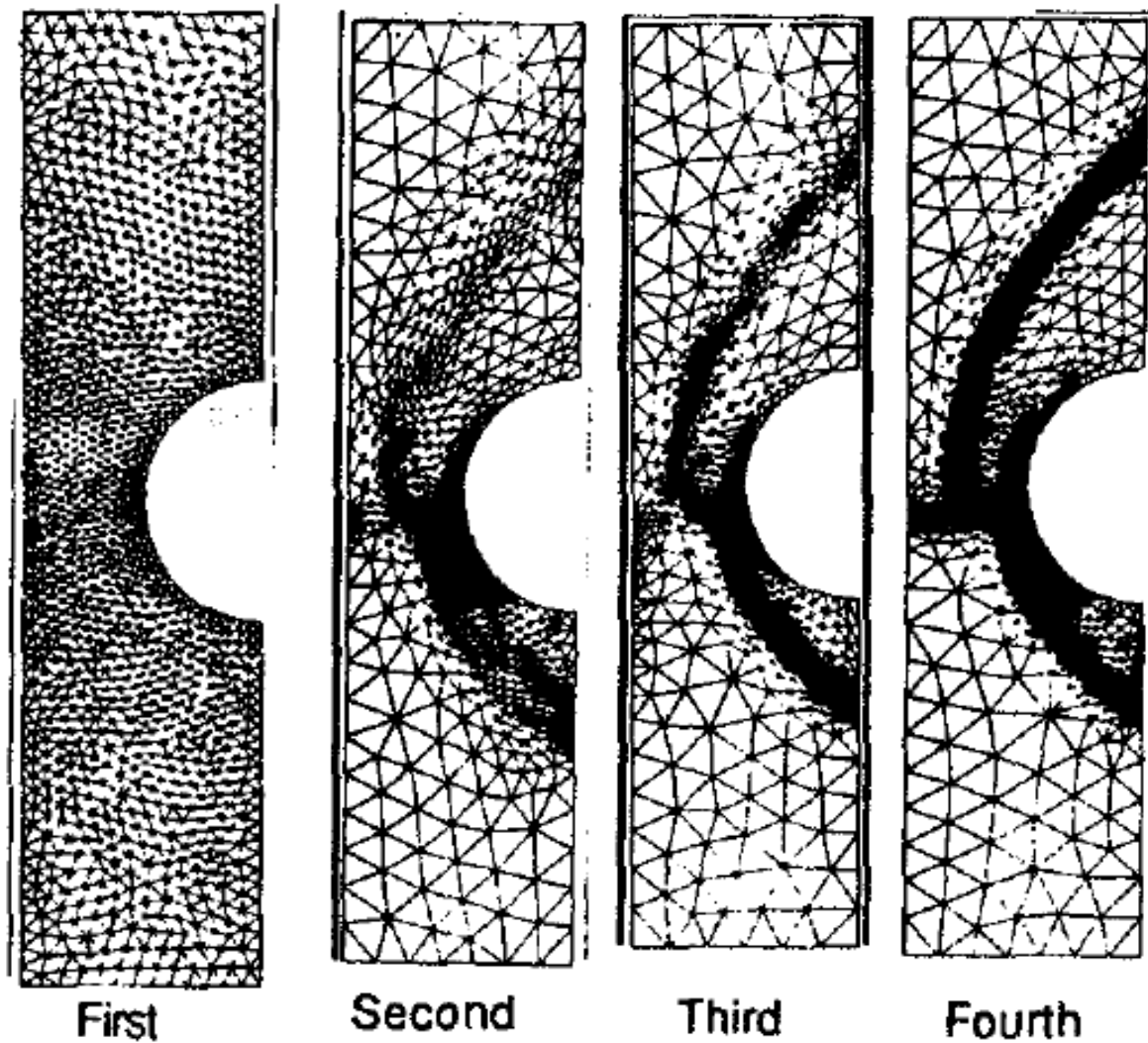


**Figure 2-15.** Adaptive re-meshing technique for a Type IV interaction (image reprinted with permission of the American Institute of Aeronautics and Astronautics [25]).

Since 3D interactions are modeled in the current study, the rest of this section describes previous work that deals with shock-on-fin interactions. Berry and Nowak [8] investigated the increase in peak heating due to shock-on-fin interactions during Test 6692 in the 20-Inch Mach 6 Air Tunnel. This study prompted the current work as discussed briefly in section 1.2.

The goal of Test 6692 was to experimentally determine the effect of the fin sweep angle on the expected increase in the peak heating on a leading edge or strut of a hypersonic vehicle, perhaps with a scramjet engine like the proposed NASP, due to different types of 3D shock-shock interactions. Temperatures measured using Macor® test articles instrumented with thin-film gages were reduced using 1D heat transfer codes. Of the six Edney [2] types of shock-shock interactions, the Type IV interaction was of special interest because this interaction produces a supersonic jet that increases the temperature in a localized region on the model surface. For a  $9^\circ$  shock generator (SG) angle, a Type IV interaction occurs if the test article angle of attack, relative to a 2D plane perpendicular to the Mach 6 air flow, is either  $0^\circ$  (producing a jet that curls

upward) or  $-15^\circ$  (producing a jet that directly impinges on the test article surface). Berry and Nowak [8] postulated that the peak heating increase for a wind tunnel run with a 0.25 in-radius model at  $-15^\circ$  angle of attack might grow from nearly seven times the baseline value (refer to image b in Figure 2-16) to a factor of ten if lateral conduction effects were considered in the heat transfer analysis. A separate run with the test article angled at  $-25^\circ$  produced a Type III interaction in which a shear layer impinged on the surface of the test article. The peak heating increase in this case was again nearly seven times the baseline value, as shown in image b in Figure 2-17.

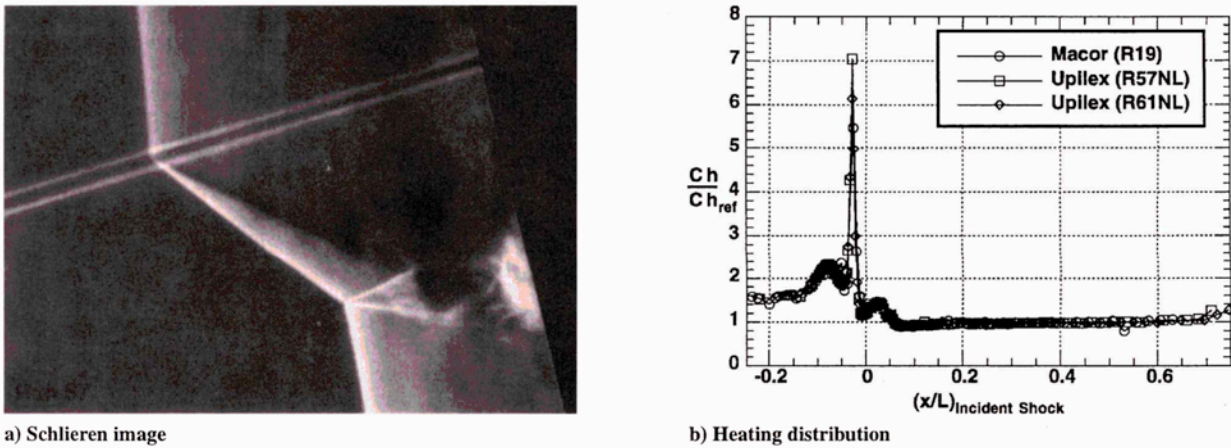


**Figure 2-16.** Schlieren image and peak heat transfer augmentation plot for a Type IV interaction with a 0.25 in-radius test article at a  $-15^\circ$  AoA (image used with Berry's permission [8]).

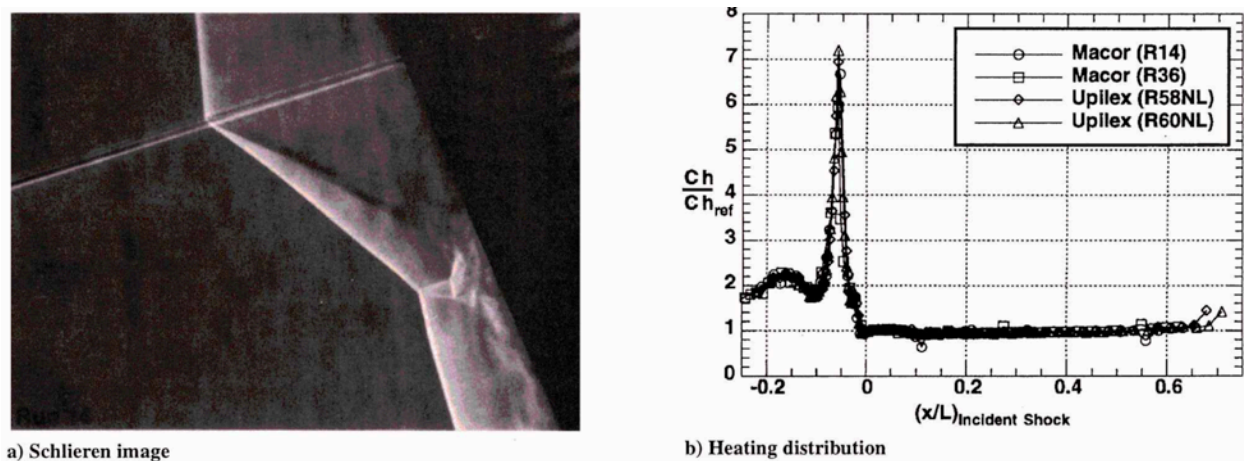


**Figure 2-17.** Schlieren image and peak heat transfer augmentation plot for a Type III interaction with a 0.25 in-radius test article at a  $-25^\circ$  AoA (image used with Berry's permission [8]).

The goal of the current study is to calculate the peak heating augmentation along the leading edge of test articles with similar geometries to those in [8]. Additional nose radii were tested to determine the effect of nose diameter on the need to consider lateral conduction as a point of reference for models of different sizes in future 20-Inch Mach 6 Air Tunnel tests.

In Test 6692 [8], 0.25 in-radius cylindrical Macor® rods instrumented with thin-film gages either vapor-deposited or etched in an Upilex® layer on the surface were bonded into metal holders with a 7° slope back from the cylinder on either side. The metal test articles used in the oil flow visualization runs and the fused silica test articles in the phosphor thermography runs in the current study were designed similarly with either a 0.25 in, 0.50 in, or 0.75 in nose radius and a 7° sweep from the leading edge to the back of the test articles. For a clearer picture of the design of these models, refer to the drawings in Appendix B.

The majority of the wind tunnel runs in Test 6692 and the current study were conducted at a Reynolds number of  $2.1 \times 10^6/\text{ft}$ . The flat plate SG was angled at 9° to the flow for the runs in Test 6692, excluding the runs in which the plate was removed to provide a baseline case with no incident shock. The shock-interaction heat transfer runs in the current study were conducted with the same SG angle, and for baseline cases the SG plate was removed.

Bushnell conducted experiments in the Langley Mach 8 variable-density wind tunnel that involved shock-shock interactions on 1.0 in-diameter cylinders in [27] and [28]. These cylinders were used to represent leading edges on a hypersonic vehicle that might be subjected to shock-shock interactions during flight, as the diagram in Figure 2-18 demonstrates.

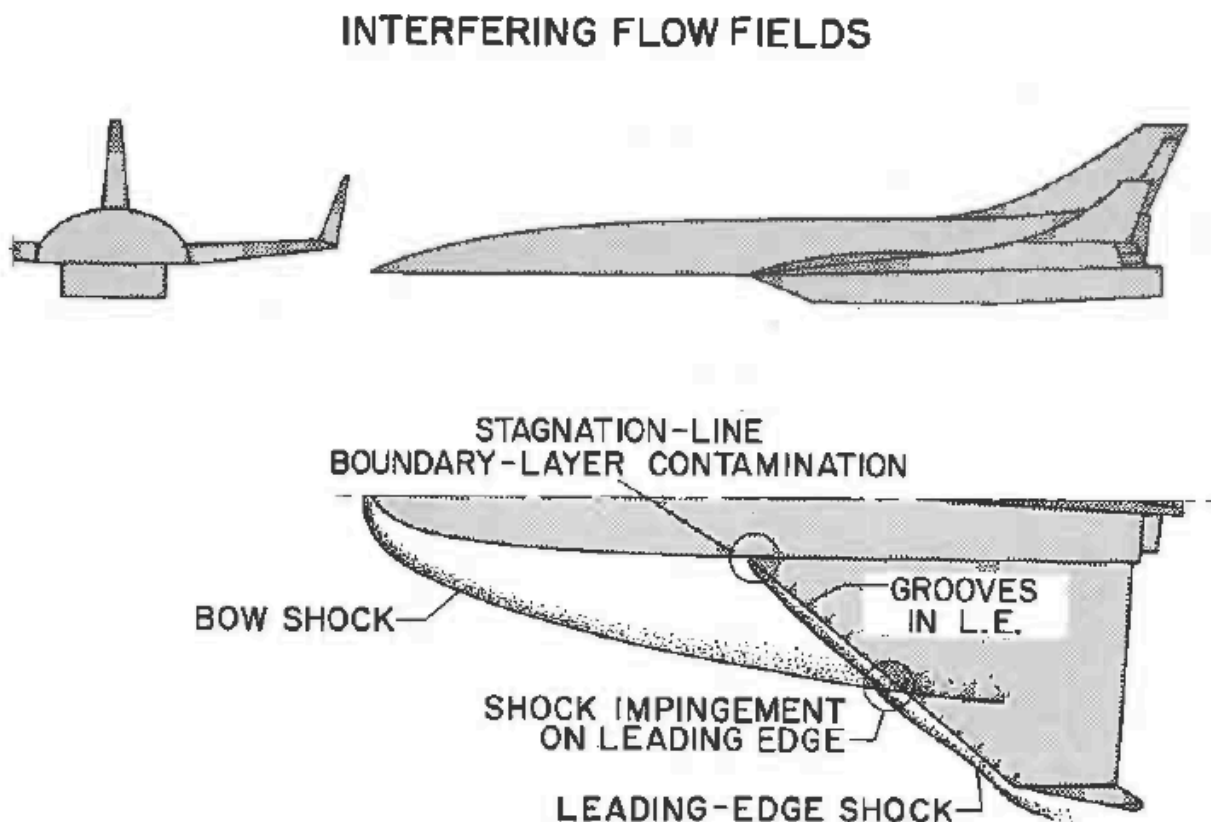


**Figure 2-18.** Sketch of a possible shock-shock interaction between the vehicle bow shock and a leading-edge shock in hypersonic flow (image used with Bushnell's permission [28]).

In his 1965 study, Bushnell tested cylinders machined from stainless steel (type 347) that were swept at either 45° or 60° relative to a 2D vertical plane normal to the Mach 8 flow [27]. In 1968, Bushnell used unswept (0° sweep) cylinders made from a glass and mica composite material with a low thermal conductivity [28]. In both tests, the oblique incident shock was produced with a stainless steel flat plate shock generator inclined at 12° to the flow.

In reference [27], Bushnell instrumented two cylinders with thermocouples and two cylinders with pressure orifices, with a minimum spacing of 0.25 in between the sensors as shown in Figure 2-19. Bushnell conducted experiments in which the cylinders were either attached to or separated from the SG wedge during a run. The separation distance between the SG wedge and the fully-injected cylindrical model was 0.63 in in the latter type of runs, which are more similar to the current study. This distance ensured the edge of the swept cylindrical model was outside of the boundary layer in the flow over the flat plate. Bushnell calculated the boundary layer thickness to be 0.15 in for Mach 8 flow at a location 1 ft from the sharp leading edge of the SG wedge. For the same reason, the test articles in the current study were positioned at least 0.5 in above the SG wedge to ensure the flat plate boundary layer would not affect the flow around the test article leading edge.

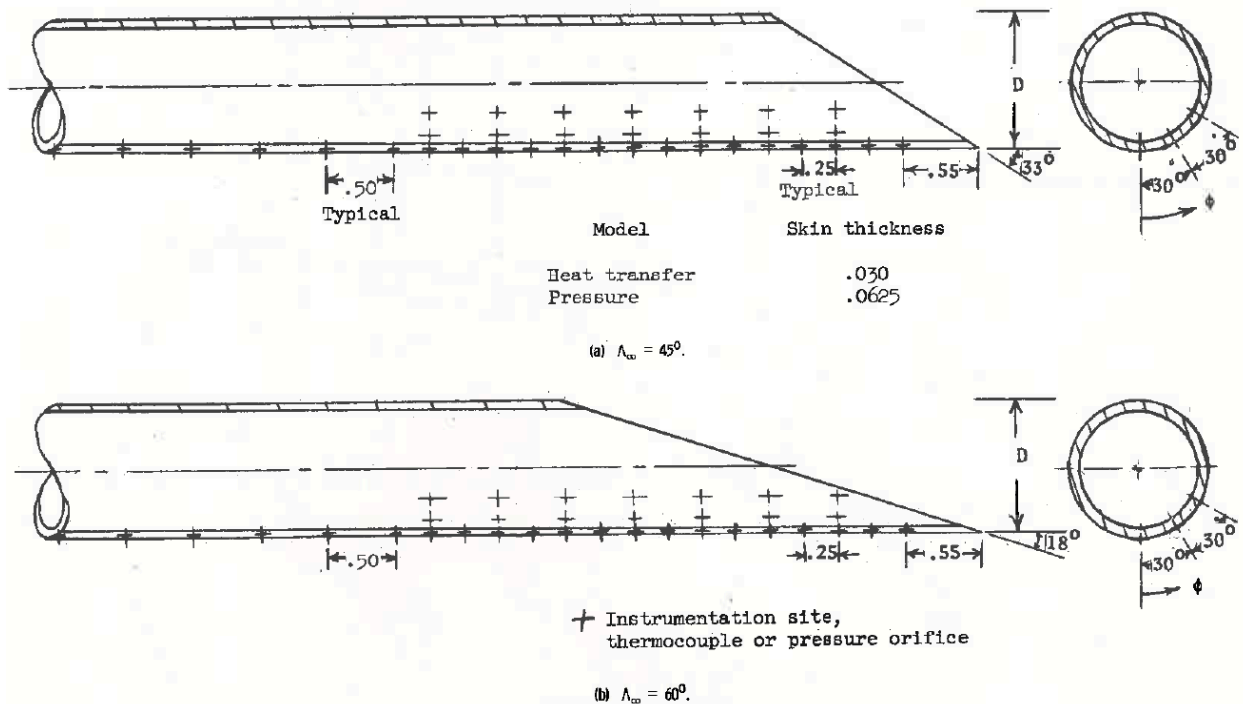


**Figure 2-19.** Diagram of the cylindrical models instrumented with either thermocouples or pressure orifices, with non-dimensional lengths based on the cylinder diameter (image used with Bushnell's permission [27]).

Schlieren images in Bushnell's report suggest the 45° and 60° test article angles yielded Type VI shock-shock interactions, as shown in Figure 2-1. A sketch of the typical flow pattern for this type of interaction is shown in Figure 2-20. These sweep angles were not included in the run matrix for the current study since the focus of Tests 6976 and 6983 was on Type III and IV

interactions. Bushnell calculated the heat transfer along the leading edge from the thermocouple temperature data. The maximum heating data agreed well with predicted heat transfer assuming an infinite swept cylinder as in reference [29]. Bushnell concludes that the incident shock and cylinder bow shock intersection produced a pressure gradient in the span-wise direction on the cylinder but did not produce a peak in the heat transfer. However, the smallest separation of the sensors on these models was nearly 17 times larger than the 0.015in minimum thin-film-gage spacing in the Berry and Nowak study [8], which suggests a peak in heat transfer might have existed in that region without being detected.

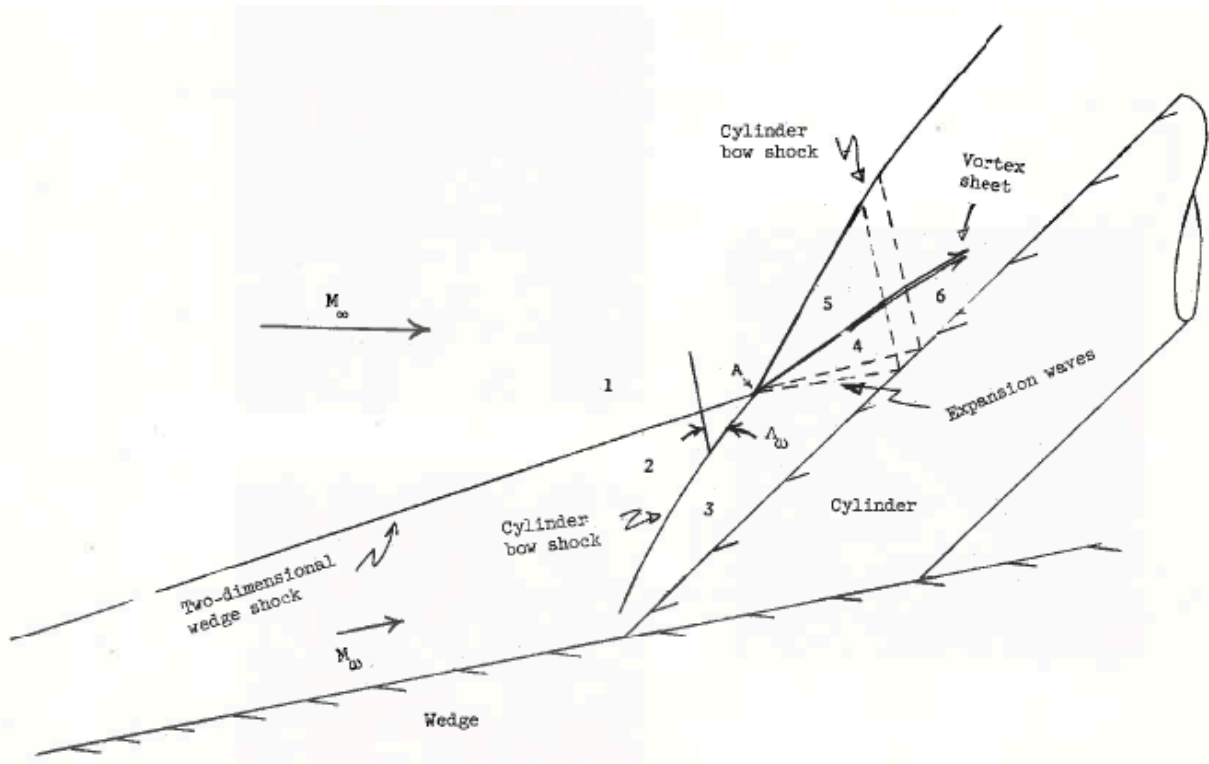


**Figure 2-20.** Sketch of a typical schlieren photograph that shows the inviscid flow-field phenomena associated with the intersection of two right running shocks (image used with Bushnell's permission [27]).

For the study in reference [28], Bushnell instrumented the cylinders with a temperature-sensitive paint to provide surface temperatures over the entire test article. This cylinder was tested with a  $0^\circ$  angle of attack to obtain a heating profile along the stagnation line both with the wedge (shock impingement case) and without the wedge (baseline case). In Figure 2-21, Bushnell compares the increase in heating over the baseline value relative to the non-dimensional distance between the shock impingement location and the separated flow at the edge of the cylinder. The distance is defined in the plot as  $\Delta/D$ , which corresponds to the distance along the leading edge from the effective root of the cylinder to the vortex sheet impingement ( $\Delta$ ) divided by the diameter of the cylinder ( $D$ ) in the symbols used in Bushnell's paper. Bushnell concludes that for a "practical case" in which the incident shock impinges reasonably far out on the leading edge, the increase in heating for the unswept fin is lower than if the impingement location is close to the separated flow region.



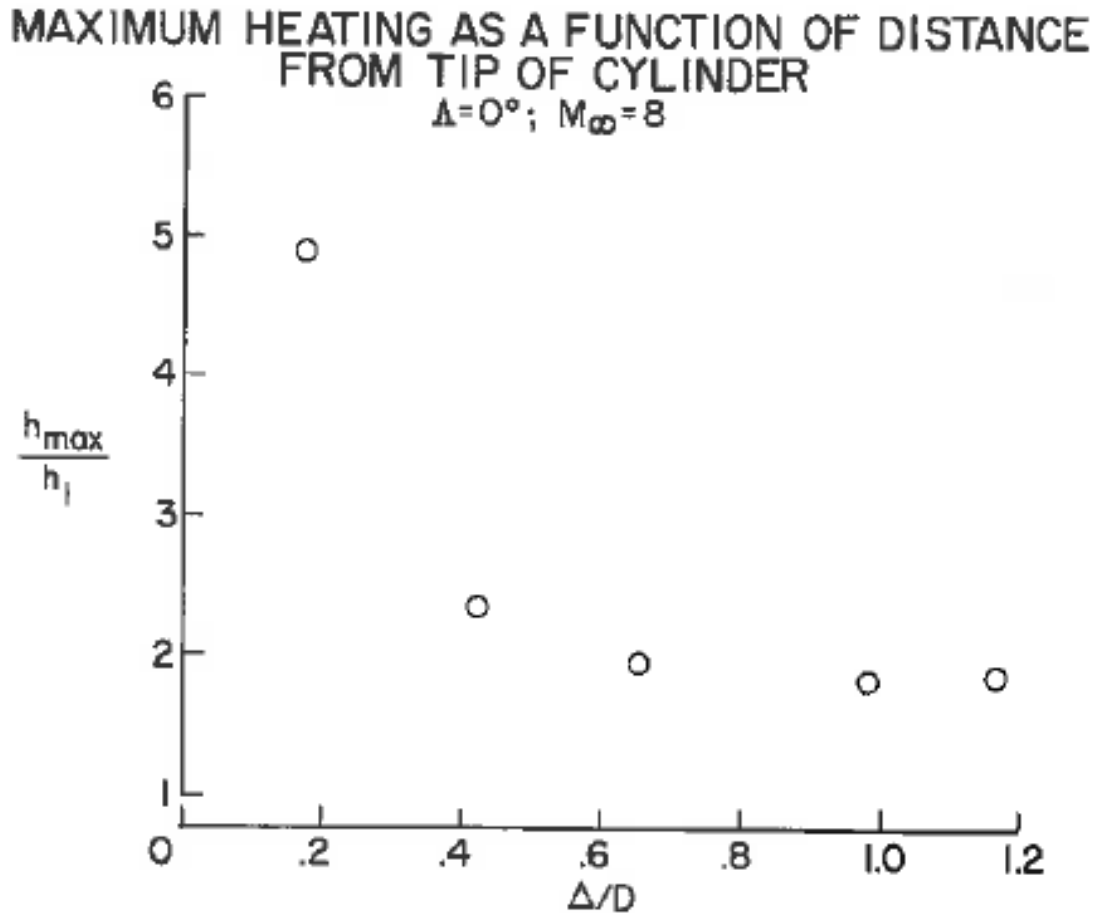


**Figure 2-21.** Increase in peak heating due to shock impingement as a function of the non-dimensional distance from the tip of the cylinder (image used with Bushnell's permission [28]).

Keyes and Hains [13] experimented with shock-shock interactions on hemispheres, a  $30^\circ$  wedge, and a 1.0 in-diameter cylindrical fin for a range of tunnel and flow conditions. Based on observations during these tests, Keyes and Hains developed semi-empirical techniques to be used in engineering design calculations to estimate the peak heating and pressures for different types of interactions. The runs with hemispheres represent the shock-on-cowl case, but a silica-based epoxy cylinder was also tested to investigate Type IV and V shock-on-fin interactions.

Schlieren images as well as pressure and heat transfer profiles for the glancing Type IV interaction (referred to as Type IVa) on an unswept cylinder in approximately Mach 6 flow are shown on pages 81 and 112-116 in reference [13]. Compared to the  $9^\circ$  SG angle used in the majority of the runs in the current study, the incident shock angle varied from  $10^\circ$  to  $20^\circ$  in these tests. The information for a cylindrical fin with a  $10^\circ$  SG angle in Mach 5.94 flow is shown in Figure 2-22.

The flow vortices in these schlieren images are clearer than in the current study, but the supersonic jet leaving the triple point of the shock-interaction is less clear due to the contrast of the images. Keyes and Hains explain that the supersonic jet turns up and interacts with the

unswept cylinder's boundary layer due to a large pressure difference across the width of the jet. Keyes and Hains note that due to real gas effects, the heating on an actual vehicle may be much higher than the predicted values from perfect gas experiments in the wind tunnels.

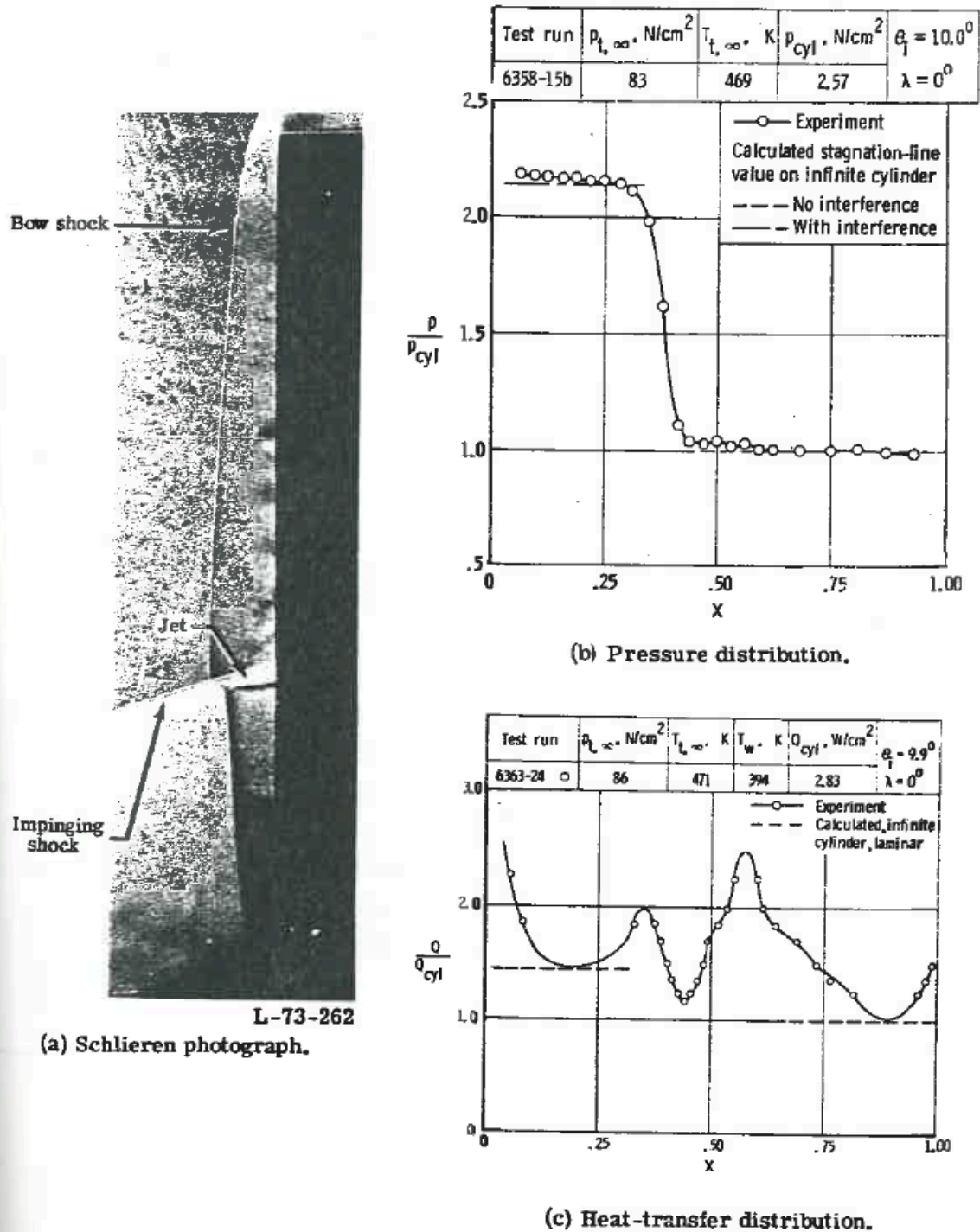


**Figure 2-22.** Schlieren, pressure and heat transfer data for a Type IVa interaction on a fin at Mach 5.94 in air with a SG angle of  $10^\circ$  (image reproduced from a NASA report [13]).

Carter and Carr [30] performed a flight experiment to study the heat transfer to an unswept cylinder in a 3D shock-on-fin type of shock-shock interaction. A 0.75 in-diameter cylinder was attached to an axial cylinder in a perpendicular configuration and mounted on a rocket so that the bow shock surrounding the hemispherical nose and cylindrical body of the axial cylinder impinged on the shock around the attached transverse cylinder. Figure 2-23 shows a photograph of this rocket and attached cylinder configuration. Temperature data was obtained remotely from thermocouples on the cylinder when the two-stage rocket launched from NASA Wallops Island and accelerated up to Mach 5.5.

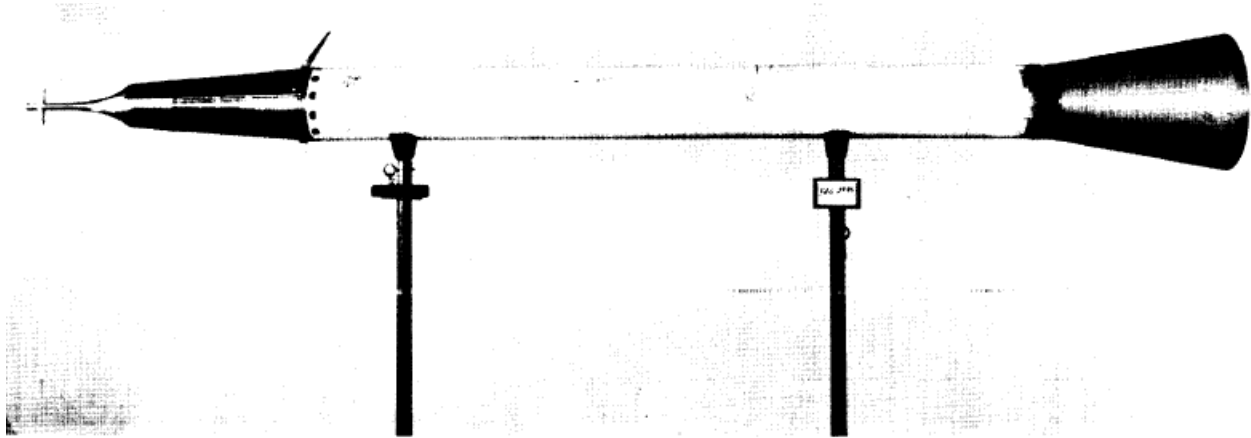


**Figure 2-23.** Image of the rocket and the attached unswept transverse cylinder used in a shock-shock interaction flight experiment (image reproduced from a NASA report [30]).

The non-dimensional data in Figure 2-24 shows the magnitude of the experimental heat transfer coefficients along the leading edge of the cylinder relative to a theoretical laminar heat transfer coefficient. These non-dimensional heat transfer coefficients vary as the Mach number increases due to the acceleration of the rocket. Based on the flight data from sensors along the stagnation line of the cylinder, the heating increase (assuming one-dimensional heat transfer) was up to two times the predicted level for Mach numbers above 4. An arrow in each plot indicates the approximate location of the shock intersection on the unswept transverse cylinder. Data from the flight test revealed no localized increase in heating, and overall a lower heating rate, compared to the results from a wind tunnel test with an unswept cylinder with different geometry and test conditions in the Langley Unitary Plan wind tunnel.

The case investigated in the flight experiment is similar to the  $0^\circ$  angle of attack case and the radius of the cylinder is halfway between the two smallest geometries in the current study. However, since the cylinder in this case was attached to the rocket, boundary layer separation of the flow at the base of the cylinder also affected the heating rate. The incident shock angle also differs between this experiment and the current study.

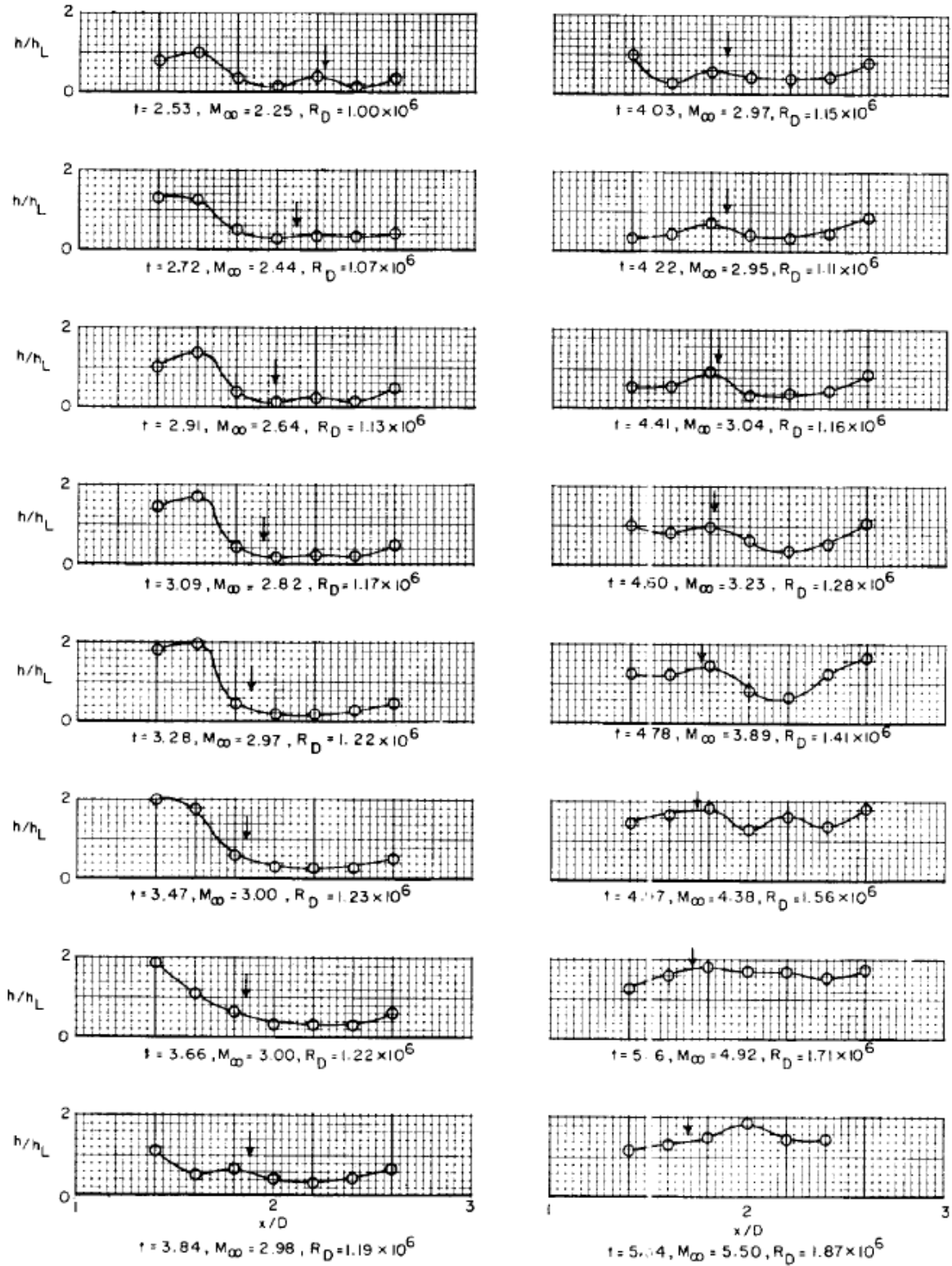


**Figure 2-24.** Ratios of experimental to theoretical laminar heat transfer coefficients as Mach number increases, with an arrow at the approximate location of the shock intersection (plots reproduced from a NASA report [30]).

Hiers and Loubsky [31] used a wind tunnel test article with a 3.5 in-long and 0.5 in-radius cylindrical leading edge on a shock generator plate to investigate the effect of shock impingement in Mach 14 flow for different sweep angles. Figure 2-25 shows a diagram of this test configuration and specifies the locations of the discrete sensors on the leading edge of the test article. As in the current study, the angle of attack of the test article and the SG plate were set independently. The thermocouple spacing along the leading edge of the cylindrical model was about 0.15 in. Hiers and Loubsky considered the conduction in the lateral direction (circumferential) to be negligible but accounted for span-wise and normal (through-thickness) conduction in the heat transfer analyses using the thermocouple data. Experimental heat transfer rates ( $\dot{q}$ ) based on the thermocouple data were divided by the Fay-Riddell [32] stagnation point heat transfer rate ( $\dot{q}_0$ ) to yield non-dimensional heat transfer data. Hiers and Loubsky [31] compare this experimental data to calculated heating rates for each case, such as the case with the SG plate inclined at  $10^\circ$  to the flow creating an incident shock to impinge on an unswept cylinder shown in Figure 2-26.

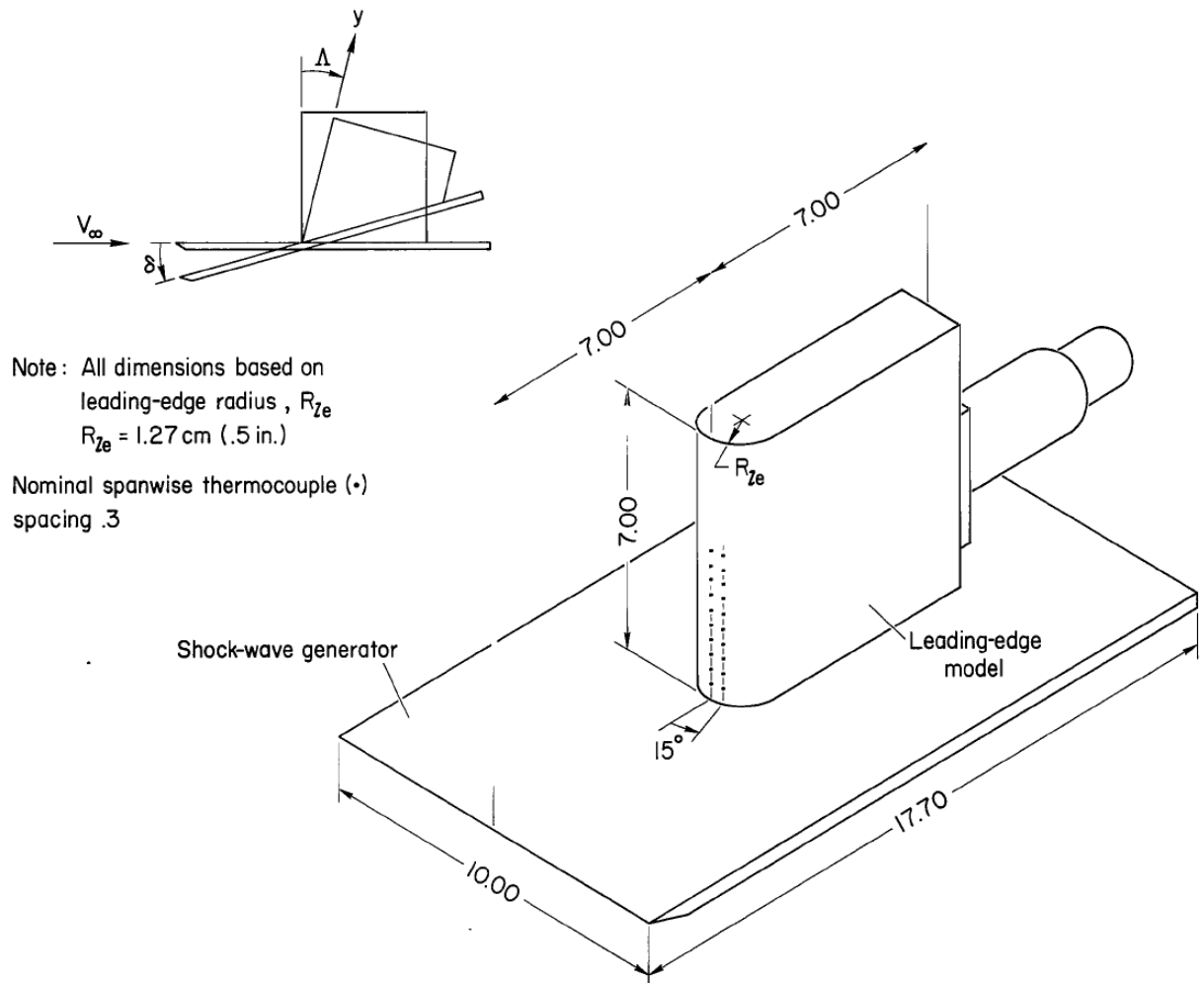


**Figure 2-25.** Sketch of the SG and the test article (image reproduced from a NASA report [31]).

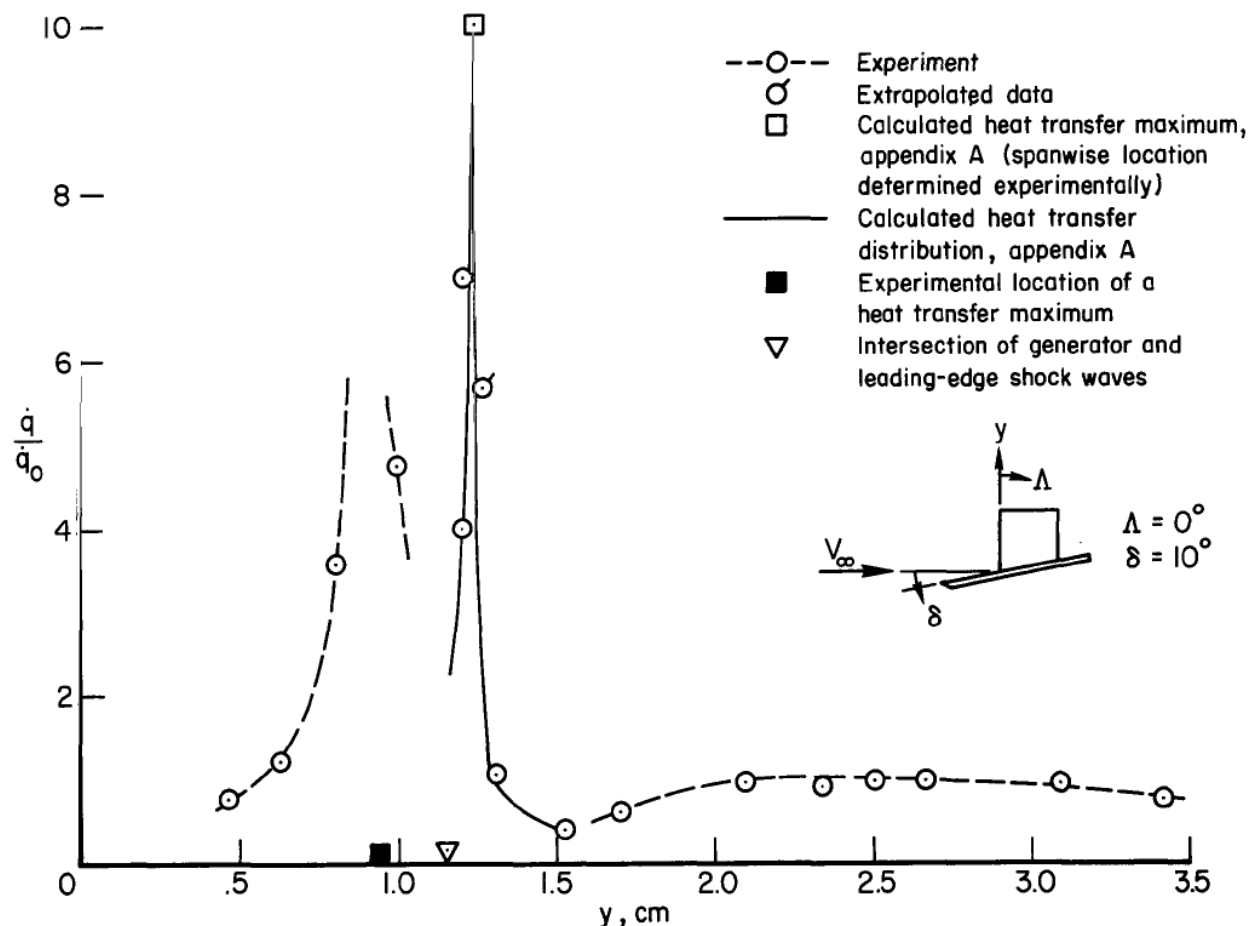
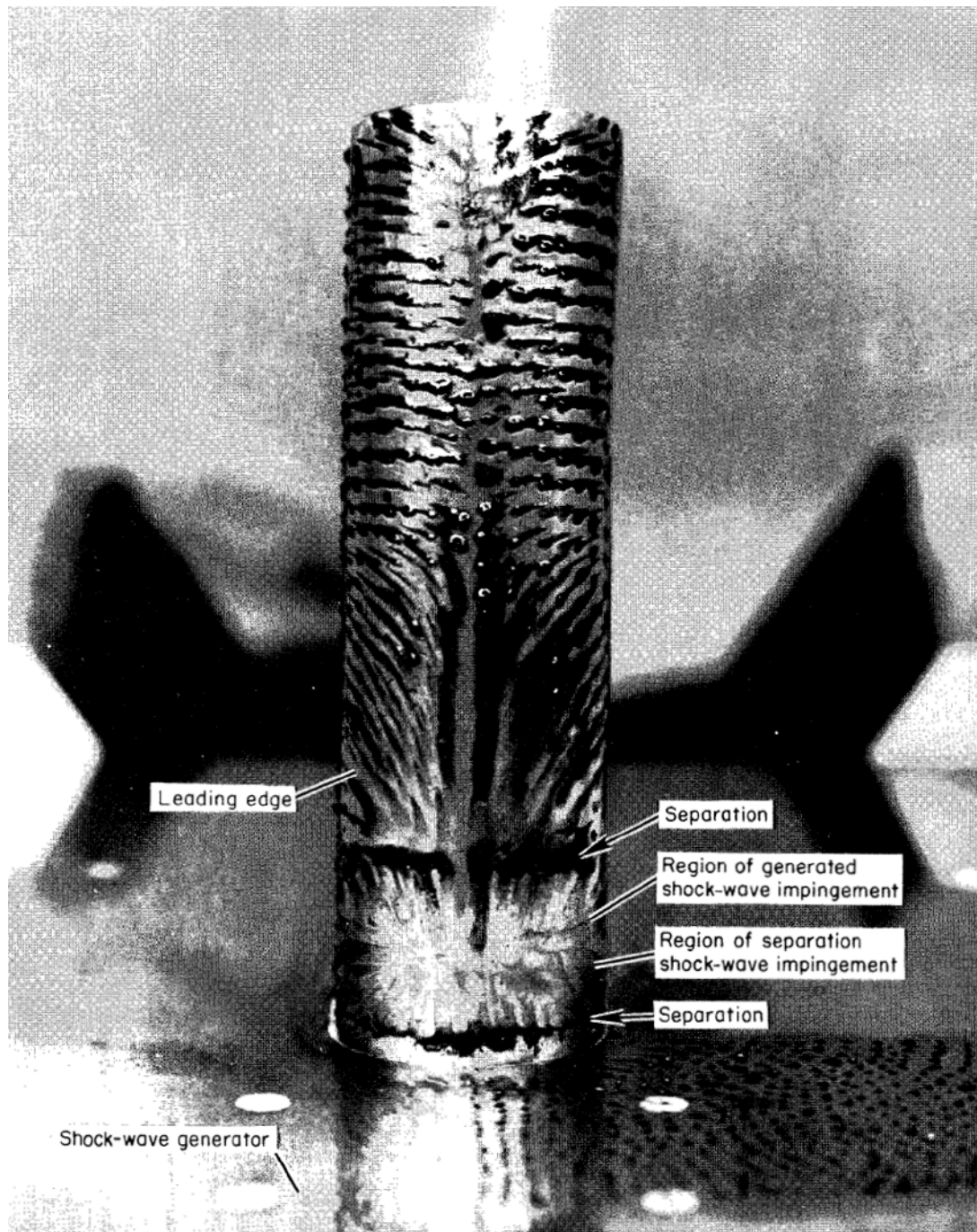


**Figure 2-26.** Stagnation line heat transfer rates for an unswept leading-edge test article with a SG angle of  $10^\circ$  and divided by a Fay-Riddell reference heat transfer rate (plot reproduced from a NASA report [31]).

Hiers and Loubsky also present oil flow images using two techniques to visualize the flow on the surface of the model. In the first technique, the entire test article surface was covered with a thin layer of low-viscosity oil mixed with powdered graphite. The second method involved applying dots of grease with a high viscosity to the surface of the test article. Similar oil flow techniques, with different mediums, were used to visualize the surface flow patterns in the current study

The image in Figure 2-27 shows an oil flow image obtained by the first technique for an unswept test article with a cylindrical leading edge after a wind tunnel run with a  $15^\circ$  SG angle [31]. The streamlines above the “region of generated shock-wave impingement” in this image are similar to those observed in the oil flow images for a  $0^\circ$  AoA in the current study, as expected. Additional regions of separation exist near the bottom of the leading edge in Figure 2-27 since the test article is not separated from the flat plate SG. The shock-BL interactions that produced this flow pattern and the associated separated regions likely also contributed to higher heating rates in that region on the test article. The schlieren data presented for a single case in this paper does not provide a clear picture of the features in the shock-shock interaction region.



A-34977.1

**Figure 2-27.** Leading-edge oil flow image for an unswept test article and a SG angle of  $15^\circ$  (image reproduced from a NASA report [31]).

Trumble and Candler [33] computationally investigated the possibility of using laser energy deposition to reduce the large increase in peak heat transfer that results from a Type IV shock-shock interaction. The flow in a Type IV shock-shock interaction case for a  $-15^\circ$  test article sweep is unsteady due to vortices generated in the flow (as described in [3] and discussed in

more detail in the next section). However, Trumble and Candler describe a laminar simulation conducted using the Data-Parallel Line Relaxation (DPLR) algorithm assuming steady-state flow to approximate the conditions for the shock-shock interactions experimentally modeled in [8]. The modeled “energy spot” due to a laser beam acting on the air in front of the shock-shock interaction was incorporated into the “steady-state” solution. Since the “pressure wave” associated with the laser energy increased the peak pressure and heat transfer on the surface of the test article, as Figure 2-28 shows, this technique was deemed unsuitable for reducing the localized peak heating caused by a Type IV shock-shock interaction.

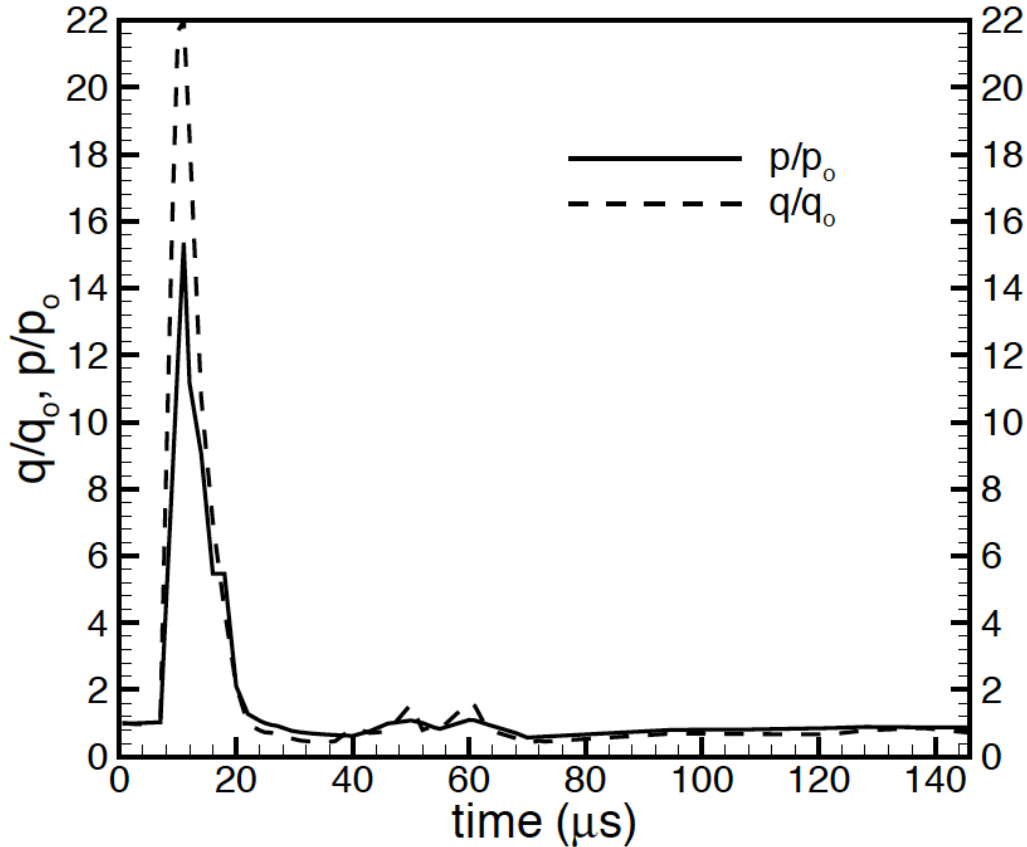


**Figure 2-28.** Peak surface pressure and heat flux due to laser energy deposition (used with Trumble’s, now Zarchi’s, permission [33]).

## 2.5. Previous evaluation of 1D and 2D heat transfer analyses

One objective of the current study is to investigate the effect of modeling the conduction through the test articles either with 1D or 2D methods. Previous computational and experimental tests demonstrated the need for multi-dimensional conduction analyses in certain circumstances. The articles referenced in this section describe analyses of the impact of lateral conduction for a variety of test configurations. The first four studies describe comparisons between 1D and either 2D or 3D numerical codes, and the final study in this section compares experimental to CFD results.



Walker and Scott [34] developed conduction codes to estimate the heat flux to a test article from a shock-shock interaction. These codes were used to determine the effect of lateral conduction on the heat flux in regions with severe temperature gradients. Walker and Scott used the thin-film-gage data from reference [8] as inputs to 1D and 2D “inverse” conduction codes for a few sample cases with the Macor® and Upilex® test articles. In a direct code, known boundary conditions (such as heat fluxes or surface temperatures) are applied “directly” to the test article geometry. In an inverse code, the boundary conditions are estimated based on known conditions elsewhere in the test article geometry. Once the solution is obtained from an inverse code, the validity of the boundary conditions is verified. If necessary, the error in the boundary conditions is reduced using an optimization routine.

A Dirichlet boundary condition, which specifies the temperature at each surface location based on the experimentally measured values at each time step, was implemented in the direct finite-volume codes. Thus, an inverse method was not deemed necessary to estimate the conduction through the test articles in the current study. Walker and Scott argue against the use of direct methods to reduce thin-film-gage temperature data to heat transfer coefficients, citing the instability associated with discretizing data to be used in Fourier’s law and the requirement to estimate the temperature distribution at intermediate time steps. These steps are described in Chapter 4 as part of the Alternating Direction Implicit (ADI) analysis for the current study. The two-step ADI method, when applied properly to a heat transfer problem, is unconditionally stable and yields reliable heat transfer results [35].

Walker and Scott [34] explain that typical inverse methods can also produce unstable solutions since the heat flux at the surface is approximated based on the temperature response through the model so that uncertainties in the interior measurements produce errors in the surface calculations. The errors due to this instability were reduced since the surface temperatures were known a priori as inputs. Walker and Scott neglect the effects of curvature of the models in both the 1D and 2D codes, assuming the geometry behaved as a flat plate in both cases. The 2D direct conduction code in the current study modeled the geometry in a cylindrical coordinate system to better approximate the areas and volumes through which the heat would be conducted.

As Figure 2-29 shows, the 2D code results for the Macor® test articles in the Walker and Scott study reveal a difference of  $\pm 20\%$  at the heat flux peaks and valleys compared to the results from a 1D code with the same temperature inputs. The heat flux values in the regions outside of the peak (where the temperature gradient between neighboring gages was smaller) were very similar between the 1D and 2D codes since both algorithms assumed flat plate geometries. Walker and Scott also conclude that the heat flux calculations could be improved by increasing the spatial resolution of the acquired temperature data as was done in the phosphor thermography test in the current study, especially for the wind tunnel runs in which the camera was zoomed in to focus on the shock-shock interaction region. Further information about this research is available in Walker’s dissertation [36].

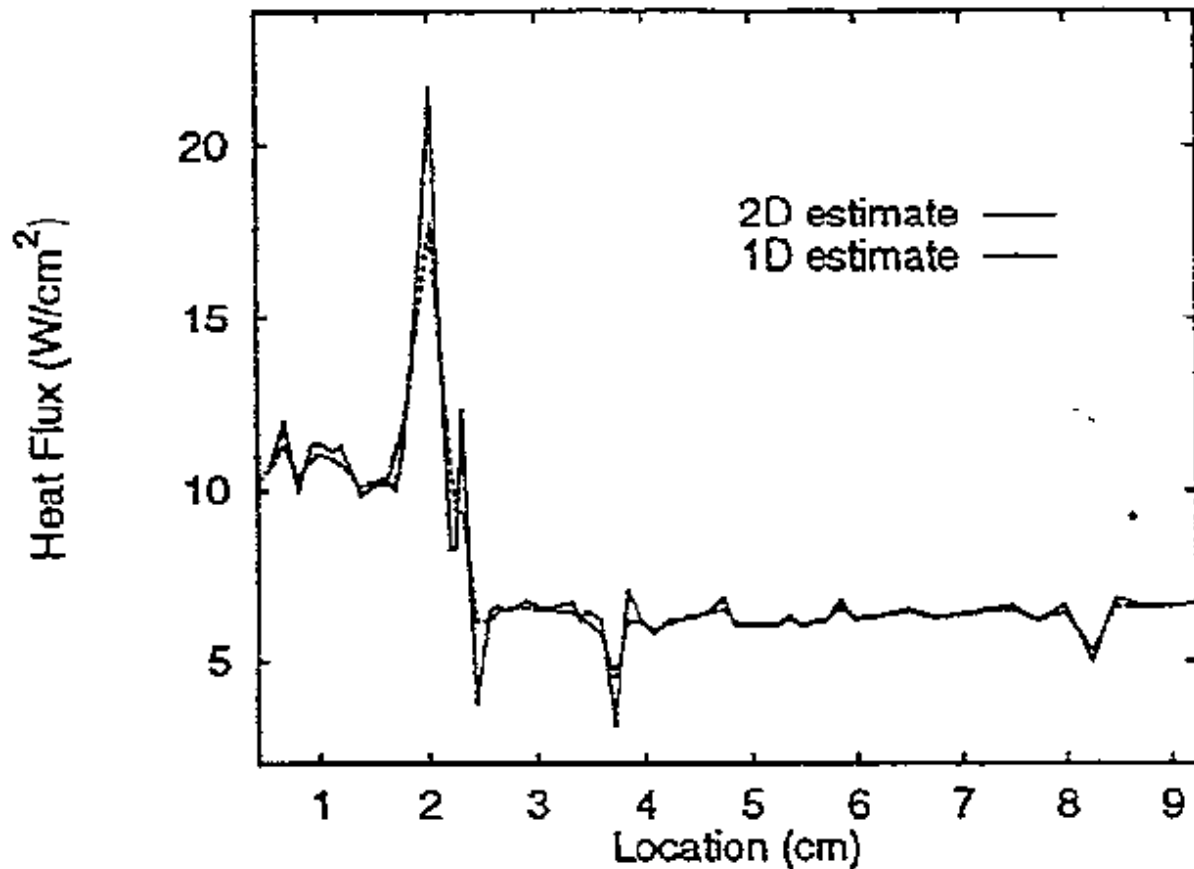


**Figure 2-29.** Comparison of one- and two-dimensional estimate for heat flux in Test 6692, Run 14 using the Macor® test article at 2 sec (image used with Walker's permission [34]).

Daryabeigi et al. [37] analyzed experimental data from the LaRC 20-Inch Mach 6 Air Tunnel using finite-volume codes that implemented the Crank Nicholson method (1D) or the ADI algorithm (2D and 3D) to approximate the conduction in a Macor® model. A model of the Hyper-X fore body was exposed to injected streams of gas that produced vortices to induce transition from laminar to turbulent flow. Using IR techniques, temperature measurements over the entire (visible) model surface were recorded. The heating striations produced by the injected gas were analyzed with codes that either neglected or included lateral conduction in the model.

Daryabeigi et al. found the 1D, through-thickness heat transfer approximation, which neglected lateral conduction in the model, yielded errors of up to  $\pm 20\%$  compared to results from a 2D finite-volume code as shown in Figure 2-30. The average temperature rise during these runs was approximately 4 K, compared to over 100 K for the fused silica test articles in the current study. Similar 1D and 2D finite-volume codes were written in Fortran to analyze the heat transfer in the cylindrical, fused silica test articles in the current study. Since a 2D conduction analysis was shown to be useful in the Daryabeigi et al. study, one goal of the current study was to implement a similar 2D algorithm in analyzing the heat transfer induced by shock-shock interactions.

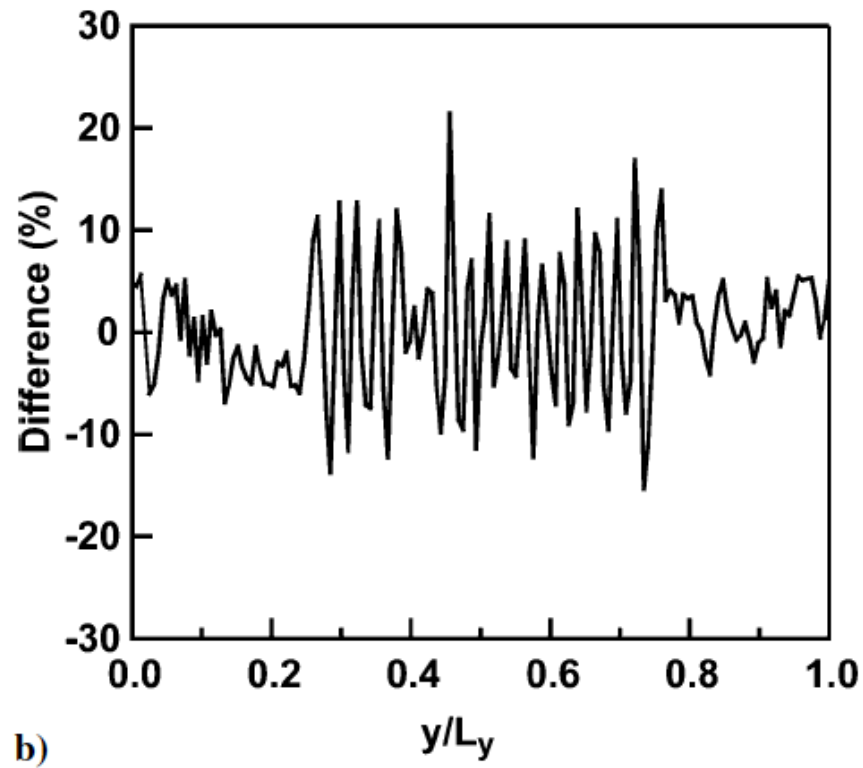
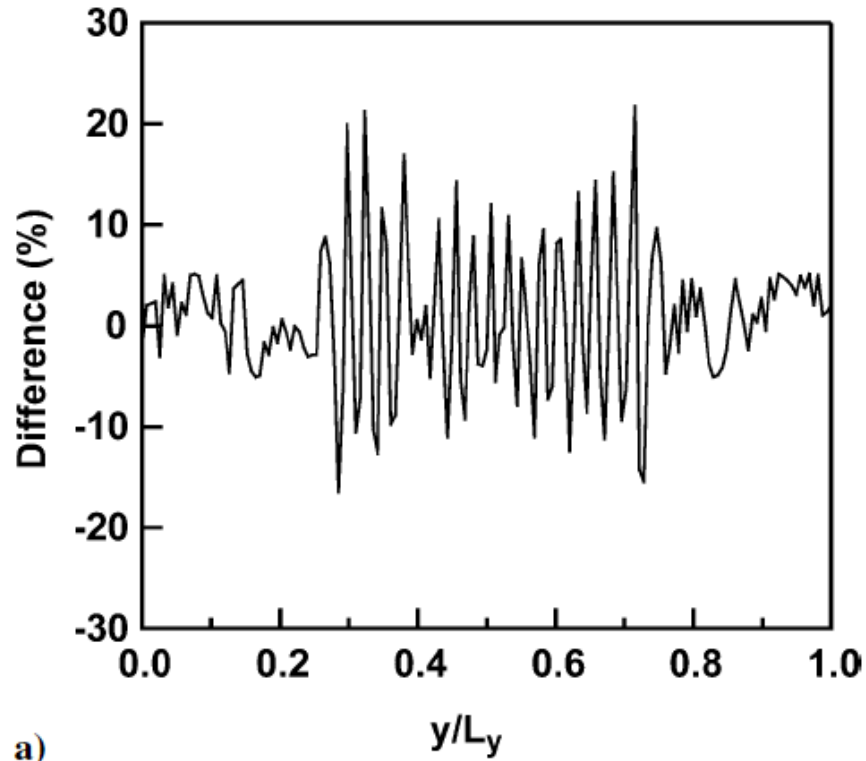


**Figure 2-30.** Relative difference between one- and two-dimensional inverse finite-volume aeroheating rates for run with gas injection at  $x/L_x$  for a) 0.25 and b) 0.50 (plots used with Daryabeigi's permission [37]).

Rufer et al. [38] tested four simulated hypersonic-vehicle breaches in the LaRC 31-Inch Mach 10 Air Tunnel as a part of the Shuttle RTF investigation. Heat flux peaks due to jet impingement of a hot gas at hypersonic speeds were measured using separate Macor® test articles instrumented with a phosphor coating and thin-film gages. The thin-film data from a linear array of sensors was reduced to heat fluxes. These experimental results were compared to CFD simulations of hot air entering a hole in the leading edge of the Shuttle Orbiter wing. The large heat flux gradients in the jet impingement region in certain runs prompted Rufer et al. to supplement the typical 1D (through-thickness) method with 2D and 3D (axisymmetric) heat transfer analyses.

In the axisymmetric 3D finite-volume method, which modeled both the lateral and through-thickness conduction, the heating profile on the test article was assumed to be the same on either side of the jet impingement location, defined as the thin-film-gage location that yielded the highest temperature during a run. In cases with a large, narrow peak heat flux, considering the lateral conduction was more critical as indicated by a difference of about 85% between the 1D and axisymmetric analyses in one test configuration, as shown in Figure 2-31. The axisymmetric heating profiles agreed with the CFD results.

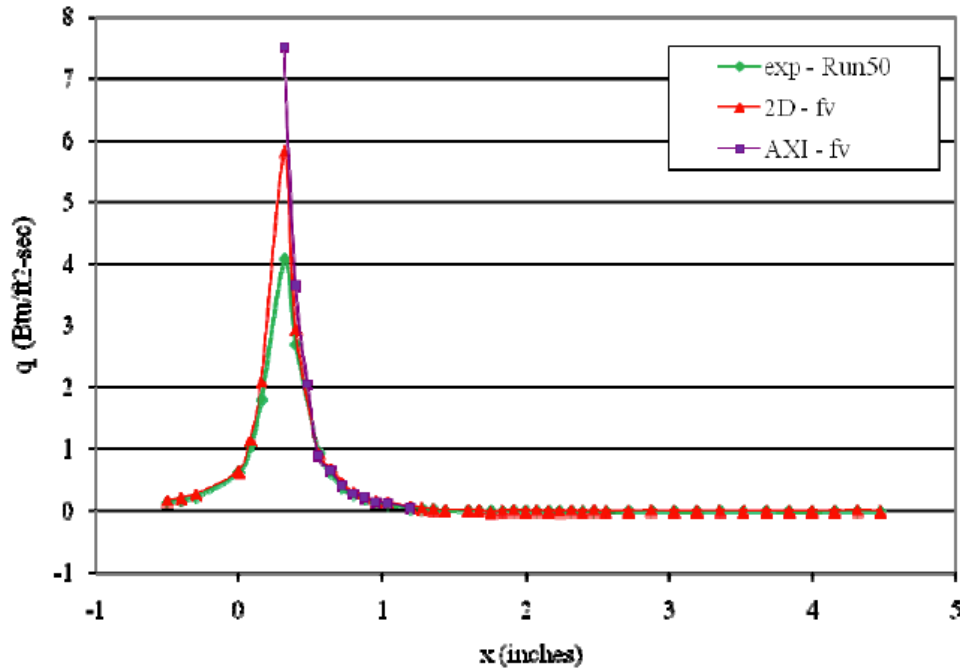


**Figure 2-31.** Heat flux for Run 50, shown along with 2D and axisymmetric finite-volume conduction effects (plot used with Rufer's permission [38]).

Coblisch et al. [39] also conducted a study to consider lateral conduction effects in wind tunnel experimental data. In this study, a double-cone model was tested in two different wind tunnels: first in a tunnel at the Calspan-University at Buffalo Research Center (CUBRC) which operated for only milliseconds at a time, and then in the Hypervelocity Wind Tunnel No. 9 at the Arnold Engineering Development Center (AEDC) in runs that lasted 15 seconds. Coaxial thermocouple data measured at the model surface were used as a Dirichlet boundary condition, with known values at each time step, to compute the heat flux to the model.

Coblisch et al. performed a 2D transient, axisymmetric analysis in ANSYS using finite elements to analyze the conduction in the model since the typical 1D finite wall thickness or “semi-infinite slab” models would be insufficient at the longer runs times in AEDC Tunnel 9. Heat transfer coefficients were obtained from an energy balance at the surface of the test article. The conduction analysis in this study showed a 2D solution was not required for the double-cone investigation. High-speed schlieren videos with a framing rate near 10000 fps revealed an unsteady flow near the model, so the peak heat flux region moved to different surface locations during the run, reducing the effect of the lateral conduction by decreasing the magnitude of the peak temperature gradients in that direction. The peak measured lateral heat flux in plot b in Figure 2-32 is nearly half the predicted value, so the corrected 2D heat flux in Figure 2-33 is not much higher than if lateral heat transfer is neglected, as in plot a in Figure 2-32.

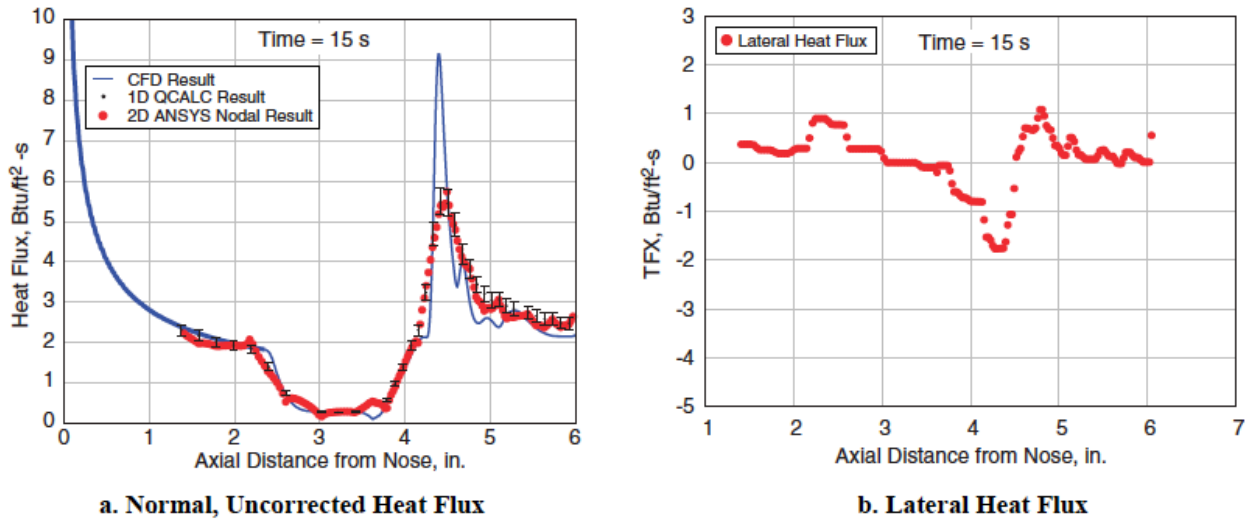


**Figure 2-32.** Heat flux data on a double-cone configuration based on (a) estimated lateral heat flux and (b) calculated lateral heat flux in Run 2894 (plots used with Coblisch’s permission [39]).

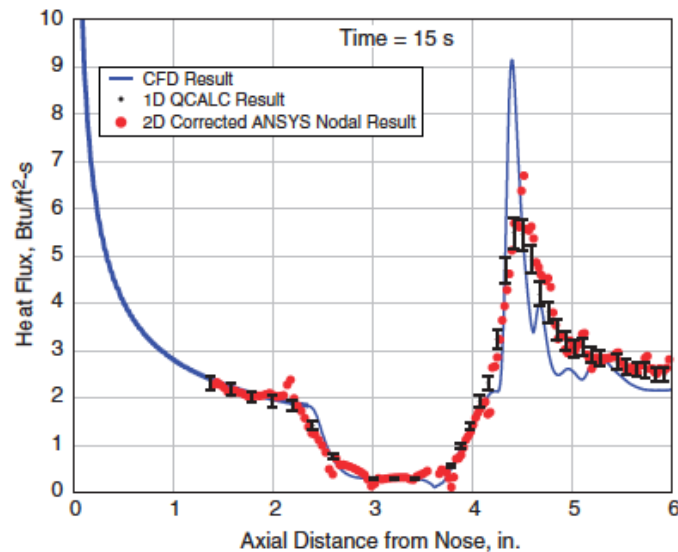


**Figure 2-33.** Corrected heat flux data, considering calculated lateral heat flux, for Run 2894 (plot used with Coblisch’s permission [39]).

Finally, Wright et al. [3] conducted numerical simulations using the General Aerodynamic Simulation Program (GASP) and the Data Parallel Line Relaxation (DPLR) CFD codes for flow conditions and test article geometries similar to the Berry and Nowak study discussed in section 2.4. In particular, Wright et al. used structured cylindrical meshes with spherical caps at either end to approximate the geometry of the 0.25 in-radius test article leading edge. Although the actual model has sharp corners at the extreme locations on the leading edge, this grid shape is acceptable because the edge effects do not impact the heat flux in the shock-shock interaction region. Wright et al. ran the CFD code with the grid inclined at  $0^\circ$ ,  $-15^\circ$  and  $-25^\circ$  to the Mach 6 flow, as in the current study, assuming an ideal planar shock angle of  $16.75^\circ$  for the incident oblique shock. The simulations in the Wright et al. study were not time-accurate, as were the simulations in the current study, but instead yielded averaged solutions over several iterations.

These CFD simulations predicted a peak augmentation of 8 for the  $-15^\circ$  or “ $15^\circ$  forward swept” Type IV interaction, 6.5 for the  $-25^\circ$  Type III interaction, and only 1.6 times the baseline value for the  $0^\circ$  glancing Type IV interaction. Wright et al. calculated the density gradients in the flow around the cylindrical fin based on the computed flow field and compared these results to the experimental zoom schlieren data from [8]. Experimental and computed schlieren images for the Type III and Type IV shock-shock interactions are shown in Figure 2-34. The images shown in the left column in this figure are clearer because the Type IV interaction images were scanned from original images of the experimental and computed schlieren with Wright’s permission. Similar numerical schlieren calculations were performed in LAURA for selected cases in the current study, as discussed in Chapter 5. The experimental and computational schlieren data suggest vortices are present in the flow for Type III and IV interactions that correspond to  $-15^\circ$  and  $-25^\circ$  test article angles of attack.

## **2.6. Impact of the current research**

The results of this thesis contribute to the knowledge of 3D shock-on-strut interactions in hypersonic flight. This thesis is the first known published study in which global thermal imaging techniques are used in conjunction with multi-dimensional thermal analyses to investigate high heating rates associated with shock-shock interactions. The phosphor thermography technique provided temperature and heat transfer data with an increased spatial resolution compared to the discrete sensors typically used in prior shock-shock interaction studies. Additionally, the current study provides information about shock-shock interactions from improved experimental tools such as high-speed zoom schlieren and two separate oil-flow techniques. Finally, an improved computational technique (the modified LAURA code) is utilized in this study to demonstrate the capability of the updated code to simulate the density gradients and heat transfer behavior associated with shock-shock interactions.

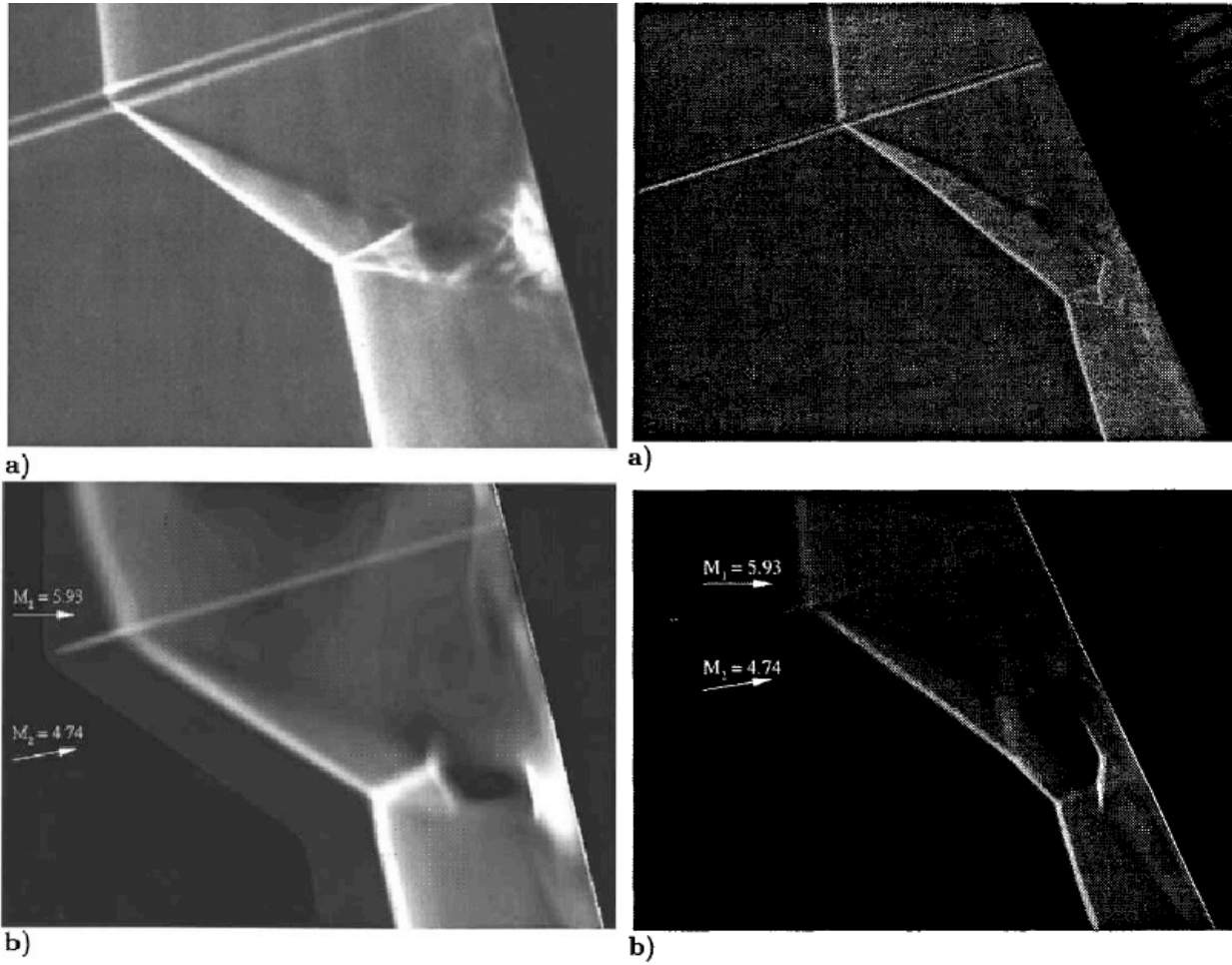


**Figure 2-34.** Images of a) experimental and b) computed schlieren data for the shock-shock interaction region on a 0.25 in-radius test article at a  $-15^\circ$  AoA (left images) and at a  $-25^\circ$  AoA (right images) in Mach 6 flow (images used with Wright's permission [3]).

### 3. Chapter 3: Wind tunnel experiments for this study

This chapter outlines the set-up and data acquisition methods used to conduct experiments in the 20-Inch Mach 6 Air Tunnel. A description of this Langley Aerothermodynamics Laboratory (LAL) facility is followed by explanations of the test set-up and how each type of test article was fabricated. Section 3.4 includes tabulated configuration information for each tunnel entry with the different types of test articles. Finally, the data acquisition hardware and methods used to collect each kind of wind tunnel data are described in section 3.5.

The current wind tunnel experiment was split into three separate wind tunnel entries as Table 3-1 shows due to tunnel schedule constraints and the availability of the test articles. During the first wind tunnel entry, Test 6976, legacy test articles instrumented with thin-film gages were used in an exploratory study to test a custom zoom schlieren system using a regular Kodak camera that obtains images at 30 fps. During Phase 1 of Test 6983, oil flow visualization and high-speed (around 1000 fps) zoom schlieren videos and images were obtained using metal test articles and Phantom 9 cameras. Finally, during Phase 2 of Test 6983, fused silica test articles were used to obtain temperature data through a phosphor thermography technique and higher-speed (at least 7900 fps) zoom schlieren videos and images.

**Table 3-1.** Tunnel entries in the current wind tunnel experiment.

Test	Purpose	Entry Date	# of Runs
6976	Exploratory study to test a custom zoom schlieren system	March 2012	9
6983 (Phase 1)	Conducted oil-flow visualization test with metal models and obtained high-speed zoom schlieren data	August 2012	21
6983 (Phase 2)	Performed phosphor thermography tests with fused silica models, and higher-speed zoom schlieren	October 2012	33

#### 3.1. Facility (20-Inch Mach 6 Air Tunnel)

Test articles instrumented with thin-film gages, a phosphor coating or layers of black paint for oil-flow testing were exposed to shock-shock interactions in the 20-Inch Mach 6 Air Tunnel, a facility in the LAL at NASA LaRC [40]. The 20-Inch Mach 6 Air Tunnel is a perfect gas facility that has well-characterized flow uniformity and composition [41]. The tunnel reservoir stagnation pressure and temperature,  $P_{t,1}$  and  $T_{t,1}$ , are accurate to within  $\pm 2\%$ .

The LaRC 20-Inch Mach 6 Air Tunnel is a blow-down wind tunnel. Dry air from two high-pressure bottle fields is transferred to a 600-psia reservoir, where an electrical resistance heater heats the air to a maximum temperature of 1000 °R. The flow passes through two filters installed



between the heater and the settling chamber before entering the test section at Mach 6, as shown in Figure 3-1. The upstream filter captures particles larger than 10  $\mu\text{m}$ , and the downstream filter is rated to block 5- $\mu\text{m}$  particles. The maximum tunnel operating pressure is 475 psia [42].

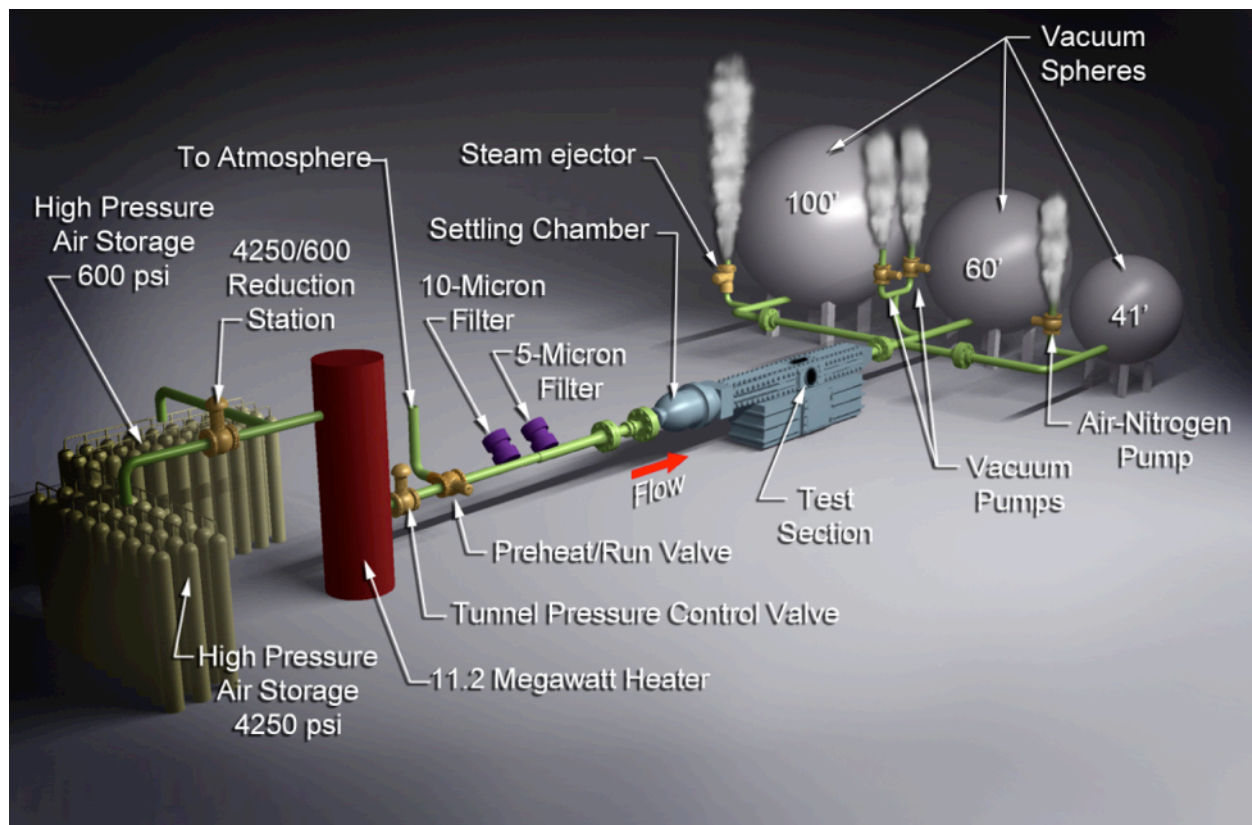


**Figure 3-1.** LAL 20-Inch Mach 6 Air Tunnel.

As sketched in Figure 3-2, the settling chamber contains a perforated conical baffle at the entrance and internal screens. The top and bottom walls of the fixed-geometry, two-dimensional nozzle in Figure 3-2 are contoured and the side walls (not shown in the figure) are parallel. The 0.34 in by 20 in nozzle throat opens into a 20.5 in by 20 in test section. The nozzle length from the throat to the test section window center is 7.45 ft. This wind tunnel exhausts either into combined 41-ft-diameter and 60-ft-diameter vacuum spheres, a 100-ft-diameter vacuum sphere, or to the atmosphere through an annular steam ejector. Perfect-gas, free-stream flows with Mach numbers between 5.8 and 6.1 and Reynolds ( $Re$ ) numbers between  $0.5 \times 10^6/\text{ft}$  and  $7.3 \times 10^6/\text{ft}$  are possible in this facility [43]. Runs at lower flow  $Re$  numbers ( $0.5 \times 10^6/\text{ft}$  to  $2.0 \times 10^6/\text{ft}$ ) are easier to set up and to conduct when the air is exhausted to the steam ejector.

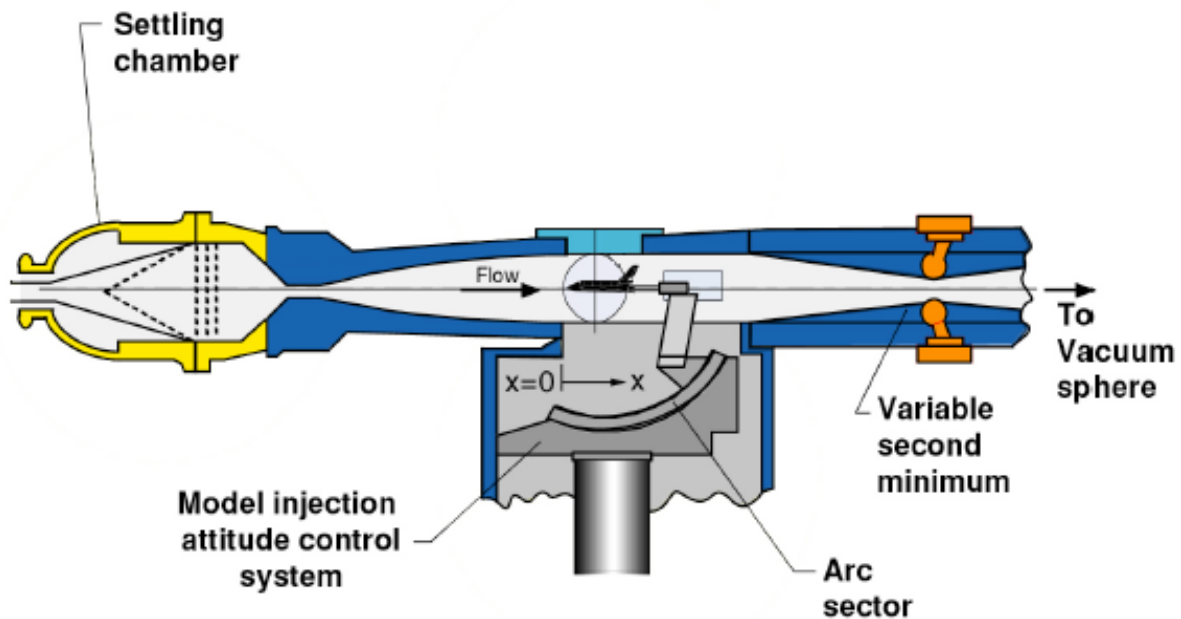


**Figure 3-2.** 20-Inch Mach 6 Air Tunnel layout.

Test articles are mounted on the arc-sector injection system located in a housing below the test section, as shown in Figure 3-2. Aeroheating tests generally have total run times of 30 sec, with typical model injection times of approximately 1.5 sec and model residence time on the tunnel centerline of approximately 5-10 sec. Nominal flow conditions (used for planning purposes) for this wind tunnel at Re numbers close to 1, 2 and 4 million/ft are shown in Table 3-2, while the actual conditions for this study are provided in Table 3-3. The actual flow conditions were calculated by averaging the parameters for nine runs in Test 6976, thirty runs at  $Re = 2.1 \times 10^6/\text{ft}$  and two runs at  $Re = 1.1 \times 10^6/\text{ft}$  in Test 6983. The parameters for  $Re = 4.1 \times 10^6/\text{ft}$  in Test 6983 correspond to the one run that was conducted at that Re number.

**Table 3-2.** Nominal flow conditions in the 20-Inch Mach 6 Air Tunnel.

$M_\infty$	$Re_\infty, \text{ft}^{-1} \times 10^{-6}$	$P_{t,1}, \text{psi}$	$T_{t,1}, ^\circ\text{R}$	$P_\infty, \text{psi} \times 10^2$	$T_\infty, ^\circ\text{R}$	$V_\infty, \text{ft/s}$
5.88	1.0	59	882	4.2	111.7	3047
5.98	2.0	124	922	8.1	113.7	3122
5.99	4.0	250	911	16.1	111.8	3103

**Table 3-3.** Actual mean flow conditions in Tests 6976 and 6983 in 20-Inch Mach 6 Air Tunnel.

Test	$M_\infty$	$P_{t,1}, \text{psia}$	$T_{t,1}, ^\circ\text{R}$	$Re_\infty, \text{ft}^{-1} \times 10^{-6}$	$\rho_\infty, 10^{-4} \text{slug/ft}^3$	$T_\infty, ^\circ\text{R}$	$V_\infty, \text{ft/s}$
6983	5.90	60.5	875.1	1.1	0.33	110.3	3035
6976	5.96	126.4	894.7	2.1	0.64	110.7	3073
6983	5.96	125.5	898.5	2.1	0.63	111.3	3082
	6.00	252.2	901.6	4.1	1.23	110.5	3087

The flow conditions in the 20-Inch Mach 6 Air Tunnel during the wind tunnel experiment were calculated using a program called GasProps [44]. This code calculates the Re number and other flow properties in LAL wind tunnels based on coefficients for the equation of state for the test gas, the measured reservoir pressure and temperature, and the test section Pitot pressure during a wind tunnel run.

### 3.2. Experimental set up

In the current study, a flat plate with a sharp leading edge was angled to turn the Mach 6 flow upstream of the test article either  $6^\circ$  or  $9^\circ$  from horizontal. This flat plate produced an incident shock. The oblique shock angle for a given shock generator (SG) orientation was calculated using the online Compressible Aerodynamics Calculator [45]. The predicted changes in the flow properties behind the planar incident shock are provided in Chapter 5. The required relative height of the test article above the flat plate was determined based on the estimated incident shock angle and the calculated thickness of the boundary layer over the SG.

Figure 3-3 to Figure 3-8 below are graphical representations of the hardware in the tunnel for the runs with the SG flat plate installed. Similar images of these computer-aided design (CAD) models were used prior to the wind tunnel experiment to estimate the camera view angles through the top and side wind tunnel windows to ensure the visibility of the leading edge of the test article in each test configuration. Arbitrary colors were selected for the components in these images to indicate these test set-up images were computer generated. Figure 3-4 through Figure 3-6 show each of the three test article geometries (in white) at a single representative angle of attack through the side tunnel window. Figure 3-7 and Figure 3-8 provide views of a test article through the top tunnel window. In separate wind tunnel runs, the upper tip of the leading edge of the test article was swept either  $0^\circ$ ,  $15^\circ$ , or  $25^\circ$  forward of vertical. These angles are defined as  $0^\circ$ ,  $-15^\circ$ , and  $-25^\circ$  test article angles of attack (AoA), respectively, in the remainder of this thesis.

Figure 3-3 shows the arc sector positioned below the test section in the 20-Inch Mach 6 Air Tunnel. Ten bolts (five on each side) secure an I-beam to the arc sector using a 1 in-thick spacer to center the test article in the core flow of the wind tunnel. A strut is fastened to the I-beam using three bolts on either side of the strut. The appropriate strut head plate is bolted to the top surface of the strut to support a flat plate SG at an angle of either  $6^\circ$  or  $9^\circ$  from horizontal. The stainless steel flat plate is 6 in wide and 17 in long with a sharp leading edge. A 0.5 in-diameter sting is inserted into a stainless steel support with an adjustable height that is bolted into the strut head plate behind the flat plate. The appropriate test article is bolted to the sting through a component used to change the angle of attack of the test article, called the “fin adjuster” in Appendix B.

A detached bow shock forms around the test article during the run. The SG is used to establish a planar oblique shock that intersects the shock formed around the test article and establishes the interaction pattern. Different types of shock interaction patterns were created depending on the angle of attack of the test article and the incident shock angle from the flat plate. The features of the Type III and IV shock-shock interactions that formed are shown in Figure 2-1.

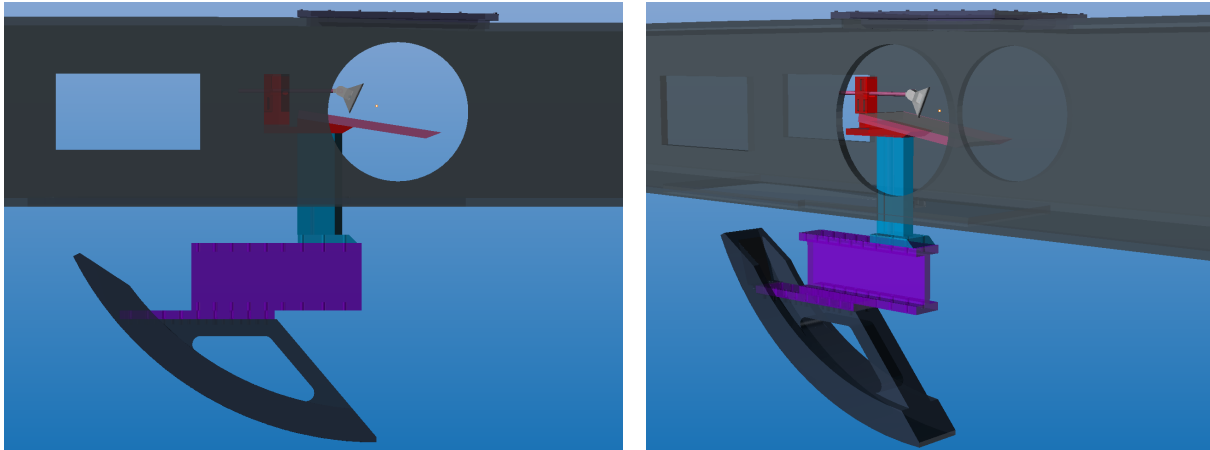


**Figure 3-3.** Side-view renderings of tunnel set-up with arc sector, I-beam, and strut.



**Figure 3-4.** Side-view rendering of 0.25 in-radius fused silica test article at 0° AoA.

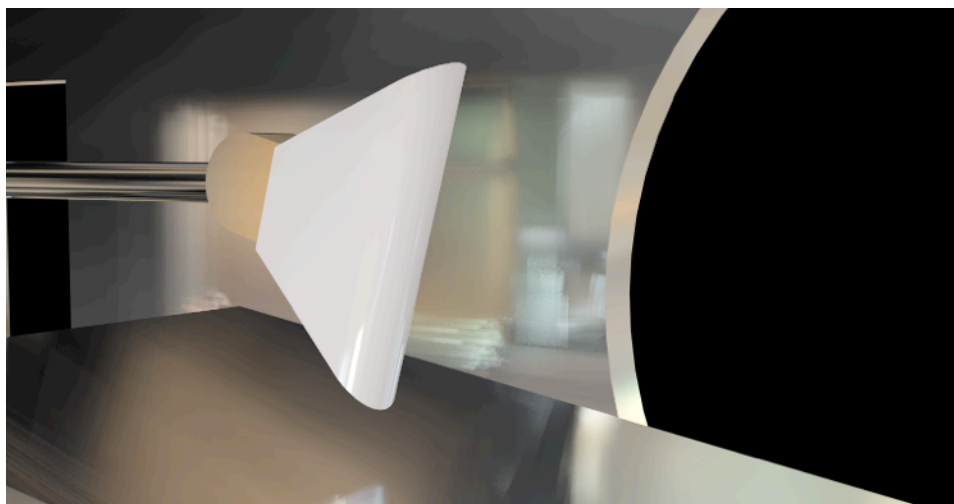


**Figure 3-5.** Side-view rendering of 0.5 in-radius fused silica test article at -15° AoA.

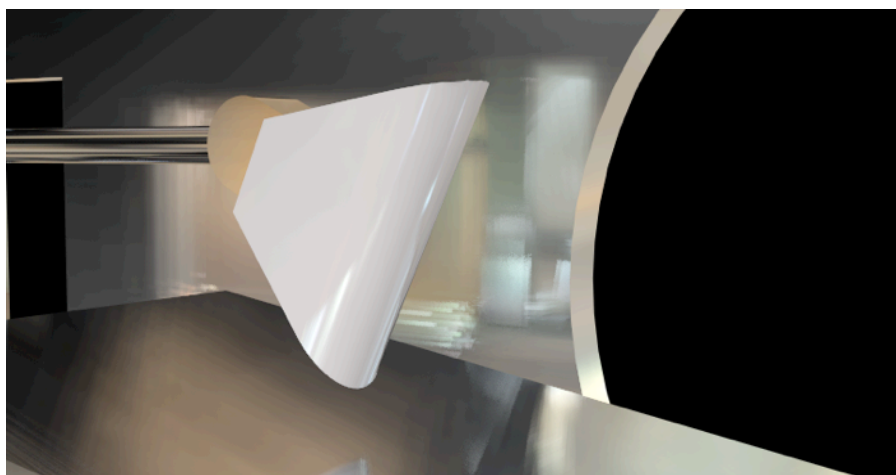


**Figure 3-6.** Side-view rendering of 0.75 in-radius fused silica test article at  $-25^{\circ}$  AoA.



**Figure 3-7.** Top-view rendering of 0.5 in-radius fused silica test article at  $0^{\circ}$  AoA.

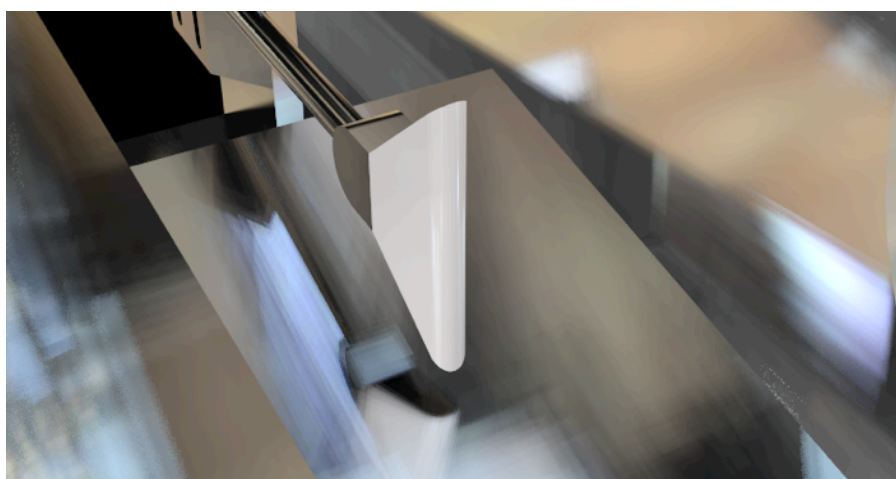


**Figure 3-8.** Slanted top view of 0.25 in-radius fused silica test article at  $0^{\circ}$  AoA.

Photos of the hardware taken during the test entries are shown in Figure 3-9 through Figure 3-12. In these images, the test article support system is retracted into the “box” below the tunnel test section. Figure 3-9 shows a 0.25 in-radius phosphor-coated fused silica test article mounted in the support system in preparation for a baseline heating run as evidenced by the lack of a flat plate SG. In Figure 3-10, the flat plate is installed with a 9° angle to produce a shock-shock interaction between a 16.7° incident shock and the bow shock around the test article.

A single embedded thermocouple is installed at the surface of the fused silica test articles shown in Figure 3-9 and Figure 3-10. In these figures, the thermocouple is located near the top of the test article on the far side that is not visible in the image. This thermocouple position is implied in the images by the location of the insulation (on top of the sting and the fin adjuster) that protects the lead wires from the thermocouple. The thermocouple bead is not visible to the phosphor thermography camera during the runs that correspond to Figure 3-9 and Figure 3-10. Figure 3-11 shows a test article rotated 180° to position the thermocouple at the bottom of the test article on the side that is visible to the camera, and Figure 3-12 shows a zoomed-in view of the same run configuration. Although the thermocouple is just below the phosphor coating, the bead is visible in these latter two figures, and the bead location is labeled in Figure 3-12. The thermocouple and metal inserts in the fused silica models are described in more detail in sections 3.3.3.1 and 3.5.2.1.

The stainless steel fin adjuster is also shown more clearly in Figure 3-12. The adjuster is secured to the sting on one side using a 10-32 bolt, nut and washer and bolted on the other side to a metal insert with threaded holes that is bonded into the fused silica test article. A hinge pin with a retaining ring allows the test article to be rotated through any angle of attack between -45° and 45° from horizontal. Refer to Appendix B for detailed diagrams of the test hardware.

In Test 6976, the test article AoA was set using a scale mounted on the sting that was marked with angles at 5° intervals. Inaccuracies in the test article angle using this method stemmed from the orientation of the bolted support hardware. If components of the support hardware were not level, the sting would not be horizontal and the angle would be measured relative to an improper reference point. To eliminate the errors in angle measurement encountered in Test 6976, an inclinometer was used in Test 6983 to set the angle of attack before the bolt on the angle of attack adjuster was tightened.

A laser beam was used to check the orientation of the leading edge of the test article, and the sting was rotated in the support hardware as needed to ensure a vertical leading edge. The laser was turned off after each alignment and was not on during the runs. The laser beam can be seen wrapping around the test article in Figure 3-9.



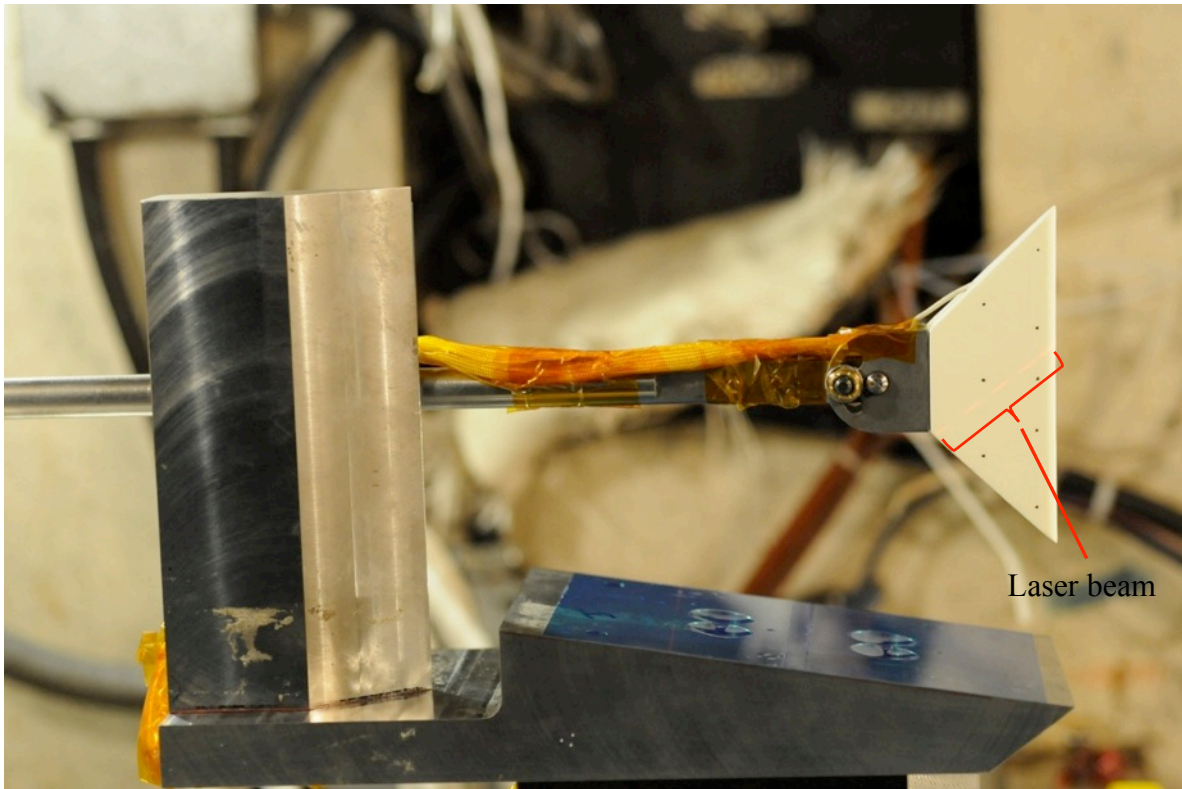


**Figure 3-9.** Fused silica (0.25 in-radius) test article in support hardware without the SG.

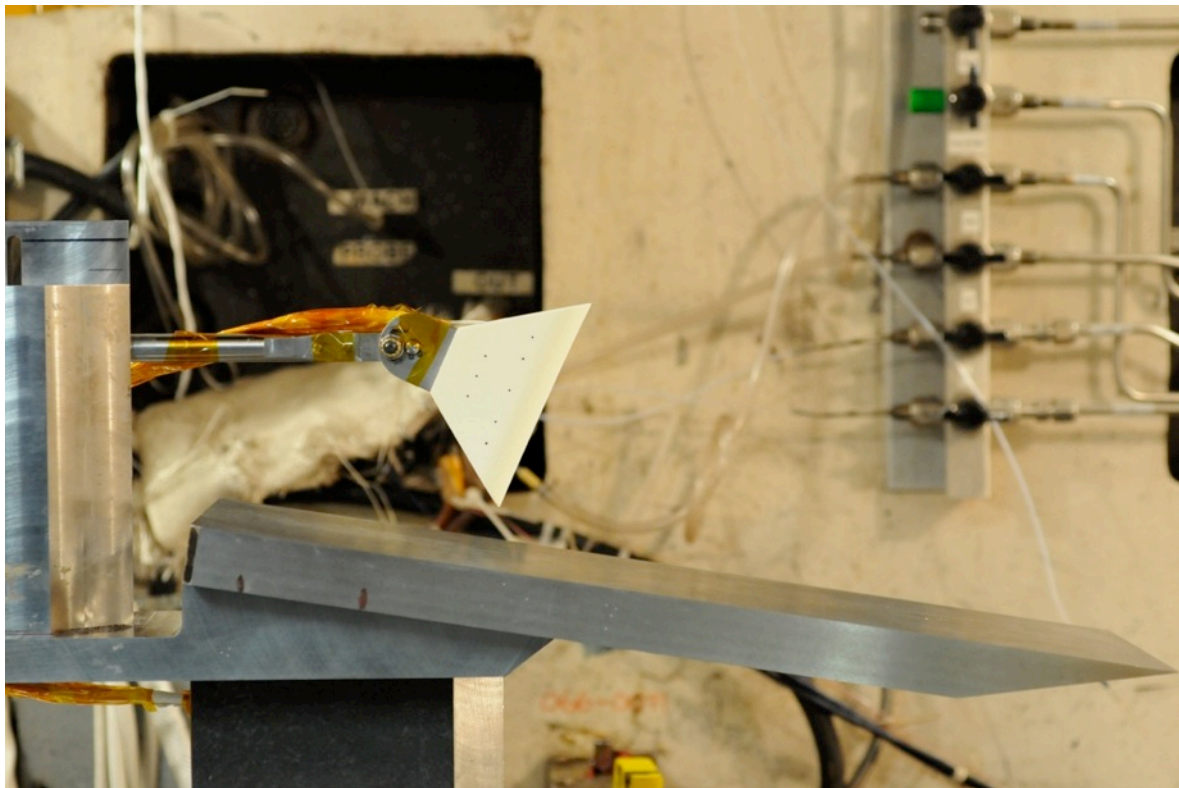


**Figure 3-10.** Fused silica (0.75 in-radius) test article in support hardware with the 9° SG.

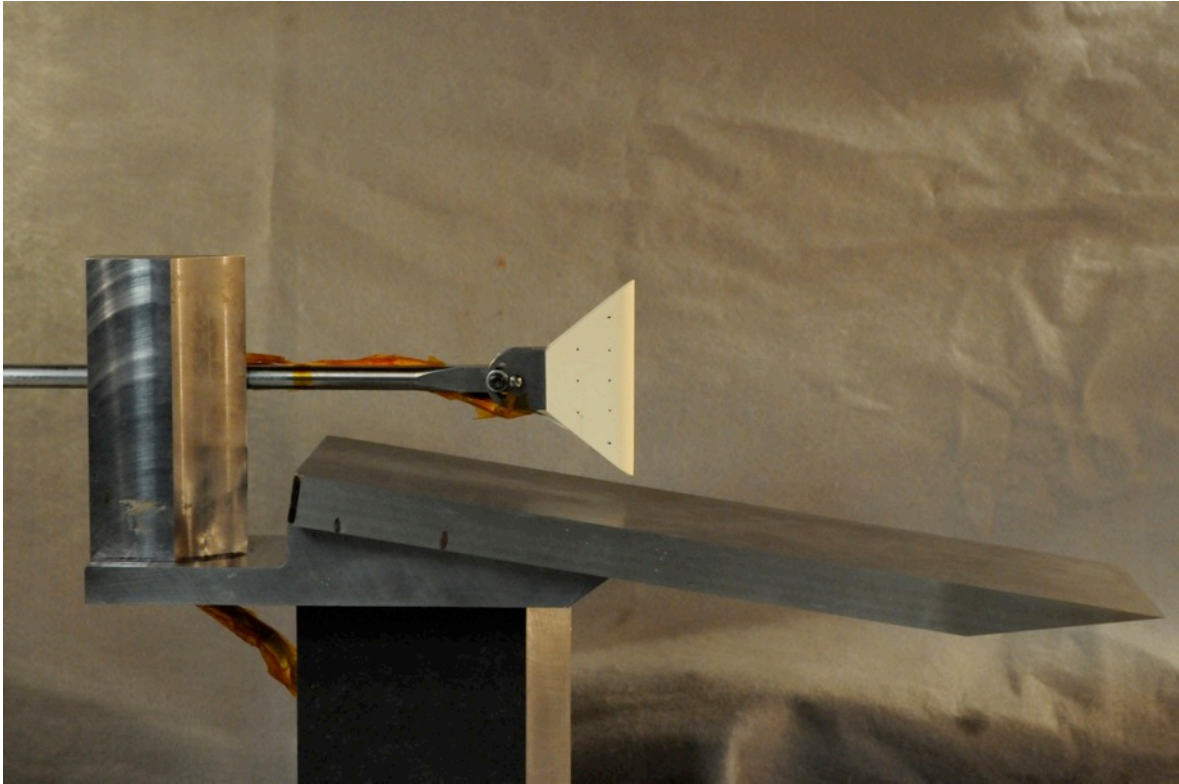


**Figure 3-11.** Fused silica (0.50 in-radius) test article with thermocouple near the bottom.

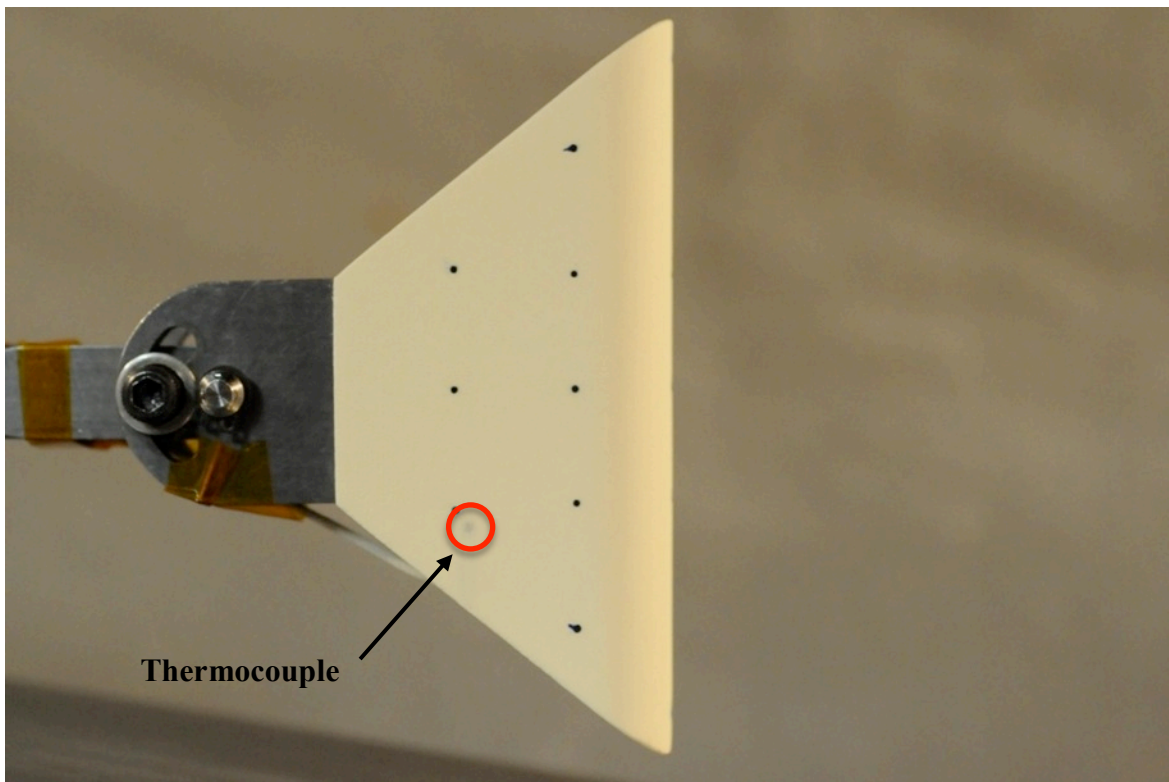


**Figure 3-12.** Close-up of 0.50 in-radius fused silica test article showing thermocouple bead.



The test article was always positioned at least 0.5 in above the flat plate SG or strut head plate to eliminate interactions between the tip of the test article and the flat plate boundary layer flow. During some of the runs in which the 0.75 in-radius test articles were angled at  $-25^\circ$ , the test article was raised to 0.75 in above the SG plate. Otherwise, the larger bow shock around this test article intersects the boundary layer in the flow above the flat plate far enough ahead of the test article to produce additional interactions that impinge on the surface of the test article. This phenomenon is discussed in more detail in Chapter 5.

### 3.3. Test articles

Macor® thin-film-gage, phosphor-coated fused silica, and metal oil-flow test articles were used in the experiments described in this thesis. Images of these test articles are included in Figure 3-13. The steps required to fabricate and calibrate these types of test articles differ so each process is described in more detail in the following sections. Data is collected from the entire surface of the fused silica and metal test articles so the “calibration” step in those sections is comprised of applying fiducial marks as a physical reference and conducting a Quality Assurance (QA) analysis of the actual test article dimensions. An additional calibration of the overall phosphor system is explained in section 3.3.3.3, though this calibration is not performed for individual test articles with the phosphor coating. The thermal properties of the fused silica and Macor® substrate materials are included in Appendix A.

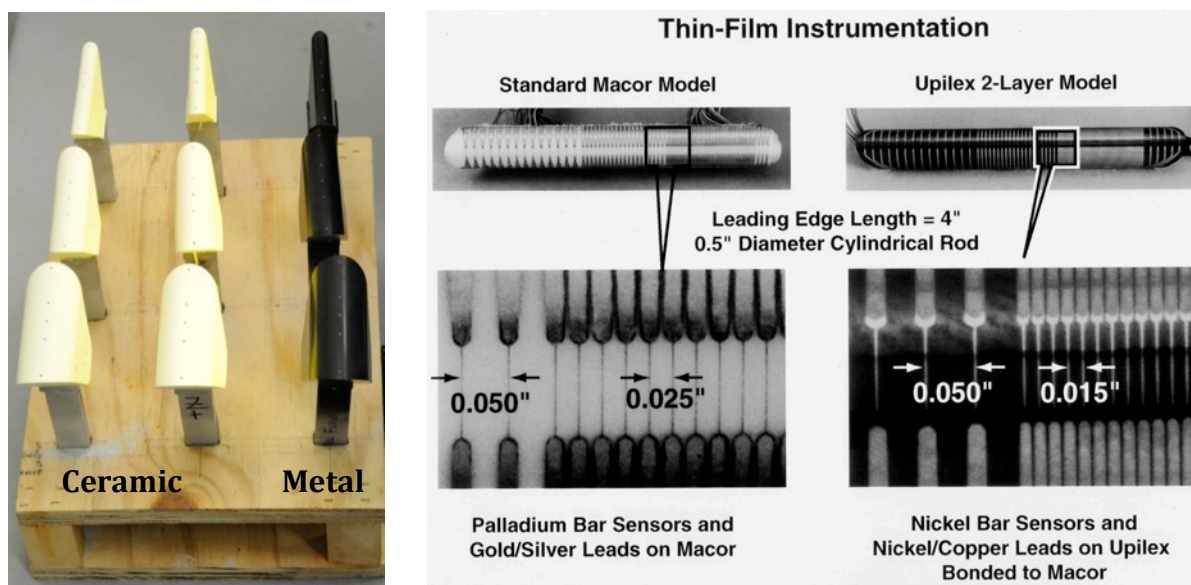


**Figure 3-13.** Fused silica, 15-5 stainless steel (painted black), and thin-film-gage test articles (image of thin-film test articles used with Berry’s permission [8]).

#### 3.3.1. Thin-film test articles (Tests 6692/6976)

Three different types of test articles were instrumented with thin-film-gages for Test 6692 [8]. Cylindrical Macor® rods, with a 0.5 in diameter and roughly 4 in long, were used as the substrate material for the thin film gages. The thin-film material and application technique differ

between these three test articles as described in the next two sections. For all three types of test articles, the gage spacing was minimized in the region of interest (near the point of the shock-shock interaction) and relaxed elsewhere. The minimum spacing was 0.010 to 0.025 in between gage centers depending on the technique used to apply the gages to the substrate material. The maximum spacing was about 0.1 in towards the top of the cylinder. These test articles were built and tested nearly twenty years prior to the current study. Thus, many of the thin-film gages on these test articles were not expected to yield accurate data. However, these test articles were considered for use in a preliminary study to test the custom zoom schlieren system and to learn about the basic features of shock-shock interactions.

#### **3.3.1.1. Fabrication of test article with standard thin-film gages (Painted 1, 2)**

Thin-film gages were vapor deposited on one Macor® test article using a standard mechanical deposition technique [8]. The “Standard Macor® Model” in Figure 3-13 represents this test article, which was heavily utilized during Test 6692. The minimum spacing between gages on this model is 0.025 in, which was the reasonable limit for spacing with accurate deposition on a curved surface. Since the palladium bar sensors were applied directly to the Macor® substrate, Berry and Nowak used Macor® thermal properties in 1DHeat to conduct a one-dimensional heat transfer analysis of the results for the Macor® test article. A different technique was implemented to improve gage spacing, but these test articles were not ready in time for Test 6692 and thus were never used. In this technique, similar thin-film gages were hand painted on two additional test articles called Painted 1 and Painted 2. The gages on the Painted 2 test article were re-calibrated, as section 3.3.1.3 describes, and this test article was used during Test 6976. The smallest spacing between the hand-painted gages was roughly 0.01 in, with slight variations in the spacing due to the lack of precision associated with manually painting the gages on the test articles.

#### **3.3.1.2. Fabrication of test article with etched gages on polyimide film (Upilex®)**

A different thin-film-gage application method was used to prepare the Upilex® test article in Figure 3-13 [8]. Nickel gages were etched in a 50- $\mu$ m-thick, Upilex® polyimide film on a flat surface before the Upilex® layer was bonded to the semi-cylindrical rod using a room-temperature vulcanized (RTV) silicone. This additional step eliminated the difficulty associated with maintaining gage spacing on a curved surface for the vapor-deposited gages. The smallest gage spacing on this two-layer test article is 0.015 in. Berry and Nowak used a one-dimensional, finite-volume heat transfer analysis in the 1DHeat program to account for the different thermal properties of the Macor® and Upilex® layers.

#### **3.3.1.3. Calibrations of thin-film test articles**

The Painted 1, Painted 2, and Upilex® test articles from the 1997 Berry and Nowak test were pulled from storage at NASA LaRC [8]. An ohmmeter was used to check whether a sufficient number of the sensors still provided a resistance and, therefore, might yield temperature data during wind tunnel testing. In this preliminary analysis, approximately 45% of the Painted 1 gages, 84% of the Painted 2 gages, and 71% of the Upilex® gages provided a reasonable, non-infinite resistance between 100 and 200  $\Omega$ . Since the Painted 1 and Painted 2 test articles have

similar vapor-deposited thin-film patterns and more gages were operable on Painted 2, only the Painted 2 test article was re-calibrated.

The Painted 2 and Upilex® test articles were recalibrated using a hot-oil bath. The Painted 2 calibration spanned a temperature range from 75 °F to 225 °F in increments of 25 °F, while the temperature range of the Upilex® calibration was from 75 °F to 425 °F in increments of either 75 °F or 50 °F for separate intervals in the calibration. To avoid possible damage to the old vapor-deposited gages on the Painted 2 test article in a calibration using two separate oil baths, the upper limit of the Painted 2 calibration was restricted to a temperature of 225 °F. For each calibration, the test article was placed in an oil bath that was heated to the specified temperatures. Each calibration proceeded from the minimum temperature to the maximum temperature and returned to the minimum temperature to check for hysteresis in the measurements. The dwell time at each temperature was approximately half an hour. Approximately 60-70% of the Painted 2 gages and 66% of the Upilex® gages functioned properly during the calibration.

Prior to the initial wind tunnel test in March 2012, the Macor® Painted 2 and Upilex® test articles were bonded into metal holders using a room-temperature vulcanized (RTV) rubber as demonstrated in Figure 3-14. This RTV is suitable for high-temperature applications. The sting holding the Painted 2 test article was then inserted in the support hardware in the wind tunnel, and cables connected to the thin-film gages were attached to data acquisition channels in the tunnel. The thin-film-gage cables were covered with a high-temperature sheath material and taped to the sting during each run as shown in Figure 3-15.

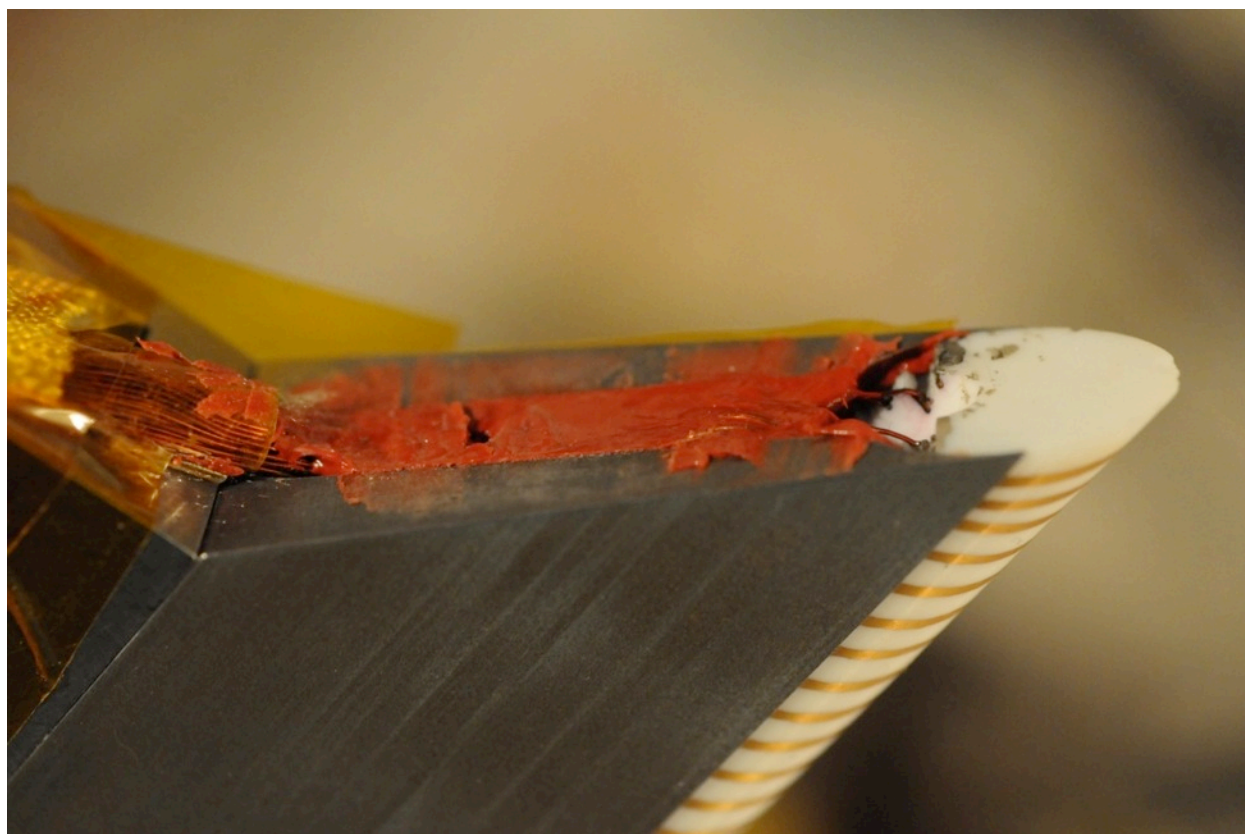


**Figure 3-14.** Red high-temperature RTV silicone bonded Macor® rods into metal holders.

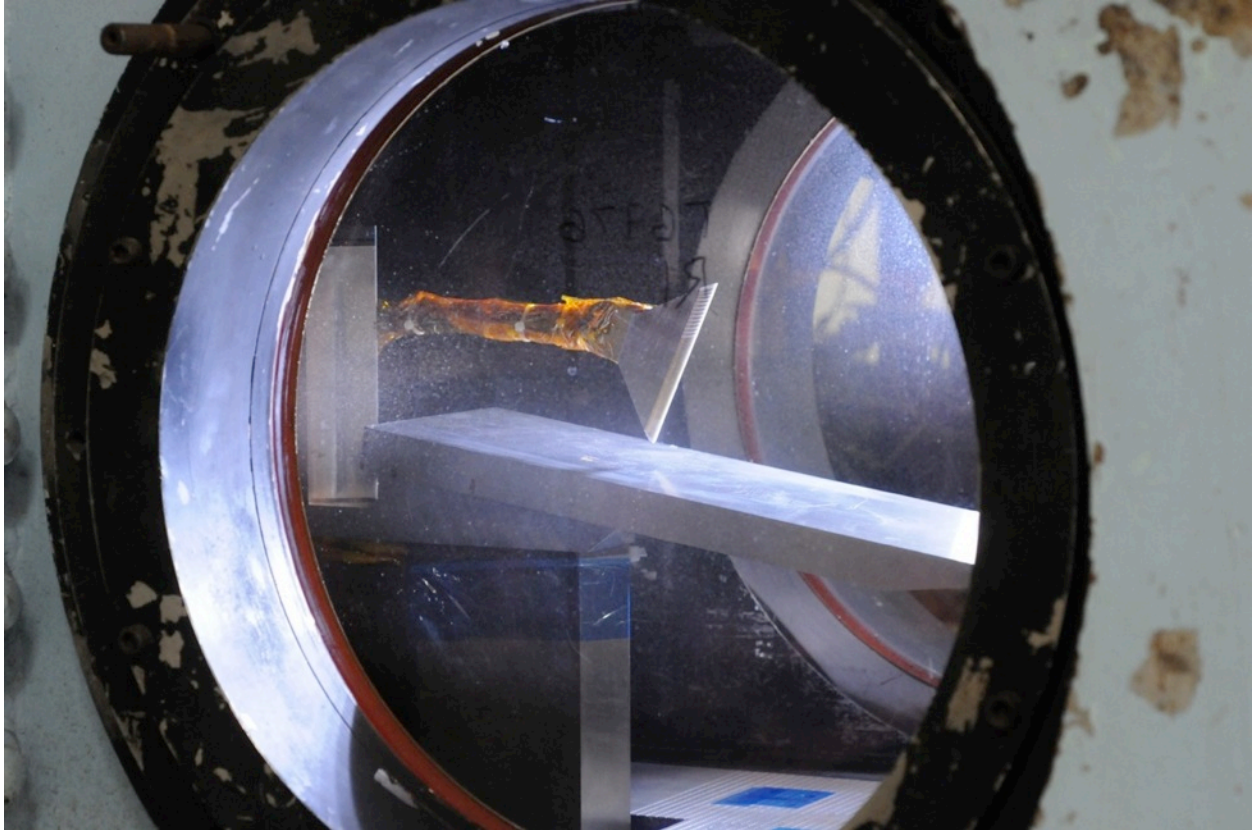


**Figure 3-15.** Painted 2 test article mounted on the sting in the support hardware and inserted in the tunnel.

A diagnostic check was conducted to ensure all the channels on the data acquisition board were properly wired. This test revealed a majority of the gages in the shock-shock interaction region were no longer operable. Resistance readings with an ohmmeter confirmed several gages that yielded acceptable outputs during the preliminary analysis and calibrations no longer provided a non-infinite resistance. As the pictures in Figure 3-16 and Figure 3-17 below demonstrate, one assumed reason for the sudden gage failure is that the lead wires on the thin-film gages were cut or otherwise damaged either due to handling or the procedure followed in mounting the test articles in the sharp metal holders after the calibrations were completed. In some cases, the damage to the sensors is visible near the stagnation line of the test article. Many of the gages in the shock-shock interaction region failed so the thin-film data from Test 6976 is not included in this thesis. Tunnel entry 6976 still was conducted using the thin-film-gage test articles primarily to learn lessons for later tunnel entries and to obtain preliminary schlieren images of the shock-shock interactions both with a 6° and a 9° SG angle.



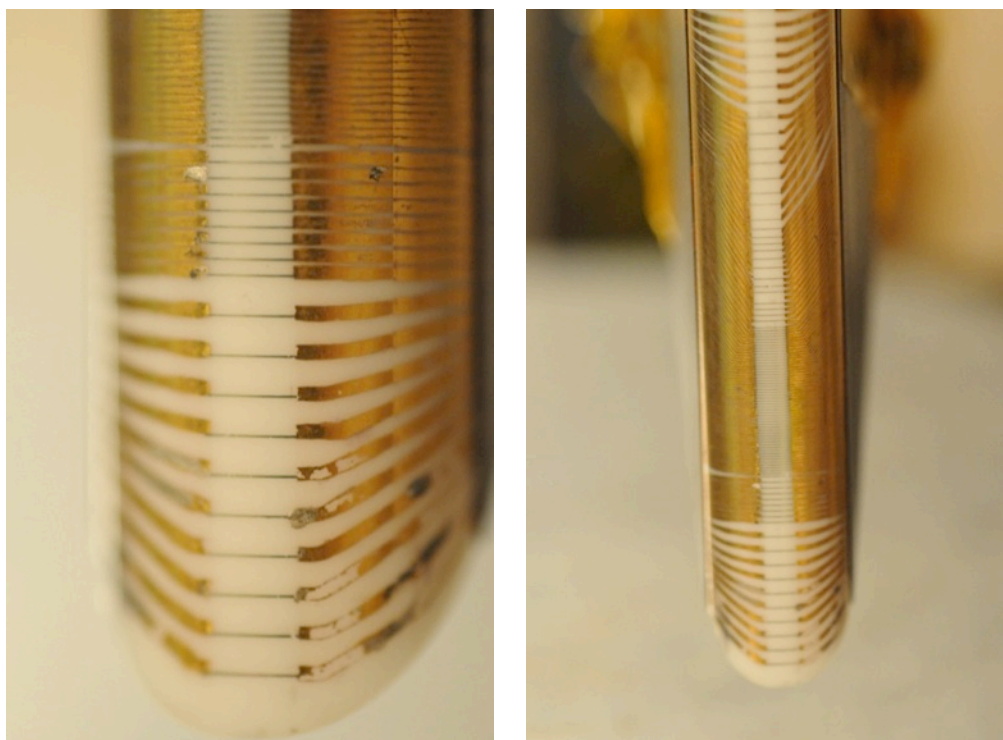


**Figure 3-16.** Damaged sensors on Painted 2 test article.

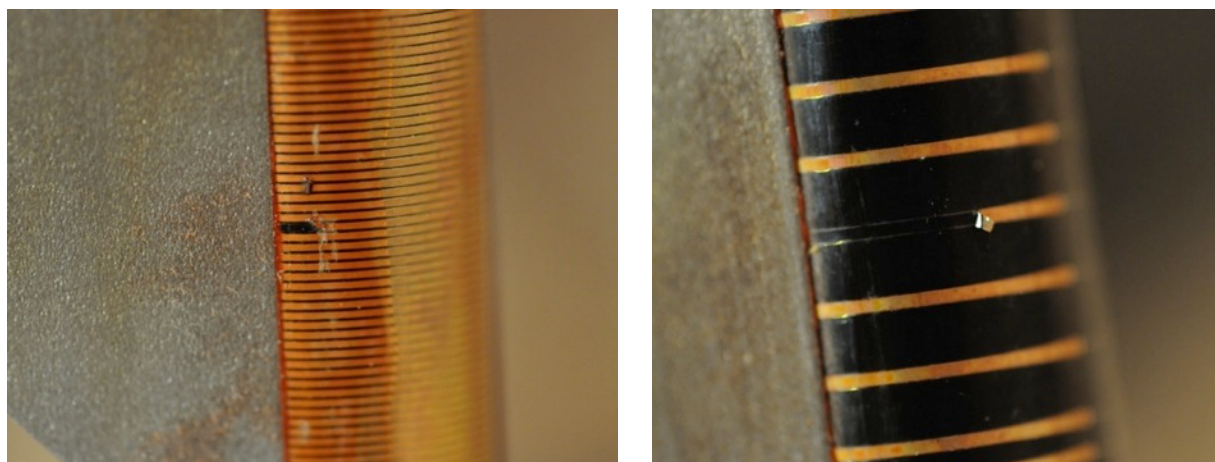


**Figure 3-17.** Damaged sensors (cut wires) on Upilex® test article.

### **3.3.2. Oil flow test articles (Test 6983)**

Oil flow tests were conducted to visualize the streamline patterns on the surface of the test articles at each set of conditions of interest in the current study. The oil flow patterns of surface streamlines in the vicinity of the off-surface shock-shock interactions provide insight into the flow behavior. These patterns also were used to verify the streamlines in the CFD simulations. Metal test articles were used instead of ceramic test articles to minimize the likelihood that the oil would be absorbed into the model surface during a run, thus, allowing the test articles to be reused during subsequent runs.

### 3.3.2.1. Metal test article fabrication

A wire electrical discharge machine (EDM) was used to cut three oil-flow test articles from 15-5 stainless steel per the drawings in Appendix B. The surfaces of these test articles were then polished smooth before Rust-Oleum® high-temperature BBQ flat black paint (heat resistant up to 1200 °F) was sprayed on the surface of each test article. Black paint was selected to provide sufficient contrast with a white-pigmented oil in images and videos during the oil flow wind tunnel runs. The 0.25 in-radius model received three coatings of the black paint, while the larger models were coated with five paint layers. The smallest and largest test articles received minor damage during the wind tunnel testing likely due to small particles impacting the surface of the test article and exposing a small region of the metal test article below the black paint in one or two locations. However, these test articles were rotated 180° to move the damaged coating away from the region of interest (near the shock-shock interaction) during the majority of the testing. Figure 3-18 shows the 0.75 in-radius metal test article, without a coating of oil, inserted into the tunnel test section and illuminated with UV light to reveal the fluorescent fiducial marks described in the following section.

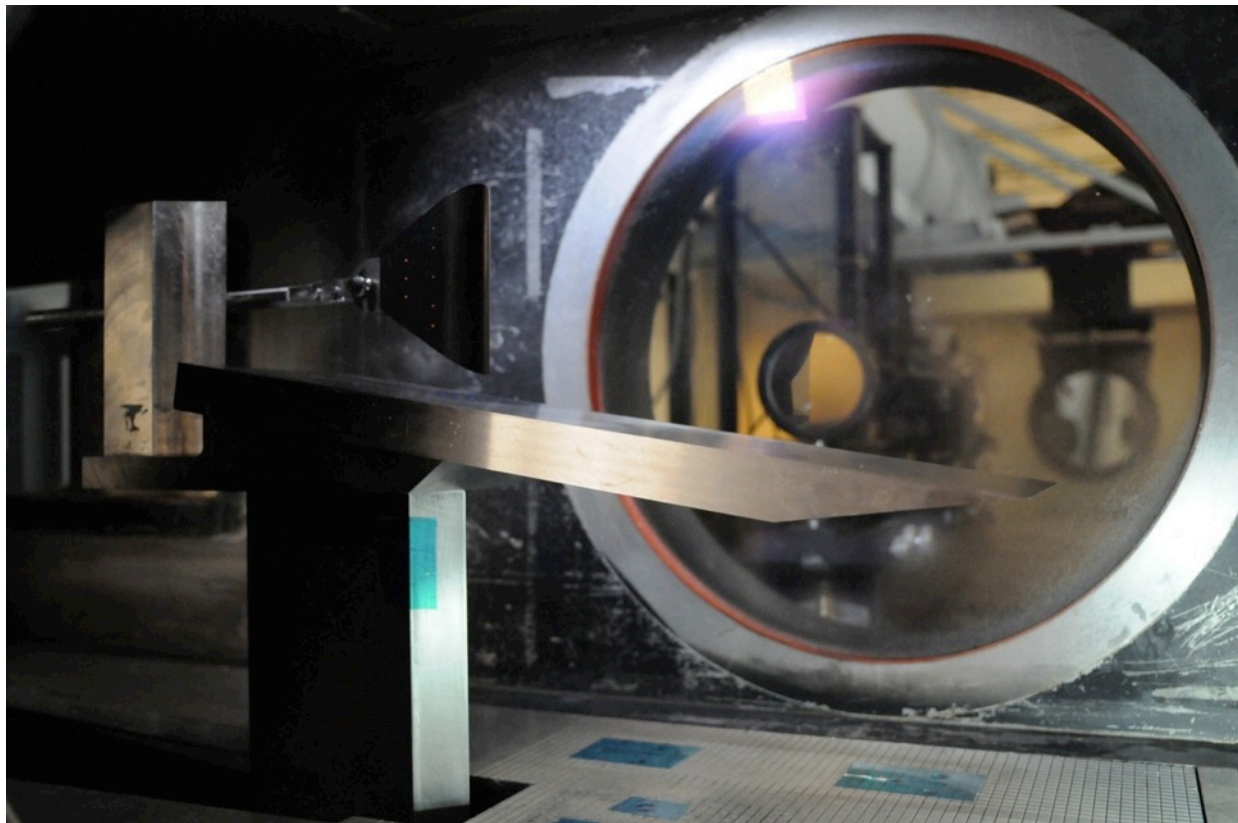


**Figure 3-18.** Metal test article (0.75 in-radius) used in oil flow visualization runs.

### 3.3.2.2. Fiducial mark application

Fiducial marks are dots applied to a test article in specified locations that can be used to correlate distances between features on an image to the physical dimensions of the test article. To

facilitate direct comparisons between the surface streamline locations and the regions of peak heating due to the shock-shock interactions, fiducial marks were applied in the same pattern to both the oil-flow and the phosphor-coated test articles. Since the oil-flow models were painted black, the typical Dykem® Hi-Spot blue ink would not be visible on the surface of these test articles. Instead, Testors® fluorescent enamel paint was suggested as a possible medium to apply the fiducial marks.

A scrap piece of aluminum was sprayed with two layers of the Rust-Oleum® black paint. A spare ruby-tipped probe, similar to the probes used in the coordinate measuring machine (CMM) to mark fiducials, was used to apply practice fiducial marks. Practice dots were applied to the surface of the painted aluminum piece shown in Figure 3-19 to determine the proper technique to generate visible fiducial marks that were not large enough to significantly affect the flow over the test article. The fiducial locations on the test articles were marked with orange enamel paint to provide a sharp contrast between the black surface paint and the white oil pigment when illuminated with 360 nm UV light.

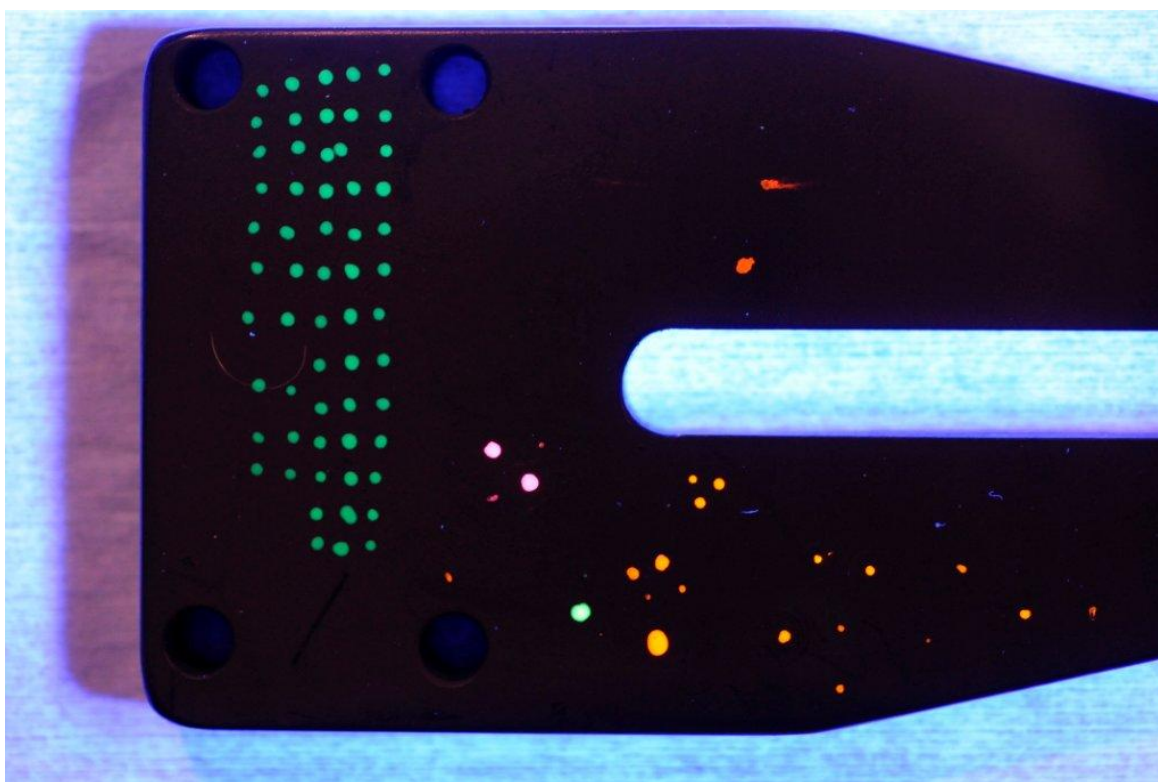


**Figure 3-19.** Practice enamel-paint fiducial marks on scrap metal (illuminated by UV light).

### **3.3.2.3. Quality Assurance analysis of oil flow test articles**

In addition to applying fiducial marks, the Quality Assurance Branch also used the CMM to measure key dimensions on the metal test articles. These test articles were machined according to the drawings included in Appendix B. The measured dimensions are labeled in the diagram in Figure 3-20. The only dimension that is not shown in the figure is the “starboard side wall angle” which is a nominally 7° slope to the hidden side of the test article (relative to the test

article orientation in the image) from the tangent point of the leading edge. This dimension is similar to the “port side wall angle” shown in the diagram.

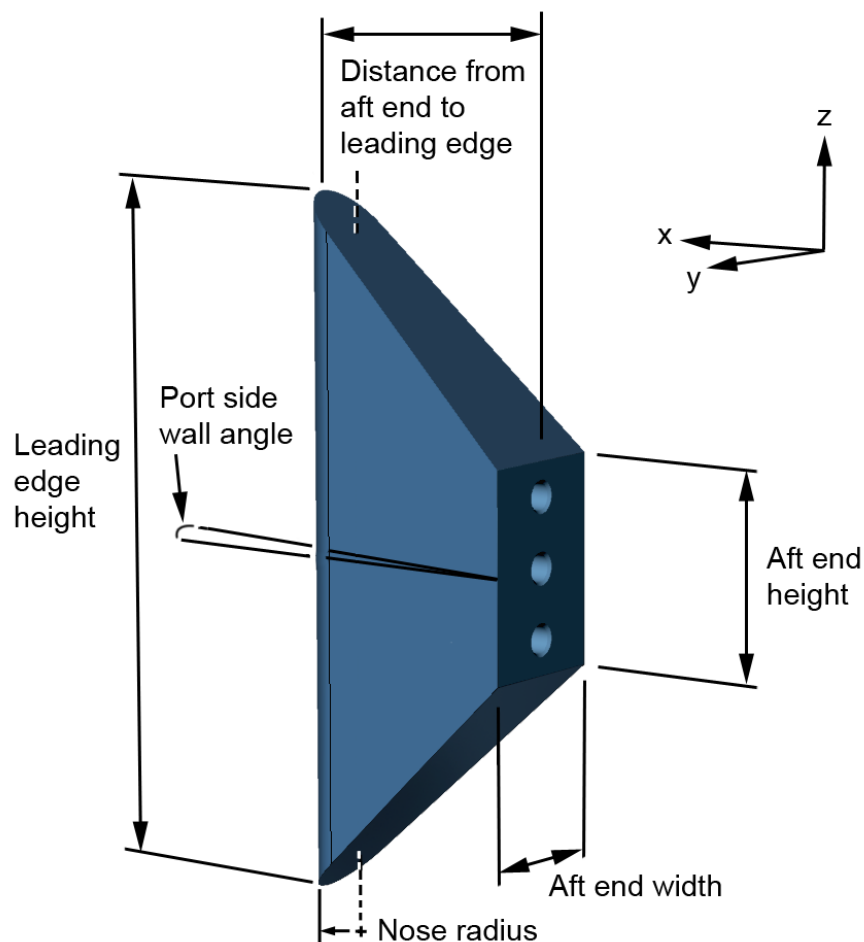


**Figure 3-20.** Diagram of the dimensions measured with a CMM on the metal and the fused silica test articles (a 0.25 in-radius metal test article is shown for reference).

Table 3-4 shows the pertinent dimensions of the metal test articles compared to the nominal dimensions listed in the drawings. As the percent deviation values in the last column of the table suggest, the metal test articles were machined within a tight tolerance to the most important dimensions listed on the drawings (such as the nose radius). For each measurement, specified in separate rows, the dimensions listed from top to bottom are arranged in order of increasing leading-edge radius. For more information on the test article measurements and fiducial mark locations, refer to the tables in Appendix B.



**Table 3-4.** Key dimensions of metal test articles. Unless otherwise specified, units are inches.

Dimension	Nominal	Actual	Percent Deviation (%)
Nose radius	0.25	0.2507	0.2800
	0.50	0.5021	0.4200
	0.75	0.7513	0.1733
Distance from aft end to the leading edge	1.51	1.509	0.0662
	1.76	1.7601	0.0057
	2.01	2.0114	0.0697
Leading edge height	4.00	3.9955	0.1125
		4.0281	0.7025
		4.0014	0.0350
Port side wall angle	-7.00°	-7.0870°	1.2429
		-6.9977°	0.0329
		-7.0202°	0.2886
Starboard side wall angle	7.00°	6.9432°	0.8114
		7.0278°	0.3971
		7.0248°	0.3543
Aft end width	0.814	0.8125	0.1843
	1.318	1.3177	0.0228
	1.822	1.8229	0.0494
Aft end height	1.20	1.1999	0.0083
		1.2016	0.1333
		1.2001	0.0083

### 3.3.3. Fused silica test articles instrumented with a phosphor coating (Test 6983)

Phosphor-coated fused silica test articles were created using the following process. Although fused silica models have been used frequently in other phosphor thermography tests, a slightly different procedure was used to produce the fused silica models for this study.

#### 3.3.3.1. Fabrication of fused silica test articles

First, CAD models were generated from drawings of the legacy test articles from Test 6692 [8]. To ensure the angle of the test article geometry on either side of the leading half cylinder was 7° as in the legacy drawings, the distance between the centerline of the half cylinder and the back mounting surface of the test article listed in the legacy drawings was increased slightly for all three test article configurations. The dimensions and CAD renderings of the current test articles are shown in Appendix B. A 7° angle was selected to ensure the flow around the test article

continued down the tunnel rather than turning upstream and interfering with the shock-shock interaction.

The CAD geometries were first used to generate wax patterns of the test articles. Six patterns were made in a ThermoJet wax printer to provide one primary and one back-up model for each of the three configurations. The wax parts were cleaned to remove the built structures used in the layer-build process of the rapid prototyping system.

Next, the wax patterns were used to generate molds in the shape of the fused silica test articles. Fused silica was poured into the molds using a pour gate (an access hole) built into the model geometry. Typically, the silica is added to the mold in a “pour and dump” process in which the ceramic is poured into the mold through a large gate and excess silica is poured out. In the usual fabrication process, these steps are repeated until a fused silica shell forms that is approximately 0.25 in thick. The gate diameter decreases with each pour step as fused silica dries in the gate. However, for the models used in this test, the gate was very small and likely would close completely before sufficient fused silica was poured into the model if the “pour and dump” procedure was followed. Therefore, the mold was filled with fused silica and no attempt was made to pour out the excess material. This process created solid, porous fused silica test articles, rather than a hollow fused silica shell. This deviation from the typical method used to fabricate fused silica test articles facilitated a two-dimensional conduction assumption through a half cylinder to represent the test article leading edge in the finite-volume codes used to analyze the surface heat transfer.

The test article geometry was cleaned up and the pour gate removed for each configuration. The fused silica test articles were then dried and sintered to form bonds between the particles of the material and improve the strength of the test article. Refer to reference [46] for more details on the process of firing fused silica models.

An opening was included in the back of the fused silica test article geometries to accommodate a mounting plate, which is a metal insert with drilled and tapped holes for screws to attach the model to the sting and the support hardware. The size of the opening in the fused silica test articles includes a 0.005 in clearance on four sides of the model. This gap was included to provide room for application of GE RTV 102 silicone to bond the metal inserts into the sintered test articles. The maximum temperature of this bonding agent is 400 °F.

Three small, custom-built thermocouples were fabricated and installed in the primary fused silica test articles, one thermocouple for each test article geometry. Computer-generated images in Figure 3-21 to Figure 3-23 show the steps required to construct the thermocouples and insert the sensors in the fused silica models. To begin the process, Type K thermocouple lead wires were inserted into a UNITEK TC welder. The welding chamber was purged with Argon to prevent oxidation of the wires and to ensure impurities did not form in the welded thermocouple junction. The welder discharged an electric arc to melt equal parts of each wire to form a thermocouple bead.

As shown in Figure 3-21, the thermocouple bead and a segment of the lead wires were flattened to move the sensing portion of the thermocouple as close to the surface of the fused silica test

article as possible. The flattened bead was 0.055 in wide and 0.045 in thick. As Figure 3-22 shows, the bead and lead wires were spot welded to 5 mil, Type K thermocouple wire using a UNITEK spot-weld device. These thin wires were selected to reduce the required depth of the groove in the surface of each fused silica test article.

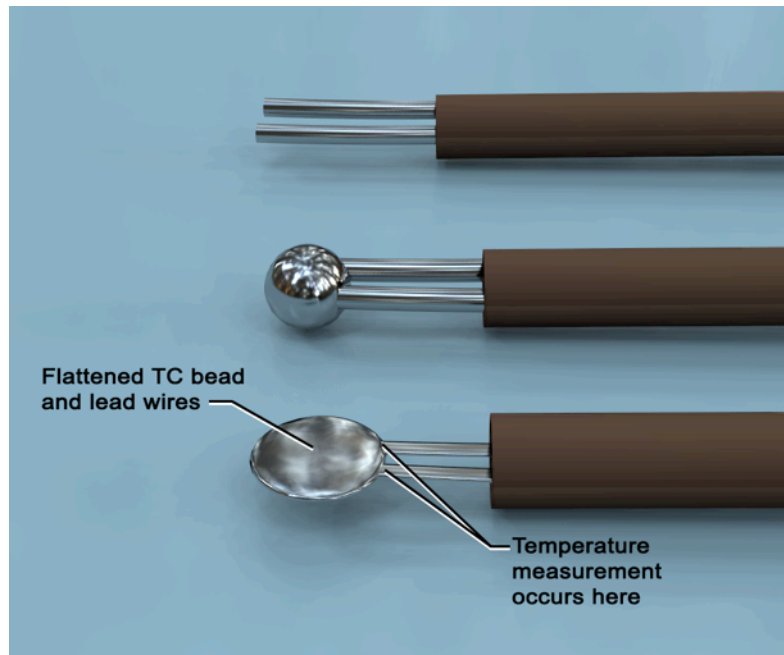


**Figure 3-21.** A 0.02 in-diameter bead was welded onto 10 mil, Type K thermocouple (TC) wire using a UNITEK TC welder, and the bead and lead wires were flattened with crimping pliers.

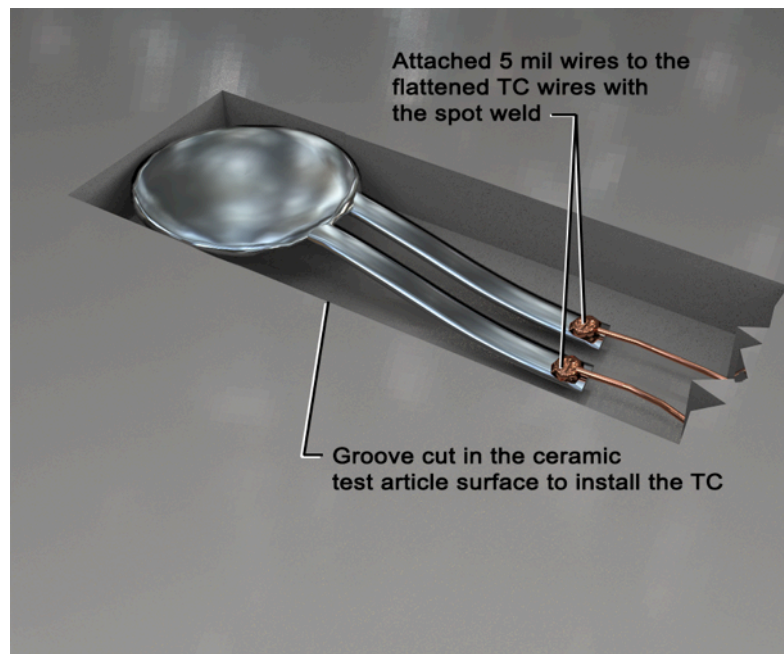


**Figure 3-22.** TC inserted into a groove in the surface of the fused silica test article with a 0.01 in depth beneath the bead and a width and depth of 0.075 in beneath the lead wires.

One thermocouple was embedded in the outer surface of each primary fused silica test article and held in place with alumina cement as shown in Figure 3-23, with the bead vertically aligned with the set of fiducials farthest aft on each fin model. The depth of the groove and the distance between the thermocouple bead and the surrounding fused silica were minimized to more accurately measure the fused silica surface temperatures. These temperature transducers were used to verify the model surface temperatures at a single location during a given run and to validate the assumptions in the 1D and 2D conduction codes. The change in temperatures measured by these thermocouples between the time the pre-run phosphor thermography image was recorded and the time the run began was used to offset the leading-edge, pre-run temperatures input to the 1D and 2D finite-volume codes in the heat transfer analyses.

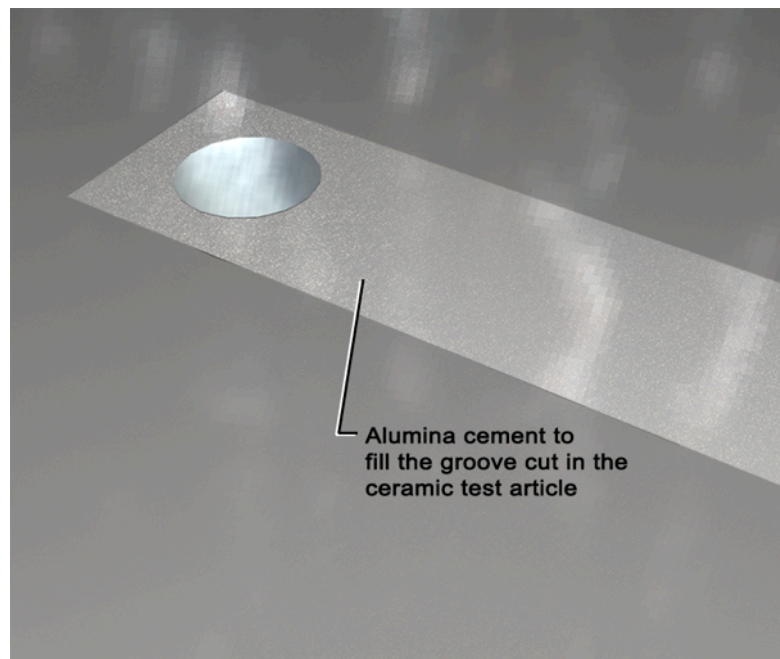
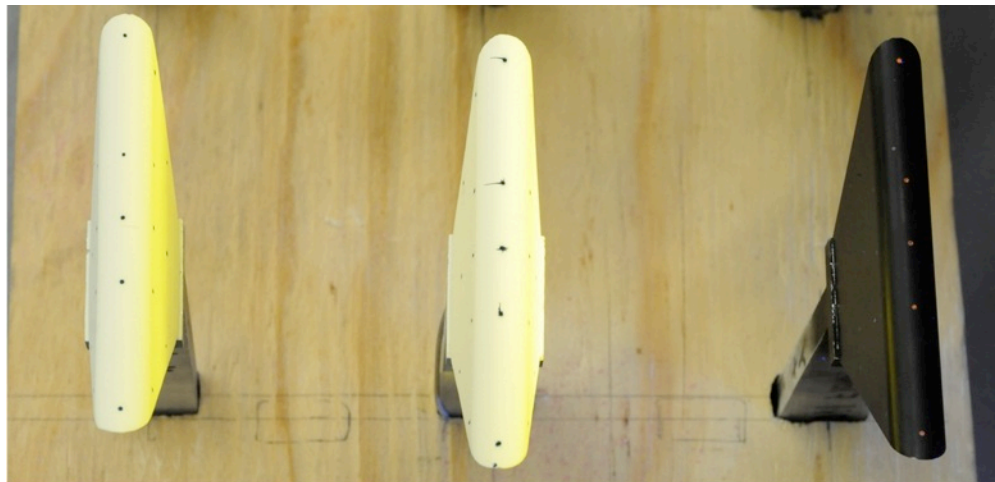


**Figure 3-23.** The 0.075 in wide by 0.075 in deep groove in the fused silica test article was filled in with alumina cement to secure the TC bead in place.

Finally, the fused silica models were covered by a phosphor mixture composed of ZnCdS: Ag, Ni and  $\text{La}_2\text{O}_2\text{S: Eu}^{3+}$ . These components work together as a two-color relative intensity phosphor coating that is sensitive to temperature changes on the surface of a wind tunnel model. A phosphor-coated test article with an embedded thermocouple is shown in Figure 3-12.

### 3.3.3.2. Fiducial mark application

The Quality Assurance Branch at NASA Langley applied fiducial marks to the surface of the fused silica test articles using Dykem® Hi-Spot blue ink [46]. The fiducial marks are arranged in the same pattern for all the test articles that share the same nose radius. Figure 3-24 shows the marked test articles, including the back-up fused silica models (left column), the primary fused silica test articles (middle column), and the metal oil flow test articles (right column). The back-up fused silica test articles were not used during the test.



(a)  $r_{\text{nose}} = 0.25$  inches



(b)  $r_{\text{nose}} = 0.50$  inches



(c)  $r_{\text{nose}} = 0.75$  inches

**Figure 3-24.** Primary and back-up fused silica test articles and metal oil flow test articles.

As is seen in the middle column of test articles in Figure 3-24, the fiducials on the primary fused silica test articles spread out or “ran” during the test. One possible explanation for the fiducial

smearing is that the Dykem® ink used to mark the fiducial locations slightly exceeded the published shelf life of twenty-four months [47]. Also, the stagnation temperatures during the test may have changed the viscosity of the ink and made it more likely to run. The fiducial movement meant additional pixels away from the shock-shock interaction along the leading edge did not provide temperature data.

### **3.3.3.3. Calibrations of phosphor system**

Multiple calibrations are required to conduct a phosphor thermography test in the NASA LaRC wind tunnels [5]. First, the response of the camera system used to acquire the data is calibrated independently. Next, the windows in the wind tunnel are calibrated to determine the transmissivity of the glass in the red and green parts of the spectrum. Finally, the intensity response of a given batch of the phosphor mixture relative to temperature is calibrated through a series of tests. The information from these tests is averaged to generate a look-up table (LUT) of temperatures relative to red and green intensity values. This LUT is used to calculate the test article surface temperatures using intensity values at each pixel in an image of the test article.

These calibrations are repeated as necessary. A phosphor calibration was completed for a new batch of the phosphor coating between the first and second wind tunnel entry in Test 6983. Oil flow visualization tests were conducted and high-speed zoom schlieren data was acquired during the first wind tunnel entry in Test 6983. Heat transfer runs with the fused silica test articles occurred during a second wind tunnel entry using the calibrated new batch of the phosphor coating.

### **3.3.3.4. Quality Assurance analysis of fused silica test articles**

A CMM was used to measure dimensions on the fused silica test articles. These dimensions are shown in the diagram in Figure 3-20. The “starboard side wall angle” also was measured on these test articles, but this dimension is not included in the diagram. CAD models were used to create patterns for these test articles with dimensions that match the drawings in Appendix B. Table 3-5 shows the key dimensions of the primary fused silica test articles compared to the nominal dimensions in the drawings. Again, for each measurement specified in separate rows, the dimensions listed from top to bottom are arranged in order of increasing leading-edge radius.

The percent deviation between the actual and nominal dimensions is greater for fused silica test articles because this material is not machined but is rather formed using a casting process, which inherently produces parts that are less precise than machined parts. This substrate material also shrinks slightly during the drying and sintering process, though the theoretical minimum linear shrinkage of fused silica is only 0.75% [46]. For more information on the test article measurements and the fiducial mark locations, refer to Appendix B.

**Table 3-5.** Key primary fused silica test article dimensions. Unless otherwise specified, units are inches.

Dimension	Nominal	Actual	Percent Deviation (%)
Nose radius	0.25	0.258	3.2000
	0.50	0.5074	1.4800
	0.75	0.7644	1.9200
Distance from aft end to the leading edge	1.51	1.4907	1.2781
	1.76	1.7349	1.4261
	2.01	1.9579	2.5920
Leading edge height	4.00	4.0215	0.5375
		4.0349	0.8725
		3.9672	0.8200
Port side wall angle	-7.00°	-7.4937°	7.0529
		-7.4440°	6.3429
		-7.4776°	6.8229
Starboard side wall angle	7.00°	7.2911°	4.1586
		7.5651°	8.0729
		8.0405°	14.8643
Aft end width	0.814	0.834	2.4570
	1.318	1.3351	1.2974
	1.822	1.8385	0.9056
Aft end height	1.20	1.1776	1.8667
		1.1977	0.1917
		1.2169	1.4083

### 3.4. Experimental run matrix (Tests 6976 and 6983)

The current shock-shock interaction study was conducted in three separate wind tunnel entries identified as Test 6976 and Test 6983 (which was split into two parts). Macor® and Upilex® test articles instrumented with thin-film gages, metal test articles used in oil flow visualization runs, and fused silica test articles instrumented with a phosphor coating were used, respectively, in these groups of wind tunnel runs. For all of the runs in these wind tunnel entries (excluding a series of runs dedicated to conducting a Re number sweep during Test 6983), the nominal Mach number was 5.96.

All of the wind tunnel runs in Tests 6976 and 6983, except for the aforementioned Re number sweep, were conducted at a Re number of  $2.1 \times 10^6/\text{ft}$ . This Re number was chosen primarily due



to the fact that the temperature rise during a run with this flow condition is ideal for the temperature range of the phosphor coating. At a lower  $Re$ , the temperatures on the model surface remain low during a normal aeroheating wind tunnel run, while at higher  $Re$  the temperatures quickly exceeded the temperature range of the phosphor coating. A nominal  $Re$  of  $2 \times 10^6/\text{ft}$  was the focus of the previous study as well [8]. One benefit of choosing a  $Re$  of  $2.1 \times 10^6/\text{ft}$  is that the total temperature and pressure of the flow required for this condition can be set fast enough to conduct between eight and ten runs in one day in the 20-Inch Mach 6 Air Tunnel, which allows for the best productivity in the facility.

A  $Re$  number sweep was conducted in Test 6983 with two runs at  $1.1 \times 10^6/\text{ft}$ , one run at  $2.1 \times 10^6/\text{ft}$ , and one run at  $4.1 \times 10^6/\text{ft}$  for the 0.25 in-radius test article at a  $-15^\circ$  AoA. Zoom schlieren videos were recorded during this sweep to compare the flow behavior at the different  $Re$  numbers. The peak temperatures in the shock impingement region on the test article for the  $Re = 4.1 \times 10^6/\text{ft}$  case exceeded the phosphor system limit before the test article reached the tunnel centerline and could be photographed. The sweep in Test 6983 confirmed the reasoning above for the selection of a nominal  $Re$  number for the remainder of the runs.

In Test 6976, the flat plate SG was angled alternately at  $9^\circ$  and  $6^\circ$  and zoom schlieren photos were taken of the resulting shock-shock interactions. These angles were selected to ensure the flow conditions behind the incident shock would heat up the model in the impingement region but not cause the temperatures to go out of the measurable range of the phosphor mixture immediately for the  $Re = 2.1 \times 10^6/\text{ft}$  cases. As expected, zoom schlieren images for a  $6^\circ$  SG angle indicated weaker shock-shock interactions than the  $9^\circ$  SG produced. All of the runs in Test 6983 were conducted either without a SG plate installed or with a  $9^\circ$  SG angle to optimize the time spent in the wind tunnel, since replacing the hardware required to incline the SG plate at a specific angle takes at least an hour. Instead, the SG was angled at  $9^\circ$  and phosphor thermography data was obtained both with the typical camera settings and with a zoomed-in camera view to increase the spatial resolution of the acquired temperature data points.

Three test article AoA, namely,  $0^\circ$ ,  $-15^\circ$  and  $-25^\circ$ , were considered in the current study. These angles of attack, when paired with a  $9^\circ$  SG angle (or a  $16.7^\circ$  oblique shock angle), yield Type IV and Type III interactions, respectively. These shock-shock interaction types were visually confirmed in zoom schlieren videos and images recorded during Tests 6976 and 6983.

### **3.4.1. Test 6976 run matrix**

In March 2012, wind tunnel runs were conducted using the thin-film-gage test articles described in section 3.3.1. Table 3-6 shows the run matrix for this tunnel entry. The goal of this test was to compare data obtained at similar conditions to the Test 6692 results using the same thin-film test articles. Before the test, a sufficient number of gages in the approximate shock-shock interaction region along the leading edge of the Painted 2 and Upilex® test articles yielded reasonable temperature calibration curves to justify reusing these models. However, several additional gages failed prior to the test, as described in section 3.3.1.3, so the thin-film data from this test will not be discussed in this thesis. Instead, the runs in Table 3-6 were conducted to obtain zoom schlieren videos at 30 fps of the shock-shock interactions for cases with the SG at  $6^\circ$  and  $9^\circ$  from horizontal.



**Table 3-6.** Thin-film-gage test articles run matrix.

Run Matrix, Part A (8 test runs)						
Test Article	# Runs	$Re_{\infty}$ $ft^{-1} \times 10^{-6}$	SG Angle	Leading Edge AoA	Phosphor	Schlieren
Macor®, thin-film gage: 0.5-in diameter	1	2.2	9°	0°	No	Kodak
	1	2.1	9°	-15°	No	Kodak
	1	2.1	9°	-25°	No	Kodak
Upilex®, thin-film gage: 0.5-in diameter	1	2.2	9°	0°	No	Kodak
	1	2.1	9°	-15°	No	Kodak
	1	2.1	9°	-25°	No	Kodak
	1	2.1	6°	0°	No	Kodak
	1	2.1	6°	-15°	No	Kodak
	1	2.1	6°	-25°	No	Kodak

**3.4.2. Test 6983, Phase 1 run matrix**

The oil-flow runs shown in Table 3-7 were conducted in the 20-inch Mach 6 Air Tunnel in August 2012. During these runs, zoom schlieren videos of the shock-shock interactions were obtained with a high-speed Phantom 9 camera from Vision Research, Inc. since some of the interactions under consideration are unsteady. At least two runs were conducted for each model at each of the three angles of attack. During the first run, the flow was visualized by covering the test article with several small dots of oil mixed with a white pigment prior to injecting the test article into the flow. During the second run, the entire surface of each test article was covered with the white oil and pigment mixture. Two techniques were implemented because the oil dot technique provides information about the movement of individual streamlines on the test article surface, but the oil coating technique is more repeatable between runs and provides insight into the regions of high shear on the test articles. Additional repeat runs were conducted as needed to obtain better oil flow streamlines or different zoom schlieren videos.

**Table 3-7.** Metal test articles for the oil-flow visualization run matrix.

Run Matrix, Part B (21 test runs)						
Test Article	# Runs	$Re_{\infty}$ $ft^{-1} \times 10^{-6}$	SG Angle	Leading Edge AoA	Phosphor	Schlieren
Metal, oil-flow: 0.5-in diameter	2	2.1	9°	0°	No	Phantom 9
	3	2.1	9°	-15°	No	Phantom 9
	2	2.1	9°	-25°	No	Phantom 9
Metal, oil-flow: 1.0-in diameter	2	2.1	9°	0°	No	Phantom 9
	2	2.1	9°	-15°	No	Phantom 9
	2	2.1	9°	-25°	No	Phantom 9
Metal, oil-flow: 1.5-in diameter	2	2.1	9°	0°	No	Phantom 9
	2	2.1	9°	-15°	No	Phantom 9
	4	2.1	9°	-25°	No	Phantom 9

### 3.4.3. Test 6983, Phase 2 run matrix

The 20-inch Mach 6 Air Tunnel runs in Table 3-8 were performed using the phosphor-coated fused silica test articles in October 2012. Though a column for IR data is not included in the table, the temperatures along the leading edge of the fused silica test articles also were measured with an IR camera during each of these runs. Due to complications in calibrating the IR camera to calculate temperatures from the images, the IR data was only qualitative and is not presented in this thesis. The “yes/no” in the phosphor category indicates a repeated run because phosphor data was not recorded during the initial run. Schlieren data was obtained using a high-speed Phantom 12 camera (with higher resolution than the Phantom 9) from Vision Research, Inc.

**Table 3-8.** Fused silica test articles run matrix.

Run Matrix, Part C (32 test runs)						
Test Article	# Runs	$Re_{\infty}$ $ft^{-1} \times 10^{-6}$	Shock Generator Angle	Leading Edge AoA	Phosphor	Schlieren
Fused silica, phosphor-coated: 0.5-in diameter	1	2.1	None	0	No	Phantom 12
	1	2.1	None	0	Yes	None
	1	2.1	None	-15	Yes	None
	1	2.1	None	-25	Yes	Phantom 12
	1	2.1	9°	0	Yes	Phantom 12
	1	1.1	9°	-15	Yes	Phantom 12
	1	2.1	9°	-15	Yes	Phantom 12
	1	4.1	9°	-15	Yes	Phantom 12
	1	2.1	9°	-25	Yes	Phantom 12
	1	2.1	9° (zoomed in)	0	Yes	Phantom 12
	1	1.1	9° (zoomed in)	-15	Yes	Phantom 12
	1	2.1	9° (zoomed in)	-15	Yes	Phantom 12
	1	2.1	9° (zoomed in)	-25	Yes	Phantom 12
Fused silica, phosphor-coated: 1.0-in diameter	1	2.1	None	0	Yes	Phantom 12
	1	2.1	None	-15	Yes	Phantom 12
	1	2.1	None	-25	Yes	Phantom 12
	1	2.1	9°	0	Yes	Phantom 12
	1	2.1	9°	-15	Yes	Phantom 12
	1	2.1	9°	-25	Yes	Phantom 12
	2	2.1	9° (zoomed in)	0	Yes	Phantom 12
	1	2.1	9° (zoomed in)	-15	Yes	Phantom 12
	1	2.1	9° (zoomed in)	-25	Yes	Phantom 12
Fused silica, phosphor: 1.5-in diameter	1	2.1	None	0	Yes	Phantom 12
	1	2.1	None	-15	Yes	Phantom 12
	1	2.1	None	-25	Yes	Phantom 12
	1	2.1	9°	0	Yes	Phantom 12
	1	2.1	9°	-15	Yes	Phantom 12
	2	2.1	9°	-25	Yes/No	Phantom 12
	1	2.1	9° (zoomed in)	0	Yes	Phantom 12
	1	2.1	9° (zoomed in)	-15	Yes	Phantom 12
	1	2.1	9° (zoomed in)	-25	Yes	Phantom 12

### 3.5. Wind tunnel data acquisition

Several instruments were utilized to obtain the temperature, oil-flow, and schlieren data from these wind tunnel tests. The next sections describe the hardware that was used during the wind tunnel runs to acquire these different forms of data.

#### 3.5.1. Oil flow test articles

Videos of the oil flow movement along the side of the test article were recorded through the side tunnel window at a framing rate of 100 fps during the wind tunnel runs as shown in Figure 3-25. A type 2B UV filter covered the lens of a Phantom 9 camera to reduce the blue tint from the UV lights used to illuminate the fluorescent orange fiducial marks. The resolution of these oil-flow videos is 1632 x 1200 pixels. After each oil-flow run, the test hardware was retracted from the tunnel test section and 2848 x 4288 pictures of the resulting post-test streamline patterns on the surface of the test article were captured with a Nikon D300s camera using a 360 nm UV light to illuminate the fluorescent fiducial marks.

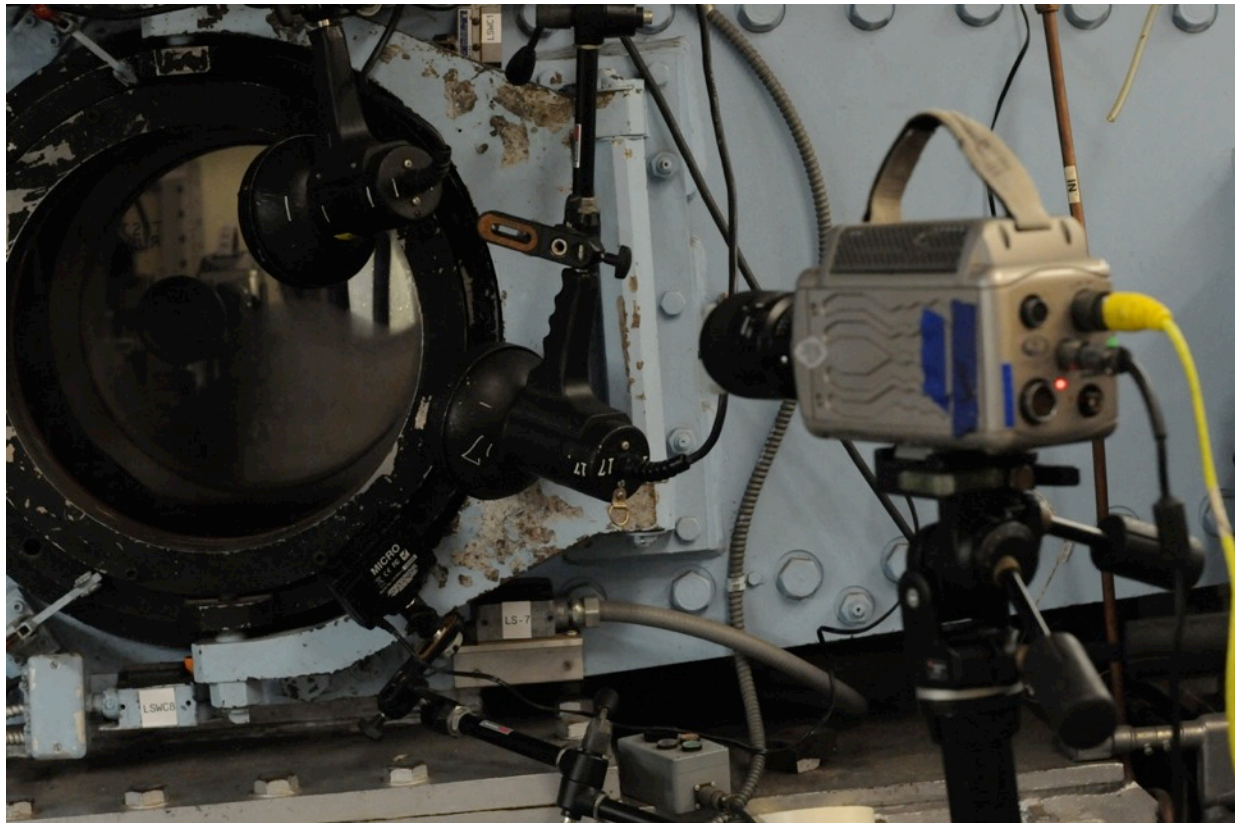


**Figure 3-25.** Phantom 9 camera used to capture oil flow videos at 100 fps with UV lights to illuminate the fluorescent fiducial marks.

During the oil flow runs, a second camera was aimed through the top window to capture the movement of the streamlines specifically along the leading edge of the test articles. This Hitachi camera, shown in Figure 3-26, recorded 30 fps videos of the streamlines during the oil flow runs.



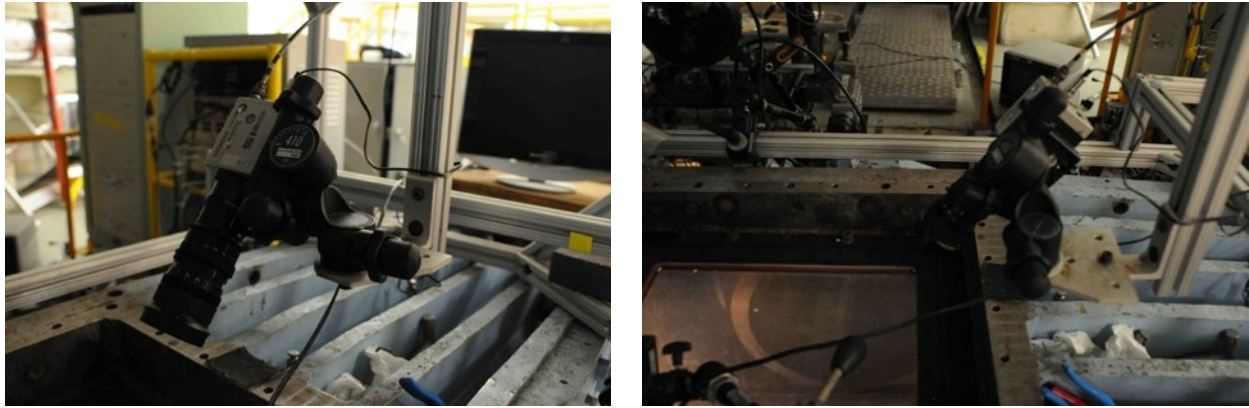


**Figure 3-26.** Hitachi camera aimed at the leading edge of the oil-flow test articles through the top window.

As discussed in section 3.4.2, two different oil flow techniques were used to visualize the streamlines on the surface of the metal test articles. In the first method, a base coat of 350 centipoise (cP) oil was applied to the test article and dots of 350 cP oil mixed with a titanium white pigment were flicked onto the surface of the test article as shown in Figure 3-27. The motion of the dots of oil revealed the flow streamlines in this case.

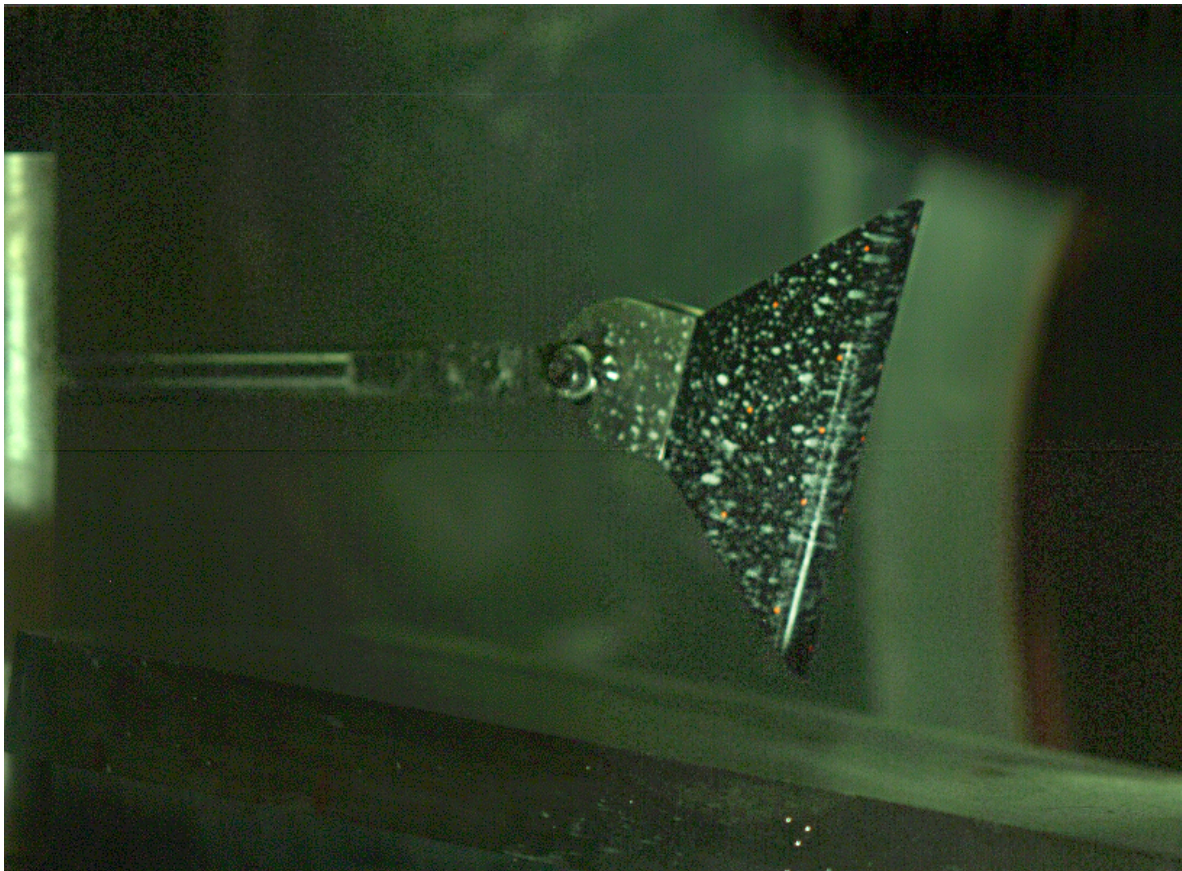


**Figure 3-27.** Example of a metal test article covered with white oil dots near the beginning of the run.



The second method was similar to the first but involved covering the test article with a full layer of the 350 cP oil mixed with pigment as shown in Figure 3-28. High viscosity oil was selected to reduce the amount of the pigmented oil blown off the test article due to high shear levels during each run. A preliminary test with a base coat of 200 cP oil and 200 cP pigmented dots was conducted which revealed the need for the higher viscosity oil. This second method is used to better visualize the regions of high and low shear in the flow on the test article surface, while the first method is used to track the streamline movement.

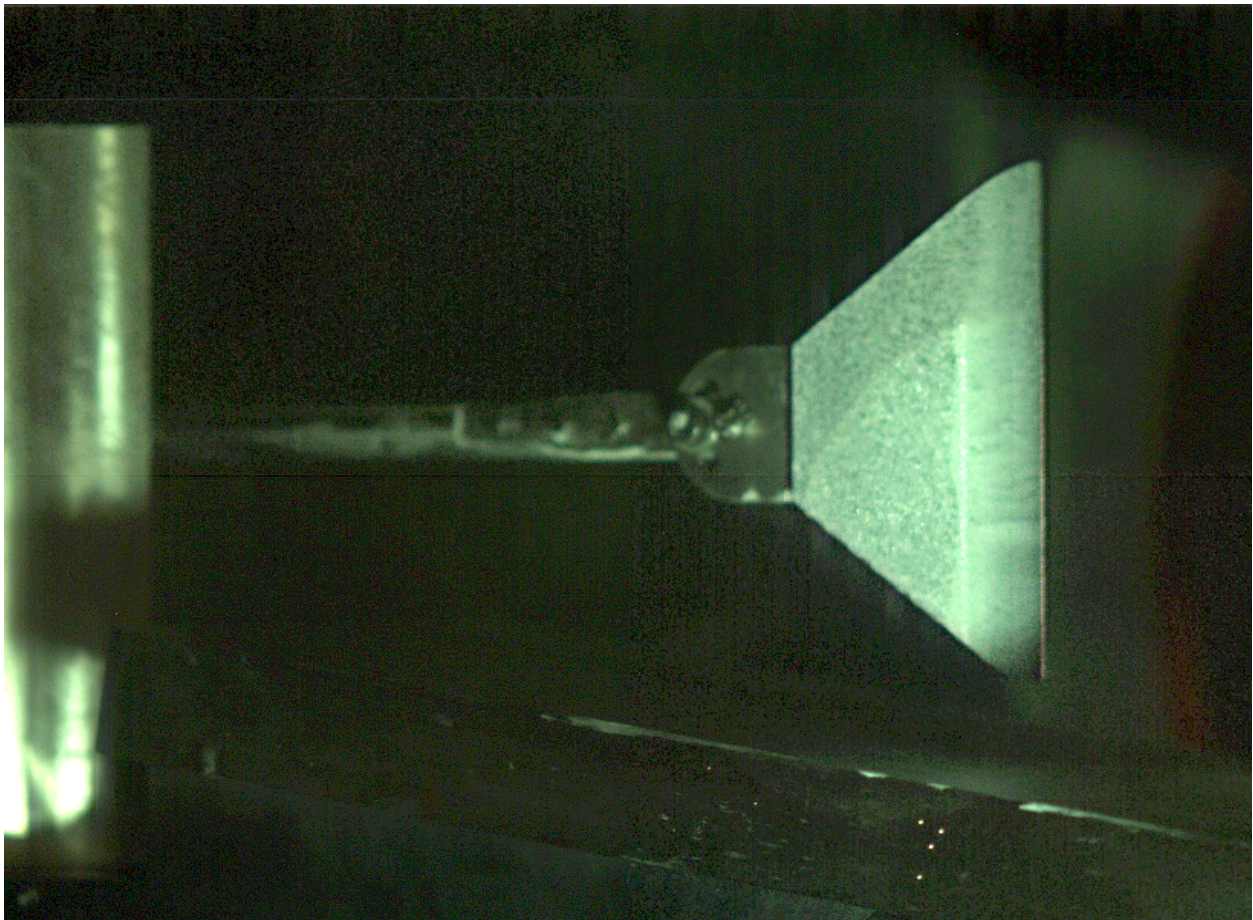


**Figure 3-28.** Example of a metal test article covered with a white oil layer near the beginning of the run.

### **3.5.2. Fused silica test articles instrumented with a phosphor coating**

Fused silica test articles coated with a thin layer of phosphors were used to measure surface temperatures for different shock-shock interaction cases. These surface temperatures were used in different codes to calculate heat transfer coefficients assuming 1D and 2D conduction through the test articles.

### 3.5.2.1. Phosphor and thermocouple temperature data

Phosphor thermography was implemented in the current study to obtain a temporal record of surface temperatures for the test articles during the wind tunnel runs. In references [4] and [5], Merski discusses a data reduction program, IHEAT, used to obtain quantitative wind tunnel aeroheating data. The two-color, relative-intensity phosphor thermography method is routinely used to determine the global surface temperature distribution on hypersonic wind tunnel models. This technique uses a phosphor mixture that fluoresces in the visible spectrum when illuminated with ultraviolet light. The intensity of the red and green fluorescence depends upon the amount of incident ultraviolet light on the model and the local surface temperature of the phosphor. The phosphor mixture is suspended in a silica ceramic binder and applied to the models with an airbrush. The final phosphor coating thickness is approximately 0.001 in.

During a phosphor thermography aeroheating test, a ceramic model is placed in a wind tunnel test section, and UV lights are used to illuminate the surface of the model. A 3-CCD (Charge Coupled Device) camera captures fluorescence intensity images of the illuminated phosphor model as heated hypersonic flow passes over the model. The phosphor mixture is calibrated by recording images of a piece of fused silica with the phosphor coating as the temperature varies from about 22 °C (72 °F) to 170 °C (338 °F). The red and green components of these images are used to construct a three-column LUT that correlates red and green pixel intensity combinations to temperatures.

Information from the calibration and time-sequenced images from the wind tunnel run are input to IHEAT to determine the global temperature distribution over the entire model surface (with temperature data at each image pixel that corresponds to a location on the test article). The assumptions and equations used to obtain enthalpy-based heat transfer coefficients from IHEAT as well as from the 1D and 2D finite-volume conduction codes are described in section 4.2.

For the baseline heating cases without a shock-shock interaction, the phosphor thermography images were recorded at 10 fps after the initial images were taken when the model reached the tunnel centerline. During the runs with a shock-shock interaction, the phosphor data was acquired at 30 fps (the maximum framing rate of the 3-CCD camera) to obtain the maximum amount of global temperature data before the leading-edge temperatures exceeded the phosphor system limit. The resolution of the phosphor thermography images is 640 x 480 pixels.

Separate runs were conducted for each test article configuration with the phosphor camera either zoomed out to capture the full side and leading edge of the test article or zoomed in to see only the areas near the shock-shock interaction on the side and the leading edge. The spatial resolution of the phosphor data ranged from 0.0105 in to 0.015 in between the acquired temperatures for the zoomed-out cases, and was about 0.004 in for the zoomed-in cases. These spatial resolutions are sufficient for the heat transfer experiments and compare well with the minimum thin-film-gage spacing of 0.015 in in [8] deemed necessary to capture the narrow heating spike accurately.

During the initial (baseline) heat transfer wind tunnel runs, the thermocouple was positioned in an upper corner away from the shock-shock interaction and hidden from the view of the

phosphor camera. When the phosphor camera was zoomed in on the shock-shock interaction region, the model was rotated 180° so the thermocouple was positioned in the lower corner on the visible side of the model. This latter thermocouple location was within the region of increased heating that wrapped around the test article from the shock-shock interaction on the leading edge. The thermocouple data was obtained at 30 Hz to correspond to the maximum thermographic phosphor data acquisition rate.

The fused silica test articles were illuminated with 360 nm UV light during the run so the relative intensity of the emitted light from the phosphor system could be used to calculate the test article surface temperatures. When the tunnel flow conditions (total pressure and total temperature) were close to the levels required for a run, the test article was inserted into the tunnel and the position of the UV lights aimed at the test article were adjusted as demonstrated in Figure 3-29.

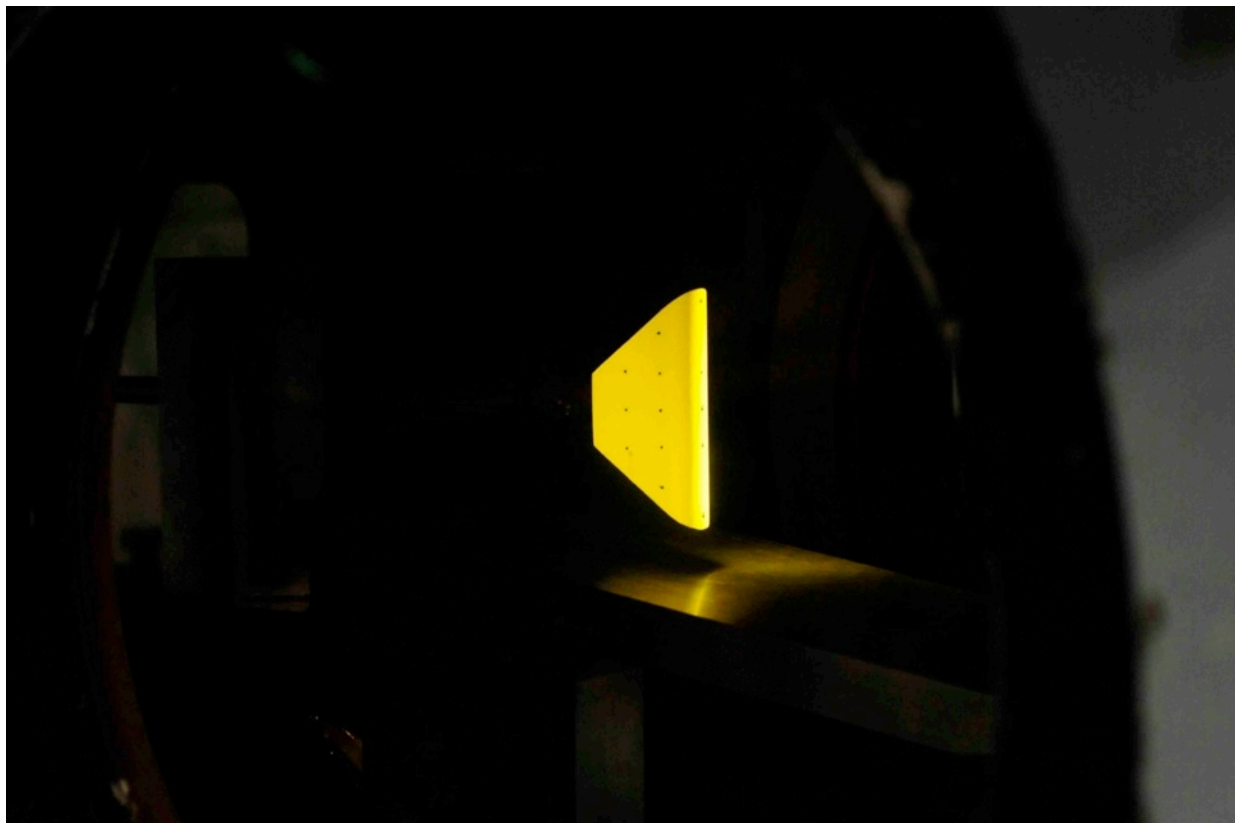


**Figure 3-29.** 0.5 in-radius fused silica test article in the tunnel with 360 nm UV illumination.

#### **3.5.2.2. Infrared (IR) temperature data**

A FLIR SC6000 camera with a 50 mm lens was used to obtain global, infrared measurements along the leading edge of the phosphor-coated fused silica test articles. The original IR videos provided qualitative temperature gradients, which could not be accurately converted to quantitative temperatures after the test was completed. The images in Figure 3-30 show the IR camera aimed through a zinc-selenide infrared window on the top of the wind tunnel.



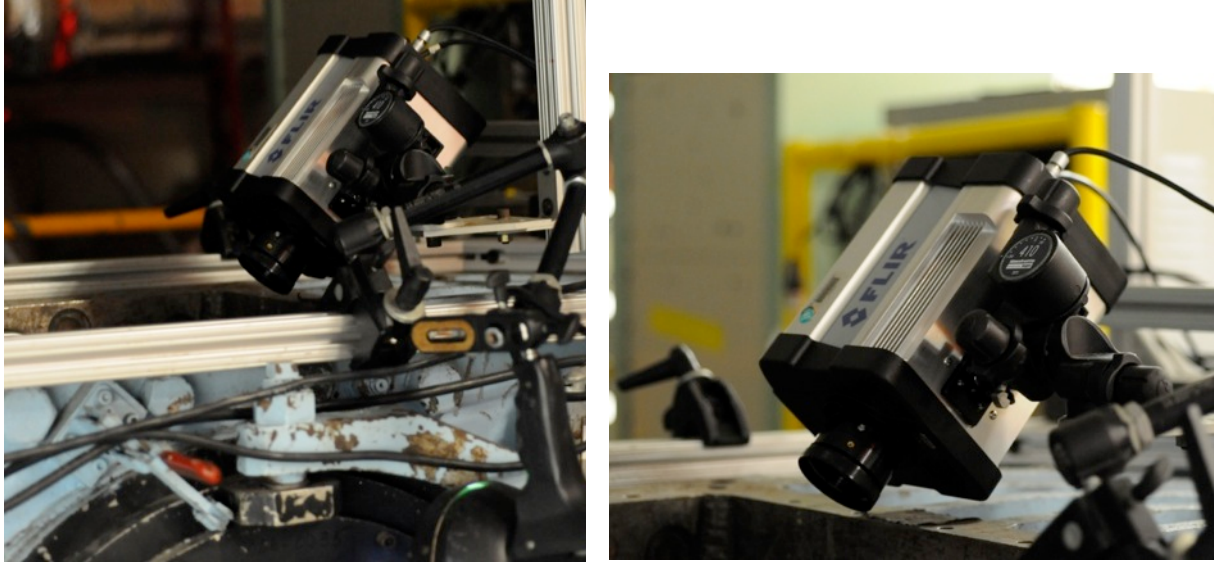


**Figure 3-30.** FLIR SC6000 IR camera mounted above the wind tunnel test section.

The framing rate for all of the IR runs was 120 fps, which is four times faster than the 30-fps phosphor system. The IR videos of the baseline heating cases were captured at a resolution of 640 x 512 pixels, the maximum resolution for the IR camera. For the cases with a shock-shock interaction, the videos were recorded for a digitally cropped region around the leading edge at a resolution of 496 x 244 pixels. The location of this digital window frame was shifted to different locations between runs based on the camera view during the pre-run model injection to ensure the full leading edge of the test article was visible as the angle of attack and the leading-edge radius of the test article varied.

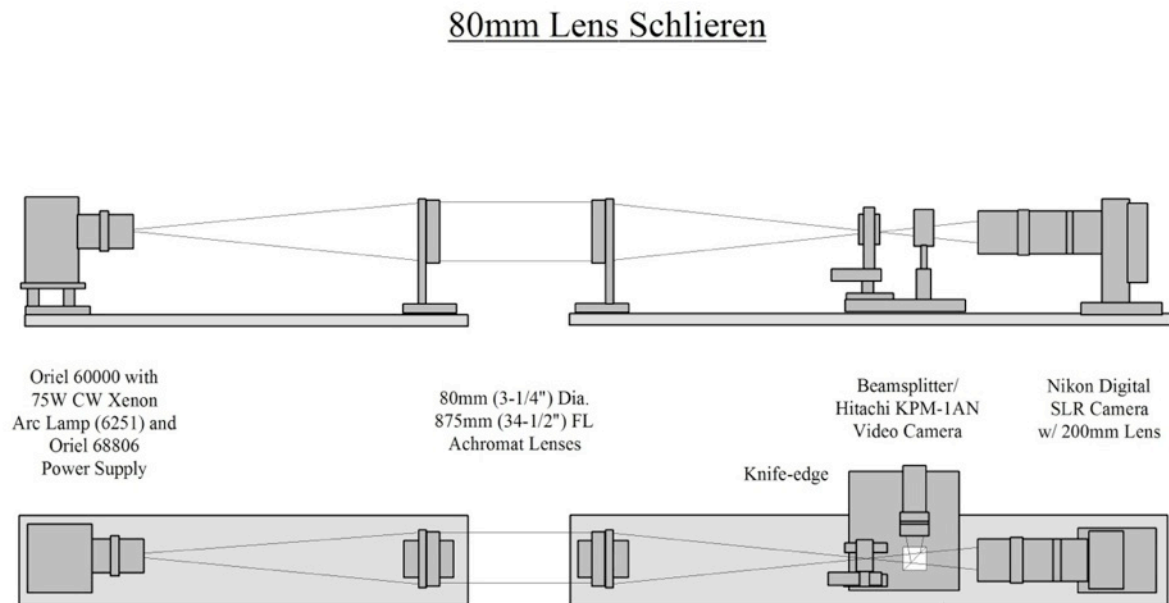
### **3.5.3. Zoom schlieren cases**

The flow density gradients during the wind tunnel runs were recorded using a custom zoom schlieren system set up specifically for this study. Standard schlieren systems typically utilize the entire field of view available from the wind tunnel windows to acquire density gradient videos and images. Zoom schlieren systems use a set of lenses with a continuous light source to focus on (and magnify) a smaller region of interest in the flow.

Zoom schlieren data was collected using three different cameras over the span of the wind tunnel experiment. Initially, a Kodak DCS PRO SLR/n camera with a 200 mm lens was used to obtain Schlieren videos at 30 fps for cases with the flat plate SG angled at 9° and 6° to the flow. In an attempt to obtain a clearer picture of the shock-shock interaction, schlieren data was recorded with a Phantom 9 camera with a 1632 x 1200 resolution at a framing rate of 1000 fps, and a resolution of 1408 x 800 pixels at 1600 fps. During the final wind tunnel entry, a Phantom 12 camera was used to obtain 0.1-0.2 sec video clips of the shock-shock interactions at framing rates between 7900 fps and 28000 fps and corresponding resolutions between 1024 x 768 and 512 x 384 pixels. A 105-mm lens was used during the runs with the Phantom 9 camera, and a 135-mm lens was used with the Phantom 12 camera. A 200-mm lens was available, but this lens was not used because part of the shock interaction region would not be visible to the camera.



The zoom schlieren test set-up is depicted in Figure 3-31 and Figure 3-32. The diagram is titled either 80 mm or 100 mm “Lens Schlieren” to indicate the change in the size of the region viewed by the zoom schlieren data acquisition system. The larger diameter lenses were only available during Test 6983 and were used to provide more flexibility in setting the region of interest for the schlieren data. A continuous light source, labeled as Oriel 60000 in the diagrams, sent a beam of light through the lenses, illuminating part of the test article and the surrounding flow during the run. A knife-edge on the other side of the tunnel (shown on the right in the diagrams) was adjusted as needed to provide proper contrast between the different density gradients in the flow. The camera that recorded the zoom schlieren videos was set up behind the knife-edge and beam splitter. As described above, a low-speed camera was used during Test 6976, while high-speed Phantom 9 and Phantom 12 cameras were used during the two phases of Test 6983, respectively.

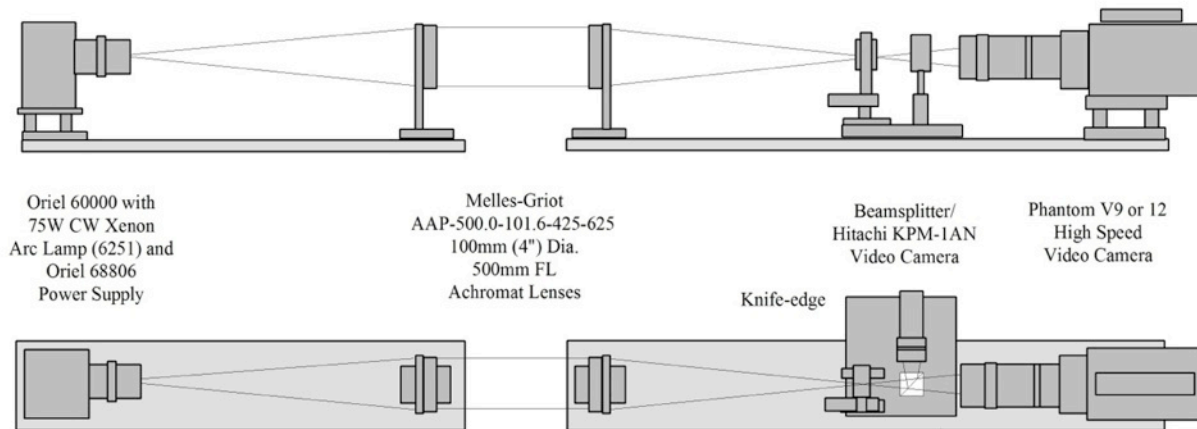


Not to Scale

Stephen B. Jones  
January 30, 2013

**Figure 3-31.** Test 6976 zoom schlieren set-up (used with permission of Steve Jones, not previously published).

## 100mm Lens Schlieren



Not to Scale

Stephen B. Jones  
January 30, 2013

**Figure 3-32.** Test 6983 zoom schlieren set-up (used with permission of Steve Jones, not previously published).

The physical hardware for the two halves of the zoom schlieren set-up in the diagrams is shown in Figure 3-33 and Figure 3-34. The 4 in-diameter circular region of light in Figure 3-35 shows the area where the schlieren system recorded density gradients. Run 22 is the first run with the phosphor-coated fused silica models. Prior to this run, the light source for the zoom schlieren system was turned on manually and left on during the phosphor data acquisition process, using the set-up in Figure 3-33. The intensity of the bright light source on the test article interfered with the acquired phosphor data, producing a circular region with higher temperature readings on the model images during the run. Therefore, in subsequent runs, a shutter was used to block the light while the phosphor data was collected, and the shutter was opened to obtain the schlieren data at the end of each run as shown in Figure 3-36.

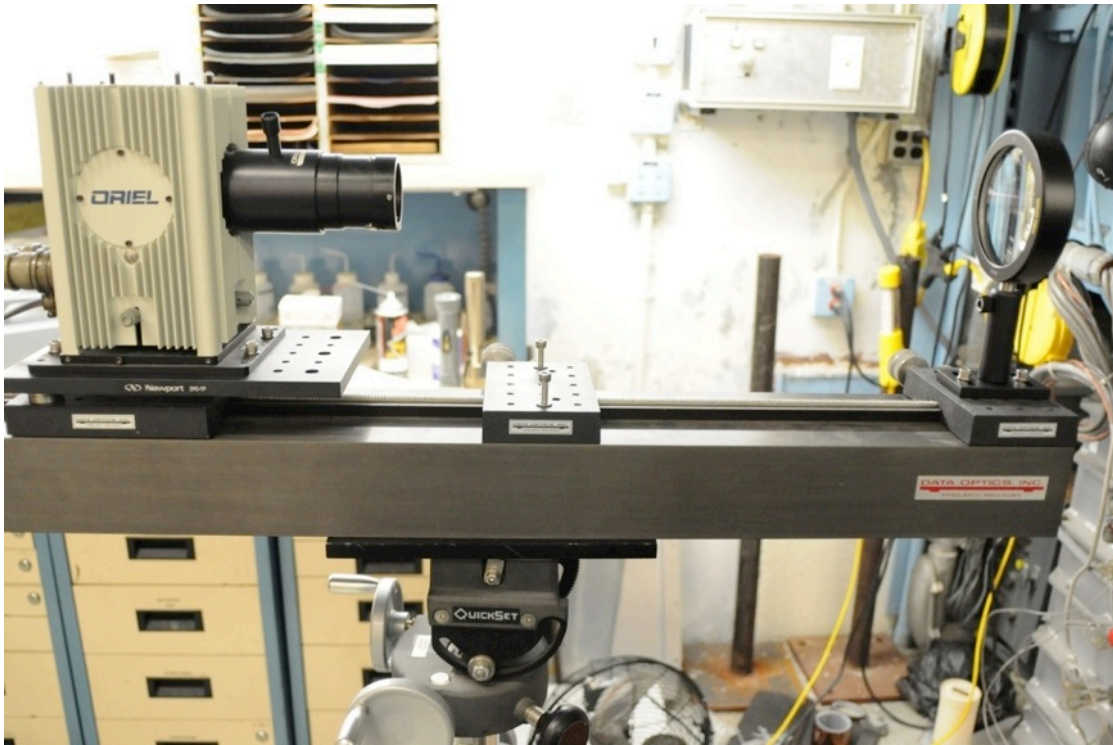


**Figure 3-33.** Test 6983 zoom schlieren set-up on the front side of the tunnel with the newer light source.

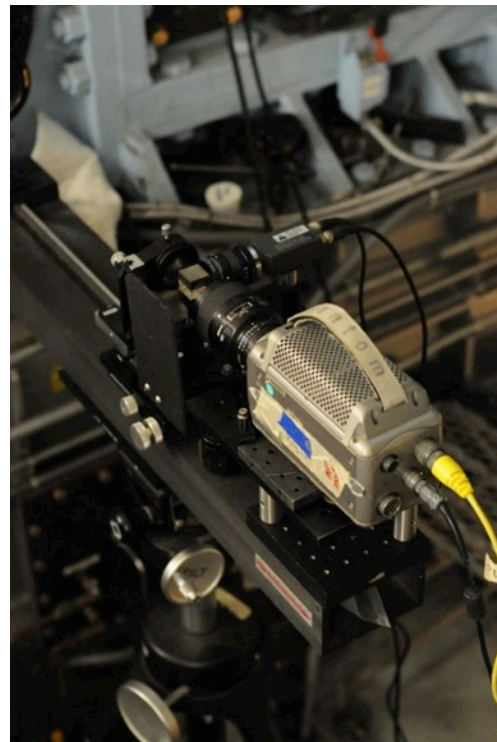
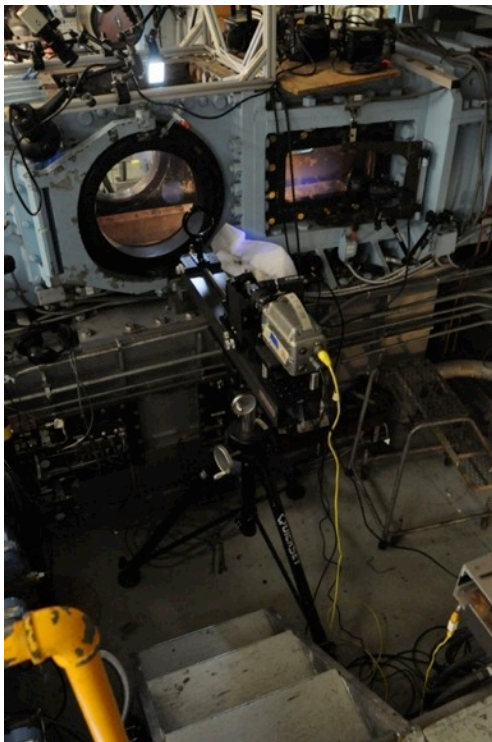


**Figure 3-34.** Zoom schlieren set-up on the other side of the tunnel with the Phantom camera installed.



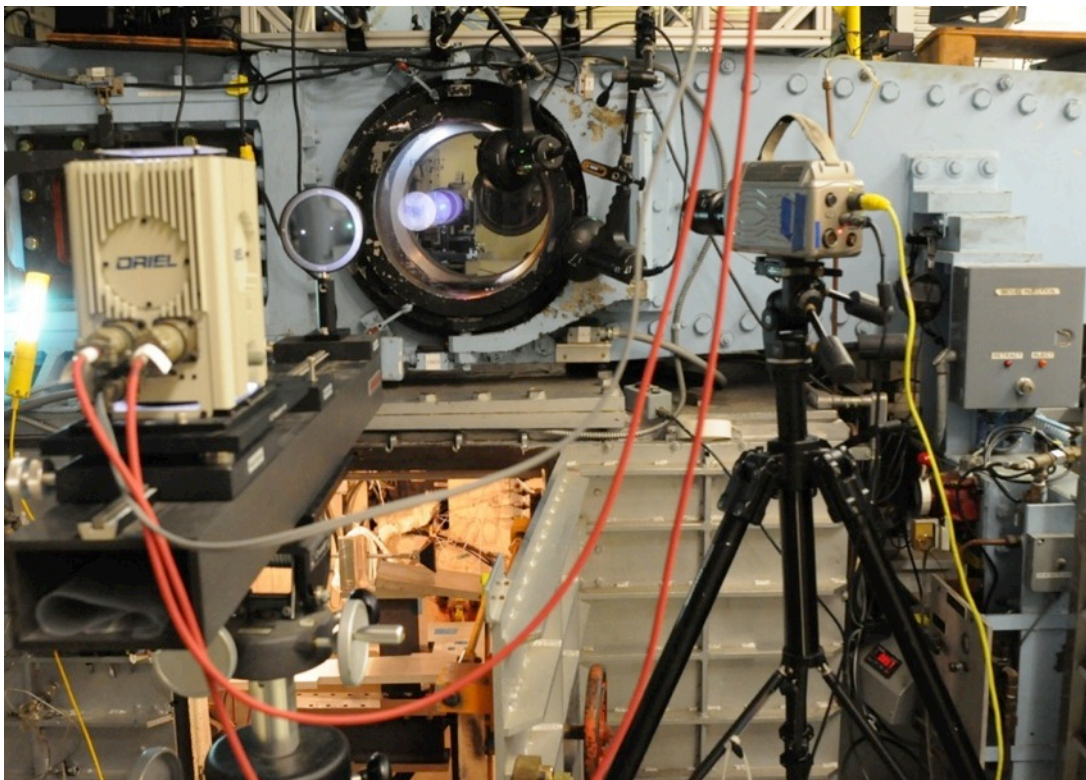


**Figure 3-35.** Test 6983 zoom schlieren set-up with the light source turned on.

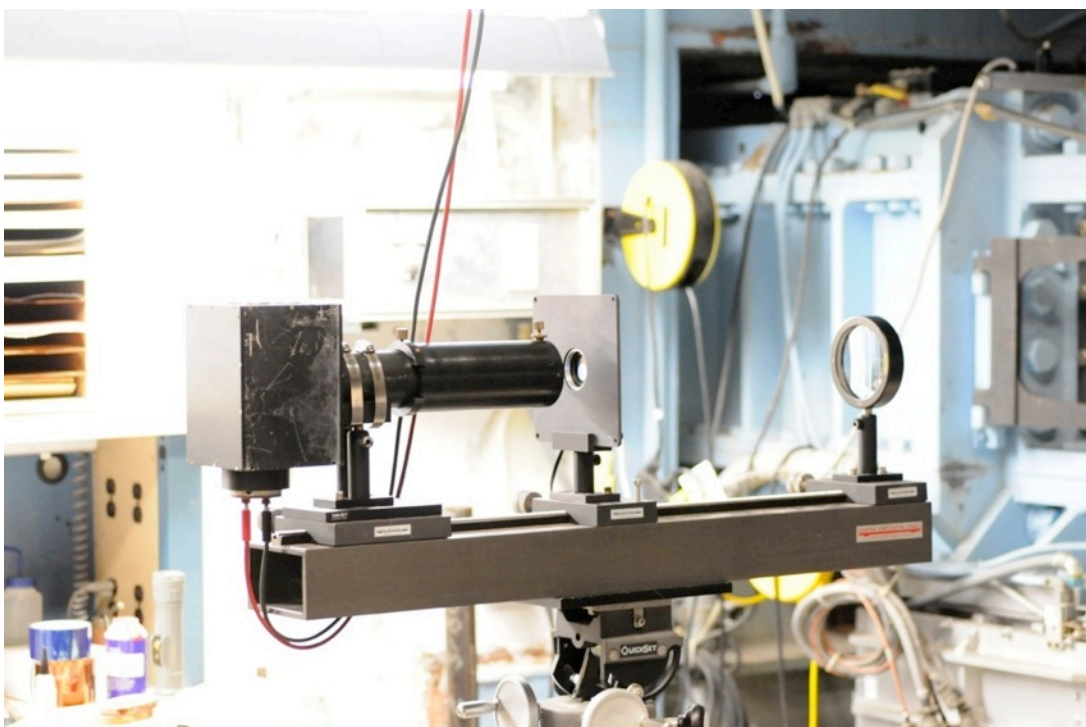


**Figure 3-36.** Test 6983 zoom schlieren set-up with the shutter to block light until the end of the run.

## 4. Chapter 4: Numerical analysis

During the wind tunnel runs in the second phase of Test 6983, phosphor thermography and IR techniques were used to measure global surface temperatures on the test articles instrumented with a phosphor coating. The phosphor covering on the leading edge and on one side of the surface of each test article was viewed with a Kodak camera through the tunnel side window. A FLIR SC6000 IR camera aimed through the top wind tunnel window recorded the thermal radiation from the leading edge of each test article. For more information on how these two sets of data were acquired, refer to section 3.5. As section 3.4.3 explains, qualitative IR data was obtained which will not be discussed in this thesis. Phosphor thermography surface temperature data was used in the IHEAT (1D) and finite-volume (1D and 2D) codes to calculate heat transfer coefficients for each test article and SG configuration. These data reduction programs utilize the algorithms and assumptions described in the following sections.

### 4.1. Temperature data (IHEAT)

IHEAT was used to convert the phosphor intensity images of the test articles to surface temperatures. Currently, the legacy IHEAT phosphor thermography data reduction program is being updated and transitioned to a MATLAB graphical user interface (GUI) from the PV-Wave programming language. These changes to IHEAT, which include new features intended to improve the speed and simplicity of the heat transfer analysis, will be detailed and discussed in a separate document to be published at a later date. An image of the test article recorded with no flow through the tunnel test section (called a “pre-run” image) and images at multiple time steps during the run (referred to as frames) were loaded into the code. These images were converted to contour maps of the surface temperatures using a LUT that relates red and green intensities to temperatures at each pixel that corresponds to a position on the test article. The  $x/L$  locations and temperatures in line cuts along the leading edge at multiple time steps during a run were used to generate input files for the finite-volume conduction codes. These temperatures were also used directly in IHEAT to calculate heat transfer coefficients. The heat transfer analysis methods used to reduce this temperature data are described in section 4.2.

### 4.2. Heat transfer analyses

Surface heat transfer coefficients based on the temperature readings for the fused silica test articles instrumented with a phosphor coating were calculated using IHEAT and 1D and 2D finite-volume conduction codes. These programs were used to determine the optimum method to predict heating profiles if fused silica test articles are exposed to sharp temperature gradients, which in this study were produced by shock-shock interactions. The IHEAT program source code was developed through a NASA Langley Co-op internship and, thus, is subject to NASA export control laws and NASA software release regulations. However, the finite-volume conduction codes are available by request from the author of this thesis.

#### 4.2.1. One-dimensional semi-infinite code (IHEAT)

The IHEAT code is the primary method used to analyze phosphor thermography data obtained in Langley’s hypersonic facilities (additional discussion provided in Chapter 3). IHEAT neglects

the thickness of the phosphor coating on the surface of the test article [5]. This 1D code also assumes the test article is semi-infinite in the through-thickness dimension, so heat applied at the surface does not reach the back of the test article during a short wind tunnel run.

In the 20-Inch Mach 6 Air Tunnel, the test gas is not calorically perfect, which means the gas specific heat is not constant [5]. Thus, convective heat transfer coefficients,  $c_h$ , are calculated from a convective heat transfer,  $\dot{q}_{conv}$ , equation based on an enthalpy difference rather than a temperature difference, ie.,

$$\dot{q}_{conv} = c_h(h_{aw} - h_w) \quad (4-1)$$

Laplace transforms are used to modify the conduction and convection equations so that the enthalpy of the air at the test article wall temperature,  $h_w$ , is not calculated directly in IHEAT. The adiabatic wall enthalpy,  $h_{aw}$ , is calculated in IHEAT based on a thermodynamic property curve-fit equation in McBride et al. [48] using the wind tunnel total temperature [5]. As a test article passes through the wind tunnel test section boundary layer, the heat transferred to the test article changes with time. Thus, the heat transfer during test article insertion is treated as a delayed step heating process [37]. An effective time,  $t_{eff}$ , is calculated as

$$t_{eff} = t_{run} - t_{corr} \quad (4-2)$$

in which the time required for the test article to travel halfway through the test section boundary layer during model insertion (or the correction time,  $t_{corr}$ ) is subtracted from the time when the test article first reaches the tunnel centerline (or the run time,  $t_{run}$ ). The transformed conduction equation requires only two temperatures, an initial temperature and a temperature at a given point during the wind tunnel run, to calculate the value of  $c_h$  at that time in the run [5]. Therefore, two images of the test article (one pre-run image and one run image) are converted to temperature mappings and used in IHEAT to calculate the heat transfer coefficients at every pixel that corresponds to a visible point on the test article.

Heat transfer coefficients output from IHEAT are typically non-dimensionalized using a Fay and Riddell [32] stagnation point heat transfer coefficient. This reference heat transfer coefficient divisor is calculated for a sphere with a radius equal to the characteristic nose radius of the test article (the leading edge radius in this study) using the flow conditions from the wind tunnel run. Non-dimensional heat transfer coefficients from this program are therefore listed as  $c_h/c_{h,FR}$  in the global contour mappings in Chapter 5.

#### 4.2.2. Finite-volume conduction calculations

Two direct, finite-volume (FV) codes were written in Fortran to approximate the conduction in the phosphor-coated fused silica test articles. The 1D code assumed heat was conducted through the thickness of the test article, while the 2D code considered conduction both in the through-thickness and lateral directions. The purpose of the 1D FV code in the present study is to provide a direct comparison between the 1D algorithm in IHEAT and the assumptions in the FV codes. Since the IHEAT code neglects the effect of surface curvature, the 1D FV code also does not include a curvature correction factor.

The diagram in Figure 4-1 shows the cylindrical geometry used in the 2D code to approximate the test article leading edge. The side profile of each test article is shaped like a trapezoid with sloping top and bottom edges from either end of the leading edge. To simplify the FV calculations, the code assumed a cylinder with dimensions equal to the length of the leading edge (4 in) and the appropriate nose radius. A rectangular plane bounded by the stagnation line on the leading edge to the centerline of the cylinder (in red in Figure 4-1) defined the boundaries of the nodes in both FV codes. The 2D code used cylindrical cell volumes that surrounded nodes in the rectangular plane. Definitions of the areas and volumes around the nodes in the 2D grid are provided in section 4.2.2.2. The coordinate systems shown in the figure apply to both FV codes.

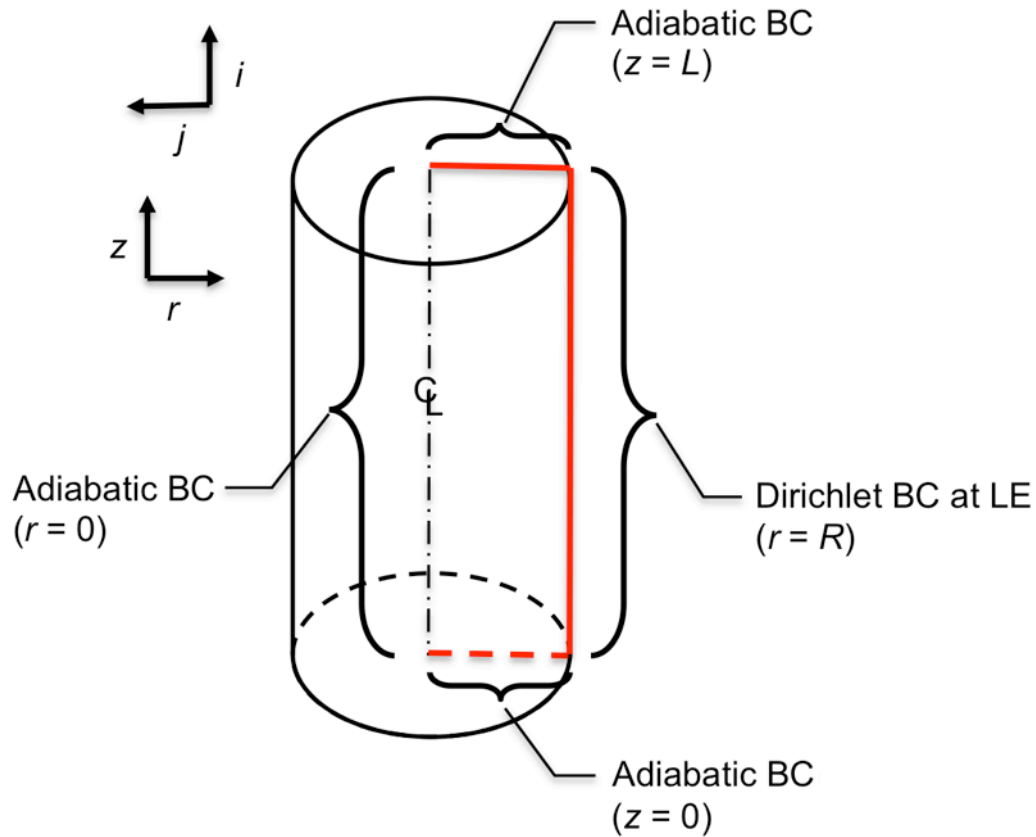


**Figure 4-1.** Overall view of the boundary conditions of the cylindrical leading edge modeled in the 1D (neglecting curvature) and 2D (using cylindrical coordinates) FV codes.

As Figure 4-1 indicates, two boundary conditions are applied to the grid of finite volumes in the 1D code, and four boundary conditions are applied in the 2D code. A Dirichlet boundary condition is applied at the surface ( $r = R$ ) in both codes using the known temperatures,  $T_P$ , of the test articles at each time step. An adiabatic boundary condition (no heat transfer) is assumed at the cylinder centerline ( $r = 0$ ) in both codes. The boundary conditions at the top ( $z = L$ ) and bottom ( $z = 0$ ) of the cylinder in the lateral direction are also adiabatic in the 2D code. Adiabatic boundaries are assumed because temperature data is not available for nodes outside of the rectangular plane. Thus, the discrete heat transfer expressions that include nodal information external to the boundary nodes are assumed to be equal to zero.



Prior to each phosphor thermography wind tunnel run, the test article was inserted into the tunnel and a pre-run image of the test article was recorded. The test article was then retracted until the tunnel flow conditions reached the appropriate levels to take data at a specified flow unit Re number. A thermocouple embedded in the test article measured the temperature in one location prior to the run and continuously at 30 Hz as the injection process began. These thermocouple temperatures indicated the test article heated up between the pre-run and the beginning of the run. The initial temperature,  $T_0$ , at the surface of the test article at the beginning of the run was estimated to be the average of the pre-run temperatures along the leading edge offset by the difference in the thermocouple measured temperatures between the time the pre-run image was taken and the time the run began, namely,

$$T_0 = T_{pre-run,avg} + T_{offset,TC} \quad (4-3)$$

The initial temperature distribution through the test article upon reaching the wind tunnel centerline was approximated using the 1D, semi-infinite heat conduction equation (assuming a constant thermal conductivity,  $k$ ), with an enthalpy-based convective boundary condition

$$-k \frac{\partial T}{\partial t}(0, t) = c_h [h_{aw} - h_w(t)] \quad (4-4)$$

The expression employed in IHEAT from [48] was used to calculate the adiabatic wall enthalpy,  $h_{aw}$ , in the FV code equations as well to minimize the differences in assumptions between the programs. In both FV codes, the enthalpy of the air at the wall temperature,  $h_w$ , was calculated using the test article surface temperatures represented by the variable  $T_P$ ,

$$h_w = 2326.1(0.2345(1.8T_P) + 9.786(10^{-6})(1.8T_P)^2 + \frac{943.6}{1.8T_P} - 1.57) \quad (4-5)$$

Equation (4-5) uses values of  $T_P$  at the appropriate time step and location along the leading edge of the test article to calculate each  $H_w$  as a function of time. The analytical solution for the assumed initial temperature distribution through the test article,  $T(x, t)$ , is provided by

$$T(x, t) = T_0 + \{h_{aw}[T(0, t)/h_w(t)] - T_0\} [\text{erfc}(\eta) - \exp[c_h h_w(t)x/T(0, t)k + \lambda^2]\text{erfc}(\lambda + \eta)] \quad (4-6)$$

The  $\text{erfc}$  represents the complimentary error function. The location  $x$  is defined as the distance from the surface into the test article so that  $x = 0$  in at the surface. The time  $t$  in the following equations is the “effective” time ( $t_{eff}$ ) defined in section 4.2.1. The other parameters listed in the equation above are defined in the following equations:

$$\eta = \frac{x}{2\sqrt{\alpha_d t}} \quad (4-7)$$

$$\lambda = \frac{c_h h_w(t)\sqrt{t}}{T(0, t)\beta} \quad (4-8)$$

$$\beta = \sqrt{\rho c_p k} \quad (4-9)$$

The variable  $\alpha_d$  is the thermal diffusivity,  $\rho$  is the density,  $c_p$  is the specific heat, and  $k$  is the thermal conductivity of the test article material, fused silica. The variable  $\beta$  is the thermal product, and the variables  $\eta$  and  $\lambda$  are non-dimensionalized factors derived from the other variables in the equations. The temperature  $T(0,t)$  is evaluated at the surface of the test article at each time step. The solution to the equation at the surface of the test article is shown in

$$\frac{T(0,t) - T_0}{[h_{aw} - h_w(t)]T(0,t) - T_0} = 1 - e^{\lambda^2} \text{erfc}(\lambda) \quad (4-10)$$

This equation is used to solve for the value of  $\lambda$  in equation (4-8) by iterating until the difference between the expressions on the left and right sides of equation (4-10) is less than  $1e-5$ . The heat transfer coefficient is calculated at the end of each full time step in both the 1D and 2D FV codes. An energy balance between radiation, convection, and 2D conduction heat transfer at the test article surface that is solved for the convective heat transfer coefficient for each surface volume is given by

$$\rho c_p V \frac{\partial T}{\partial t} = \frac{\partial}{\partial r} \left( A_{cond} k \frac{\partial T}{\partial r} \right) + \frac{\partial}{\partial z} \left( A_{cond} k \frac{\partial T}{\partial z} \right) - [A_{rad} \epsilon \sigma (T_{i,j}^4 - T_{tw}^4)] - A_{conv} c_h (h_{aw} - h_w) \quad (4-11)$$

The variables  $A_{cond}$ ,  $A_{rad}$  and  $A_{conv}$  represent the areas through which heat is transferred by conduction, radiation, and convection, respectively. These variables vary depending on the volume for which the heat transfer is computed. The FV codes output a dimensional heat transfer coefficient based on the temperature data at each pixel along the leading edge of the test article. The 1D code loops through input data to derive a heat transfer coefficient at every pixel individually, while the 2D code calculates the data for the full leading edge using a line implicit scheme. These heat transfer coefficients are then non-dimensionalized to determine the relative magnitude of the peak heating in the shock-interaction region compared to the baseline heating (no interaction). The heat transfer coefficients at  $x/L = 0.75$  to  $x/L = 0.85$  along the leading edge are relatively far away from both the peak heating region and the leading-edge fiducial marks. In the runs for which the full leading edge was visible in the image, these coefficients were averaged to provide a reference coefficient to non-dimensionalize the data.

For the wind tunnel runs in which the camera was zoomed in on the shock-shock interaction region, the reference heat transfer coefficient from the corresponding zoomed-out run was used to non-dimensionalize the heat transfer coefficients. Using a reference value from a separate run affects the magnitude of the peak heat transfer coefficients in the zoomed-in runs, but this assumption is necessary to visually compare the spatial resolution of the zoomed-in and zoomed-out non-dimensional data for each test configuration in the results in Chapter 5.

#### 4.2.2.1. One-dimensional FV code

The continuous 1D heat transfer equation is shown in

$$\rho c_p \frac{\partial T}{\partial t} = \frac{\partial}{\partial r} \left( k \frac{\partial T}{\partial r} \right) \quad (4-12)$$

The left side of the equation represents energy stored in the object due to a temporal temperature gradient,  $\partial T / \partial t$ . The right side represents heat conducted through the object due to a second-order spatial temperature gradient,  $\partial^2 T / \partial r^2$ . The parameters,  $\rho$ ,  $c_p$ , and  $k$ , in the heat transfer equation are shown as constant values. In both the 1D and 2D FV conduction codes, the thermal properties of  $c_p$  and  $k$  depend on temperature and are updated after each full time step. The thermal conductivity calculation uses an average temperature,  $T_{avg}$ , calculated from two adjacent nodes in the radial ( $j$ ) direction, ie.,

$$T_{avg} = \frac{T(j) + T(j+1)}{2} \quad (4-13)$$

The specific heat is calculated using the temperature at each node. The fused silica thermal property equations are given in Appendix A. The diagram in Figure 4-2 shows the first few nodes for the 1D code approximated geometry. The cylindrical areas around each node are not considered in this approximated geometry. Heat transfer into and out of the volume around each node (represented by the arrows crossing the red dashed lines) is assumed in the radial direction with a uniform spacing of  $\Delta r$  between each node (or  $\Delta r/2$  on either side of the nodes). The experimentally determined surface temperature  $T_p$  as a function of time is applied as a Dirichlet boundary condition at the surface of the test article.

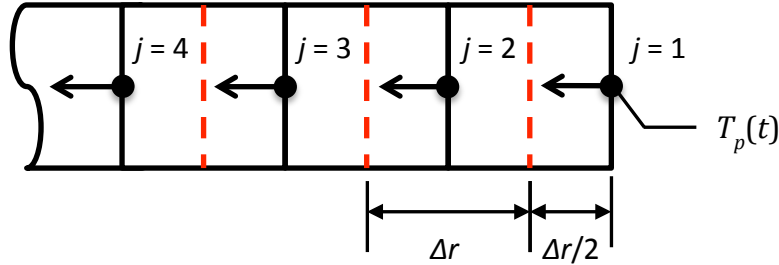


**Figure 4-2.** Diagram of the first few nodes below the test article surface in the 1D FV code.

Since cylindrical test articles were used in this study, the FV discrete form of the heat transfer equation is defined in cylindrical coordinates as

$$\rho c_p V \left( \frac{T_j^{n+1} - T_j^n}{\Delta t} \right) = \frac{k_{j-1} A}{\Delta r_{j-1}} (T_{j-1}^n - T_j^n) + \frac{k_j A}{\Delta r_j} (T_{j+1}^n - T_j^n) \quad (4-14)$$

The variable  $\Delta r$  is the nodal spacing in the radial direction ( $j$ ). The variable  $V$  is the volume of each cell defined by

$$V = A \Delta r \quad (4-15)$$

$A$  is the area over which the heat is transferred. The definition of the volume is substituted into equation (4-14) and the common areas are cancelled to yield the simplified 1D equation, ie.,

$$\rho c_P \Delta r \left( \frac{T_j^{n+1} - T_j^n}{\Delta t} \right) = \frac{k_{j-1}}{\Delta r_{j-1}} (T_{j-1}^n - T_j^n) + \frac{k_j}{\Delta r_j} (T_{j+1}^n - T_j^n) \quad (4-16)$$

The volumetric heat capacity, represented in the 1D code as  $\rho c_P \Delta r$ , was calculated at each node in the test article geometries at the end of each time step using specific heats based on the updated temperature distribution. The Crank-Nicolson algorithm was applied to the temperature differences on the right-hand side of the equation to yield

$$\begin{aligned} \rho c_P \Delta r \left( \frac{T_j^{n+1} - T_j^n}{\Delta t} \right) &= \frac{k_{j-1}}{2\Delta r_{j-1}} (T_{j-1}^{n+1} - T_j^{n+1} + T_{j-1}^n - T_j^n) \\ &+ \frac{k_j}{2\Delta r_j} (T_{j+1}^{n+1} - T_j^{n+1} + T_{j+1}^n - T_j^n) \end{aligned} \quad (4-17)$$

The Crank-Nicolson method employs the trapezoidal rule of time integration in which the discretized spatial temperature gradient is evaluated as an average of the gradient at the current ( $n$ ) and future ( $n+1$ ) time steps [49]. This method yields an unconditionally stable time-marching scheme in the 1D FV code. Equation (4-17) is rearranged to move all of the variables evaluated at the  $n+1$  time step to the left side of the equation, resulting in

$$\begin{aligned} -\frac{k_{j-1}}{2\Delta r_{j-1}} T_{j-1}^{n+1} + \left( \frac{\rho c_P \Delta r}{\Delta t} + \frac{k_{j-1}}{2\Delta r_{j-1}} + \frac{k_j}{2\Delta r_j} \right) T_j^{n+1} - \frac{k_j}{2\Delta r_j} T_{j+1}^{n+1} \\ = \frac{\rho c_P \Delta r}{\Delta t} T_j^n + \frac{k_{j-1}}{2\Delta r_{j-1}} (T_{j-1}^n - T_j^n) + \frac{k_j}{2\Delta r_j} (T_{j+1}^n - T_j^n) \end{aligned} \quad (4-18)$$

This implicit equation is applied to every cell in the one-dimensional grid. The resulting system of equations forms a tri-diagonal system matrix that is multiplied by the temperatures at the central nodes of each cell. The following equations comprise this system matrix used in the Thomas Algorithm [35] to solve for the nodal temperatures. The test article surface temperatures ( $T_P$  at  $j = 1$ ) are known at each time step in the 1D code. The following equations apply to the volumes from  $j = 2$  just below the surface to  $j = nr$  (the number of volumes in the radial direction) at the centerline of the cylindrical leading edge:

$$\begin{aligned} j = 2: \quad & \left( \frac{\rho c_P \Delta r}{\Delta t} + \frac{k_{j-1}}{2\Delta r_{j-1}} + \frac{k_j}{2\Delta r_j} \right) T_j^{n+1} - \frac{k_j}{2\Delta r_j} T_{j+1}^{n+1} \\ & = \frac{\rho c_P \Delta r}{\Delta t} T_j^n + \frac{k_{j-1}}{2\Delta r_{j-1}} (T_{j-1}^n - T_j^n) \\ & \quad + \frac{k_j}{2\Delta r_j} (T_{j+1}^n - T_j^n) + \frac{k_{j-1}}{2\Delta r_{j-1}} T_{j-1}^{n+1} \end{aligned} \quad (4-19)$$

$$\begin{aligned} 3 \leq j \leq nr-1: \quad & -\frac{k_{j-1}}{2\Delta r_{j-1}} T_{j-1}^{n+1} + \left( \frac{\rho c_P \Delta r}{\Delta t} + \frac{k_{j-1}}{2\Delta r_{j-1}} + \frac{k_j}{2\Delta r_j} \right) T_j^{n+1} - \frac{k_j}{2\Delta r_j} T_{j+1}^{n+1} \\ & = \frac{\rho c_P \Delta r}{\Delta t} T_j^n + \frac{k_{j-1}}{2\Delta r_{j-1}} (T_{j-1}^n - T_j^n) + \frac{k_j}{2\Delta r_j} (T_{j+1}^n - T_j^n) \end{aligned} \quad (4-20)$$

$$\begin{aligned}
j = nr: \quad & -\frac{k_{j-1}}{2\Delta r_{j-1}}T_{j-1}^{n+1} + \left(\frac{\rho c_P \Delta r}{\Delta t} + \frac{k_{j-1}}{2\Delta r_{j-1}}\right)T_j^{n+1} \\
& = \frac{\rho c_P \Delta r}{\Delta t}T_j^n + \frac{k_{j-1}}{2\Delta r_{j-1}}(T_{j-1}^n - T_j^n)
\end{aligned} \tag{4-21}$$

The expression that includes the variable  $T_{j-1}^{n+1}$  (or  $T_p^{n+1}$ ) moves to the right side of equation (4-19) for the cell at  $j = 2$  since  $T_p^{n+1}$  is a known temperature. An adiabatic boundary condition is assumed for the cell at  $j = nr$ , since the node  $nr+1$  does not exist in the grid applied to the test article geometry. Thus, all the expressions in equation (4-21) that involve temperatures at  $j+1$  are assumed to be equal to zero. The energy exchanged at the surface of the test article is described in words by

$$\begin{aligned}
\text{energy stored in a cell} = & \text{energy conducted into the body through the cell} \\
& - \text{energy radiated out of the cell} \\
& - \text{energy convected out of the cell}
\end{aligned} \tag{4-22}$$

The discretized energy balance at the surface of the test article used to calculate the convective heat transfer coefficient is given by

$$\begin{aligned}
\frac{\rho c_P \Delta r}{\Delta t}(T_j^{n+1} - T_j^n) = & \frac{k_j}{2\Delta r_j}(T_j^{n+1} - T_{j+1}^{n+1} + T_j^n - T_{j+1}^n) - \left[\varepsilon\sigma\left(\{T_j^{n+1}\}^4 - \{T_{tw}^{n+1}\}^4\right)\right] \\
& - c_h(h_{aw}^{n+1} - h_w^{n+1})
\end{aligned} \tag{4-23}$$

where  $\varepsilon$  is the emissivity and  $\sigma$  is the Stefan-Boltzmann constant. Solving equation (4-23) for the dimensional, enthalpy-based heat transfer coefficient,  $c_h$ , in units of  $\text{kg/m}^2\text{-s}$  yields

$$\begin{aligned}
i = 1: \quad c_h = & \left[\varepsilon\sigma\left(\{T_j^{n+1}\}^4 - \{T_{tw}^{n+1}\}^4\right) + \frac{\rho c_P \Delta r}{\Delta t}(T_j^{n+1} - T_j^n) \right. \\
& \left. + \frac{k_j}{2\Delta r_j}(T_j^{n+1} - T_{j+1}^{n+1} + T_j^n - T_{j+1}^n)\right] / (h_{aw}^{n+1} - h_w^{n+1})
\end{aligned} \tag{4-24}$$

$$\begin{aligned}
2 \leq i \leq nz-1: \quad c_h = & \left[\varepsilon\sigma\left(\{T_j^{n+1}\}^4 - \{T_{tw}^{n+1}\}^4\right) + \frac{\rho c_P \Delta r}{\Delta t}(T_j^{n+1} - T_j^n) \right. \\
& + \frac{k_{j-1}}{2\Delta r_{j-1}}(T_j^{n+1} - T_{j-1}^{n+1} + T_j^n - T_{j-1}^n) \\
& \left. + \frac{k_j}{2\Delta r_j}(T_j^{n+1} - T_{j+1}^{n+1} + T_j^n - T_{j+1}^n)\right] / (h_{aw}^{n+1} - h_w^{n+1})
\end{aligned} \tag{4-25}$$

$$\begin{aligned}
i = nz: \quad c_h = & \left[\varepsilon\sigma\left(\{T_j^{n+1}\}^4 - \{T_{tw}^{n+1}\}^4\right) + \frac{\rho c_P \Delta r}{\Delta t}(T_j^{n+1} - T_j^n) \right. \\
& \left. + \frac{k_{j-1}}{2\Delta r_{j-1}}(T_j^{n+1} - T_{j-1}^{n+1} + T_j^n - T_{j-1}^n)\right] / (h_{aw}^{n+1} - h_w^{n+1})
\end{aligned} \tag{4-26}$$

for the positions along the leading edge from  $i = 1$  to  $i = nz$  (the number of volumes in the lateral or  $z$  direction).

#### 4.2.2.2. Two-dimensional FV code

The 2D conduction equation for a solid body in cylindrical coordinates is provided by

$$\rho c_P \frac{\partial T}{\partial t} = \frac{\partial}{\partial r} \left( k \frac{\partial T}{\partial r} \right) + \frac{\partial}{\partial z} \left( k \frac{\partial T}{\partial z} \right) \quad (4-27)$$

The expression on the left side of the equation refers to the heat stored in the body over time. The expression on the right side represents the heat conducted through the body in either the radial ( $r$ ) or lateral ( $z$ ) direction. Again,  $\rho$ ,  $c_P$ , and  $k$ , in this heat transfer equation are shown as constant values. However, in the 2D FV conduction code,  $c_P$  and  $k$  are temperature dependent and updated after each full time step. The thermal conductivity values in the radial and lateral directions use the corresponding averaged temperatures, respectively, given by

$$T_{avg,radial} = \frac{T(i,j) + T(i,j+1)}{2} \quad (4-28)$$

$$T_{avg,lateral} = \frac{T(i,j) + T(i+1,j)}{2} \quad (4-29)$$

The expression for the volumetric heat capacity, ie.,

$$V_{heat} = \rho c_P V \quad (4-30)$$

is updated at each time step based on the specific heat calculated from the node temperature, which is multiplied by the constant density and volume around the specified node. The geometry of the test article leading edge is approximated as a cylinder in the 2D code, as pictured in Figure 4-1. The diagrams in Figure 4-3 and Figure 4-4 show the relative position of the areas for a couple of nodes in the approximated cylinder geometry. The actual geometry includes more nodes in the radial and lateral directions. The red and green dashed cylinders represent the areas that bound the volumes around the two nodes through which the heat passes. These areas are defined in terms of the following coordinates:  $r$  is the radial direction,  $\phi$  is the circumferential direction, and  $z$  is the direction along the leading edge of the test article.

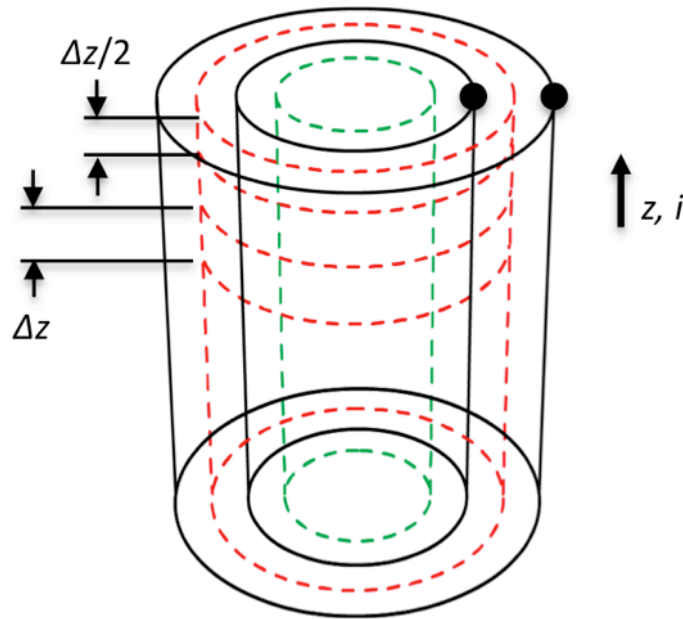


**Figure 4-3.** Side view of the approximated cylindrical leading edge of the test articles used in the 2D FV code.

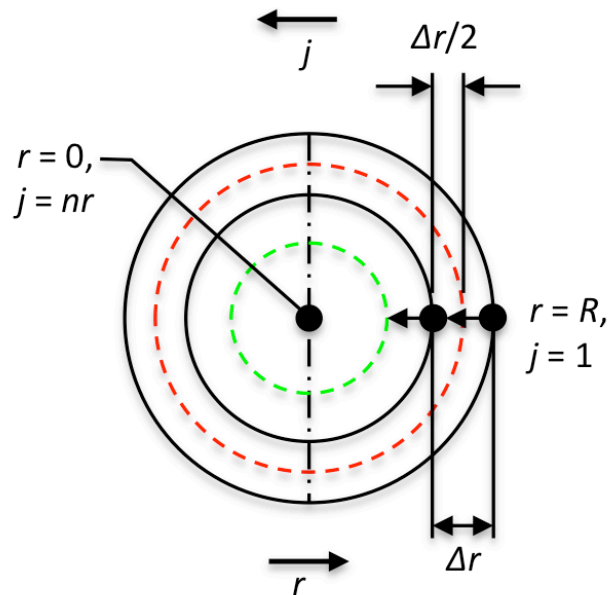


**Figure 4-4.** Top view of the approximated cylindrical leading edge of the test articles used in the 2D FV code.

In cylindrical coordinates, the areas in the  $z$  and  $\phi$  directions ( $A_z$ ) and in the  $r$  and  $\phi$  directions ( $A_r$ ) for the interior nodes and the nodes near the edges of the cylindrical geometry are defined by



$$\text{Interior:} \quad A_z = d\phi r_{mid} \Delta z \quad (4-31)$$

$$\text{Edges:} \quad A_z = d\phi r_{mid} \Delta z / 2 \quad (4-32)$$

$$\text{Surface:} \quad A_r = \pi(r^2 - r_{mid}^2) \quad (4-33)$$

$$\text{Interior:} \quad A_r = \pi(r_{mid}^2(i, j) - r_{mid}^2(i, j + 1)) \quad (4-34)$$

$$\text{Centerline:} \quad A_r = \pi r_{mid}^2 \quad (4-35)$$

The variable  $r_{mid}$  in equations (4-31) and (4-32) refers to the radial distance from the cylinder centerline where the area  $A_z$  is calculated as indicated by the dashed red and green cylinders in Figure 4-3. The height of the cylindrical area  $A_z$  near the top and bottom edges relative to the leading edge of the cylinder is  $\Delta z/2$ , and otherwise is the uniform distance  $\Delta z$ . The variables  $r$  and  $r_{mid}$  in equations (4-33) to (4-35) represent radial locations on either side of the nodes, as applicable, used to calculate the area of the appropriate annulus (for the interior and surface nodes) or circle (for the nodes at the centerline of the cylinder). Figure 4-4 illustrates this definition of  $A_r$ . Assuming three nodes exist in the radial direction, the areas are between the red dashed circle and outer black circle (surface node), between the green and red dashed circles (an interior node), and within the green dashed circle (centerline node). The volume around each node is defined using the equation for a regular cylinder and is written as

$$\text{Interior:} \quad V = A_r \Delta z \quad (4-36)$$

$$\text{Edges:} \quad V = A_r \Delta z / 2 \quad (4-37)$$

This volume equation is defined by the area of the appropriate annulus that surrounds the node ( $A_r$ ) multiplied by the height of the volume around the node ( $\Delta z$  for interior nodes or  $\Delta z/2$  for nodes near the edges of the cylinder). The 2D conduction equation is discretized using a FV, unconditionally stable, alternating direction implicit algorithm [35]. This method sweeps through the geometry of the test article twice for every time step, first in one direction for all the nodes and then in another direction using an updated temperature distribution,  $T^*$ , at the intermediate time step. The current 2D code sweeps in the  $z$  direction first, which acts as a half-step going from the known time at the “ $n$ ” iteration level to an intermediate time denoted by a star (\*) in the time-marching algorithm, as shown in

$$\begin{aligned} \frac{\rho c_P V}{\Delta t / 2} (T_{i,j}^* - T_{i,j}^n) = & \frac{k_{z(i-1,j)} A_{r(i-1,j)}}{\Delta z_{i-1,j}} (T_{i-1,j}^* - T_{i,j}^*) + \frac{k_{z(i,j)} A_{r(i,j)}}{\Delta z_{i,j}} (T_{i+1,j}^* - T_{i,j}^*) \\ & + \frac{k_{r(i,j-1)} A_{z(i,j-1)}}{\Delta r_{i,j-1}} (T_{i,j-1}^n - T_{i,j}^n) + \frac{k_{r(i,j)} A_{z(i,j)}}{\Delta r_{i,j}} (T_{i,j+1}^n - T_{i,j}^n) \end{aligned} \quad (4-38)$$

The subscripts on the thermal conductivities, areas and nodal spacing ( $\Delta z$  or  $\Delta r$ ) represent the parameters that are defined for the nodes defined in the respective temperature differences. Rearranging this implicit equation to move all of the terms evaluated at the intermediate time step to the left hand side of the equation yields

$$\begin{aligned}
& -\frac{k_{z(i-1,j)}A_{r(i-1,j)}}{\Delta z_{i-1,j}}T_{i-1,j}^* + \left(\frac{\rho c_P V}{\Delta t/2} + \frac{k_{z(i-1,j)}A_{r(i-1,j)}}{\Delta z_{i-1,j}} + \frac{k_{z(i,j)}A_{r(i,j)}}{\Delta z_{i,j}}\right)T_{i,j}^* \\
& -\frac{k_{z(i,j)}A_{r(i,j)}}{\Delta z_{i,j}}T_{i+1,j}^* \\
& = \frac{\rho c_P V}{\Delta t/2}T_{i,j}^n + \frac{k_{r(i,j-1)}A_{z(i,j-1)}}{\Delta r_{i,j-1}}(T_{i,j-1}^n - T_{i,j}^n) \\
& + \frac{k_{r(i,j)}A_{z(i,j)}}{\Delta r_{i,j}}(T_{i,j+1}^n - T_{i,j}^n)
\end{aligned} \tag{4-39}$$

The last two terms added at the end of the expression on the right hand side of the equation represent the heat transfer in the radial direction at the known,  $n$ , time step. In the first ADI loop, adiabatic boundary conditions are assumed at the stagnation line and centerline of the cylindrical nose of the test article (denoted by  $j = 1$  and  $j = nr$ , respectively). Thus, the following equations are applied to equation (4-39) as applicable:

$$j = 1: \quad \frac{k_{r(i,j-1)}A_{z(i,j-1)}}{\Delta r_{i,j-1}}(T_{i,j-1}^n - T_{i,j}^n) = 0 \tag{4-40}$$

$$j = nr: \quad \frac{k_{r(i,j)}A_{z(i,j)}}{\Delta r_{i,j}}(T_{i,j+1}^n - T_{i,j}^n) = 0 \tag{4-41}$$

Assuming the two expressions for the boundary conditions (BC) above are labeled BC1 (at  $j = 1$ ) and BC2 (at  $j = nr$ ), the  $z$  sweep of the ADI method from  $i = 1$  to  $i = nz$  is defined by

$$\begin{aligned}
i = 1: \quad & \left(\frac{\rho c_P V}{\Delta t/2} + \frac{k_{z(i,j)}A_{r(i,j)}}{\Delta z_{i,j}}\right)T_{i,j}^* - \frac{k_{z(i,j)}A_{r(i,j)}}{\Delta z_{i,j}}T_{i+1,j}^* \\
& = \frac{\rho c_P V}{\Delta t/2}T_{i,j}^n + BC1 + BC2
\end{aligned} \tag{4-42}$$

$$\begin{aligned}
2 \leq i \leq nz-1: \quad & -\frac{k_{z(i-1,j)}A_{r(i-1,j)}}{\Delta z_{i-1,j}}T_{i-1,j}^* \\
& + \left(\frac{\rho c_P V}{\Delta t/2} + \frac{k_{z(i-1,j)}A_{r(i-1,j)}}{\Delta z_{i-1,j}} + \frac{k_{z(i,j)}A_{r(i,j)}}{\Delta z_{i,j}}\right)T_{i,j}^* \\
& - \frac{k_{z(i,j)}A_{r(i,j)}}{\Delta z_{i,j}}T_{i+1,j}^* = \frac{\rho c_P V}{\Delta t/2}T_{i,j}^n + BC1 + BC2
\end{aligned} \tag{4-43}$$

$$\begin{aligned}
i = nz: \quad & -\frac{k_{z(i-1,j)}A_{r(i-1,j)}}{\Delta z_{i-1,j}}T_{i-1,j}^* + \left(\frac{\rho c_P V}{\Delta t/2} + \frac{k_{z(i-1,j)}A_{r(i-1,j)}}{\Delta z_{i-1,j}}\right)T_{i,j}^* \\
& = \frac{\rho c_P V}{\Delta t/2}T_{i,j}^n + BC1 + BC2
\end{aligned} \tag{4-44}$$

After solving equations (4-42) to (4-44) for the intermediate temperatures at every node using the Thomas Algorithm, the 2D code sweeps through nodes in the  $r$  direction. This sweep completes

a second half time step, between the intermediate time and the “ $n+1$ ” iteration level, as shown by

$$\begin{aligned} \frac{\rho c_p V}{\Delta t/2} (T_{i,j}^{n+1} - T_{i,j}^*) = & \frac{k_{r(i,j-1)} A_{z(i,j-1)}}{\Delta r_{i,j-1}} (T_{i,j-1}^{n+1} - T_{i,j}^{n+1}) + \frac{k_{r(i,j)} A_{z(i,j)}}{\Delta r_{i,j}} (T_{i,j+1}^{n+1} - T_{i,j}^{n+1}) \\ & + \frac{k_{z(i-1,j)} \cdot A_{r(i-1,j)}}{\Delta z_{i-1,j}} (T_{i-1,j}^* - T_{i,j}^*) + \frac{k_{z(i,j)} A_{r(i,j)}}{\Delta z_{i,j}} (T_{i+1,j}^* - T_{i,j}^*) \end{aligned} \quad (4-45)$$

The unknown temperatures at time step  $n+1$  are moved to the left side of the implicit equation such that

$$\begin{aligned} & - \frac{k_{r(i,j-1)} A_{z(i,j-1)}}{\Delta r_{i,j-1}} T_{i,j-1}^{n+1} + \left( \frac{\rho c_p V}{\Delta t/2} - \frac{k_{r(i,j-1)} A_{z(i,j-1)}}{\Delta r_{i,j-1}} - \frac{k_{r(i,j)} A_{z(i,j)}}{\Delta r_{i,j}} \right) T_{i,j}^{n+1} \\ & - \frac{k_{r(i,j)} A_{z(i,j)}}{\Delta r_{i,j}} T_{i,j+1}^{n+1} \\ & = \frac{\rho c_p V}{\Delta t/2} T_{i,j}^* + \frac{k_{z(i-1,j)} A_{r(i-1,j)}}{\Delta z_{i-1,j}} (T_{i-1,j}^* - T_{i,j}^*) \\ & + \frac{k_{z(i,j)} A_{r(i,j)}}{\Delta z_{i,j}} (T_{i+1,j}^* - T_{i,j}^*) \end{aligned} \quad (4-46)$$

Two additional adiabatic boundary conditions are applied in the second ADI loop at the bottom ( $i = 1$ ) and top ( $i = nz$ ) of the cylinder in the lateral direction (parallel to the leading edge of the test article). These BC3 and BC4 boundary conditions, defined by

$$i = 1: \quad \frac{k_{z(i-1,j)} A_{r(i-1,j)}}{\Delta z_{i-1,j}} (T_{i-1,j}^* - T_{i,j}^*) = 0 \quad (4-47)$$

$$i = nz: \quad \frac{k_{z(i,j)} A_{r(i,j)}}{\Delta z_{i,j}} (T_{i+1,j}^* - T_{i,j}^*) = 0 \quad (4-48)$$

are applied to equation (4-46) as applicable. The  $r$  sweep from  $j = 1$  at the test article surface ( $r = R$ ) to  $j = nr$  at the centerline of the cylindrical leading edge ( $r = 0$ ) is given by

$$j = 1: \quad T_{i,j}^{n+1} = T_p^{n+1} \quad (4-49)$$

$$\begin{aligned} j = 2: \quad & \left( \frac{\rho c_p V}{\Delta t/2} - \frac{k_{r(i,j-1)} A_{z(i,j-1)}}{\Delta r_{i,j-1}} - \frac{k_{r(i,j)} A_{z(i,j)}}{\Delta r_{i,j}} \right) T_{i,j}^{n+1} - \frac{k_{r(i,j)} A_{z(i,j)}}{\Delta r_{i,j}} T_{i,j+1}^{n+1} \\ & = \frac{\rho c_p V}{\Delta t/2} T_{i,j}^* + \frac{k_{r(i,j-1)} A_{z(i,j-1)}}{\Delta r_{i,j-1}} T_p^{n+1} + BC3 + BC4 \end{aligned} \quad (4-50)$$

$$\begin{aligned}
3 \leq j \leq nr-1: & -\frac{k_{r(i,j-1)}A_{z(i,j-1)}}{\Delta r_{i,j-1}}T_{i,j-1}^{n+1} \\
& + \left( \frac{\rho c_P V}{\Delta t/2} - \frac{k_{r(i,j-1)}A_{z(i,j-1)}}{\Delta r_{i,j-1}} - \frac{k_{r(i,j)}A_{z(i,j)}}{\Delta r_{i,j}} \right) T_{i,j}^{n+1} \\
& - \frac{k_{r(i,j)}A_{z(i,j)}}{\Delta r_{i,j}}T_{i,j+1}^{n+1} = \frac{\rho c_P V}{\Delta t/2}T_{i,j}^* + BC3 + BC4
\end{aligned} \tag{4-51}$$

$$\begin{aligned}
j = nr: & -\frac{k_{r(i,j-1)}A_{z(i,j-1)}}{\Delta r_{i,j-1}}T_{i,j-1}^{n+1} + \left( \frac{\rho c_P V}{\Delta t/2} - \frac{k_{r(i,j-1)}A_{z(i,j-1)}}{\Delta r_{i,j-1}} \right) T_{i,j}^{n+1} \\
& = \frac{\rho c_P V}{\Delta t/2}T_{i,j}^* + BC3 + BC4
\end{aligned} \tag{4-52}$$

The Dirichlet boundary condition of known temperatures ( $T_P$ ) is applied at the surface of the test article. Again, the Thomas Algorithm is used to solve this tri-diagonal system of equations for the test article temperature distribution at the next full time step,  $T_{i,j}^{n+1}$ . The 2D code dimensional heat transfer coefficients are calculated using an energy balance on the surface nodes along the test article leading edge as described in equation (4-11), in words in equation (4-22), and in discretized form in

$$\begin{aligned}
\frac{\rho c_P V}{\Delta t}(T_{i,j}^{n+1} - T_{i,j}^n) &= \frac{k_{r(i,j-1)}A_{z(i,j-1)}}{2\Delta r_{i,j-1}}(T_{i,j}^{n+1} - T_{i,j+1}^{n+1} + T_{i,j}^n - T_{i,j+1}^n) \\
&+ \frac{k_{z(i-1,j)}A_{r(i-1,j)}}{2\Delta z_{i-1,j}}(T_{i,j}^{n+1} - T_{i-1,j}^{n+1} + T_{i,j}^n - T_{i-1,j}^n) \\
&+ \frac{k_{z(i,j)}A_{r(i,j)}}{2\Delta z_{i,j}}(T_{i,j}^{n+1} - T_{i+1,j}^{n+1} + T_{i,j}^n - T_{i+1,j}^n) \\
&- A_{z(i,j)} \left[ \varepsilon \sigma \left( \{T_{i,j}^{n+1}\}^4 - \{T_{tw}^{n+1}\}^4 \right) \right] - A_{z(i,j)} c_h (h_{aw}^{n+1} - h_w^{n+1})
\end{aligned} \tag{4-53}$$

This discretized equation is rearranged to solve for the variable  $c_h$  for each volume along the leading edge from  $i = 1$  to  $i = nz$  such that

$$\begin{aligned}
c_h &= \left[ \varepsilon \sigma \left( \{T_{i,j}^{n+1}\}^4 - \{T_{tw}^{n+1}\}^4 \right) + \frac{\rho c_P V}{\Delta t A_{z(i,j)}} (T_{i,j}^{n+1} - T_{i,j}^n) \right. \\
i = 1: & + \frac{k_{r(i,j-1)}A_{z(i,j-1)}}{2\Delta r_{i,j-1}A_{z(i,j)}} (T_{i,j}^{n+1} - T_{i,j+1}^{n+1} + T_{i,j}^n - T_{i,j+1}^n) \\
& \left. + \frac{k_{z(i,j)}A_{r(i,j)}}{2\Delta z_{i,j}A_{z(i,j)}} (T_{i,j}^{n+1} - T_{i+1,j}^{n+1} + T_{i,j}^n - T_{i+1,j}^n) \right] / (h_{aw}^{n+1} - h_w^{n+1})
\end{aligned} \tag{4-54}$$

$$\begin{aligned}
c_h = & \left[ \varepsilon \sigma \left( \{T_{i,j}^{n+1}\}^4 - \{T_{tw}^{n+1}\}^4 \right) + \frac{\rho c_P V}{\Delta t A_{z(i,j)}} (T_{i,j}^{n+1} - T_{i,j}^n) \right. \\
& + \frac{k_{r(i,j-1)} A_{z(i,j-1)}}{2 \Delta r_{i,j-1} A_{z(i,j)}} (T_{i,j}^{n+1} - T_{i,j+1}^{n+1} + T_{i,j}^n - T_{i,j+1}^n) \\
& + \frac{k_{z(i-1,j)} A_{r(i-1,j)}}{2 \Delta z_{i-1,j} A_{z(i,j)}} (T_{i,j}^{n+1} - T_{i-1,j}^{n+1} + T_{i,j}^n - T_{i-1,j}^n) \\
& \left. + \frac{k_{z(i,j)} A_{r(i,j)}}{2 \Delta z_{i,j} A_{z(i,j)}} (T_{i,j}^{n+1} - T_{i+1,j}^{n+1} + T_{i,j}^n - T_{i+1,j}^n) \right] \\
& / (h_{aw}^{n+1} - h_w^{n+1})
\end{aligned}
\tag{4-55}$$

$2 \leq i \leq nz-1:$

$$\begin{aligned}
c_h = & \left[ \varepsilon \sigma \left( \{T_{i,j}^{n+1}\}^4 - \{T_{tw}^{n+1}\}^4 \right) + \frac{\rho c_P V}{\Delta t A_{z(i,j)}} (T_{i,j}^{n+1} - T_{i,j}^n) \right. \\
& + \frac{k_{r(i,j-1)} A_{z(i,j-1)}}{2 \Delta r_{i,j-1} A_{z(i,j)}} (T_{i,j}^{n+1} - T_{i,j+1}^{n+1} + T_{i,j}^n - T_{i,j+1}^n) \\
& + \frac{k_{z(i-1,j)} A_{r(i-1,j)}}{2 \Delta z_{i-1,j} A_{z(i,j)}} (T_{i,j}^{n+1} - T_{i-1,j}^{n+1} + T_{i,j}^n - T_{i-1,j}^n) \\
& \left. + \frac{k_{z(i,j)} A_{r(i,j)}}{2 \Delta z_{i,j} A_{z(i,j)}} (T_{i,j}^{n+1} - T_{i+1,j}^{n+1} + T_{i,j}^n - T_{i+1,j}^n) \right] \\
& / (h_{aw}^{n+1} - h_w^{n+1})
\end{aligned}
\tag{4-56}$$

$i = nz:$

As described previously, the heat transfer coefficients calculated in the 1D and 2D FV codes are non-dimensionalized and are presented in this form in the results in Chapter 5.

## 5. Chapter 5: Experimental measurements and results

This chapter describes the results of the current study. Zoom schlieren and oil-flow data are presented first to visualize the shock-shock interactions and the effects of these flow phenomena for the fin sweep cases of  $0^\circ$ ,  $-15^\circ$ , and  $-25^\circ$ . These three sweep angles were selected to provide two cases with strong temperature gradients in the lateral direction due to the Type IV (at a  $-15^\circ$  AoA) and Type III (at a  $-25^\circ$  AoA) shock-shock interaction regions, and one configuration for a Type IVa interaction (at a  $0^\circ$  AoA) with lower heating and, thus, smaller lateral temperature gradients. These three cases were selected to assess the need for a two-dimensional analysis method that accounts for lateral conduction. The SG is angled at either  $6^\circ$  or  $9^\circ$  in the shock-interaction wind tunnel runs, and the expected change in the compressible flow properties behind the incident shock are described in Table 5-1.

Next, the heat transfer coefficients calculated using 1D and 2D (for selected cases) methods to analyze temperature data obtained from the phosphor-coated fused silica test articles are described using contour maps and plots of data extracted from a line along the leading edge of each test article. Finally, the key results from the supplemental LAURA CFD analysis of the Type III and direct Type IV shock-shock interaction cases are briefly presented.

**Table 5-1.** Flow properties across the incident shock (IS) due to the SG angle [45].

SG angle	IS angle	$M_2/M_1$	$T_2/T_1$	$p_2/p_1$	$\rho_2/\rho_1$	$p_{02}/p_{01}$
$9^\circ$	$16.70^\circ$	0.798	1.468	3.256	2.219	0.850
$6^\circ$	$14.04^\circ$	0.864	1.285	2.274	1.770	0.946

### 5.1. Visual shock-shock interactions

Section 3.5.3 describes how the zoom schlieren data was obtained during both test 6976 and Test 6983. Unless otherwise stated, the images shown below were obtained with a 30 fps Kodak camera during Test 6976 and a Phantom 9 camera during Test 6983. Terms such as triple point, bow shock, reflected shock, and incident shock used to describe the schlieren images are defined in Figure 2-1.

The nearly vertical line in the schlieren images, typically positioned away from the test article and the associated shocks around the test article, excluding a few of the earlier Test 6976 images, is a plumb bob in the line of sight of the camera that provides a vertical reference. The orientation of the plumb bob, which hangs outside the tunnel in a pot of oil to keep the metal weight stationary, is used to verify the test article angle of attack during the run. In some of the schlieren images, the plumb bob line intersects the shocks due to changes in the relative location of the test article and the associated shocks between runs. When necessary, a second image of the same test configuration is included to show the interaction without obstruction from the plumb bob. However, the image with the plumb bob interference in the shock interaction is included to provide information that is not available in the later image after the plumb bob is relocated.

The boundary layer over the flat plate SG is visible in some of the schlieren images, and is used to determine whether interactions between the shock around the test article and the flat plate boundary layer might affect the shock-shock interaction in each case. During post-test analysis, the image saturation was modified as specified in the image captions to produce gray-scale pictures. Also, the image brightness and contrast settings were changed as needed to enhance the visibility of the shock-shock interaction. These changes are listed in the captions of the modified images. The tip of the test article is positioned at least 0.5 in above the SG to prevent interactions between the flat plate boundary layer and the test article bow shock from occurring ahead of the test article leading edge and disturbing the flow in the shock-shock interaction.

#### **5.1.1. SG angle of 9° (Test 6976)**

The shock-shock interaction data from the Berry and Nowak test [8] was obtained with the flat plate SG angled at 9° to the flow. The SG was inclined at 9° for the first wind tunnel runs in Test 6976 (described in this section) using the test articles instrumented with thin-film gages. The following sections show shock-shock interaction images for a test article with a 0.25-in nose radius at three angles of attack. The incident shock, visible in the schlieren images as a nearly straight line that originates on the left side of the image and intersects the shock around the test article, is angled at approximately 16.7° above horizontal. Images were recorded using a manual trigger to acquire a picture with a 30 fps Kodak camera. Repeat images were obtained for the Painted 2 (Macor®) and Upilex® test articles in this test so only one image from either test article is used to describe each type of shock-shock interaction. These images comprise a preliminary study to assess the capability of the zoom schlieren set-up to view the structures within the three investigated shock-shock interactions.

##### **5.1.1.1. Fin sweep of 0°**

The Painted 2 Macor® test article is shown at a 0° AoA in Figure 5-1 with the lower tip of the leading edge positioned 0.5 in above the SG. Flow density gradients indicate possible vortices above the incident shock between the bow shock and the surface of the test article. The supersonic jet and upper shear layer components of the “glancing” Type IVa interaction as well as the bow shock above the incident shock are not clearly distinguishable in this image. Since the flow features in this image are not clear, images in later sections describe the Type IVa shock-shock interaction for a 9° SG angle in more detail.



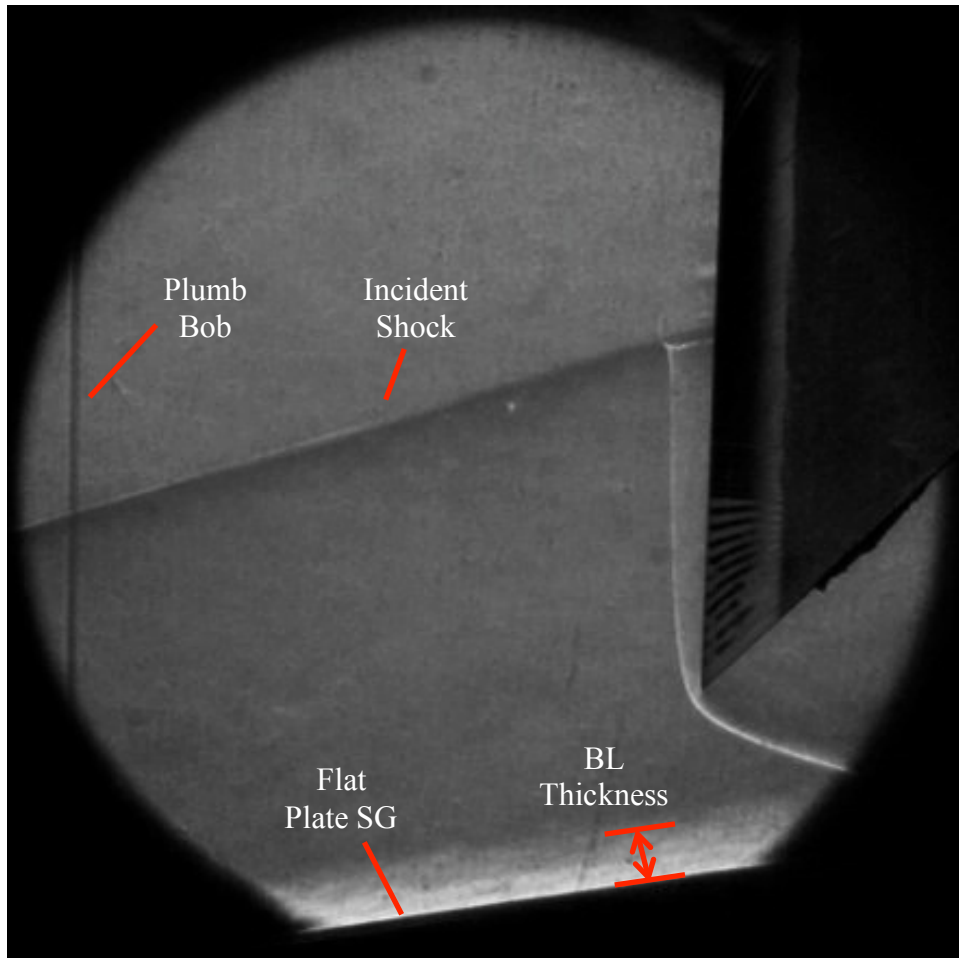


**Figure 5-1.** Zoom schlieren image of Painted 2 test article (0.25 in-radius) at a  $0^\circ$  AoA with a  $9^\circ$  SG angle (recolored with saturation: 0%; brightness: +40%; contrast: +20%).

#### 5.1.1.2. Fin sweep of $-15^\circ$

A “direct” Type IV interaction is demonstrated in Figure 5-2 with the Painted 2 Macor® test article, raised 0.5 in above the SG plate and angled at a  $-15^\circ$  AoA. This image shows that a supersonic jet emanates from the triple point and directly impinges on the surface of the test article. The image also indicates a region above the incident shock in which the density changes during the wind tunnel run. The bow shock standoff distance above the incident shock is larger than the bow shock offset below the incident shock. The image shows the flat plate boundary layer and the test article bow shock do not interact upstream of the test article leading edge in this case.

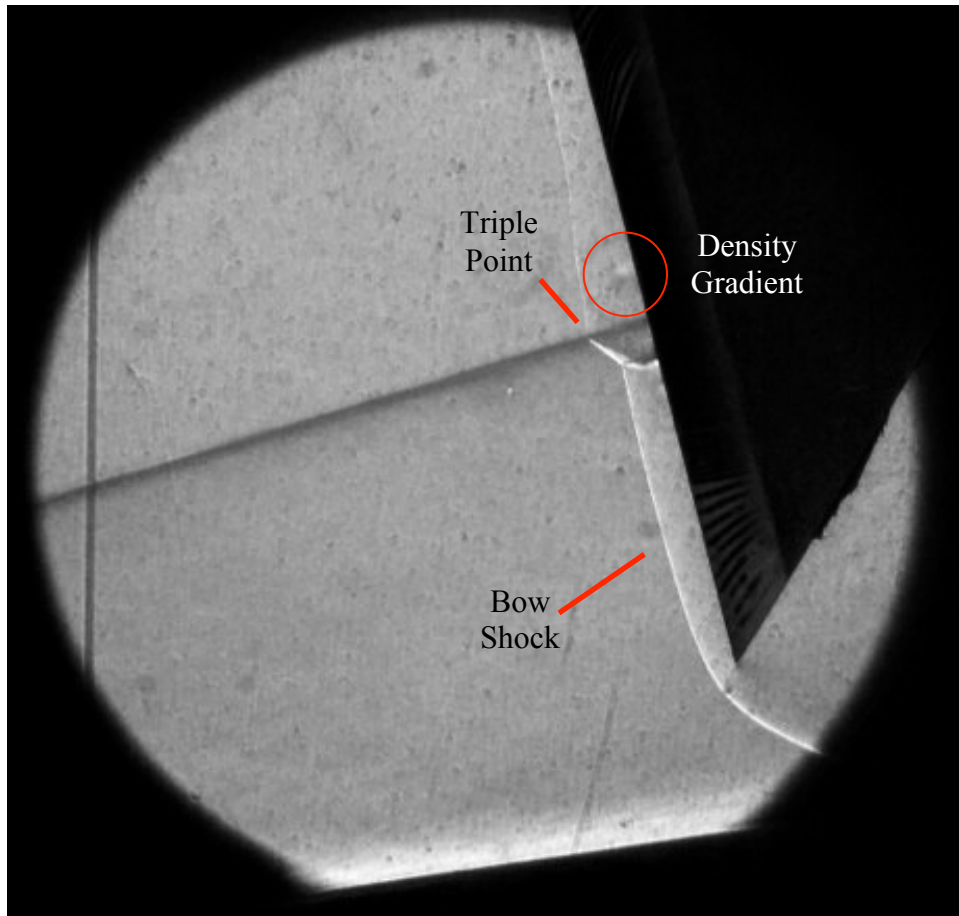


**Figure 5-2.** Zoom schlieren image of Painted 2 test article (0.25 in-radius) at a  $-15^\circ$  AoA with a  $9^\circ$  SG angle (recolored with saturation: 0%; brightness: +40%; contrast: +20%).

Images were also taken with the test article retracted from the wind tunnel with no flow so that no shocks existed in the air density gradients in the zoom schlieren view. This image, with the plumb bob visible on the left side, is shown in Figure 5-3. The two images were compared by subtracting the no-flow image from the image taken during the run, and vice a versa, in an attempt to remove the spots in the image due to pits in the wind tunnel window. Examples of this image manipulation are included in Figure 5-4 and Figure 5-5 for the Type IV shock-interaction case with the Painted 2 test article at a  $-15^\circ$  AoA.

As Figure 5-4 shows, when the shock-shock interaction image is subtracted from the wind-tunnel window (no flow) image, the resulting image displays the shock-shock interaction, the plumb bob and the boundary layer over the flat plate SG. The clarity of the shocks in Figure 5-4 is poor compared to the regular schlieren images taken during the run. For this reason, the effects of the pitted wind tunnel windows were noted but neglected in the remaining schlieren images.

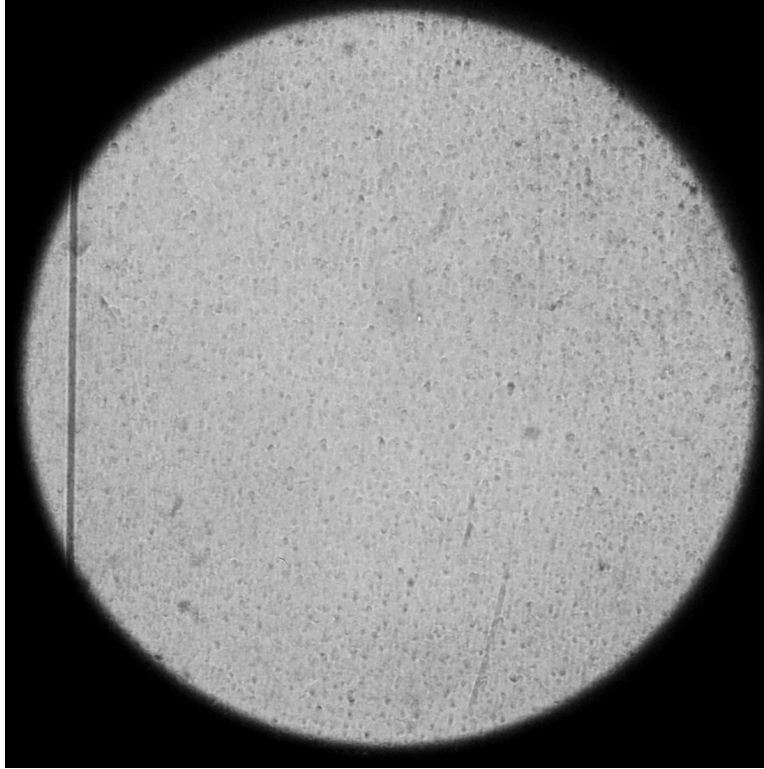


**Figure 5-3.** Zoom schlieren image with test article retracted and no flow in the wind tunnel (recolored with saturation: 0%; brightness: +40%; contrast: +20%).

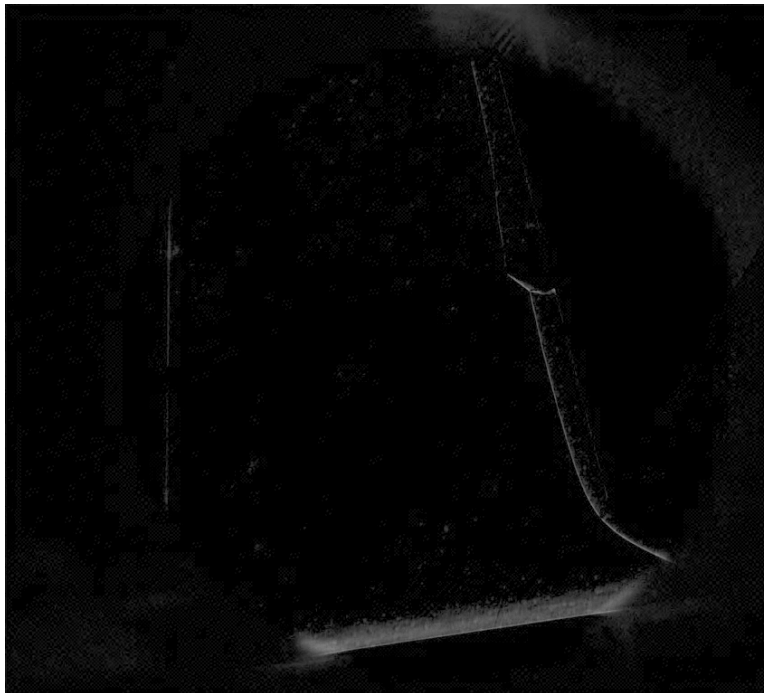


**Figure 5-4.** Shock-interaction image subtracted from the wind-tunnel window (no flow) image for the Painted 2 test article at a  $-15^\circ$  AoA with a  $9^\circ$  SG angle (recolored with saturation: 0%; brightness: +40%; contrast: +20%).

Figure 5-5 shows the resulting image when the no-flow image through the tunnel window is subtracted from the image with the inserted test article exposed to a shock-shock interaction during the run. The thin-film gages that are spaced further apart near the tip of the leading edge on the Painted 2 test article are more clearly distinguishable in this image, as are the plumb bob location, the incident shock, and the flat plate. However, the shock-shock interaction and the flat plate boundary layer are nearly the same color as the image background.

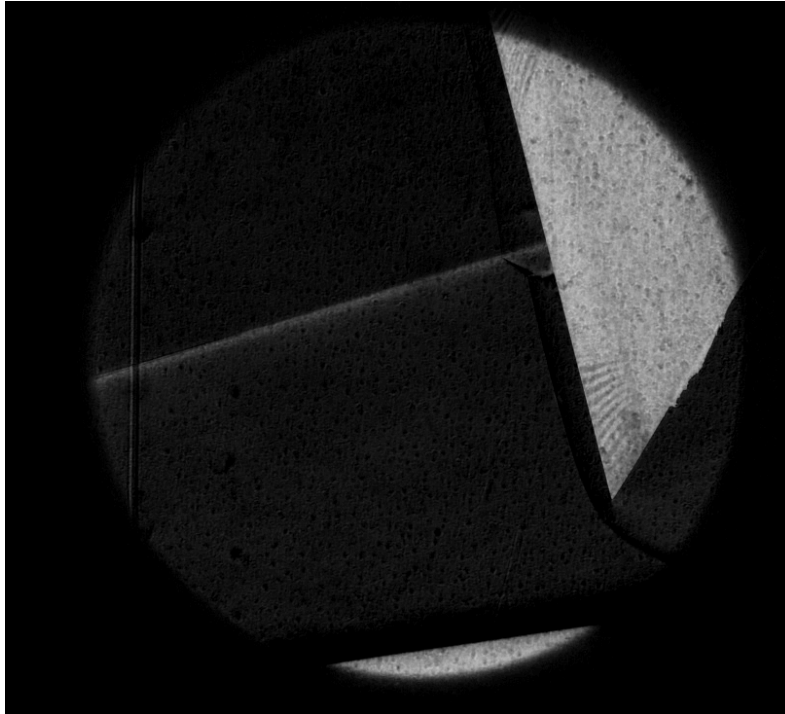


**Figure 5-5.** Wind-tunnel window (no flow) image subtracted from the shock-interaction image for the Painted 2 test article at a  $-15^\circ$  AoA with a  $9^\circ$  SG angle (recolored with saturation: 0%; brightness: +40%; contrast: +20%)

#### 5.1.1.3. Fin sweep of $-25^\circ$

A Type III interaction with the 0.25 in-radius Upilex® test article at a  $-25^\circ$  AoA is pictured in Figure 5-6. Two images taken at different times during the run are included in the figure to demonstrate the unsteadiness in this type of interaction. The upper shear layer of the interaction typically extends from the triple point to a point of attachment on the test article surface in this type of interaction as shown in the image on the right in the figure. Thus, a supersonic jet is not formed in this case. The image on the left shows a moment in the run when the unsteadiness in the flow just above the shock-shock interaction interacts with the shear layer, causing it to temporarily detach from the surface of the test article. A density gradient behind the test article indicates effects of the shock-shock interaction are carried in the flow around the test article, which correlates to changes in the heating pattern in that region on the side of the test article as discussed in later sections. Density gradients between the displaced bow shock and the surface of the test article below the shock-shock interaction in these images suggest vortices may be formed by the Type III interaction.

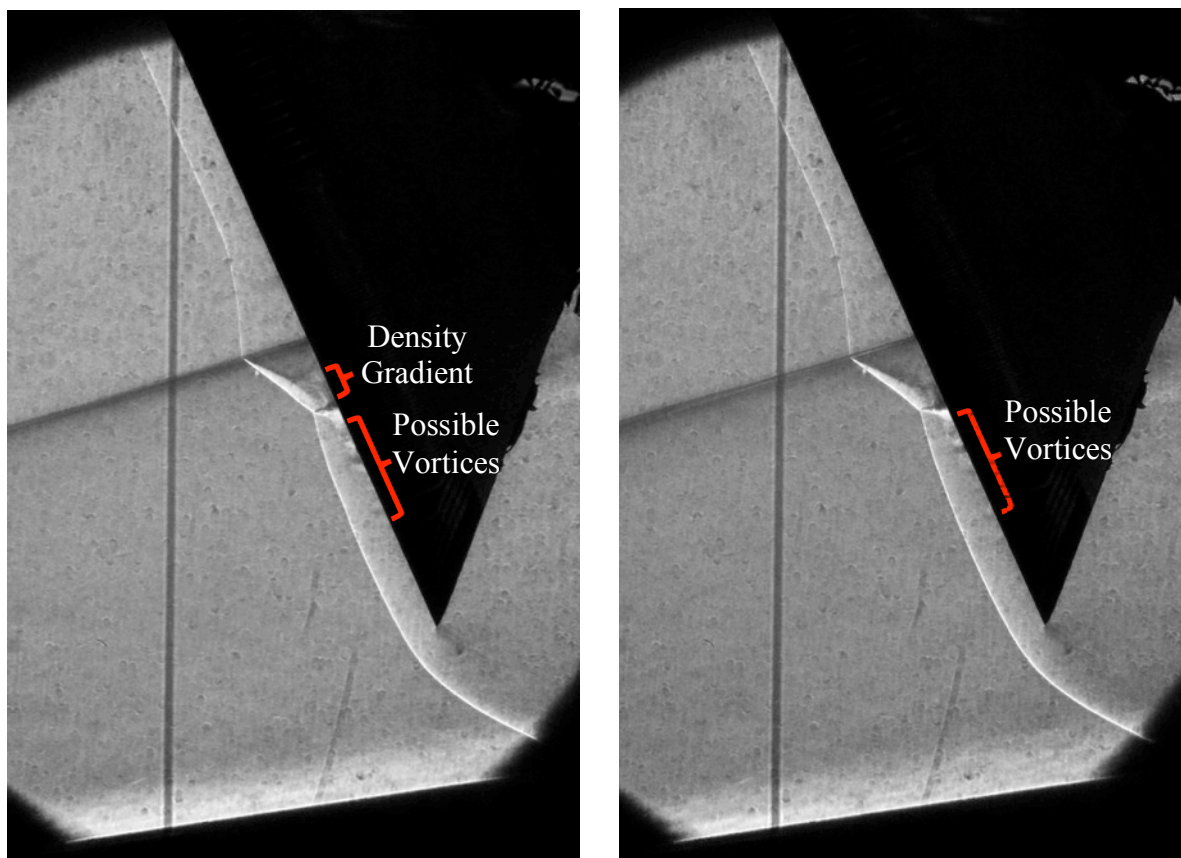


**Figure 5-6.** Two zoom schlieren images of a 0.25 in-radius Upilex® model angled at  $-25^\circ$  (recolored with saturation: 0%; brightness: +40%; contrast: +20%).

### 5.1.2. SG angle of $9^\circ$ (Test 6983)

In Test 6983, three test article geometries were tested at three angles of attack, namely  $0^\circ$ ,  $-15^\circ$  and  $-25^\circ$ . In each of these wind tunnel runs, the SG angle was kept at  $9^\circ$  to determine how the features of each type of interaction changed based on the test article nose radius. The shock-interaction flow features described using the Test 6976 zoom schlieren images are discussed further in this section based on gray-scale images obtained at higher framing rates using the Phantom cameras. Different lenses were used with the Phantom 9 and Phantom 12 cameras, as discussed in section 3.5.3, to further improve the resolution in the interaction region as the framing rate was increased. Oil flow images obtained during this test are also used to describe the behavior of the Mach 6 flow at the surface of the test articles.

#### 5.1.2.1. Fin sweep of $0^\circ$

Figure 5-7 and Figure 5-8 display images of a 0.25 in-radius test article at a  $0^\circ$  AoA recorded at a framing rate of 1000 fps and 1600 fps, respectively. The bow shock above the incident shock for a test article with this geometry is slightly clearer in Figure 5-7 than the shock in Figure 5-1. The shock interaction is so close to the incident shock for the 0.25 in-radius test article that the Type IVa features are difficult to distinguish, though a close inspection reveals a very narrow supersonic jet with a shear layer turned upward.

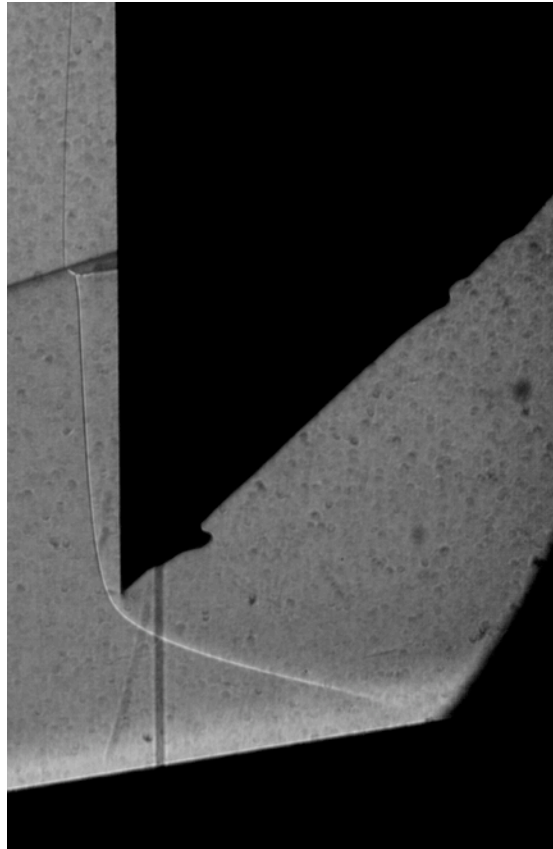


**Figure 5-7.** Zoom schlieren (1000 fps) image of a Type IVa shock-interaction for the 0.25 in-radius test article angled at a  $0^\circ$  AoA.

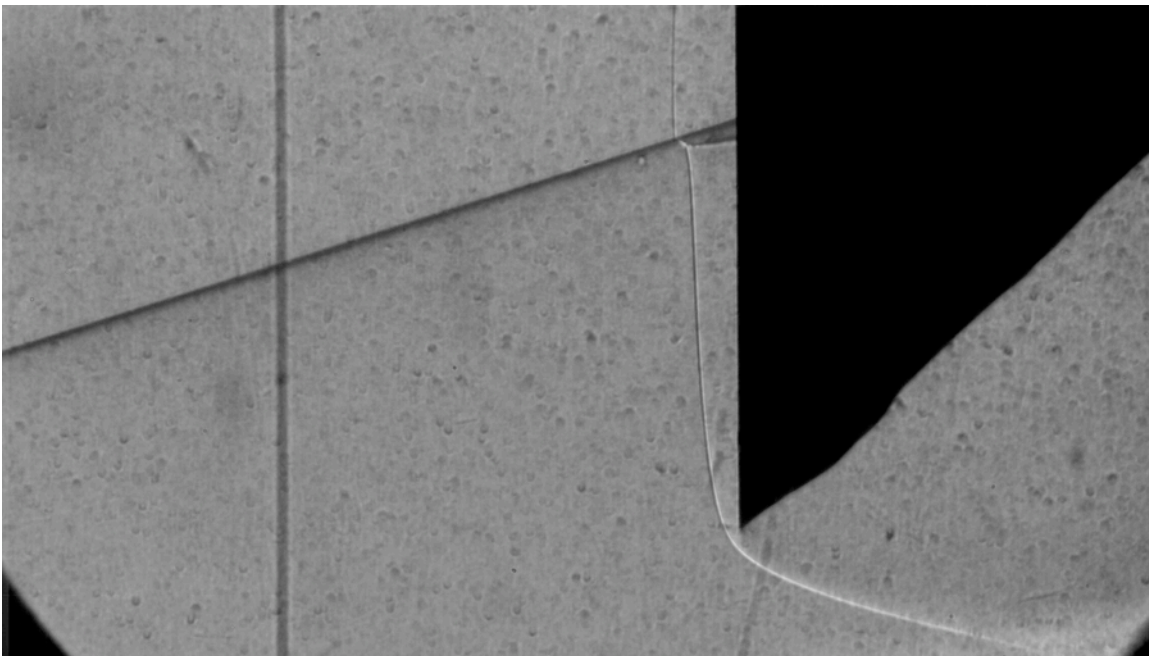


**Figure 5-8.** Zoom schlieren (1600 fps) image of the 0.25 in-radius test article at a  $0^\circ$  AoA.



The image in Figure 5-9 shows the same Type IVa interaction for the 0.5 in-radius test article at a  $0^\circ$  AoA. A density gradient behind the test article at a height slightly above the impingement point of the supersonic jet is only noticeable in the video for this configuration since the test article leading edge is positioned near the middle of the view through the zoom schlieren lenses. The incident shock is further separated from the Type IVa interaction in this case than for the smaller 0.25 in-radius test article because the bow shock offset extends further in front of the larger test article.

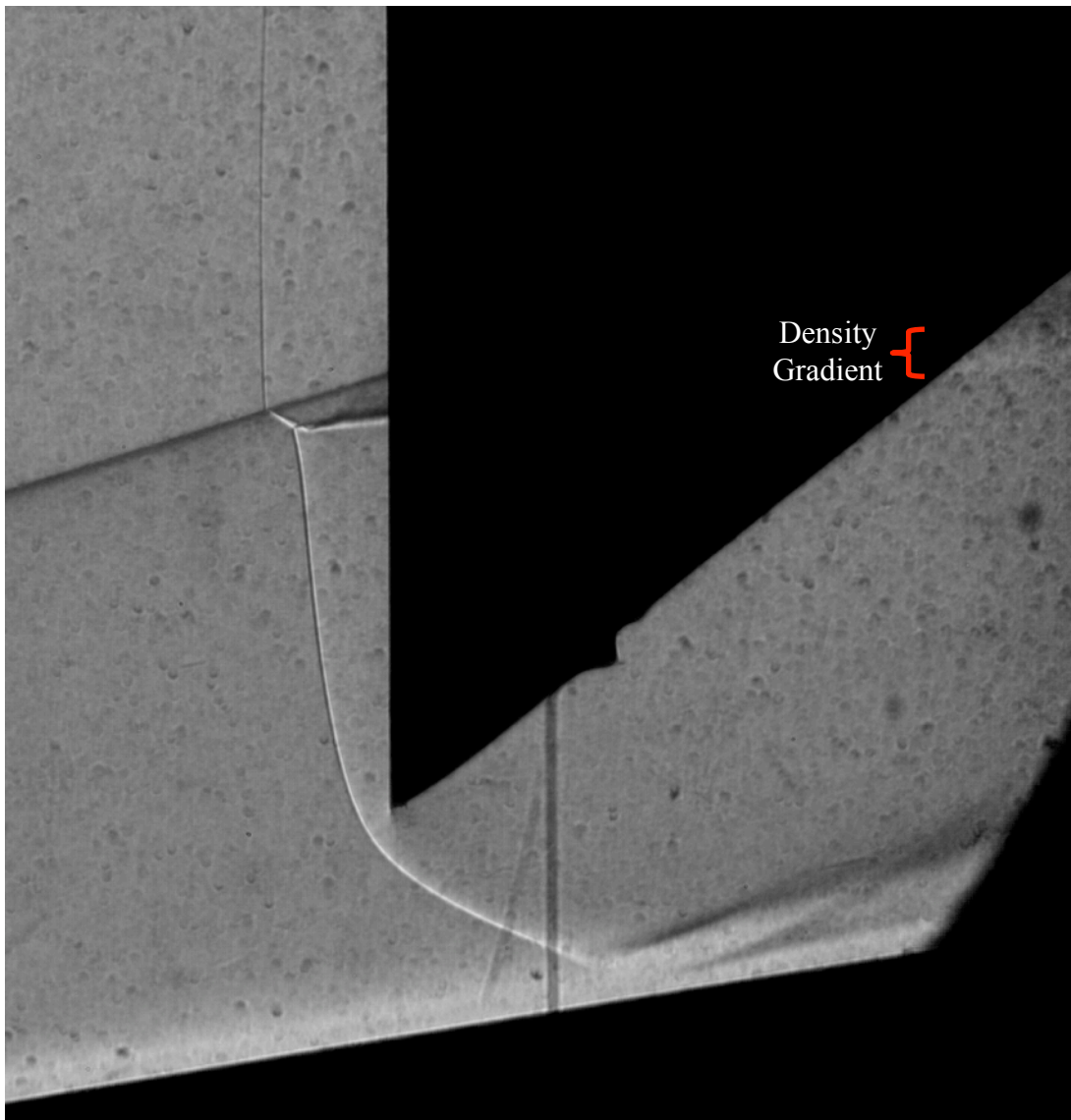


**Figure 5-9.** Zoom schlieren (1000 fps) image of a Type IVa shock-interaction for the 0.50 in-radius test article angled at a  $0^\circ$  AoA.

The image in Figure 5-10 shows the plumb bob in front of the shock-shock interaction rather than behind the test article. This cropped image shows the supersonic jet and curled-up shear layer that appears to attach to the surface near the impingement line of the incident shock, but the other shock interactions and density gradients are not available in this image.



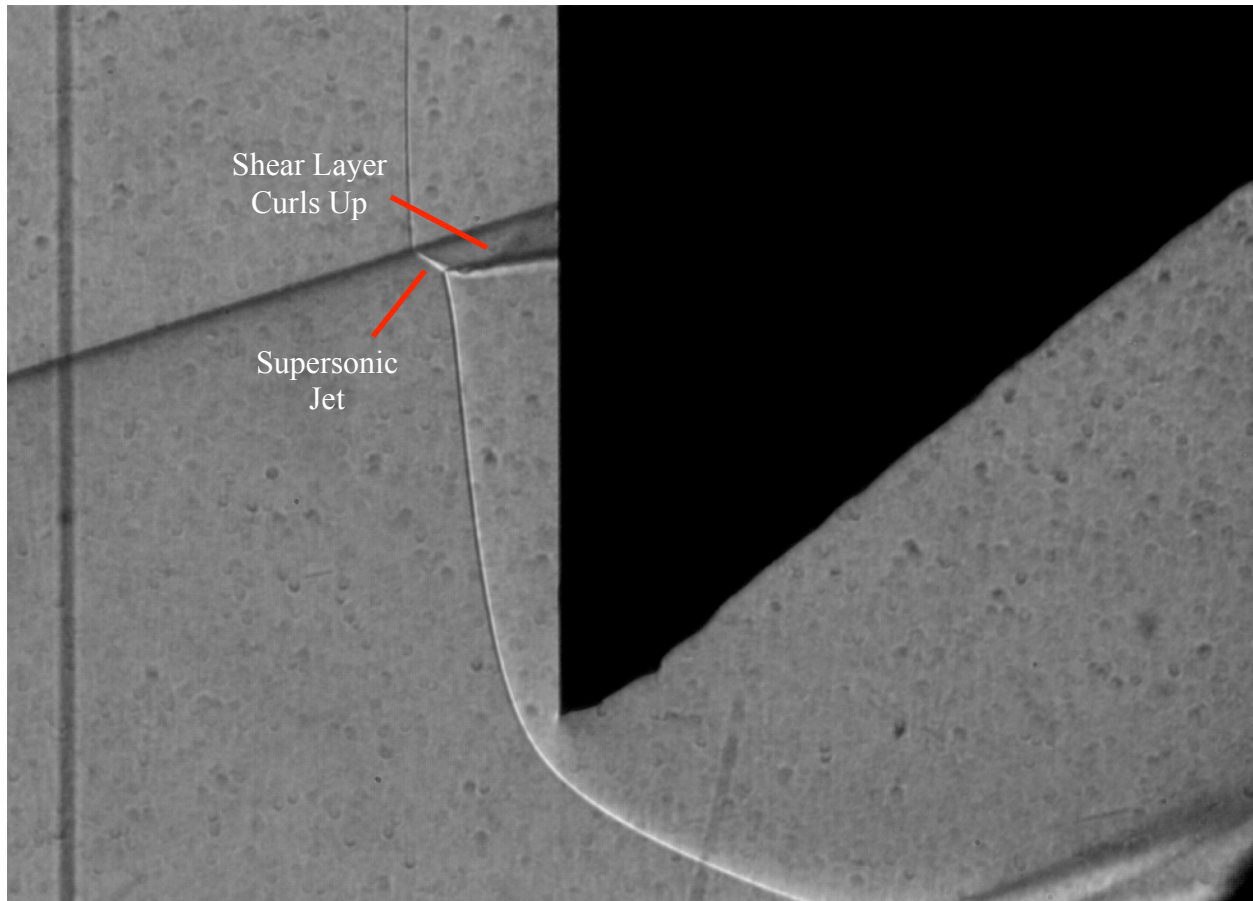


**Figure 5-10.** Zoom schlieren (1600 fps) image of the 0.50 in-radius test article at a  $0^\circ$  AoA.

Due to a larger bow shock around the 0.75 in-radius test article at a  $0^\circ$  AoA, the Type IVa interaction displayed in Figure 5-11 and Figure 5-12 are more spread out than for the smaller test articles so that the features of the interaction are easier to identify. A narrow supersonic jet extends at an angle from the triple point to the location where the bow shock is again nearly vertical, before turning to travel almost horizontally to an impingement point on the surface of the test article. A pattern of triangles formed by reflected shocks within the supersonic jet is visible in both images near the beginning of the supersonic jet. The upper shear layer above this region of shock triangles curves up toward the intersection of the incident shock and the test article surface, as evidenced by the darker region in the density gradients in the images.

A shock-BL interaction is shown behind the lower tip of the test article. This interaction between the flat plate and the shock around the test article does not appear to affect the upstream features of the shock-shock interaction. For this reason, the test article was placed 0.5 in above the flat plate SG during the remaining runs with the 0.75 in-radius test article at a  $0^\circ$  AoA.

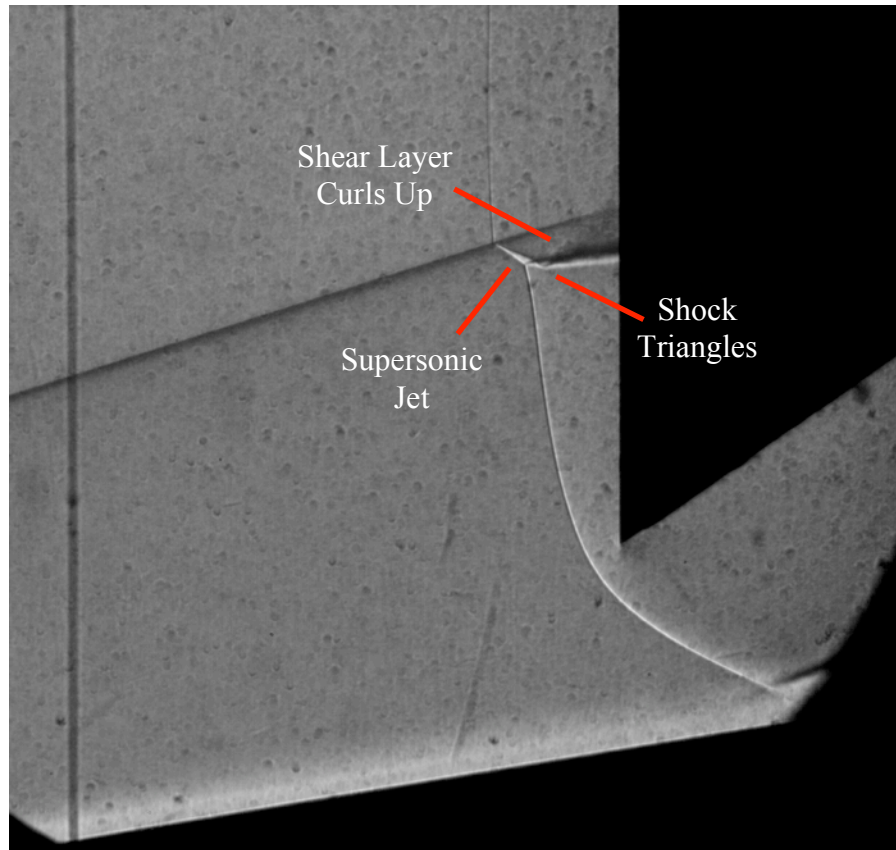


**Figure 5-11.** Zoom schlieren (1000 fps) image of a Type IVa shock-interaction for the 0.75 in-radius test article angled at a  $0^\circ$  AoA.

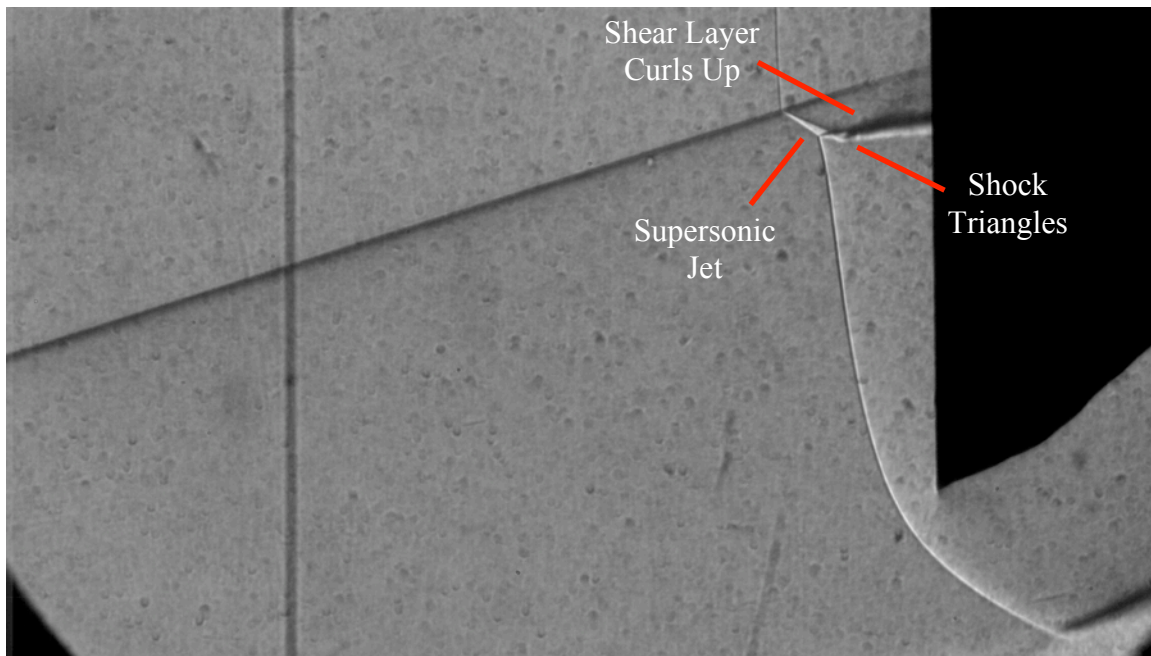


**Figure 5-12.** Zoom schlieren (1600 fps) image of the 0.75 in-radius test article at a  $0^\circ$  AoA.

Figure 5-13 shows a still image of the side of the 0.25 in-radius test article at a  $0^\circ$  AoA that is merged with a zoom schlieren image of the Type IVa shock-shock interaction for the same test article. Due to the orientation of the zoom schlieren system used to take the picture, only the side fiducials (excluding the leading edge fiducial marks) are visible in this image. The fiducial mark pattern is shown in Appendix B for reference. In this case, the fiducials positioned the second from the bottom on the leading edge and in the leftmost column on the side of the test article in the image are horizontally aligned. Also, the bottom fiducials on the leading edge and in the two columns on the side of the test article are arranged in a straight line. Thus, the curved shear layer and the supersonic jet impinge on the test article between the bottom two fiducials on the leading edge of the test article for all of the Type IVa interactions.

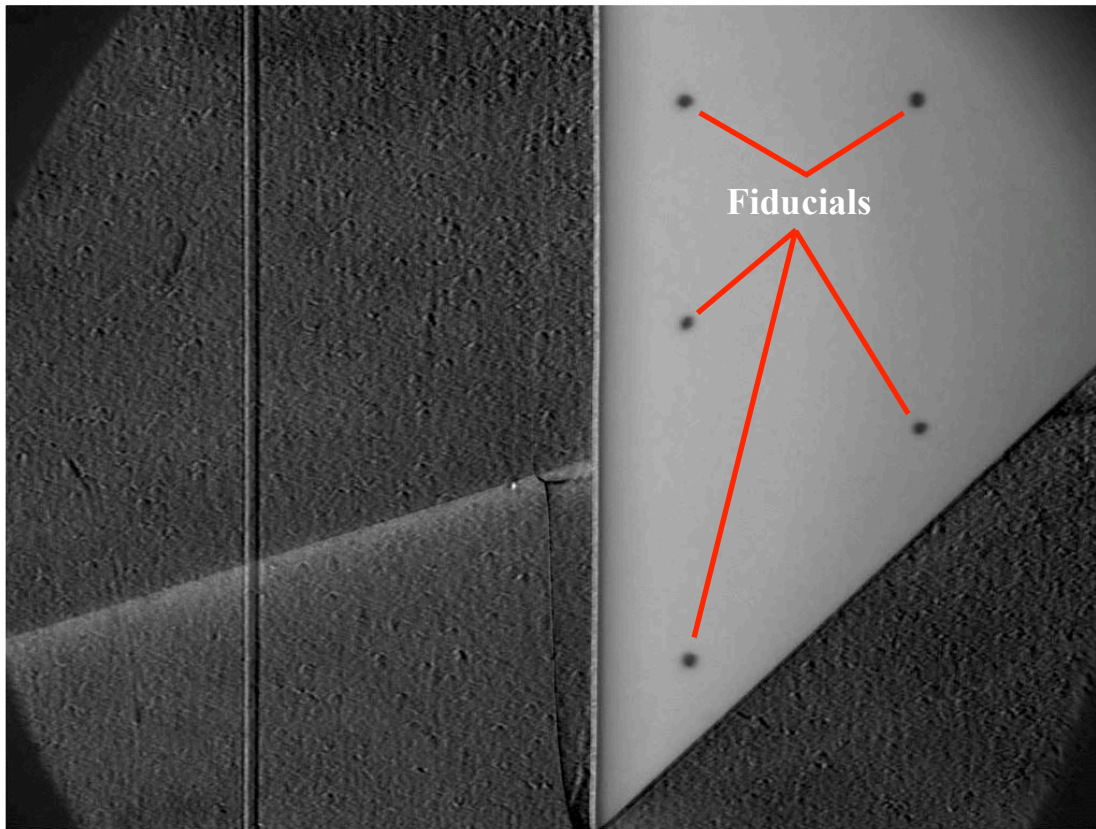


**Figure 5-13.** Phantom 12 (7900 fps) zoom schlieren image overlaid with fiducials for the 0.25 in-radius test article at a  $0^\circ$  AoA (recolored with brightness: +40%).

Oil flow images in Figure 5-14 show characteristic streamlines for this Type IVa interaction. The left image shows streamlines on a test article that was covered with dots of pigmented oil prior to the run, while the right image indicates the oil movement for a test article that was initially fully coated with oil. Fiducial marks show up as orange dots under the oil in the images. Edney [2] states that a region of dead air exists along the leading edge just below the upper shear layer attachment point in an oil-flow image of a 0.59 in-radius cylinder exposed to a Type IVa shock-shock interaction. The oil-flow streamlines shown on the leading edge of the 0.75 in-radius test article in Figure 5-14 exhibit this same behavior. The streamlines for this type of interaction also resemble the streamlines on an oil flow image for a 0.5 in-radius cylinder in [31],



with different behavior near the bottom of the leading edge since the flat plate boundary layer did not interact with the bow shock ahead of the leading edge in the current study. The features in these oil-flow images are similar to the streamline patterns observed in the 0.25 in- and 0.5 in-radius test articles.

In the images of the leading edge, streamlines travel upward from the attachment point and then turn away from the leading edge toward either the left or the right side of the test article. A horizontal line around the circumference of the leading edge in the full-coating image seems to indicate the attachment point of the curved shear layer above the supersonic jet. This line is near the location where the planar incident shock wraps around the test article, as seen in the schlieren images for this case. The incident shock likely passes outside of the bow shock around the test article for each type of shock-shock interaction and does not directly impinge on the test article. However, the location where the incident shock would impinge on the test article in the absence of a bow shock is estimated from the schlieren images, and this extrapolated “incident shock” position is used as a reference location in the oil flow images for each type of interaction.

Streamlines below the attachment point move horizontally out from around the dead air region on the leading edge, and streamlines outside the dead-air region near the lowest fiducial mark travel downward and away from the leading edge. In the region near the top of the test article, away from the shear layer attachment point and the incident shock, the oil along the stagnation line did not move. The patterns along the leading edge appear to be relatively symmetrical, yielding an approximate mirror image on either side of the stagnation line.

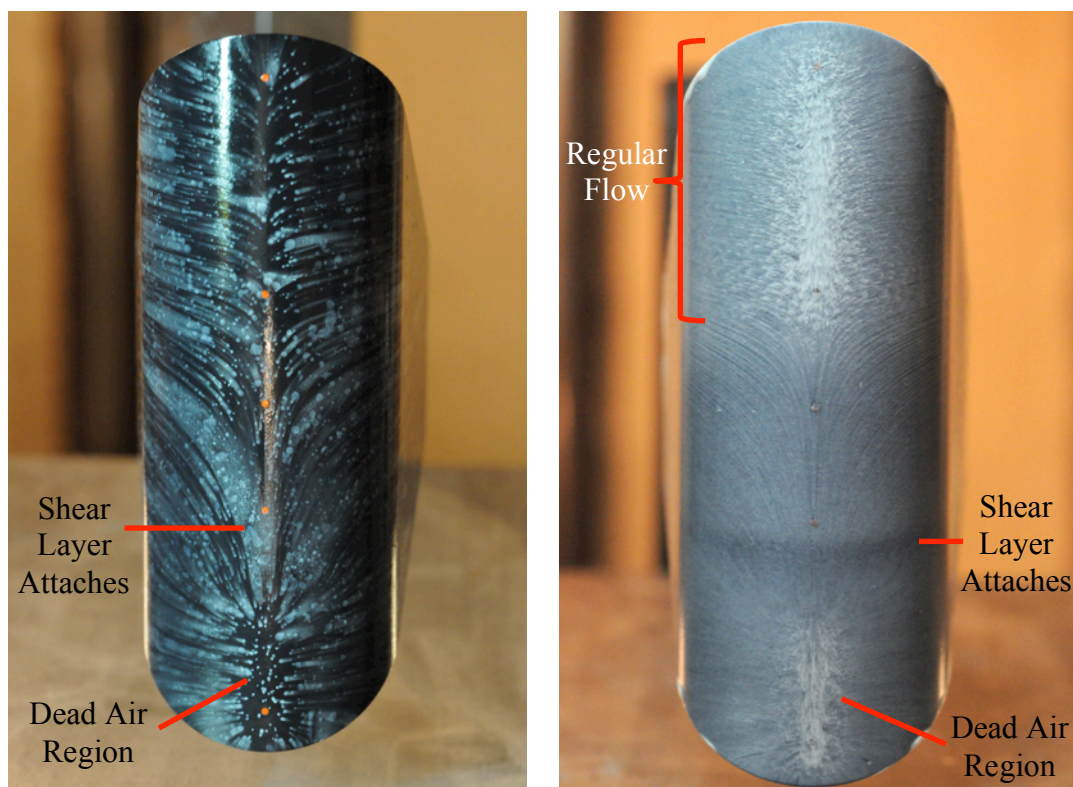


**Figure 5-14.** Leading-edge oil-flow images for the 0.75 in-radius metal test article at a 0° AoA (using the two oil-flow techniques: dots in the left image, full coating in the right image).

The images in Figure 5-15 show the streamlines in the pigmented oil on either side of the test article. Although some of the schlieren videos indicate density gradients, possibly due to vortices in the flow above the shear layer attachment point between the test article surface and the shock around the test article, nearly horizontal streamlines flow away from the leading edge on the upper portion of the test article as would be expected in Mach 6 flow through a bow shock that is nearly normal to the flow. The end of the streamlines that pass by the top two and bottom two fiducials in the first column on either side of the test article turn up or down, respectively, toward the slanted edges of the test article (as seen in video of the oil flow during the run).

This set of oil flow images demonstrates two reasons for using both the oil dots and full oil coating techniques in observing the flow patterns on the surface of the test articles. First, the size of the dots generated in the conventional technique is random, and can range from small to large in any given location. The dot sizes can be controlled somewhat by reapplying the oil prior to the run, but this method still does not yield a completely uniform grid of dots. Smaller dots of oil are less likely to move much during a wind tunnel run, while large dots of oil may spread out enough to blur the motion of the surrounding streamlines. Second, the full coating method ensures the entire surface is covered with a sufficient amount of oil to provide insight into the behavior of the surface flow, either by moving (producing streamlines) or remaining stationary during the run.

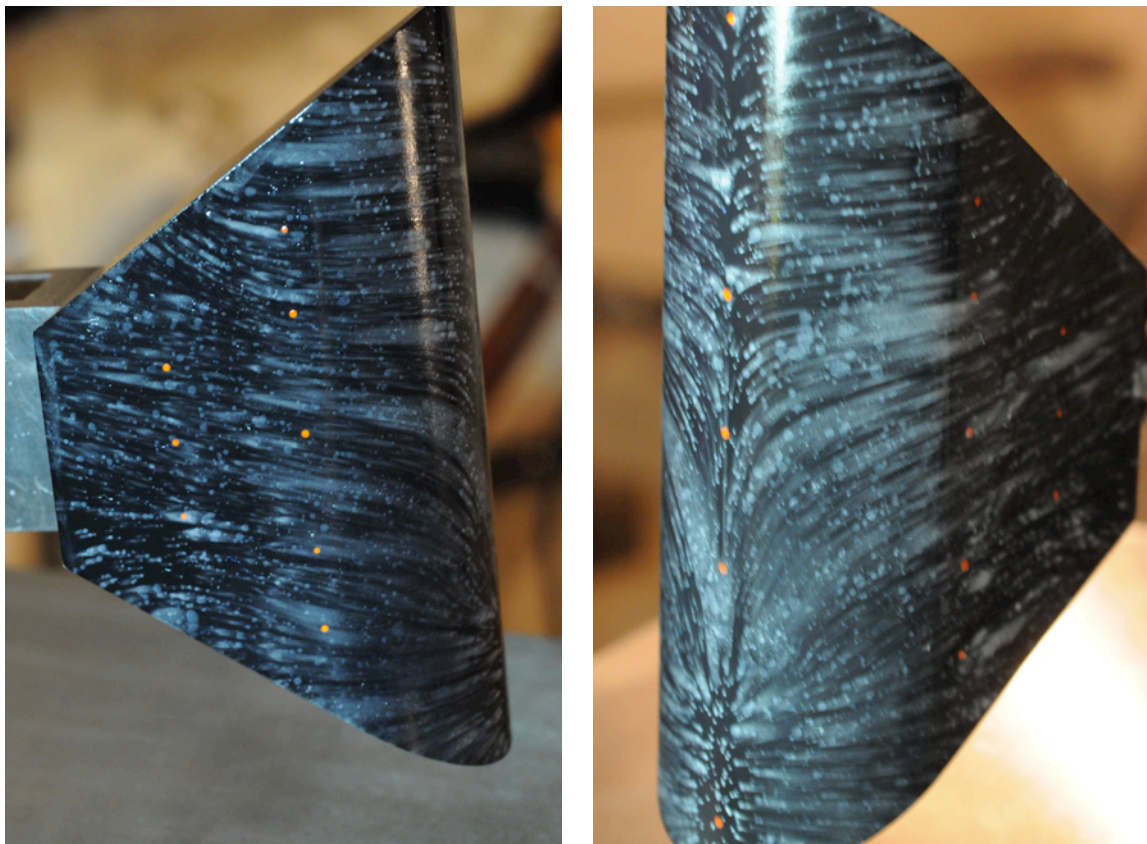


**Figure 5-15.** Side oil-flow images for the 0.75 in-radius metal test article at a  $0^\circ$  AoA (both images display streamlines produced with the oil flow dots technique).

#### 5.1.2.2. Fin sweep of $-15^\circ$

A zoom schlieren images obtained at 1000 fps for the 0.25 in-radius test article at a  $-15^\circ$  AoA is shown in Figure 5-16. The characteristic feature of a Type IV interaction is visible in this image, namely, a supersonic jet emanating from the triple point that impinges nearly perpendicularly on the surface of the test article. Although the schlieren video in this case reveals changes in the density of the air between the bow shock and the test article surface above the incident shock over time, the density gradient in that region is not clear in Figure 5-16. The shock around the test article does not interact with the flat plate boundary layer upstream of the lower tip of the test article.

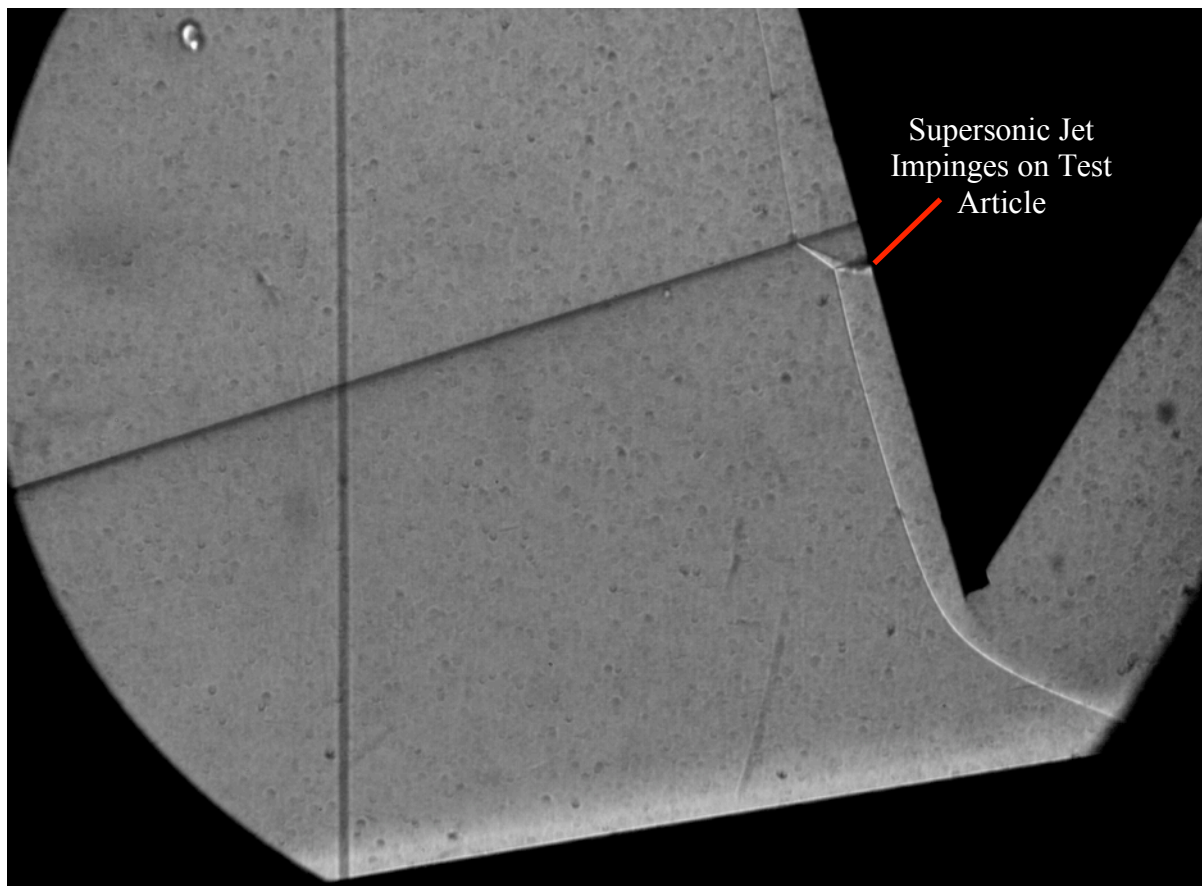


**Figure 5-16.** Zoom schlieren (1000 fps) image of a Type IV shock-interaction for the 0.25 in-radius test article angled at a  $-15^\circ$  AoA.

The images in Figure 5-17 and Figure 5-18 reveal interactions between the bow shock and the flat plate boundary layer for the 0.5 in-radius test article. These interactions occur slightly downstream of the lower tip of the test article and do not appear to affect the behavior of the Type IV shock-shock interaction. The plumb bob was positioned poorly during the wind tunnel run in which the schlieren data was obtained at 1000 fps. The plumb bob was later moved, as the image taken at 1600 fps indicates, making it easier to see the shock triangles (as sketched in Figure 2-1) that comprise the portion of the supersonic jet that impinges on the test article surface.



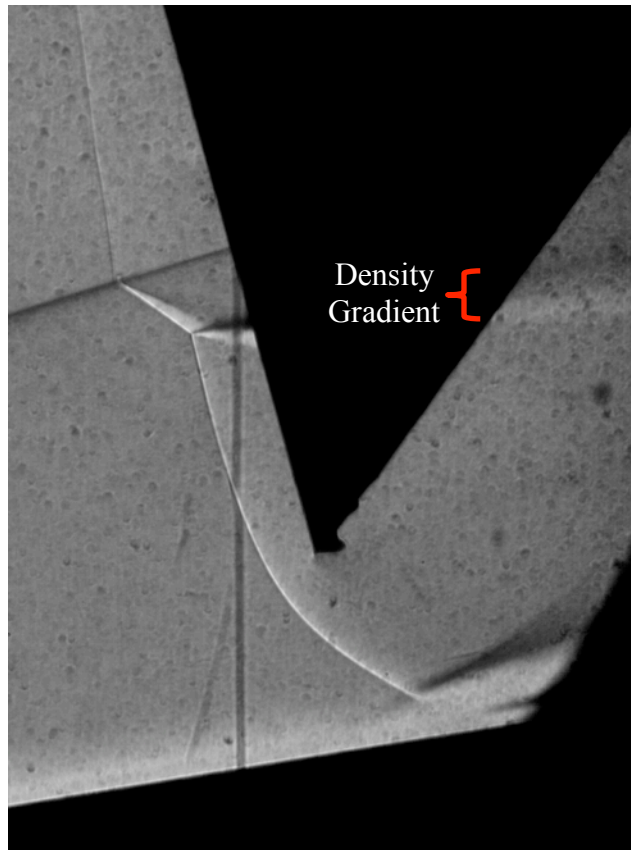


**Figure 5-17.** Zoom schlieren (1000 fps) image of a Type IV shock-interaction for the 0.50 in-radius test article angled at a  $-15^\circ$  AoA.

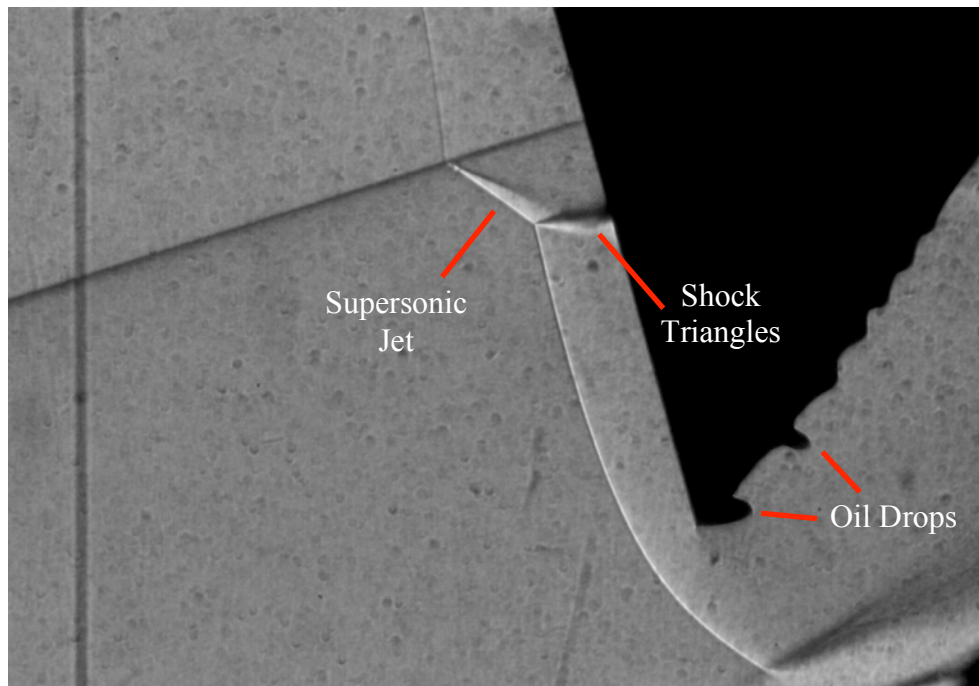


**Figure 5-18.** Zoom schlieren (1600 fps) image of the 0.50 in-radius test article at a  $-15^\circ$  AoA.



The zoom schlieren image in Figure 5-19 shows the supersonic jet produced in the Type IV interaction for the 0.75 in-radius test article. The basic features of this interaction are similar between the images for the test articles with varying nose radii. The pattern is more clearly distinguishable in this image since the bow shock standoff distance is greater for the largest test article in the study, which means the shock interaction is also larger and more spread out. The shock around the test article also interacted with the boundary layer over the flat plate SG in this wind tunnel run, producing shock-BL interactions directly below the tip of the test article. These interactions may contribute to the increased heating near the lower tip of the largest test article as discussed in a later section. Since the shock-BL interactions did not noticeably affect the flow over the test article in the zoom schlieren videos, a separation distance of 0.5 in was maintained for this test configuration in the heat transfer tests.

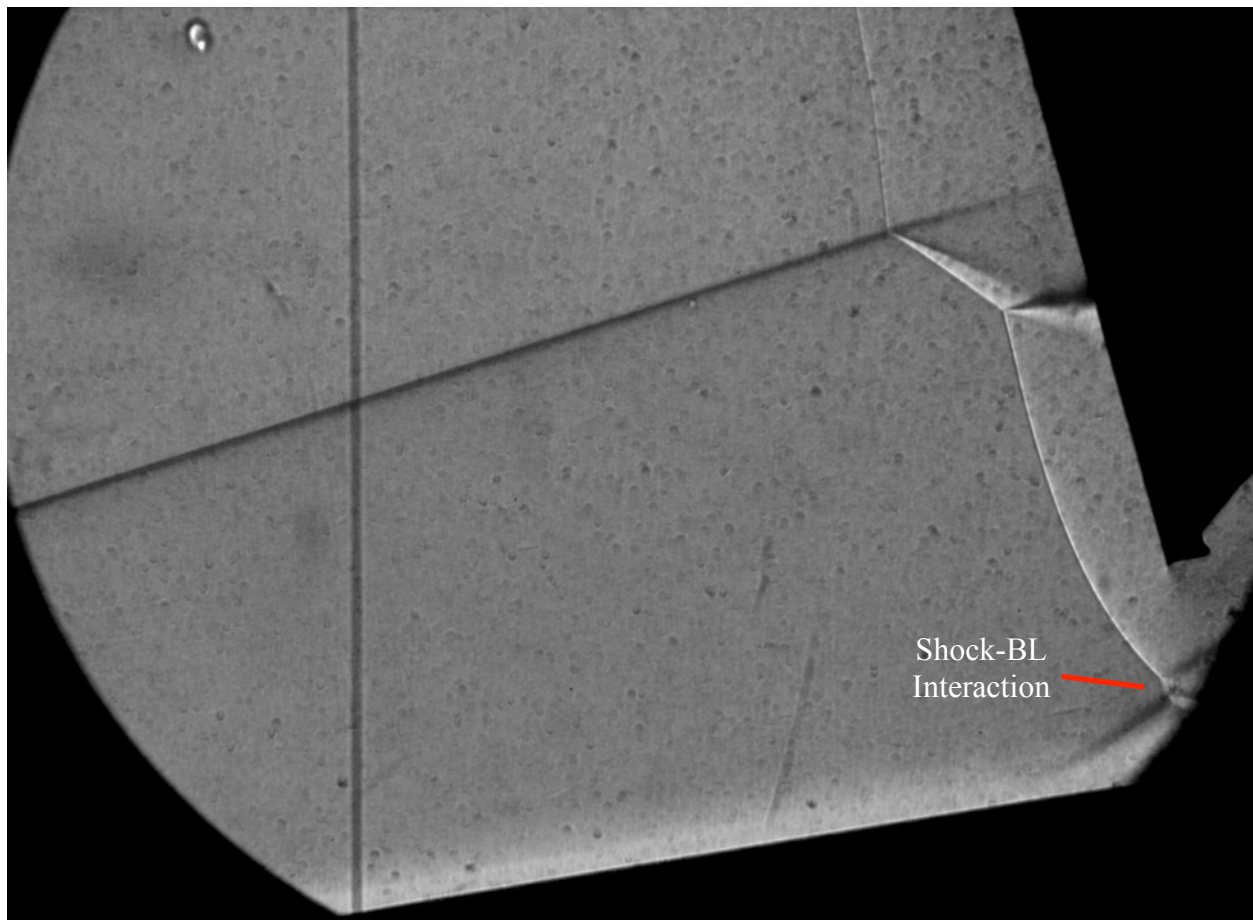


**Figure 5-19.** Zoom schlieren (1000 fps) image of a Type IV shock-interaction for the 0.75 in-radius test article angled at a  $-15^\circ$  AoA.

Figure 5-20 shows cropped images of the Type IV interaction with the 0.75 in-radius test article from the incident shock near the top of the images to the edge of the shock-BL interaction near the bottom of the images. These images (obtained at different times in the same run) show the reflected shock pattern within the supersonic jet more clearly than in the earlier cases.

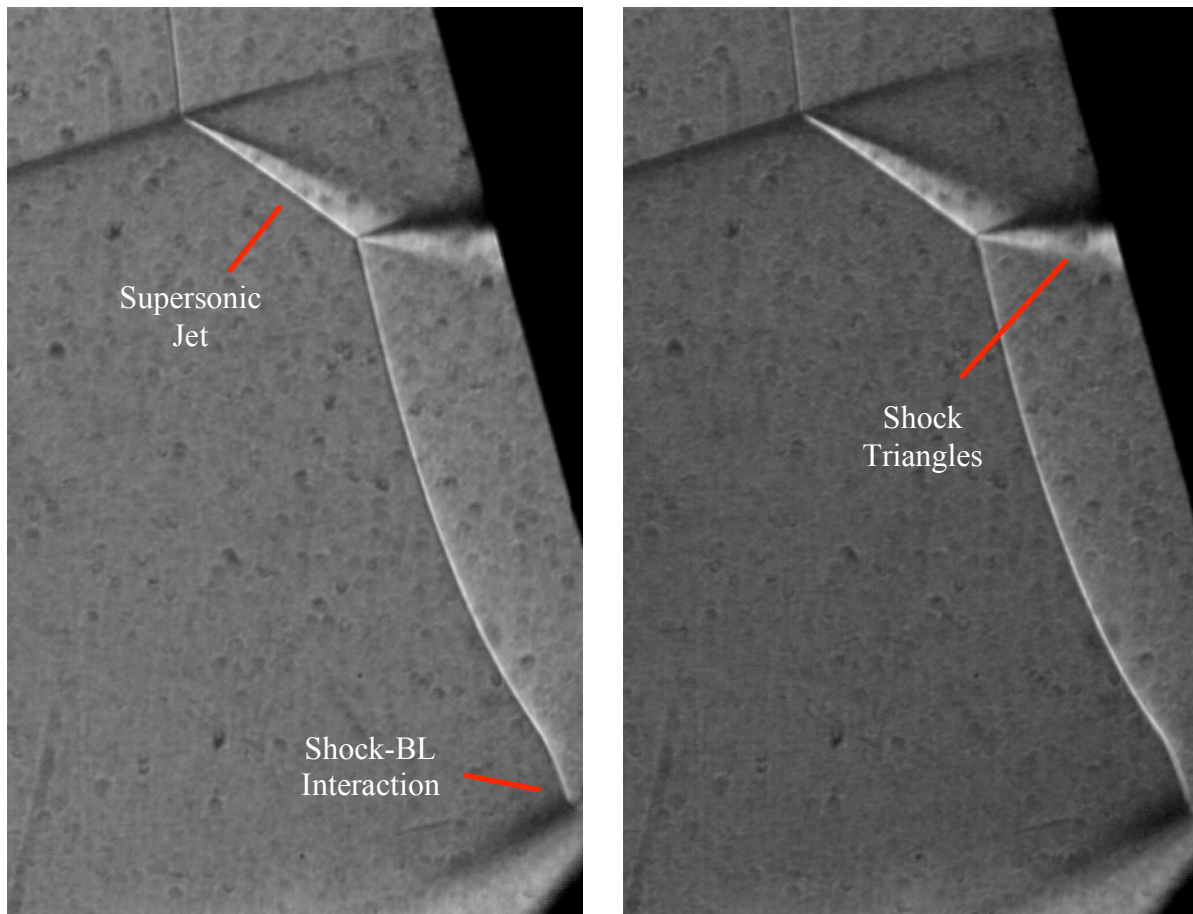


**Figure 5-20.** Zoom schlieren (1600 fps) image of the 0.75 in-radius test article at a  $-15^\circ$  AoA.

The image in Figure 5-21 shows illuminated fiducials on the side of the 0.75 in-radius test article at a  $-15^\circ$  AoA overlaid with the corresponding schlieren image. Refer to Appendix B for diagrams of the fiducial mark pattern for this test article. For the three test articles, the fiducials are positioned such that the second fiducial from the bottom on the sidewall (shown in the image) is aligned with the corresponding second fiducial along the leading edge. The upper fiducial seen on the sidewall in the image corresponds to the center point fiducial of the test article and is aligned with the middle fiducial on the leading edge. The term “aligned” for these two sets of fiducials means the fiducial marks are in a horizontal line when the leading edge of the test article is vertical.

Using these reference points, the supersonic jet of the Type IV interaction impinges on the test article surface between the bottom two fiducials on the leading edge. For the test article in the image, the edge of the region of varying density above the incident shock lies between the second and third (middle) fiducial from the bottom of the leading edge. This region of varying density, which is more clearly shown in videos than in still images, moves closer to the extrapolated incident shock location as the distance to the supersonic jet below the incident shock decreases for the smaller test articles.

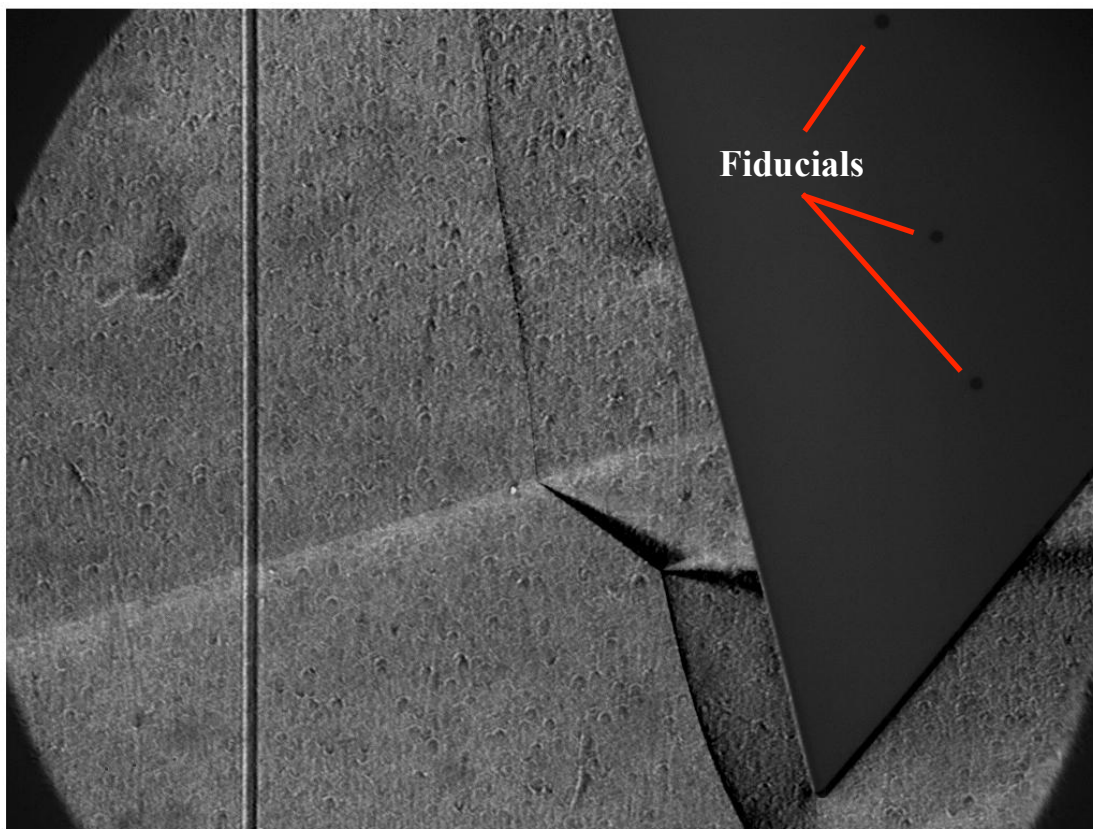


**Figure 5-21.** Phantom 12 (7900 fps) zoom schlieren image overlaid with fiducials for the 0.75 in-radius test article at a  $-15^\circ$  AoA.

Oil flow images for the 0.75 in-radius test article at a  $-15^\circ$  AoA are provided in Figure 5-22 and Figure 5-23. These images are representative of the surface streamlines produced by a direct Type IV shock interaction for the test article geometries investigated in this study. A region of stationary dots in the image on the left or undisturbed oil coating in the image on the right exists along the stagnation line near the top of the leading edge. The streamlines surrounding this stagnation region in the image generated with the oil dots technique follow a curved path down and away from the stagnation line rather than moving out from the leading edge in a nearly horizontal direction as in the oil flow images for the test article at a  $0^\circ$  AoA. This pattern is reasonable considering the orientation of the test article and the associated bow shock relative to the Mach 6 flow. Since the test article leading edge is oriented at an angle of  $15^\circ$  forward of vertical, the bow shock acts like an oblique shock that turns the horizontal flow down before the air reaches the surface of the test article and wraps around the leading edge. The bow shock around a test article at a  $0^\circ$  AoA is a nearly normal shock and, thus, the flow does not change direction.

The shear associated with the supersonic jet impingement removes the majority of the oil coating the test article in that region in the left image in Figure 5-22. The lower horizontal line on the leading edge in the two images in this figure corresponds to the edge of this high shear region



due to the supersonic jet. This line is also approximately located where the incident shock wraps around the test article (outside of the bow shock) between the two lowest fiducials on the leading edge. The lower streamlines in the left image on either side of the stagnation line resemble parabolas with a trough centered near the supersonic jet impingement. In the schlieren images for this interaction, this supersonic jet impinges on the test article in a narrow horizontal region below the incident shock, perhaps driving the parabolic streamlines away from the leading edge.

The upper horizontal line appears to be located near the upper edge of the region of varying density in the flow in front of the test article above the incident shock. This line may be due to a vortex roll-up at the leading edge caused by two opposing flows meeting with the upper flow moving down and lower flow moving up. This vortex is seen as a density fluctuation in the preceding schlieren images. The region above the second horizontal line in both images does not appear to be affected much by the flow, which suggests the region of varying density near the test article surface is below this line on the leading edge.

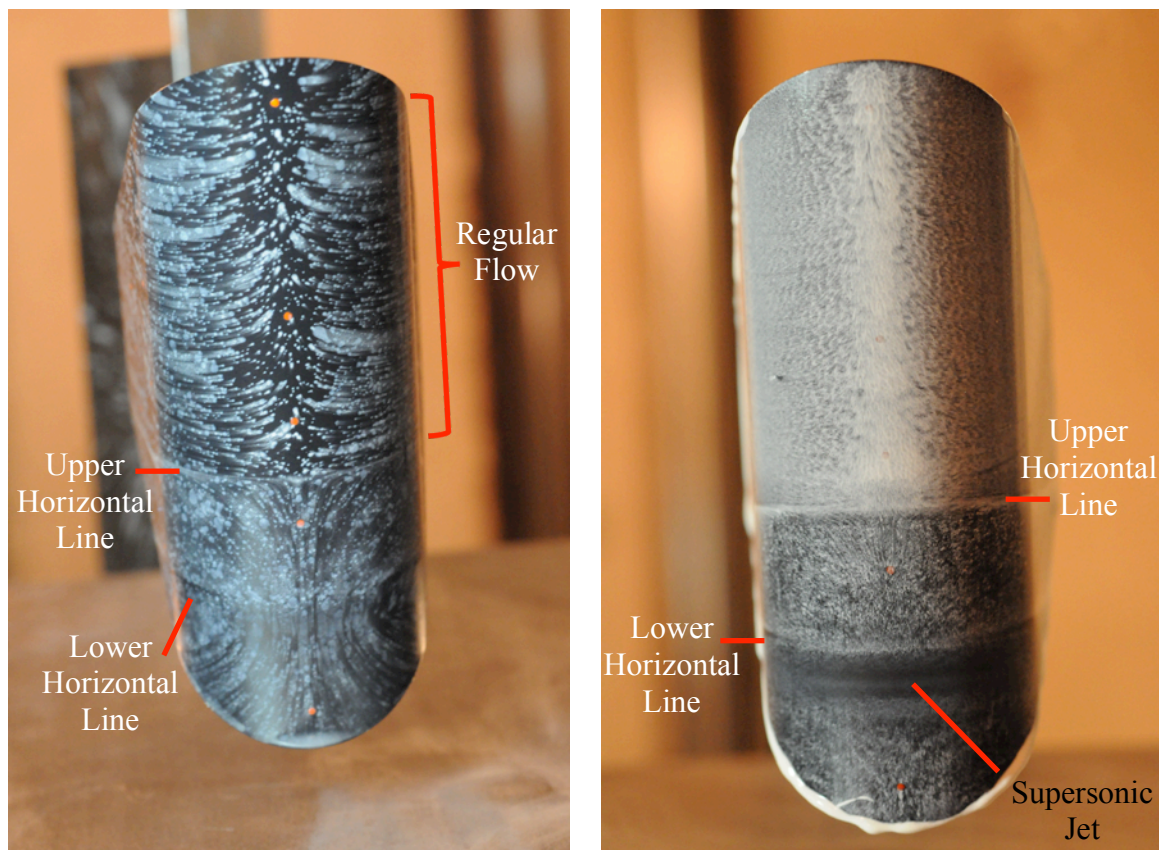


**Figure 5-22.** Leading-edge oil-flow images for the 0.75 in-radius metal test article at a  $-15^\circ$  AoA (using the two oil-flow techniques: dots in the left image, full coating in the right image).

The oil flow images in Figure 5-23 reveal the side view of the 0.75 in-radius test article. A triangular shape in the middle on the side of the test article, both in the streamlines in the left image and in the displaced oil covering in the right image, indicates the unsteadiness in the region above the incident shock also wraps around the surface of the test article, affecting the surface flow (and the surface heat transfer as is discussed in a later section). The vortex in front

of the leading edge likely continues along the sidewall but splits up into this “v-shaped” or triangular region.

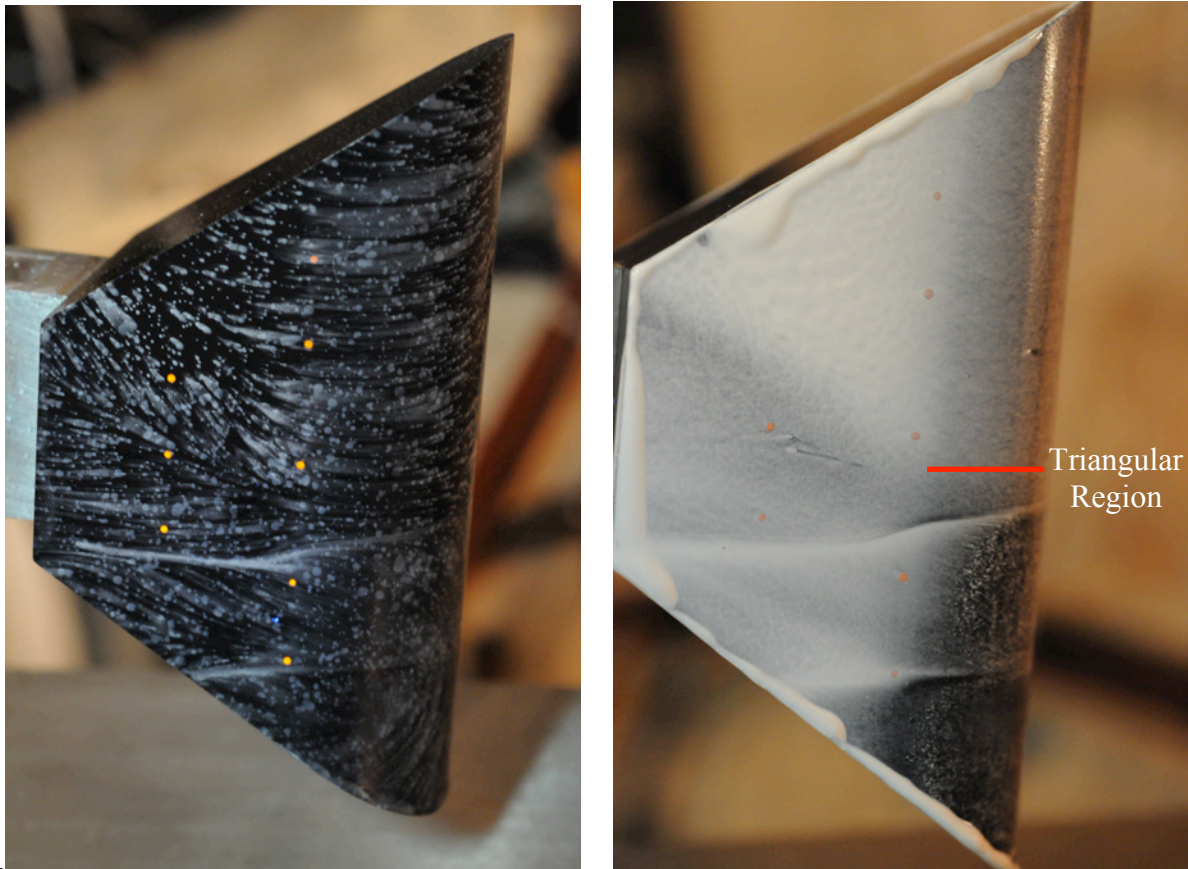


**Figure 5-23.** Side oil-flow images for the 0.75 in-radius metal test article at a  $-15^\circ$  AoA (using the two oil-flow techniques: dots in the left image, full coating in the right image).

#### 5.1.2.3. Fin sweep of $-25^\circ$

Figure 5-24 shows a Type III interaction for the 0.25 in-radius test article at a  $-25^\circ$  AoA. The zoom schlieren image obtained at 1600 fps for this case does not provide additional information and, therefore, is not included in this section. In the Type III interaction, the supersonic jet of the previous two interaction types is replaced with a shear layer that attaches to the surface of the test article. Supersonic flow exists in the triangular region between the turned bow shock and the shear layer in the image [2]. Although the shear layer attachment point is not clearly evident in the zoom schlieren images, the shear layer leaves the triple point with the incident and bow shocks at the appropriate angle to connect to the test article surface at the same location as the reflected shock. An unsteady region between the test article surface and the shear layer near the attachment point contributes to the difficulty in capturing the shear layer attachment in a still image, as is shown in later experimental and numerical schlieren images. As for Type IV interactions, the shock around this test article angled at  $-25^\circ$  does not interact with the flat plate boundary layer upstream of the test article.

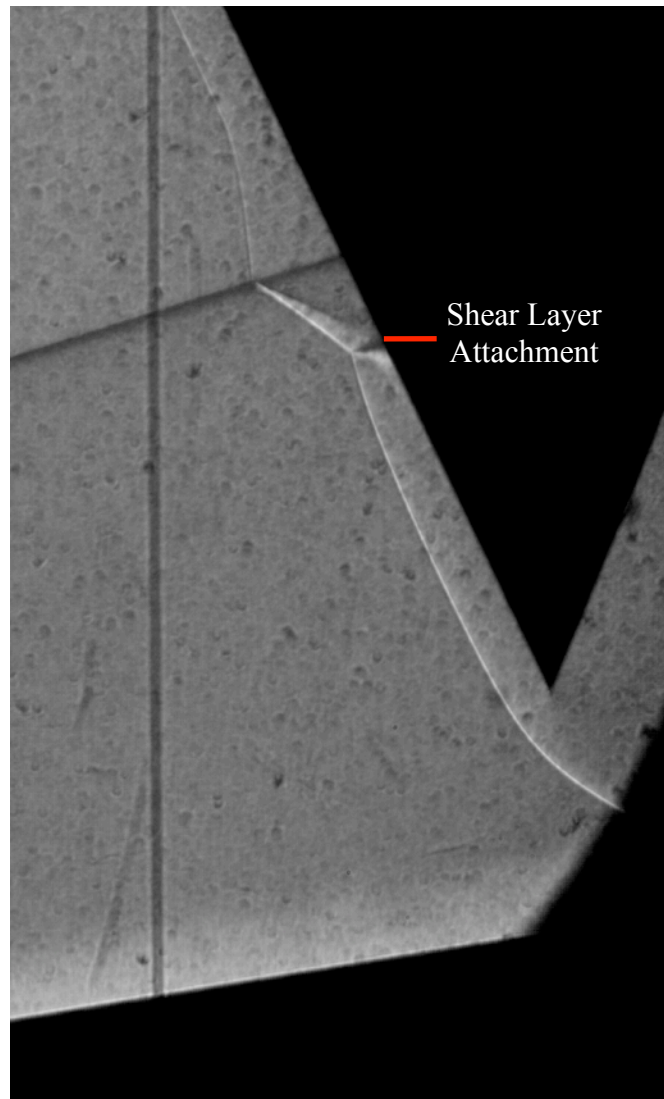


**Figure 5-24.** Zoom schlieren (1000 fps) image of a Type III shock-interaction for the 0.25 in-radius test article angled at a  $-25^\circ$  AoA.

The Type III interaction is further represented by the images in Figure 5-25 and Figure 5-26 for a 0.50 in-radius test article at a  $-25^\circ$  AoA. The plumb bob was moved to a better location away from the shock interaction between the runs represented by the two images. Both images faintly show a density gradient between the upper shear layer and the test article surface (visible in the image as a slightly lighter region) that changes the shape of the shear layer and the interaction during the run. This density gradient that interacts with the shear layer is also labeled in Figure 5-6. Only the zoomed-out image in Figure 5-25 shows the density gradient behind the test article from the shock interaction wrapping around the test article. This density gradient is marked since this gradient is visible in the zoom schlieren videos but is less distinctive in the image. The shock around the test article interacts with the flat plate boundary layer at a position slightly behind the tip of the test article, which does not appear to change the features in the shock-shock interaction.



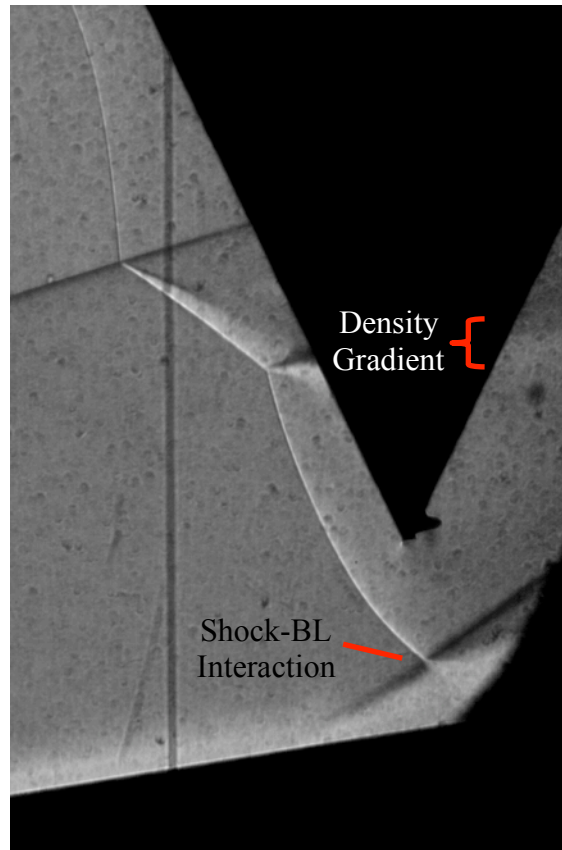


**Figure 5-25.** Zoom schlieren (1000 fps) image of a Type III shock-interaction for the 0.50 in-radius test article angled at a  $-25^\circ$  AoA.

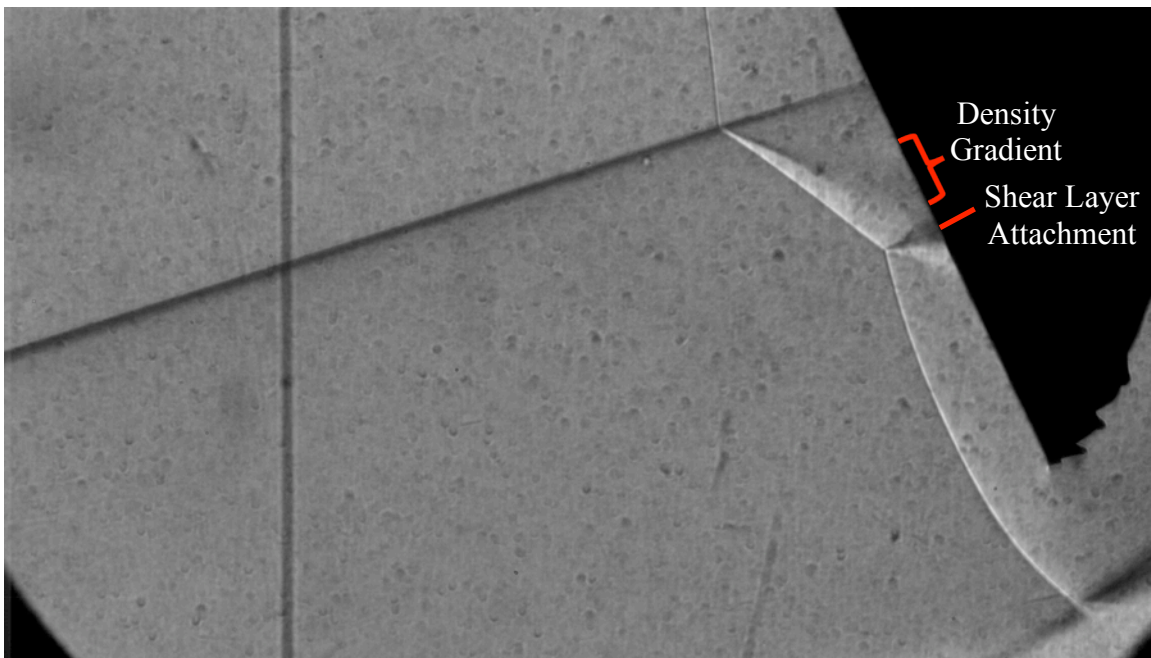


**Figure 5-26.** Zoom schlieren (1600 fps) image of the 0.50 in-radius test article at a  $-25^\circ$  AoA.



The larger bow shock standoff distance for the 0.75 in-radius test article at a  $-25^\circ$  AoA causes the shock-boundary layer interactions to occur upstream of the test article leading edge for a separation distance of only 0.5 in between the fin and the flat plate. A triangular density gradient is produced above the initial shock-BL interaction that is faintly visible in the image but is clearer in the schlieren videos. The origin of this density gradient is shown in the figure. This density gradient moves around during the run and at times appears to come into contact with the tip of the test article, potentially interfering with the already unsteady Type III shock-shock interaction.

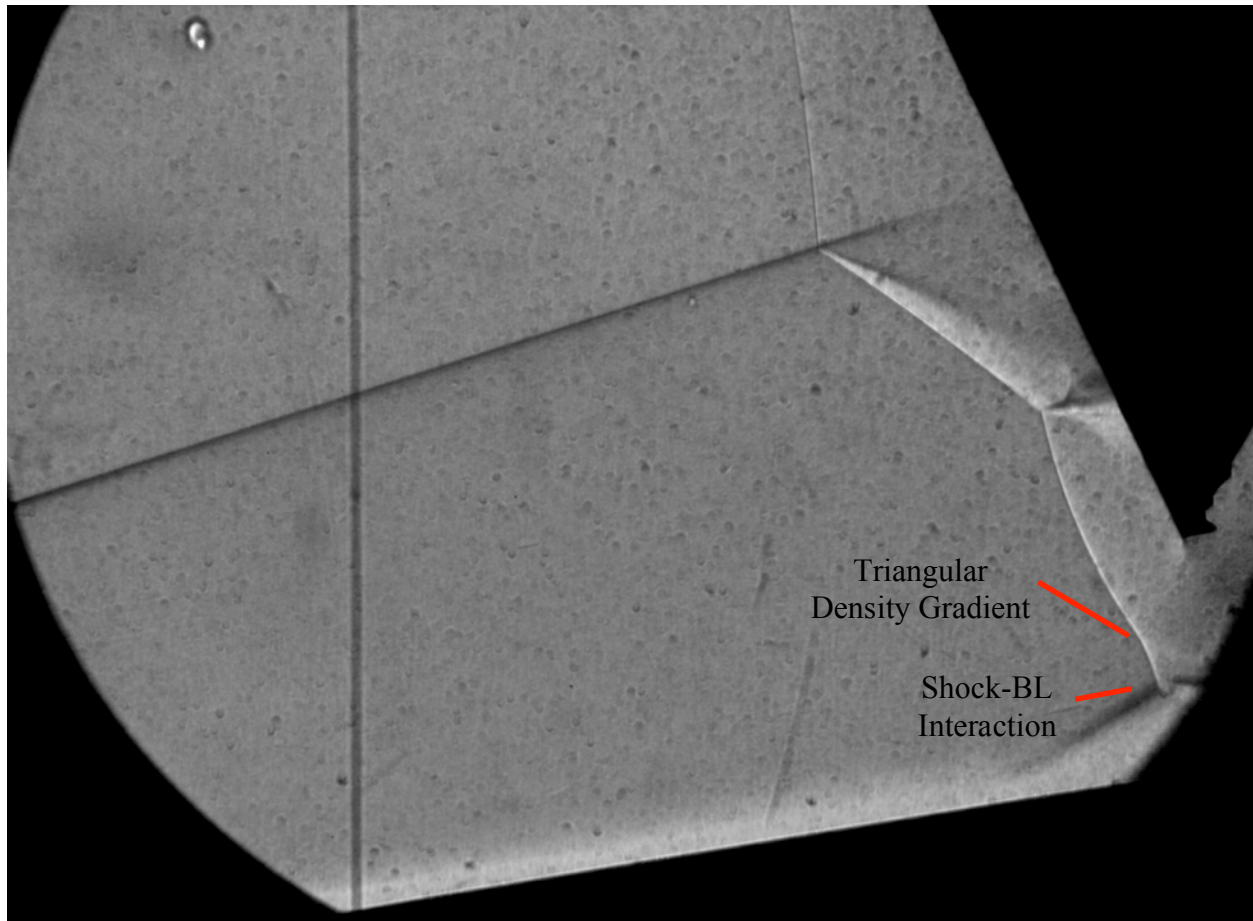


**Figure 5-27.** Zoom schlieren (1000 fps) image of a Type III shock-interaction for the 0.75 in-radius test article angled at a  $-25^\circ$  AoA.

For the test article with a 0.75 in-radius cylindrical leading edge at a  $-25^\circ$  AoA, the tip of the test article was raised to 0.75 in above the plate for a couple of the runs. This new test article location is shown in Figure 5-28. The new test article position moved the shock-BL interactions downstream of the tip of the test article. The reflected shock and shear layer impingement location were also affected. As the figure shows, the shear layer impinges on the test article very close to the lower tip of the leading edge so that edge effects are no longer negligible. Thus, the 0.75 in-radius test article was kept 0.5 in above the flat plate SG for the heat transfer wind tunnel runs in the current study, and the possible effects of the shock-BL interaction were noted.

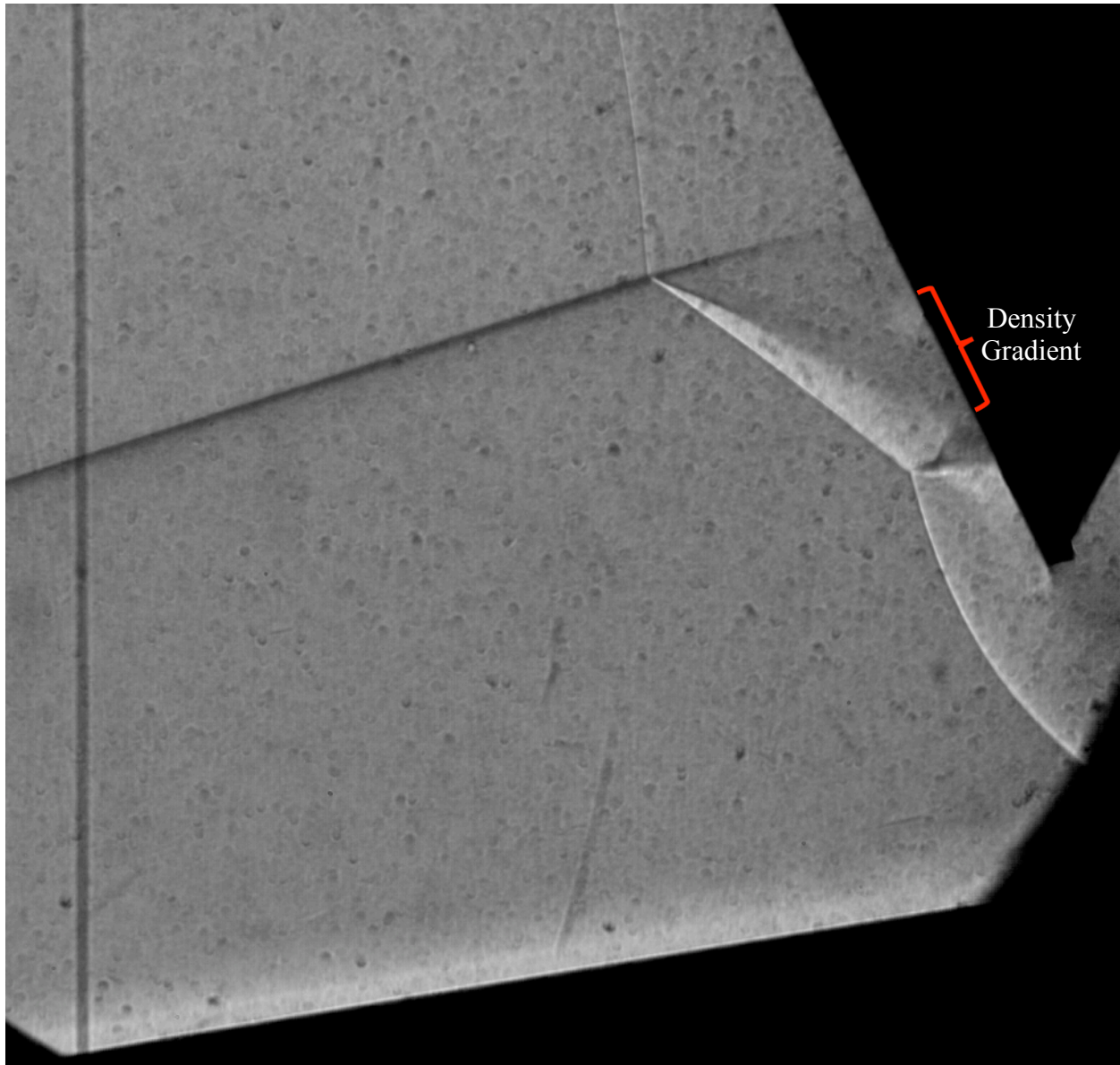


**Figure 5-28.** Zoom schlieren (1000 fps) image of the 0.75 in-radius test article at a  $-25^\circ$  AoA raised to a height 0.75 in above the flat plate SG.

The merged images in Figure 5-29 show the arrangement of the illuminated fiducials on the 0.5 in-radius test article at a  $-25^\circ$  AoA. Diagrams of the fiducial patterns on this test article are available in Appendix B. The relationship between the bottom two fiducials on the leading edge and in the leftmost column on the side of the test article is the same as for the other two test article geometries; the second fiducials from the bottom are horizontally aligned and the bottom fiducial in all three columns are arranged in a straight, slanted line. Thus, the upper shear layer, the incident shock, and the reflected shock of the Type III interaction impinge on the test article surface between the first and second fiducials from the bottom on the leading edge.

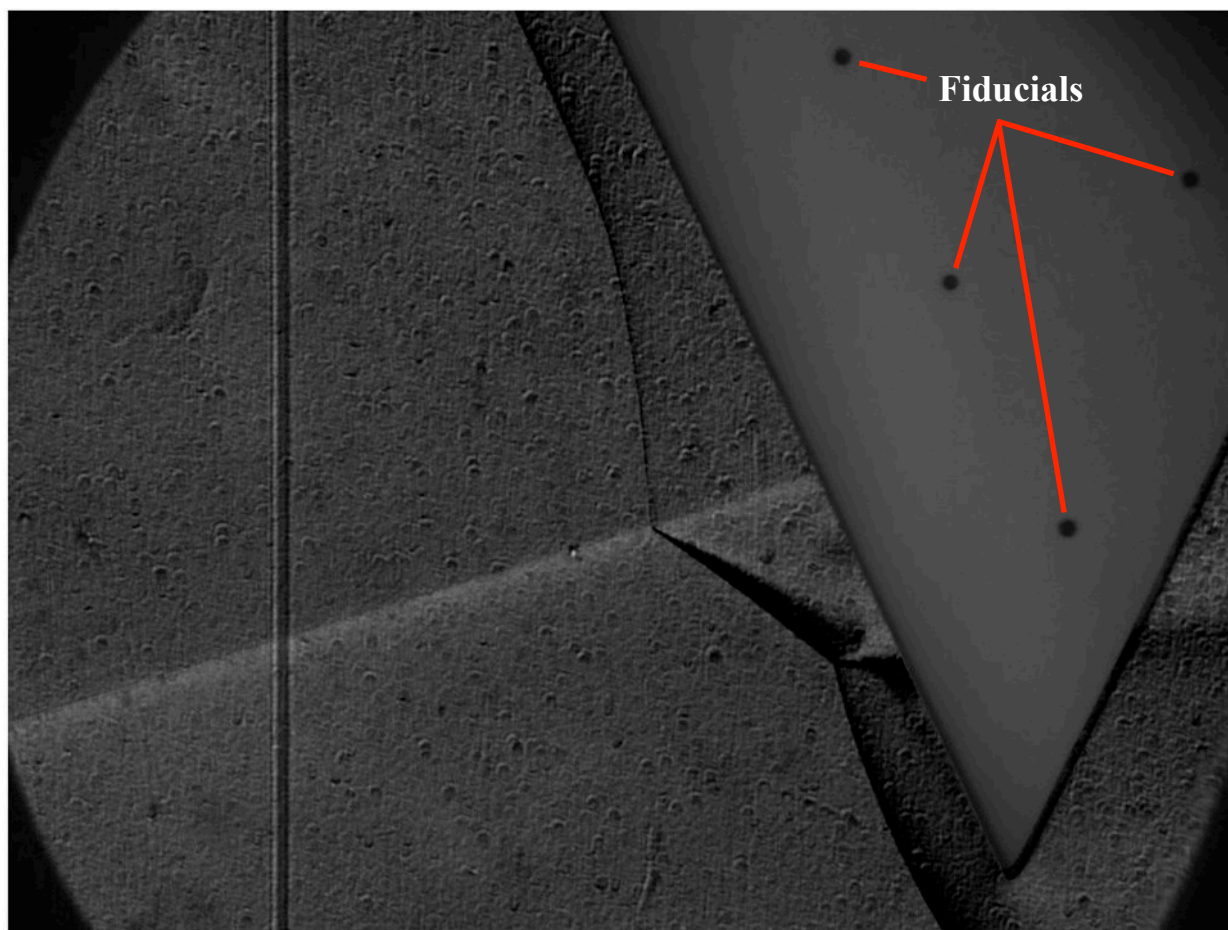


**Figure 5-29.** Phantom 12 (7900 fps) zoom schlieren image overlaid with fiducials for the 0.5 in-radius test article at a  $-25^\circ$  AoA.

The Type III shock-shock interaction mainly affects the leading-edge streamlines near the extreme lower tip of the test article as shown in Figure 5-30 for the 0.75 in-radius test article. The streamline behavior for this test article is similar to the patterns observed on the 0.25 in- and 0.50 in-radius test articles, although the shock-interaction region occurs higher on the leading edge in those cases. The pattern in the interaction region also resembles the oil flow streamlines obtained in a Type III interaction for a 1.18 in wide flat plate in [2]. As in the  $-15^\circ$  AoA oil flow images, the streamlines near the top of the leading edge in both images follow a curved path down and out from the stagnation region rather than horizontally out from the stagnation line as in the  $0^\circ$  AoA case. The streamlines for a  $-25^\circ$  AoA move farther downward than for the  $-15^\circ$  case, as expected, since the bow shock is angled farther forward so that the flow crossing the shock turns down at a sharper angle.

The shock-interaction region near the bottom of the test article produces a stagnation region below the shear layer attachment point from which the streamlines on the leading edge fan out as shown in the left image obtained using dots of oil. The motion of the flow above and below the shear layer impingement location as demonstrated in the experimental schlieren (and later in this chapter with the numerical results) agrees with the orientation of these streamlines.



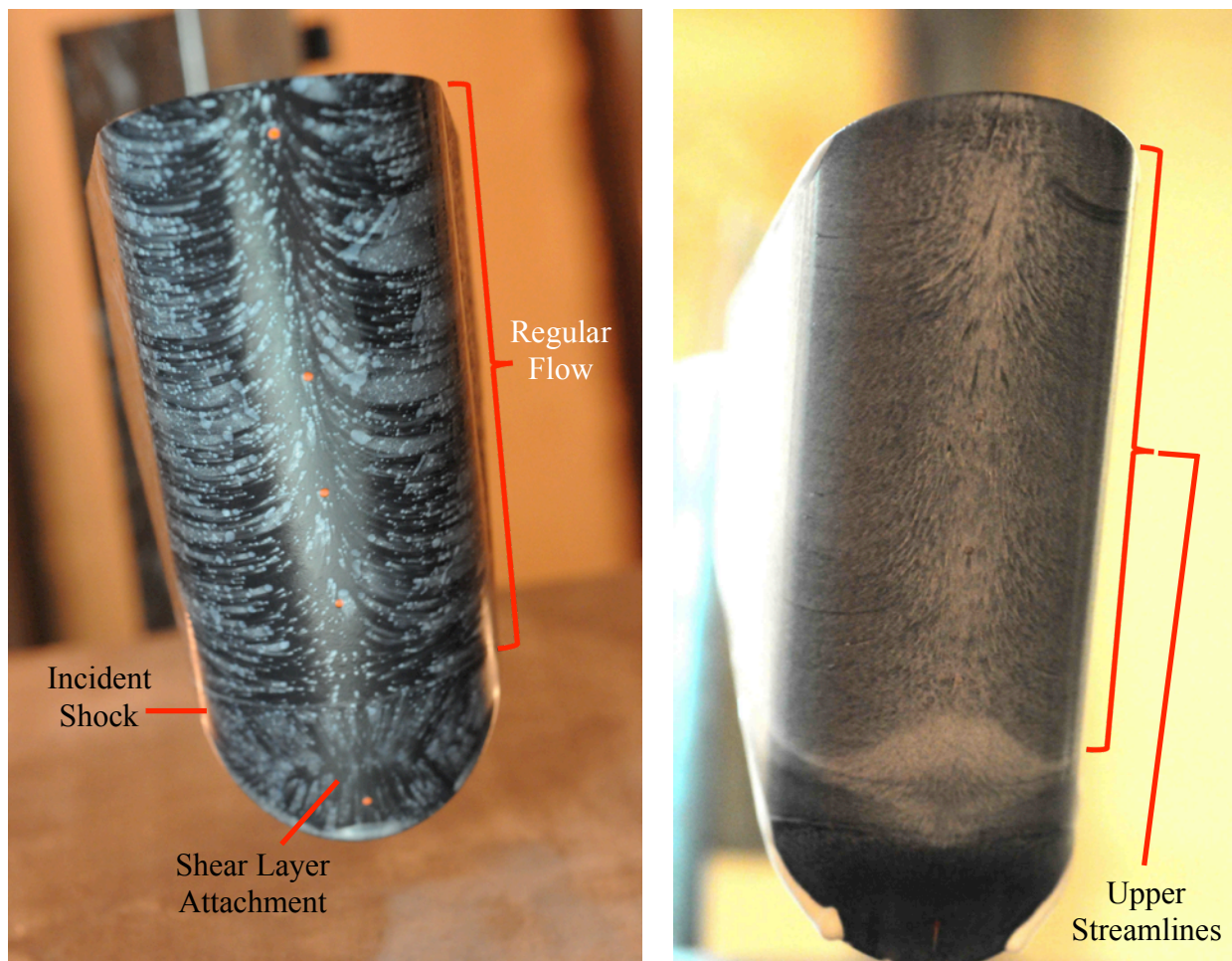


**Figure 5-30.** Leading-edge oil-flow images for the 0.75 in-radius metal test article at a  $-25^\circ$  AoA (using the two oil-flow techniques: dots in the left image, full coating in the right image).

The edge of the interaction region due to the shear layer attachment is evident as a horizontal line on the leading edge of the test article that wraps around to the side of the test article as shown in both images in Figure 5-31. This line is referred to as “incident shock” in the images in Figure 5-30 and Figure 5-31 as a reference to the approximate location where the incident shock would impinge on the leading edge in the absence of the bow shock. In the presence of the bow shock, the incident shock likely wraps around the bow shock and only the resulting shock-shock interaction interacts directly with the test article within the bow shock.

In the 2D schlieren image, the planar incident shock shows up as a line. Thus, the relationship between the incident shock and the bow shock, specifically whether or not the incident shock continues through the bow shock to impinge on the test article and affect the oil flow results, is not readily discernible. However, later discussions of the heat transfer behavior of the shock-shock interactions in section 5.2 and the LAURA CFD results in section 5.3 suggest the incident shock does not continue through the triple point to directly impinge on the test article but instead wraps around the bow shock.

The oil flow images in Figure 5-31 were captured at an angle rather than horizontally. Therefore, the “incident shock” line in the images appears to be angled downward but instead should be roughly horizontal. The streamlines in the lower part of the side view of the oil dots image turn upward slightly as the flow approaches the back of the test article. This behavior is reasonable since the schlieren images and videos indicate a density gradient behind the test article in approximately that location that is likely due to the shock interaction or associated vortices in the region below the incident shock traveling around the test article.

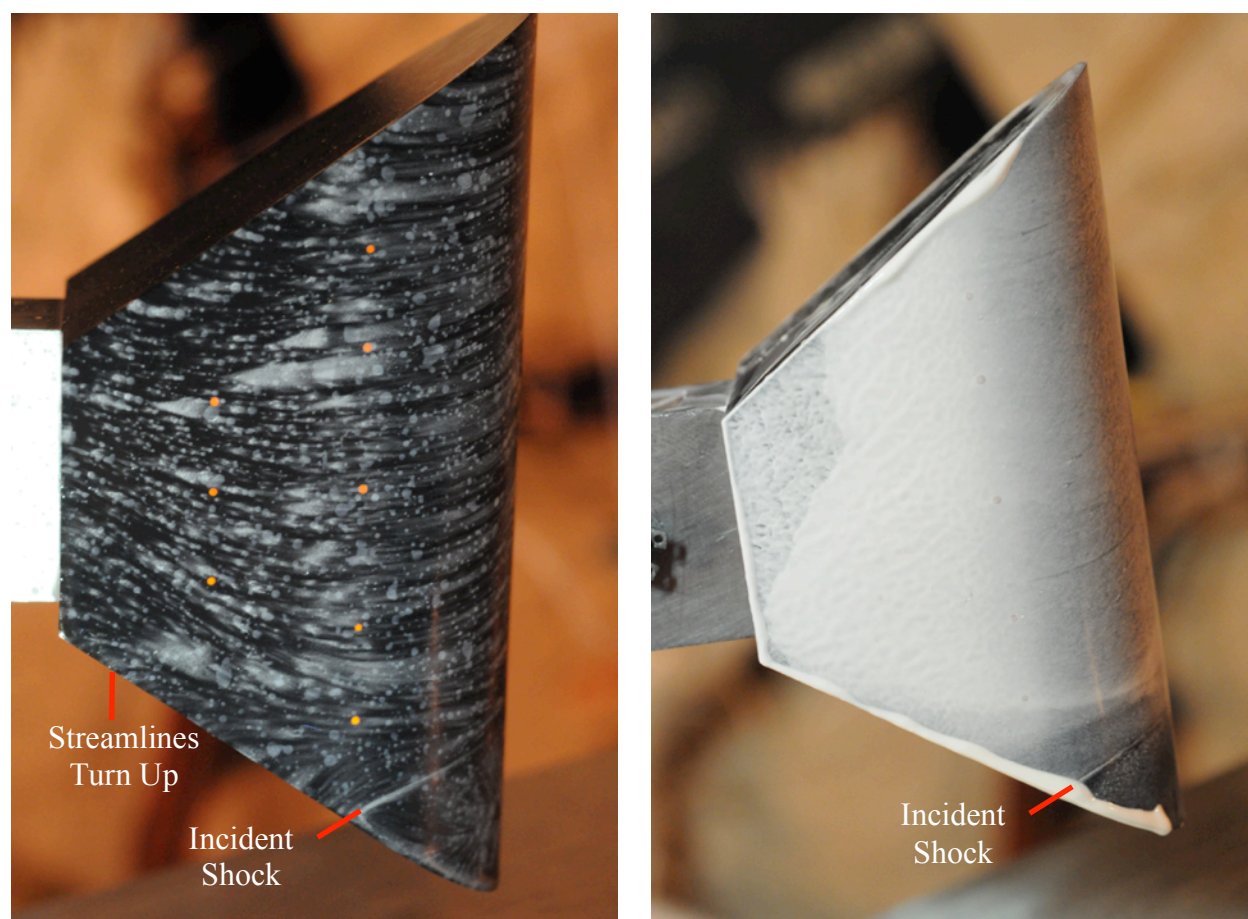


**Figure 5-31.** Side oil-flow images for the 0.75 in-radius metal test article at a  $-25^\circ$  AoA (using the two oil-flow techniques: dots in the left image, full coating in the right image).

### 5.1.3. SG angle of $6^\circ$ (Test 6976)

A few runs in Test 6976 were conducted with the SG angled at  $6^\circ$  to the flow to observe the corresponding change in the Type III and IV shock-shock interactions. As expected, the features in these shock-shock interactions are less distinct and, thus, less distinguishable since the parameters of the flow behind the incident shock do not differ as drastically from the free-stream flow as for the  $9^\circ$  SG runs (see Table 5-1). The incident shock angle in these images is about  $14.0^\circ$  above horizontal. Although the incident shock angle is less than for the  $9^\circ$  SG angle, the shock impinges on the test article in a higher location since the flat plate is only angled at  $6^\circ$

instead of  $9^\circ$  and the height of the tip of the test article is still 0.5 in above the flat plate. The schlieren images from these runs are included for reference in the following sections.

#### 5.1.3.1. Fin sweep of $0^\circ$

The Upilex® test article is shown at a  $0^\circ$  AoA in a Type IVa interaction in Figure 5-32. The interaction below the incident shock, including the shear layer that curls up from a supersonic jet, is not clearly distinguishable in this image or in the schlieren videos because the incident shock and resulting shock-shock interaction are not spaced far enough apart. The bow shock above the incident shock is also not as clear in this image as in the  $0^\circ$  AoA case for the  $9^\circ$  SG case. The bow shock does not interact with the boundary layer over the flat plate ahead of the test article.

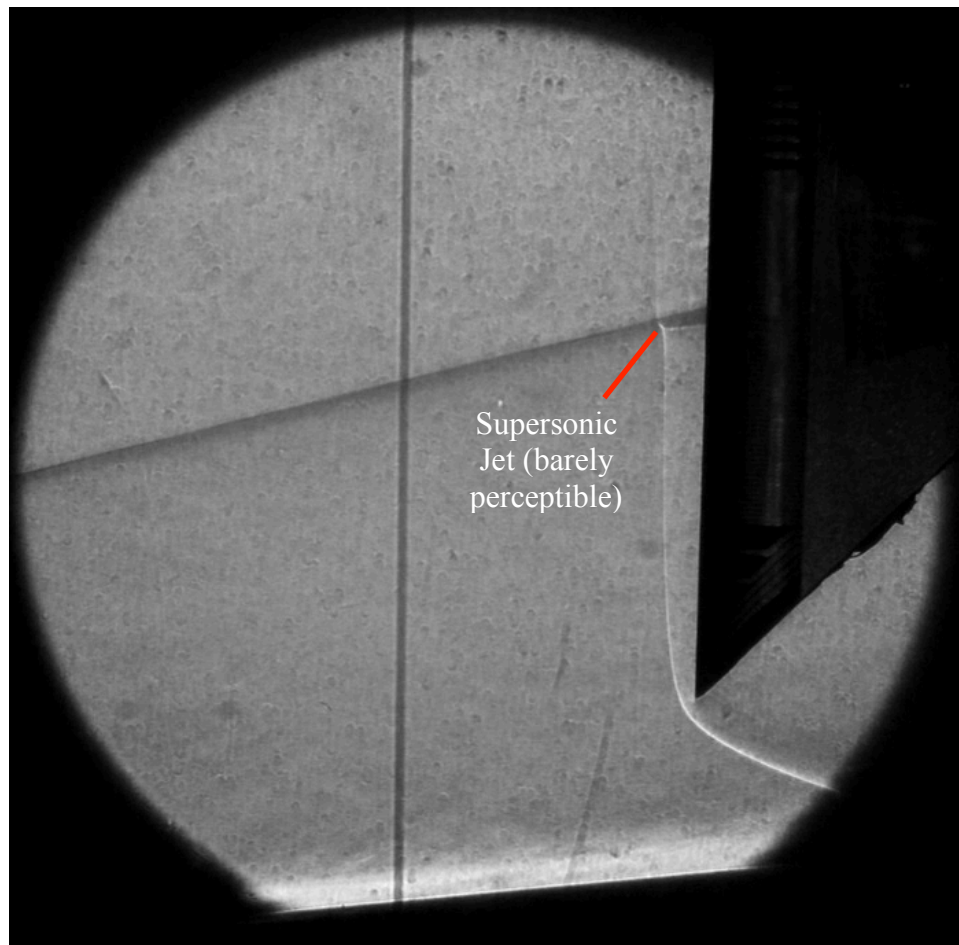


**Figure 5-32.** Zoom schlieren image of the Upilex® test article at a  $0^\circ$  AoA with a  $6^\circ$  SG angle (recolored with saturation: 0%; brightness: +40%; contrast: +20%).

#### 5.1.3.2. Fin sweep of $-15^\circ$

The supersonic jet is visible in the image of the Upilex® test article at a  $-15^\circ$  AoA in Figure 5-33, but the expected region of varying density above the shock-shock interaction appears to shrink relative to the size of this region in the  $9^\circ$  SG cases. This density gradient also moves



closer to the incident shock and, thus, is not very noticeable in this image. A density gradient behind the test article from the shock-shock interaction wrapping around the fin is also not distinguishable in this image, perhaps because the change in fluid density is too small to provide sufficient contrast due to the less significant change in fluid properties across the weaker incident shock. The supersonic jet appears to be angled further downward in this case than for the configurations with a  $9^\circ$  SG angle, which could be related to the errors in setting the test article angle of attack for Test 6976 that were discovered after the wind tunnel runs were completed.

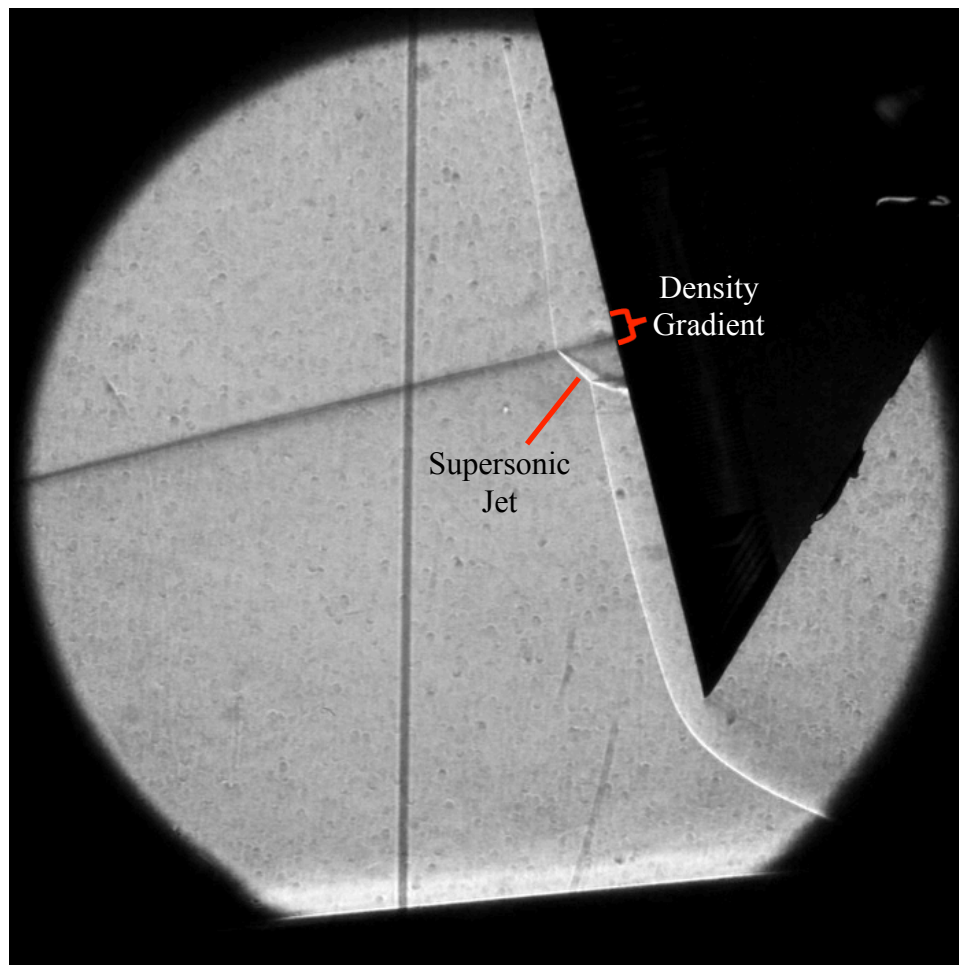


**Figure 5-33.** Zoom schlieren image of the Upilex® test article at a  $-15^\circ$  AoA with a  $6^\circ$  SG angle (recolored with saturation: 0%; brightness: +40%; contrast: +20%)

#### 5.1.3.3. Fin sweep of $-25^\circ$

Figure 5-34 shows the Type III shock-shock interaction for the Upilex® test article at a  $-25^\circ$  AoA. The upper shear layer attaches to the leading edge of the test article as expected. A faint pattern behind the test article indicates the density gradient described in the  $9^\circ$  SG cases that suggests the shock interaction wraps around the test article. Possible vortices between the bow shock and the test article surface below the shock-shock interaction are not clearly recognizable as separate from the pitting in the window of the wind tunnel.



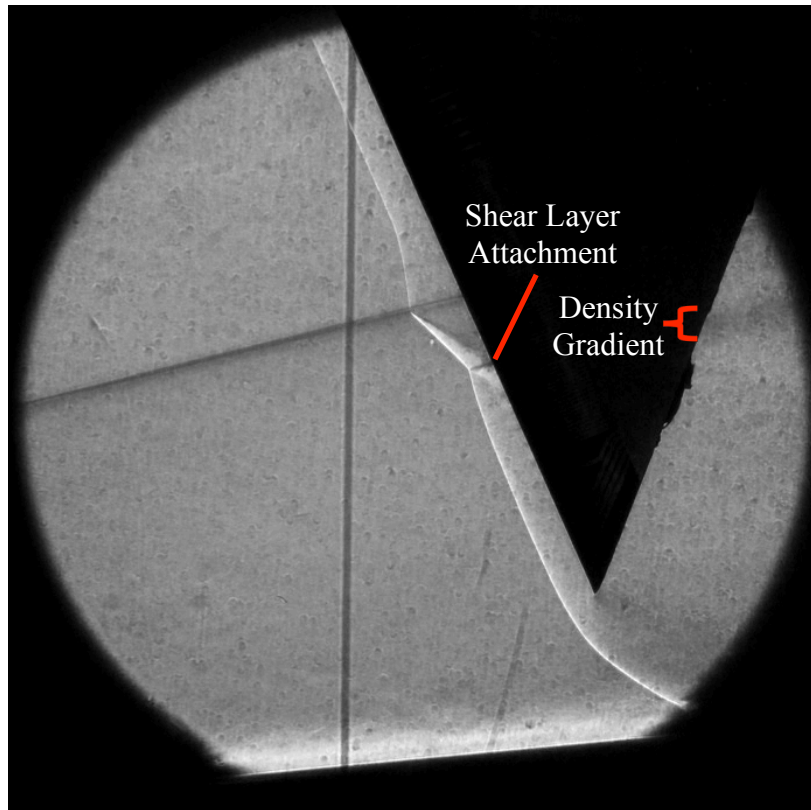


**Figure 5-34.** Zoom schlieren image of the Upilex® test article at a  $-25^\circ$  AoA with a  $6^\circ$  SG angle (recolored with saturation: 0%; brightness: +40%; contrast: +20%)

## 5.2. Heat transfer analyses

The heat transfer to the fused silica test articles is calculated using the methods described in Chapter 4. The peak temperatures in the shock-impingement region on the test articles exceeded the maximum limit of the phosphor thermography system early in the run for the Type III and direct Type IV shock-shock interactions. For that reason, the temperature data is reduced at two points in the run, both early and later in the run. In most cases, all the temperatures in the earlier line cuts were measured by the phosphor system. The earlier time shows the general trends in the heat transfer coefficients due to the different types of shock-shock interactions, while reducing the data at the later time shows the decrease in the magnitude of the coefficients (away from the peak) as the model heated up while at the tunnel centerline in the Mach 6 flow. These times are chosen based on the requirements for the 1D to 2D comparison for the Type IV shock interaction in Run 43, which is conducted at a lower Re number and, thus, yields temperature data later in the run for a case with a narrow peak and a strong temperature gradient.

The first selected time is Frame 54, which is at  $t = 1.8$  s after the beginning of the test article insertion sequence, equates to the seventh frame in the recorded 30 Hz data, and is soon after the test article reaches the wind tunnel centerline. In the temporal collapse for Run 43 in Figure 5-35, the maximum peak occurs at  $t = 1.8$  s. This temporal collapse includes zoomed-out data from every sixth frame (rather than all 151 frames) during a wind tunnel run at a  $Re = 1.1 \times 10^6/ft$  for a test article with a 0.25 in-radius at a  $-15^\circ$  AoA.

The second time chosen for data reduction is Frame 102, which is at  $t = 3.4$  s from the beginning of the run. This frame is just over halfway through the heat transfer portion of the run (which lasts 6.6 seconds). This frame yields the second largest peak in the temporal collapse in Figure 5-35 and is, thus, expected to yield a reasonable comparison between the 1D and 2D methods for Run 43.

The final frame selected for comparison in the 2D case is Frame 138, which is at  $t = 4.6$ s. This time and the previous two times are selected as bounds for the data reduction cases in the current study, because the phosphor thermography data is typically reduced in the frames between 102 and 138 for tests conducted in the 20-Inch Mach 6 Air Tunnel.

Analyzing the heat transfer at different frames would change the results for certain runs in the current study. For example, reducing the data slightly earlier in the run would yield a higher peak in the interaction region for a couple of cases by avoiding data loss in the leading-edge line cut. However, the heat transfer is analyzed using the temperature data from the same frames in every run to provide a consistent comparison between the trends in the heating profiles for each shock-interaction type and test article nose radius. The x-axis in the heat transfer plots is labeled  $x/L$ , which corresponds to the spatial location ( $x$ ) at which the heat transfer coefficient is calculated relative to the full length ( $L$ ) of the leading edge, which was 4in for each test article.

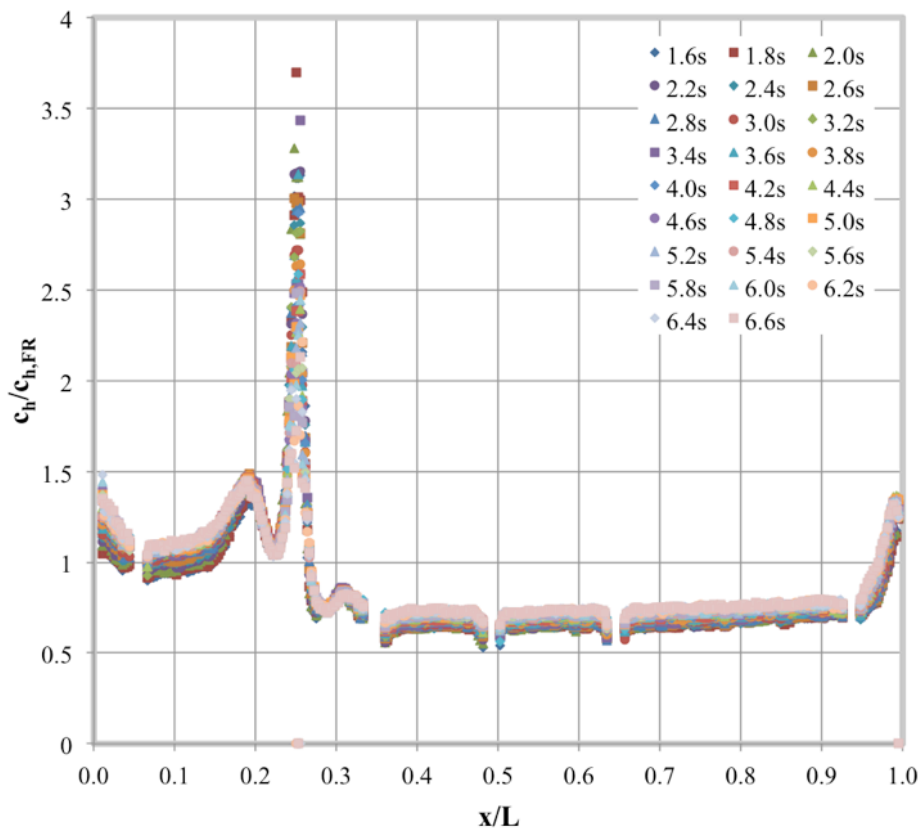


**Figure 5-35.** Temporal collapse of IHEAT  $c_h/c_{h,FR}$  for the 0.25 in-radius test article at a  $-15^\circ$  AoA with a  $Re = 1.1 \times 10^6/ft$  and using data from every sixth frame (every 0.2 s) during the run.

A similar graph in Figure 5-36 shows the change in heat transfer coefficients derived from the 2D FV code at five specified locations along the leading edge. In previous studies, the FV methods were observed to yield heat transfer coefficients that initially overshoot the final approximate value before nearly leveling out later in the run [37]. Therefore, the behavior of the heat transfer coefficients in time based on the FV code assumptions was considered in addition to the IHEAT temporal collapse.

The locations  $i = 75$  and  $i = 100$  correspond to pixel indices for heat transfer coefficient positions on either side of the sharp peak for the Type IV shock-shock interaction. The change in  $c_h$  at  $i = 75$  and  $i = 100$  is likely tied to the decrease in the peak during the run rather than an error associated with the FV code. The remaining indices are arbitrary positions along the leading edge above the shock-shock interaction and away from the end of the test article and the fiducial marks. The trend in  $c_h$  at these locations is relatively level over time rather than decreasing. This behavior suggests the predicted overshoot of the calculated heat transfer due to the assumptions in the FV conduction codes occurs before the test article reaches the wind tunnel centerline (at about 1.6 s). Therefore, reducing the heat transfer data early in the run (around 1.8 s) should not yield additional errors in the FV outputs compared to the results from IHEAT.

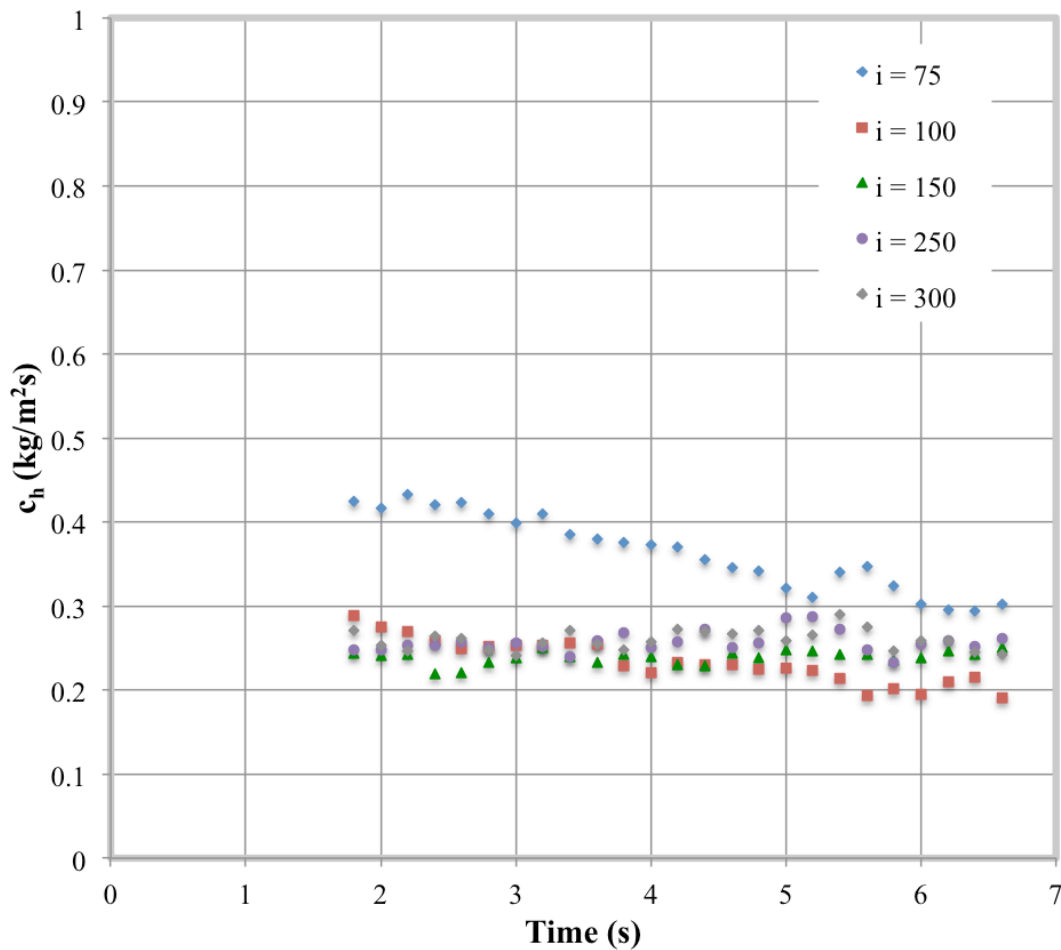


**Figure 5-36.** Enthalpy-based heat transfer coefficients from the 2D FV code at different locations (specified by the IHEAT pixel number) along the leading edge over time.

The data from Run 43 is used to check the grid convergence of the solutions from the 1D and 2D FV code used in the current study. The plots in Figure 5-37 and Figure 5-38 show the output heat transfer coefficients from the 1D and 2D codes, respectively, do not vary significantly as the number of volumes in the radial direction ( $nr$ ) is varied from 51 to 1001 for Run 43. The heat transfer coefficient variation between grids with less than or more than 101 volumes is only noticeable in the peak region and near the leading edge. A grid resolution with 1001 volumes in the radial direction is used in both the 1D and 2D FV codes for the 0.25 in-radius test article in the current study, although this number of volumes is much more than the required number to obtain a converged solution. The number of volumes utilized in the lateral direction ( $nz$ ) in the 2D code depends on the number of pixels for which temperatures are available for the leading edge line cut in any given run. A corresponding number of 2001 and 3001 volumes are used in the grids for the 0.50 in- and 0.75 in-radius test articles to maintain the same spacing  $\Delta r$  in the radial direction for all the test articles.

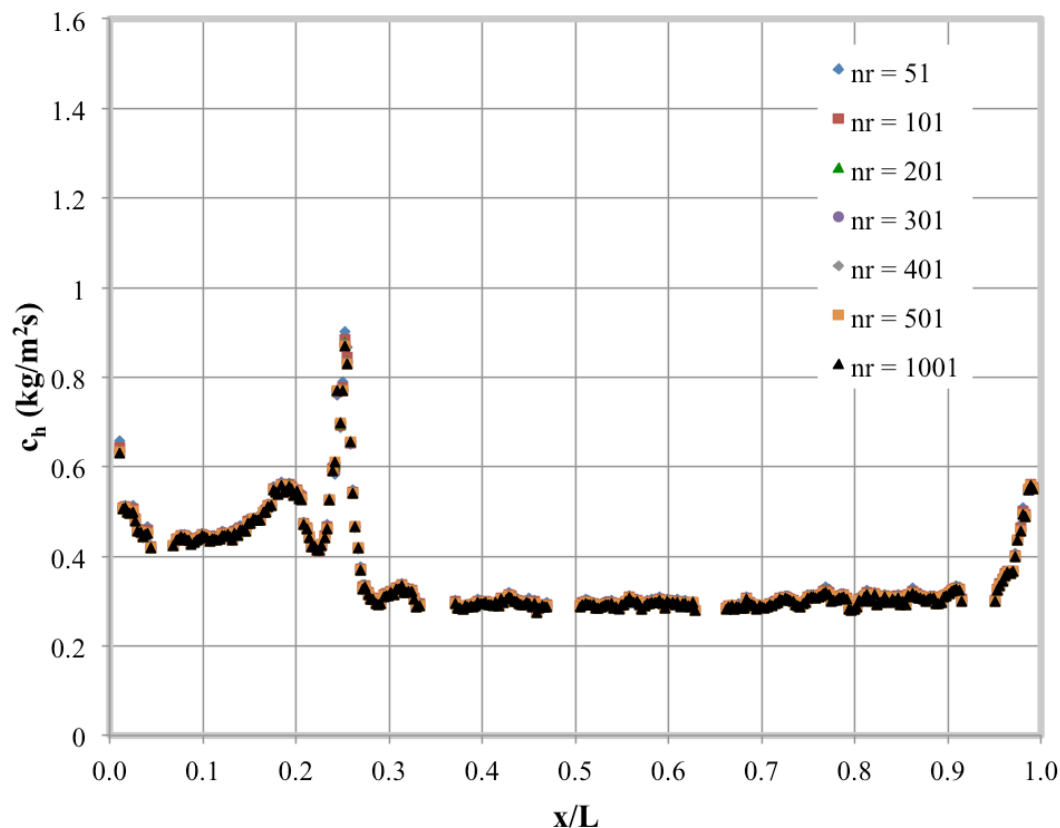


**Figure 5-37.** Grid convergence of the heat transfer coefficients along the leading edge of the 0.25 in-radius test article at a  $-15^\circ$  AoA ( $Re = 1.1 \times 10^6/ft$ ) and  $t = 4.6$  s for the 1D FV code.

Uncertainties in the phosphor thermography data depend on the rise in the test article surface temperatures. The following values of uncertainty are based on historical tests with a variety of types of test articles. On surfaces with a significant temperature rise ( $>70^\circ F$ ), uncertainties are in the range of  $\pm 10\%$ . For moderate temperature increases ( $20$ - $30^\circ F$ ), the uncertainties are roughly  $\pm 25\%$ . More information on phosphor thermography uncertainties are in references [4] and [5]. Error bars are not included in the following plots due to the density of the data in the line cuts.

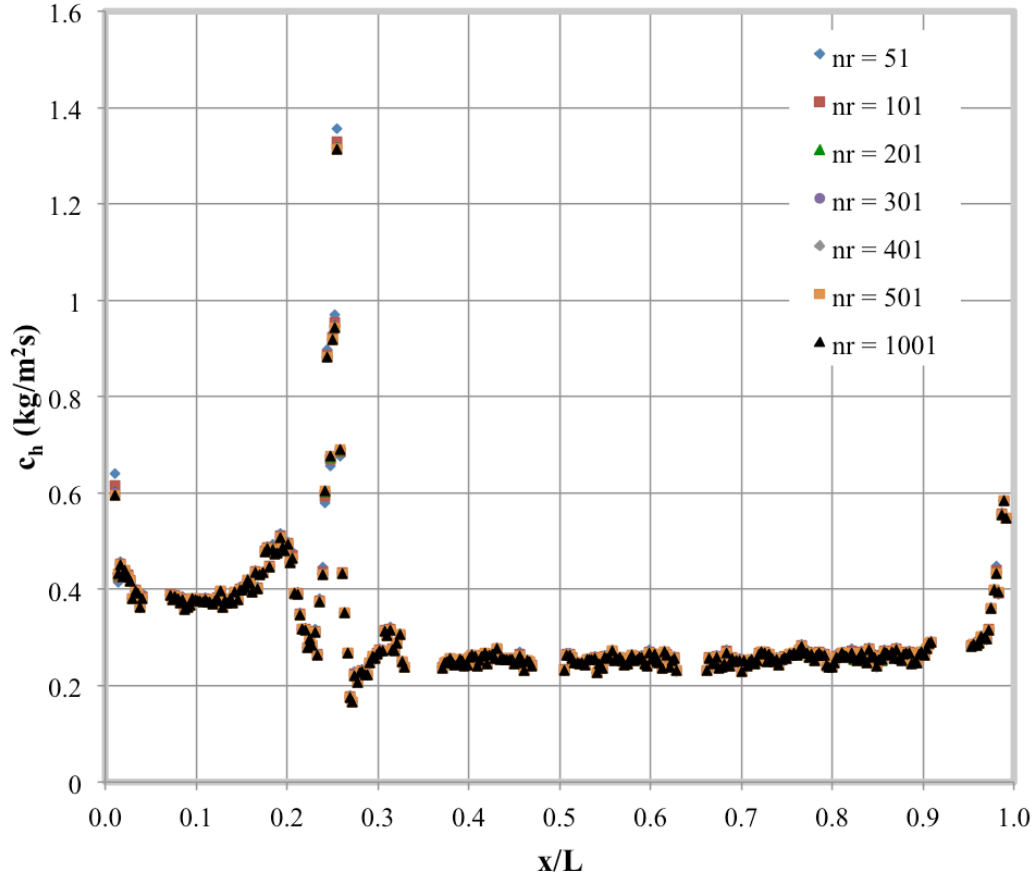


**Figure 5-38.** Grid convergence of the heat transfer coefficients along the leading edge of the 0.25 in-radius test article at a  $-15^\circ$  AoA ( $Re = 1.1 \times 10^6$ /ft) at  $t = 4.6$ s for the 2D FV code.

The following sections include contour maps of the 1D Fay-Riddell [32] non-dimensionalized heat transfer coefficients from IHEAT for the test articles at  $t = 1.8$  s into the run. Additional contour maps in Appendix C show the heat transfer patterns on the test articles at  $t = 3.4$  s, when the temperature data is also reduced to heat transfer coefficients. The images later in the run display similar heating patterns to the earlier images but also show empty (white) pixels along the leading edge where the test article temperature exceeds the maximum phosphor system limit. The limits on the color bar scale in each contour map are manually set between zero and three (unless otherwise stated) to enable direct comparisons between the different cases. This scale is selected to ensure the main features of the heat transfer pattern are visible for every test configuration, including the lower heating levels for test articles at a  $0^\circ$  AoA. Although  $c_h/c_{h,FR}$  exceeds three for a few wind tunnel runs, yielding a pink (over-scaled) shock-impingement region, the basic differences between the heating patterns are distinguished in these images. The contour maps provide a qualitative, visual reference to the heating pattern on each test article.

Quantitative heat transfer coefficients included in plots in the following sections are non-dimensionalized by an average of the coefficients in the region away from the peak heat flux, as described in section 4.2.2. Since different reference values were used to convert the heat transfer contour maps and the line cuts to non-dimensional data, the y-axis scale in the plots does not

directly correlate to the color bar on the contour maps. The gaps in the data from a line cut along the leading edge represent the fiducial mark locations. Five fiducials are used along the leading edge to align the test article vertically in the wind tunnel and to guarantee that at least two fiducial marks are visible when the camera is zoomed in on the shock-shock interaction region.

For some of the wind tunnel runs in which the camera is zoomed in on the shock interaction region, baseline heating data is not available, so the data is non-dimensionalized using the reference value from the zoomed-out run. To be consistent, each zoomed-in run uses the average value from the corresponding zoomed-out run as a reference value. The test article surface temperatures vary between runs, so this assumption yields lower non-dimensional peak heat transfer coefficients in some of the zoomed-in cases, as evidenced by the cases in which data outside the shock interaction region is available and is less than 1.0 as a non-dimensional value. Since the zoomed-in data for each configuration was obtained during a separate run later in the test, the incident shock impingement point differed slightly between runs. Thus, the  $x/L$  locations of the zoomed-in line cuts were offset to align the peaks between the two runs, while the zoomed-out data is shown for a position ( $x$ ) along the leading edge ( $L$ ) of the test article.

The phrase “incident shock impingement” in each plot refers to the location where the incident shock would hit the leading edge of the test article if the shock continued through the bow shock. This extrapolated location is seen in the schlieren images, but likely is not an actual impingement point since in several cases the heat transferred to the test article does not increase significantly in this location. Instead, this location typically corresponds to a valley or only a very small peak.

In each case, the heat transferred to the test article below the incident shock exceeds the baseline value since the flow temperature increases as air passes through the oblique incident shock. The temperatures in this region also increase more rapidly because heat is conducted down the leading edge from the shock-shock interaction region until the heat reaches the air surrounding the tip of the test article. Air has a low thermal conductivity (0.026 W/m-K at room temperature [50]). Thus, the conducted heat leaves the tip of the test article at a slower rate, causing the test article to heat up more in this region. Above the shock-shock interaction, the heat travels farther and diffuses more through the test article material before reaching the air (represented in the FV codes as an adiabatic boundary condition) surrounding the upper tip of the test article.

The peak heat transfer coefficients in the non-dimensional line cuts in the following sections follow an unusual trend. The peak heat transfer in the shock-shock interaction region increases with increasing leading-edge radius. This trend differs from the peak behavior in dimensional line cuts, in which the peak heat transfer increases as the leading-edge radius decreases, as expected. This reversal in the leading-edge radius effects occurs because the reference value used to convert the heat transfer coefficients to non-dimensional values changes in each run based on the baseline heating values away from the shock-shock interaction region for that specific run. As the leading-edge radius increases, this averaged reference value decreases, which amplifies the peak heat transfer value compared to the smaller test article geometries.

Non-dimensional heat transfer line cuts are used in the following sections to provide an estimate of the peak heating augmentation relative to the expected heat transfer for a given leading-edge radius. If a vehicle’s geometry is designed to handle the predicted heat transfer levels for known

hypersonic flow conditions, then the relative heating augmentation for the given geometry in the presence of a shock-shock interaction (if such an interaction may exist) is essential information that influences the design of the thermal protection system.

### 5.2.1. Fin sweep of $0^\circ$ and a $Re = 2.1 \times 10^6/ft$

The Type IVa shock interaction produced by a  $0^\circ$  AoA yielded the lowest peak heat transfer of the three interaction types considered in this study. Two small peaks of similar magnitude exist on either side of a trough in the heat transfer coefficients along the leading edge for this type of interaction.

#### 5.2.1.1. Leading-edge radius of 0.25 in

In Figure 5-39 and Figure 5-40, IHEAT contour maps of the heat transfer coefficients show zoomed-out (regular) and zoomed-in views of the heat transfer coefficients on the 0.25 in-radius test article at a  $0^\circ$  AoA. The non-dimensional heat transfer data along the leading edge is presented in Figure 5-41. The first peak, with  $c_h/c_{h,ref}$  approximately equal to 1.5 near  $x/L = 0.24$ , indicates the location of the incident shock impingement on the leading edge. Below that location on the leading edge, the heat transfer is relatively constant at approximately 1.4 relative to the baseline heating (defined as  $c_h/c_{h,ref} = 1$ , as shown in the region near the top of the leading edge from  $x/L = 0.5$  to  $0.9$ ). The shear layer above the reflected shock in this interaction attaches to the surface of the test article at a second peak of about 1.4 at  $x/L = 0.36$ . A trough exists between the incident shock and the shear layer attachment that corresponds to the blue gap between the two regions of higher heating near the bottom of the leading edge.

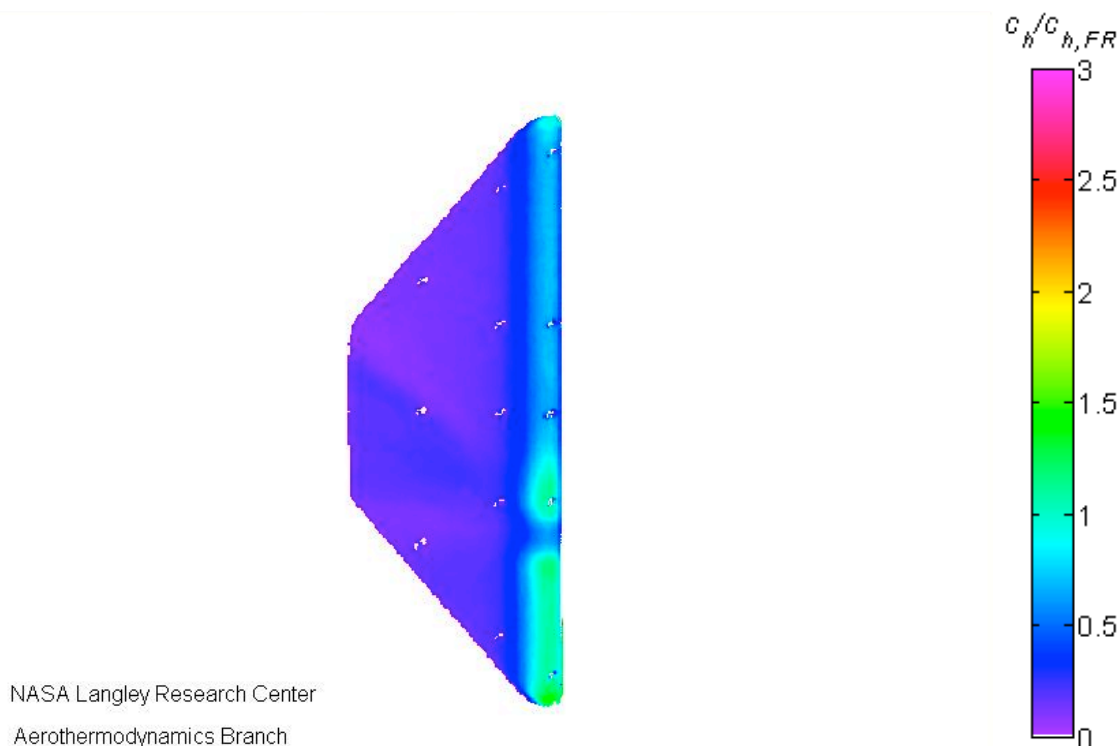


**Figure 5-39.** Run 39: IHEAT  $c_h/c_{h,FR}$  contour map for the 0.25 in-radius test article at a  $0^\circ$  AoA.



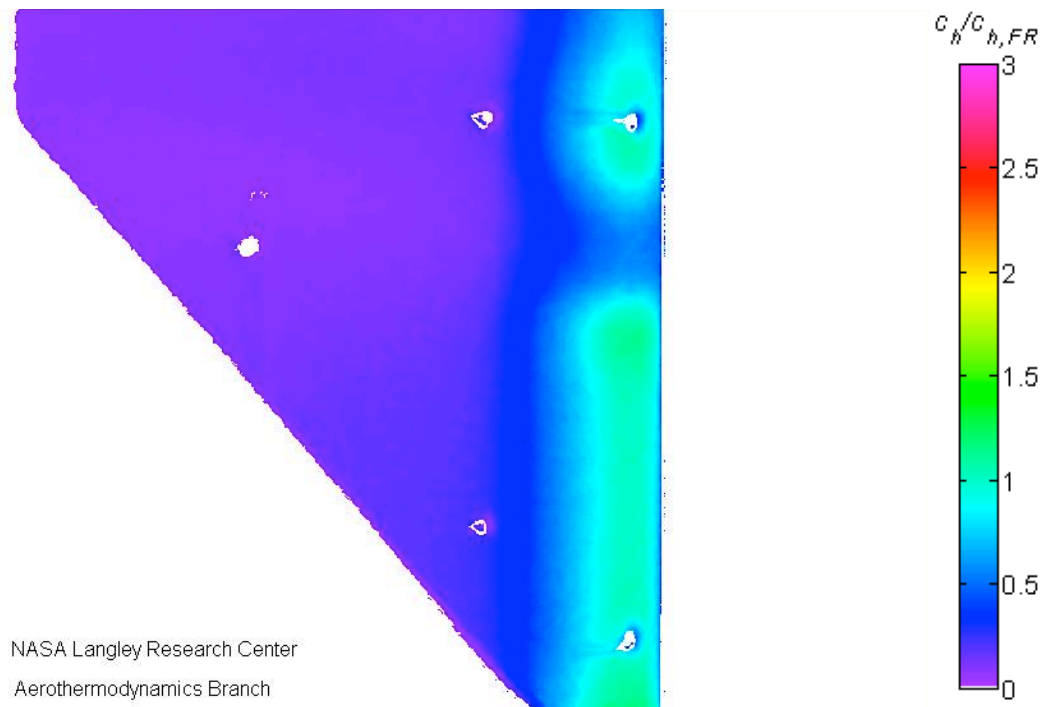


**Figure 5-40.** Run 47: IHEAT  $c_h/c_{h,FR}$  contour map for the 0.25 in-radius test article at a  $0^\circ$  AoA (zoomed in).

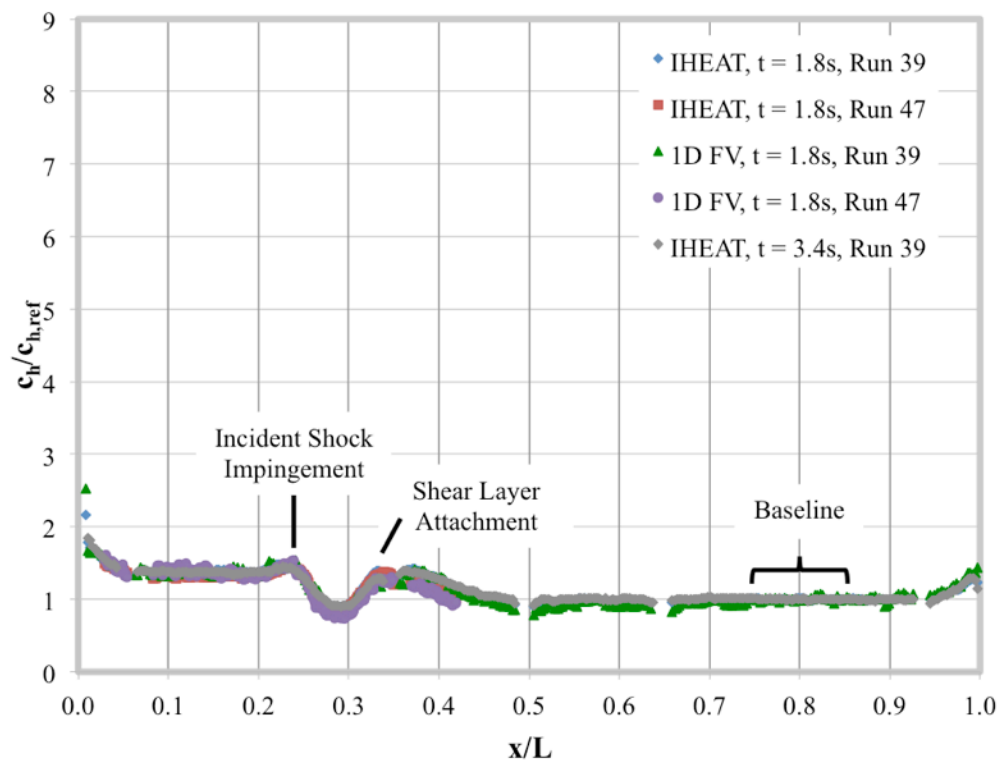


**Figure 5-41.** Non-dimensional heat transfer coefficients from the IHEAT and 1D FV codes for the 0.25 in-radius test article at a  $0^\circ$  AoA.

The plot in Figure 5-42 shows the heating trends for the Painted 1 and Upilex® test articles at a 0° AoA in Test 6692. The x-axis coordinates are labeled  $x/L_{Incident Shock}$  to indicate the heat transfer coefficients are positioned relative to the location of the incident shock impingement (at  $x/L_{Incident Shock} = 0$ ) to align the data from separate wind tunnel runs. This coordinate system is feasible for the runs from T6692 since the incident shock location can be correlated to a specific gage along the leading edge of the test article based on zoom schlieren images. This coordinate system is not viable in the current study, since the incident shock location relative to the fiducials could only be approximated for a few images in which the test article was illuminated.

The pattern in the Test 6692 data resembles the Test 6983 results. Non-dimensional heat transfer coefficients below the shock-shock interaction exposed to flow that passed through the incident shock are relatively level near 1.5 with a peak of about 1.6 near the incident shock impingement. Heating in the region above the incident shock drops slightly below 1.0 on this non-dimensional scale before rising to a peak of about 1.5 at the shear layer attachment point and then decreasing again to the level portion of the heating pattern above the shock interaction. The increased heating near the tips of the test article in Figure 5-41 is not included in Figure 5-42 since the ends of the Painted 1 and Upilex® leading edges are not instrumented with thin-film gages.

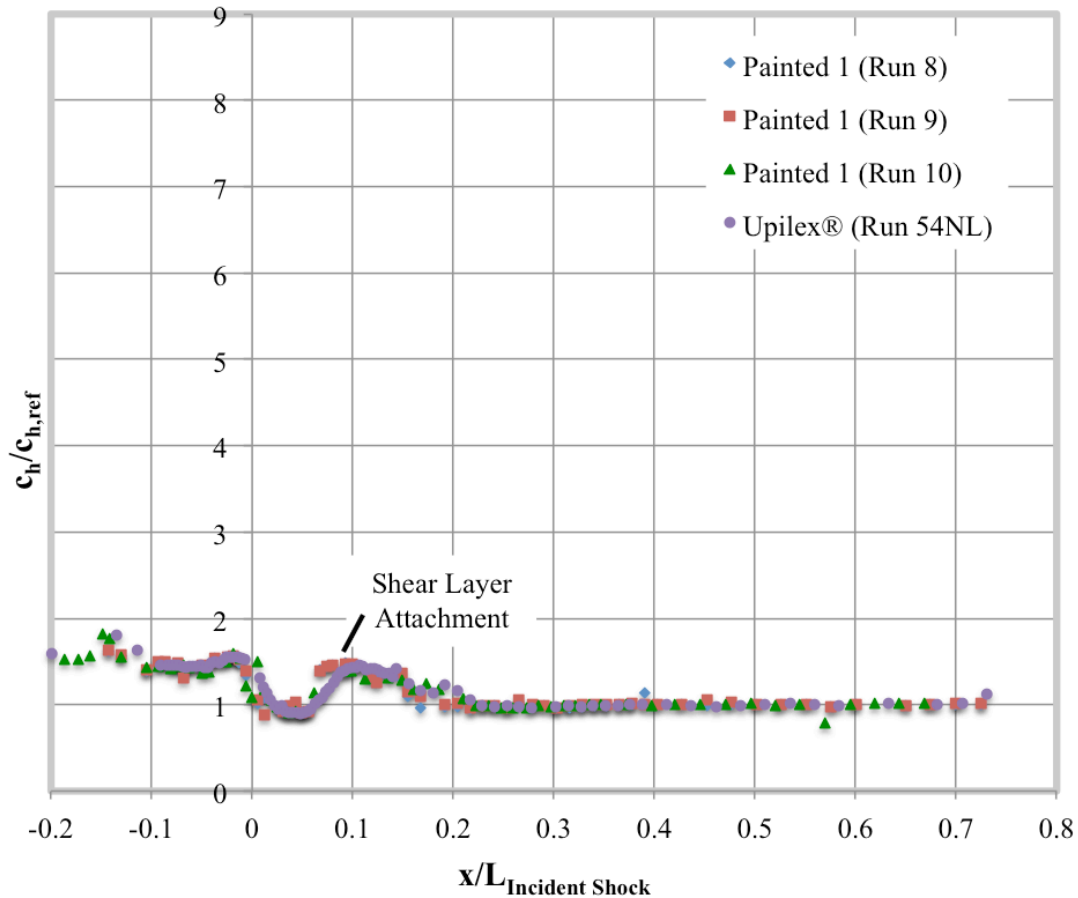


**Figure 5-42.** Non-dimensional heat transfer coefficients from the thin-film gages on the 0.25 in-radius Macor® Painted 1 and Upilex® test articles in Test 6692 at a 0° AoA (data used with Berry’s permission [8]).

### 5.2.1.2. Leading-edge radius of 0.50 in

Figure 5-43 shows the zoomed-out view of the 0.5 in-radius test article at a  $0^\circ$  AoA in Run 38, while Figure 5-44 and Figure 5-45 are zoomed-in views of the same test article from Runs 53 and 54. The line cut data in Figure 5-46 displays similar features to that for the 0.25 in-radius test article. The plot in Figure 5-47 demonstrates the repeatability of the heating pattern for this shock interaction between the two wind tunnel runs. The contour maps also resemble those for the 0.25 in-radius test article with broader heating regions at the incident shock impingement near  $x/L = 0.2$  and the shear layer attachment due to the larger nose radius. The heating region associated with the curved shear layer also extends farther up the leading edge (past the third fiducial mark), indicating a longer shear layer generated by the Type IVa shock interaction that generates a broader peak centered at about  $x/L = 0.4$  due to a greater distance between the triple point and the test article surface. The value of this broader peak is between about 1.65 (IHEAT) and 1.7 (1D FV code). The heating on the lower part of the leading edge averaged to  $c_h/c_{h,ref} = 1.6$ , rising to a peak of about 1.8 where the incident shock impinged on the test article. Again, edge effects yielded increased heating near the tips of the test article.

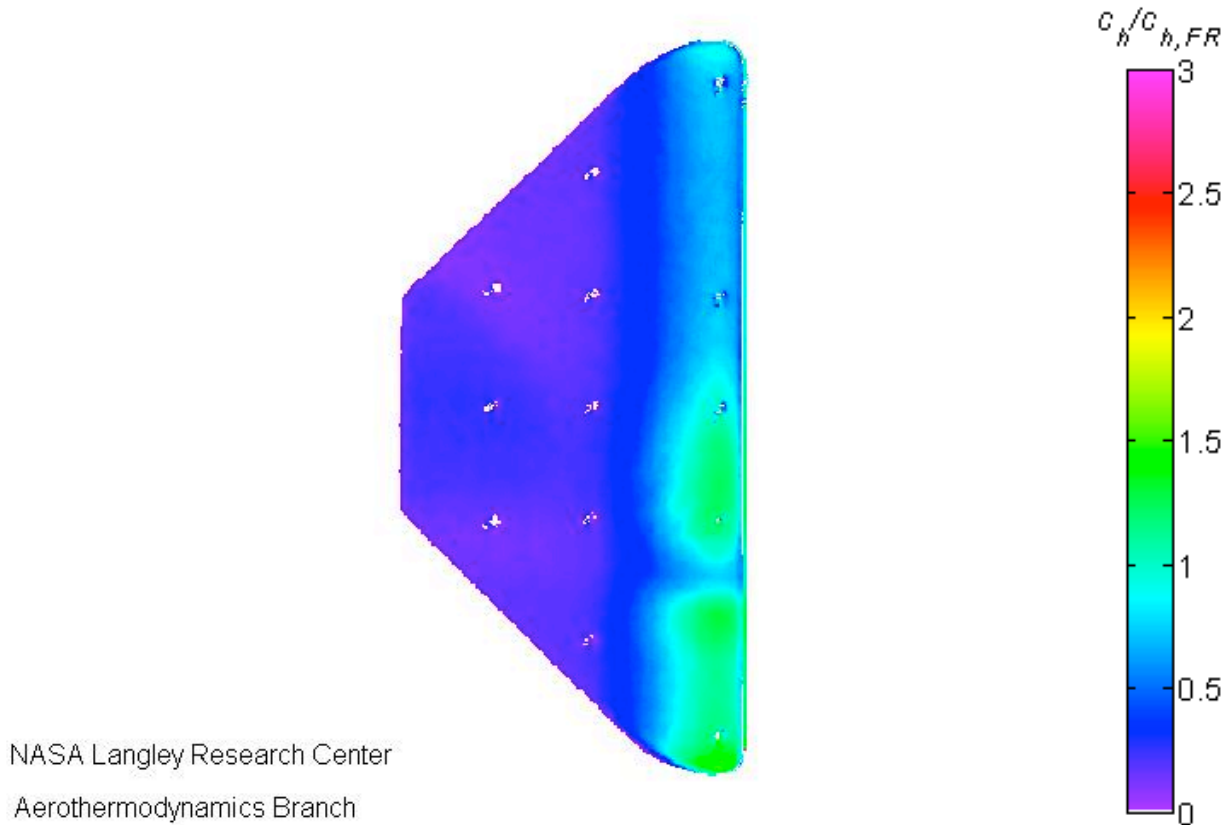


**Figure 5-43.** Run 38: IHEAT  $c_h/c_{h,FR}$  contour map for the 0.50 in-radius test article at a  $0^\circ$  AoA.

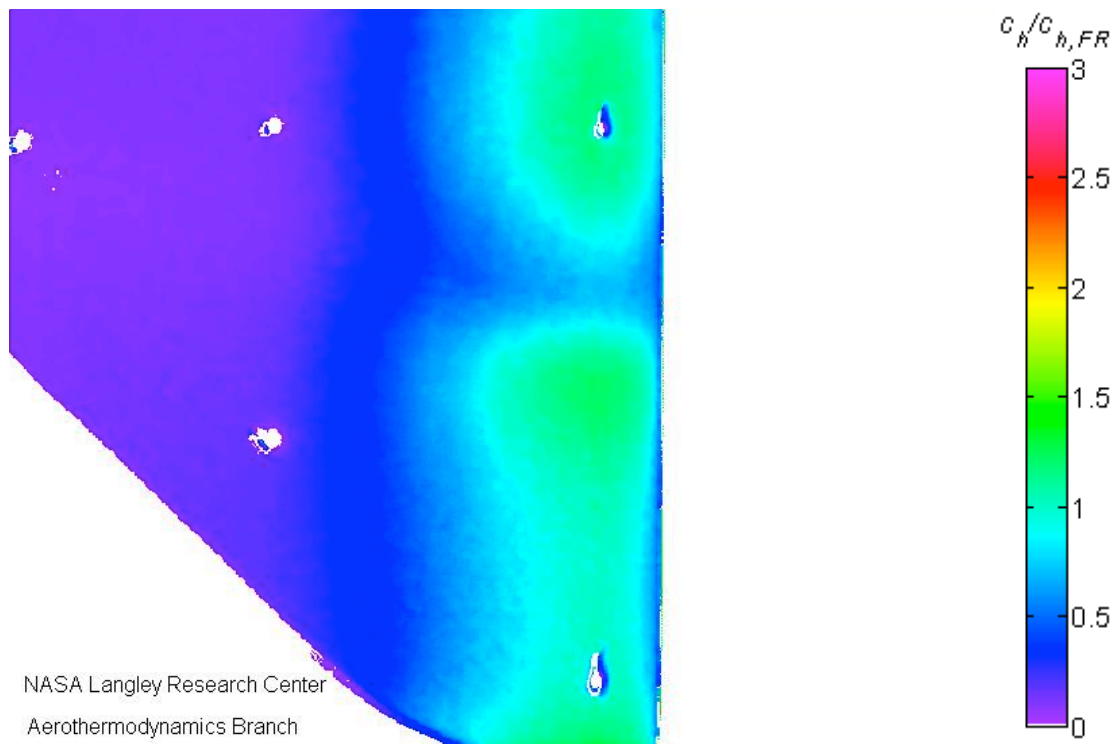


**Figure 5-44.** Run 53: IHEAT  $c_h/c_{h,FR}$  contour map for the 0.50 in-radius test article at a 0° AoA (zoomed in).

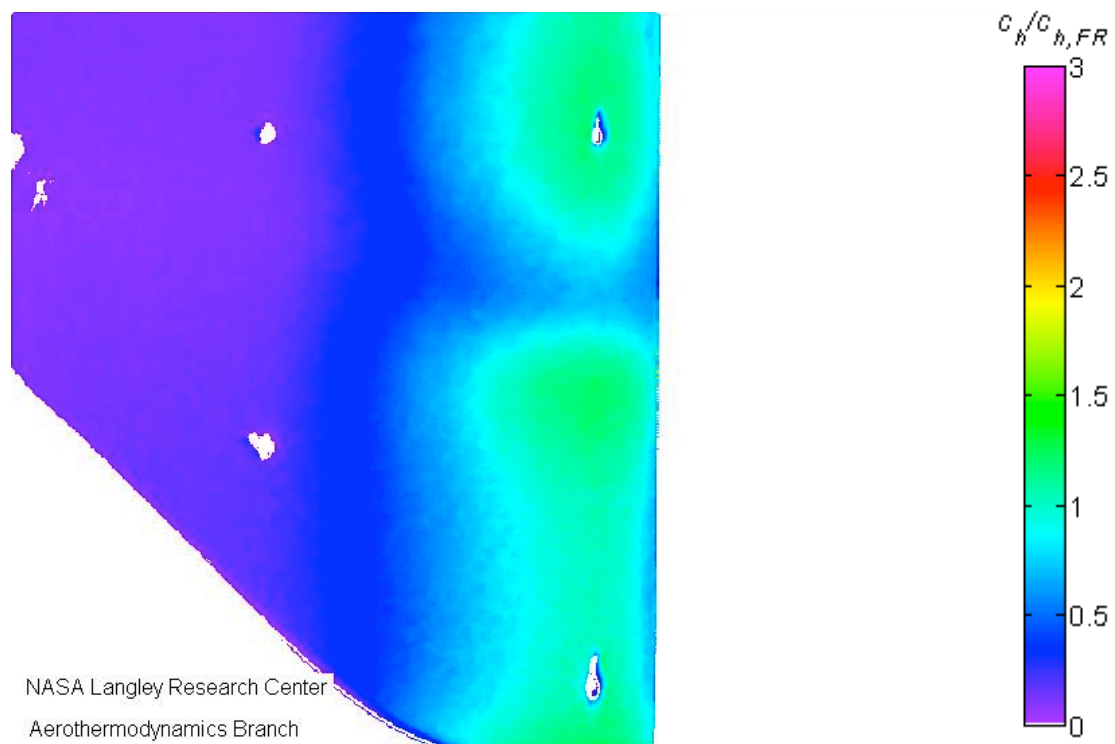


**Figure 5-45.** Run 54: IHEAT  $c_h/c_{h,FR}$  contour map for the 0.50 in-radius test article at a 0° AoA (zoomed in, repeat run).

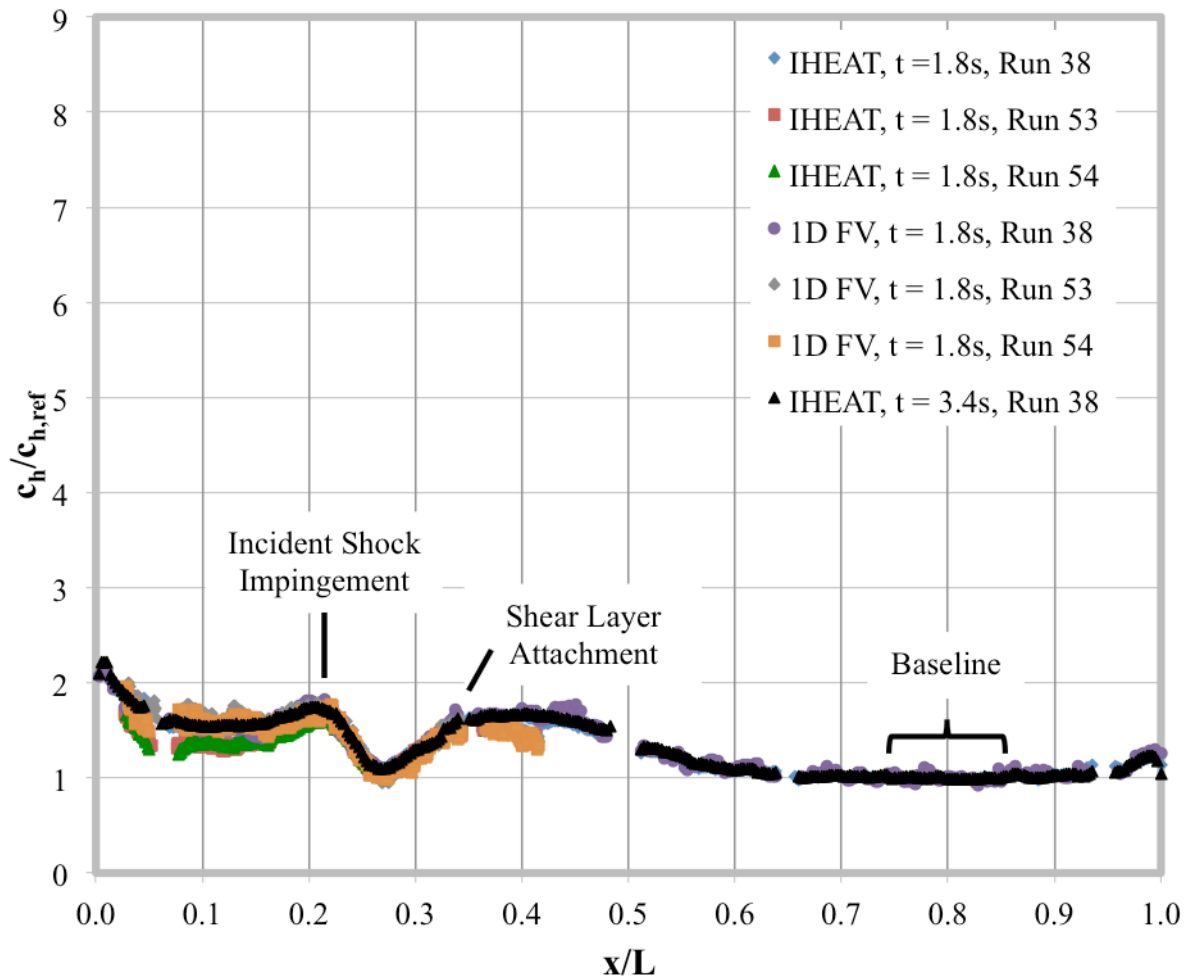


**Figure 5-46.** Non-dimensional heat transfer coefficients from the IHEAT and 1D FV codes for the 0.50 in-radius test article at a  $0^\circ$  AoA.

The graph in Figure 5-47 shows the comparison between the initial and repeated run with the 0.5 in-radius test article at a  $0^\circ$  AoA. The x-axis was changed for this plot to more clearly show the differences between the two runs using IHEAT and the 1D FV code to analyze the heat transfer. Both sets of zoomed-in data are divided by the average value from the zoomed-out run for the same method (1D FV or IHEAT) to attain the non-dimensional heat transfer coefficients. The heat transfer results for this configuration do not vary significantly between runs, especially in the IHEAT data. Therefore, repeat runs of the remaining shock interaction cases were not conducted.

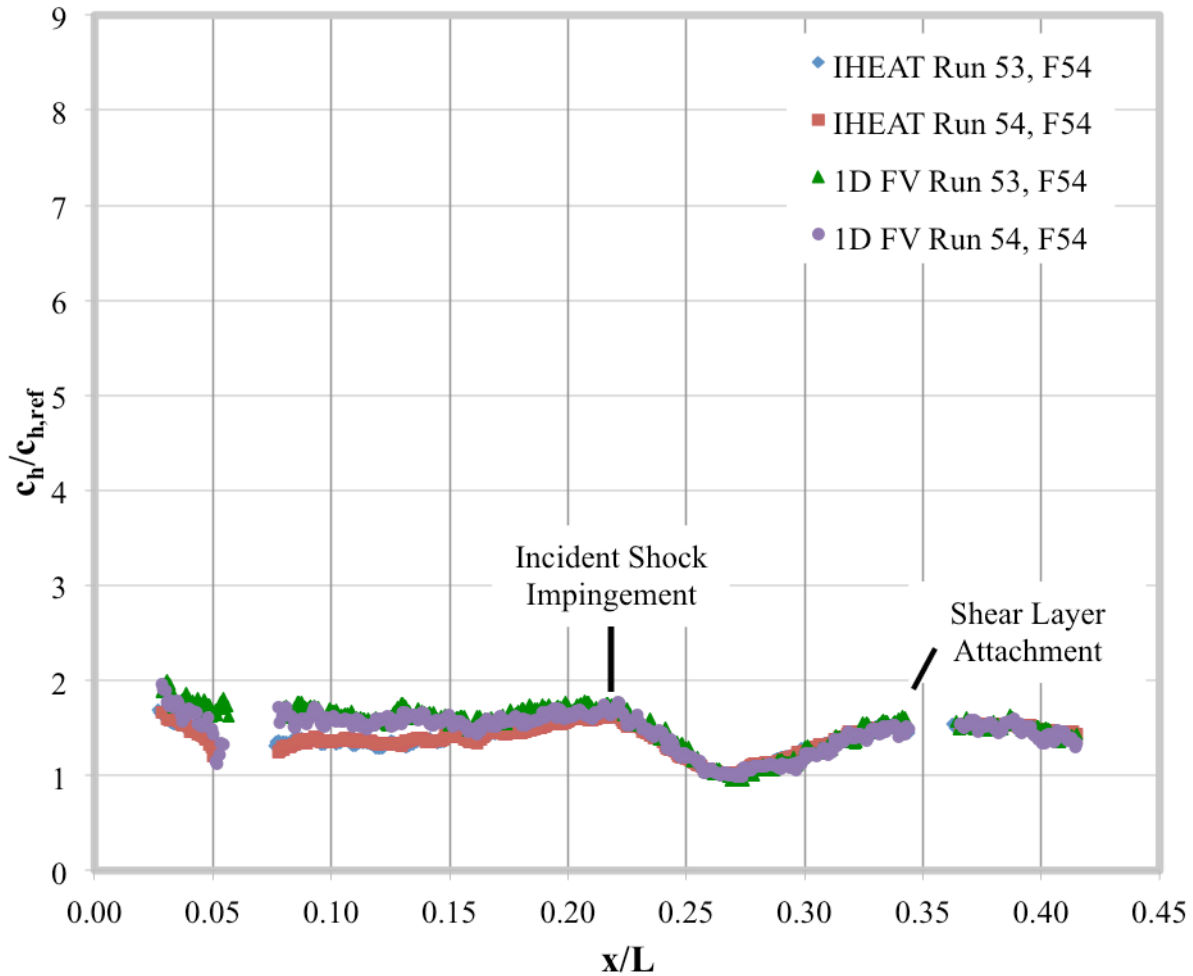
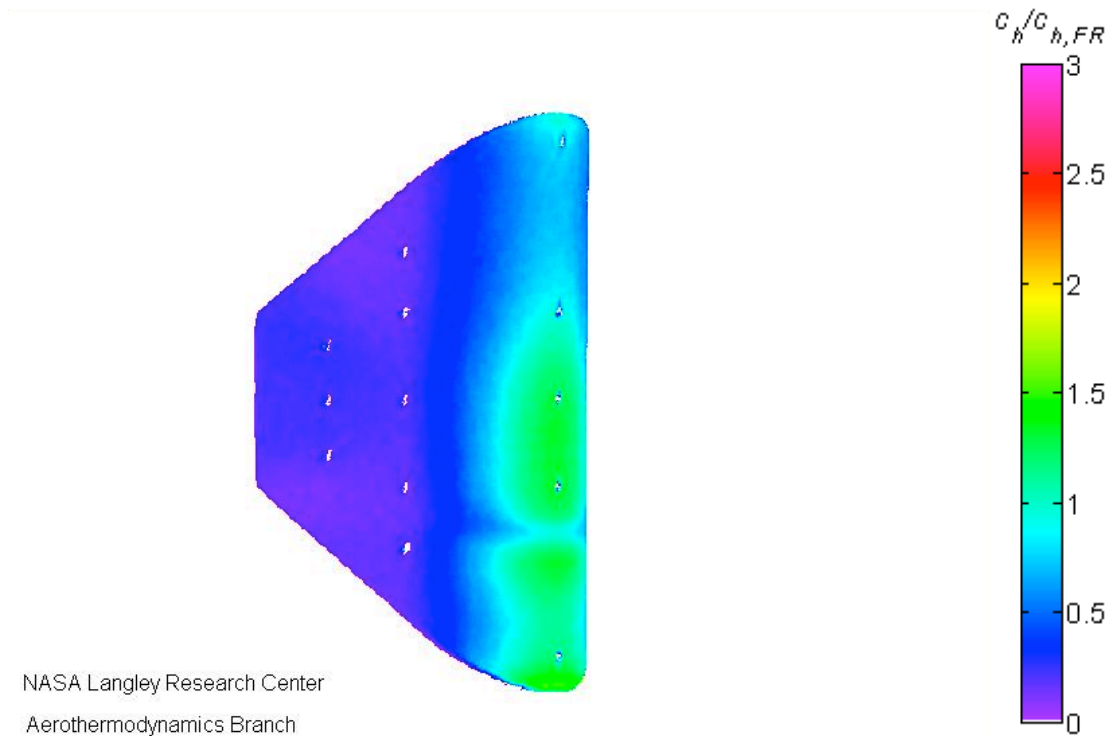


**Figure 5-47.** Non-dimensional heat transfer coefficients from the IHEAT and 1D FV codes for repeat runs zoomed in on the interaction region for the 0.50 in-radius test article at a 0° AoA.

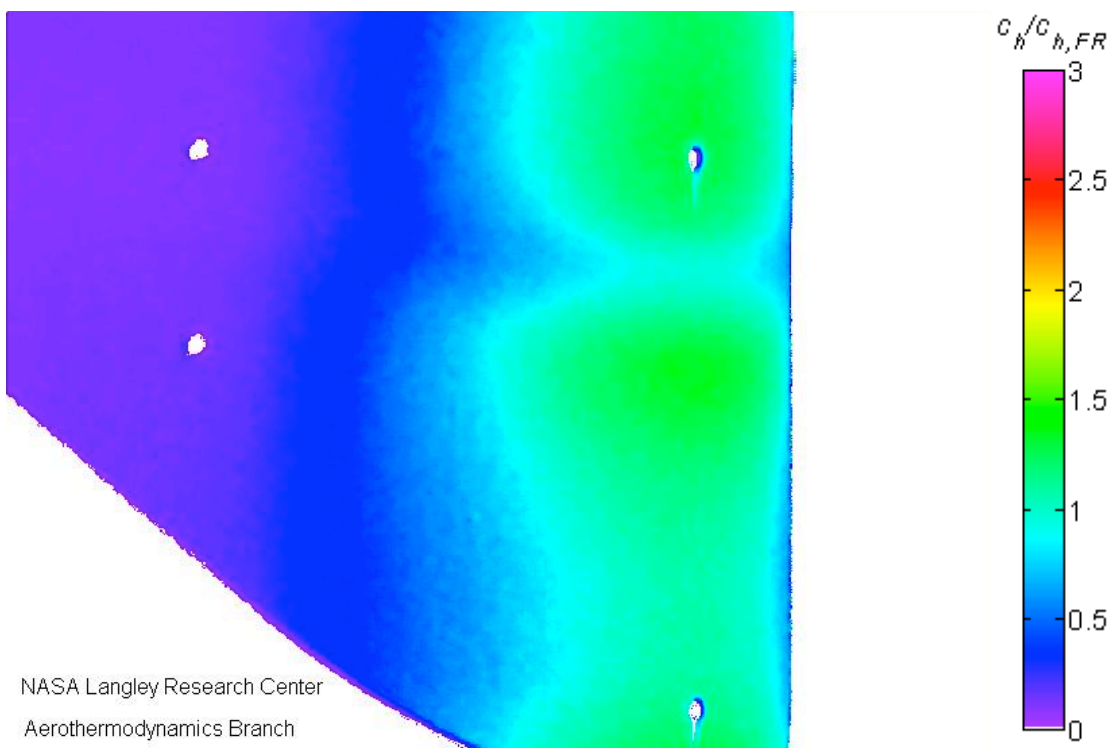
### 5.2.1.3. Leading-edge radius of 0.75 in

Figure 5-48 and Figure 5-49 show the heat transfer contour maps for the Type IVa interaction on the 0.75 in-radius test article at a 0° AoA. The separation between the two regions of elevated heating along the leading edge decreases as the nose radius of the test article increases as verified by the merging of the green surrounded by pale blue heating regions on the leading edge in contour maps. This trend is also evident from the narrower trough between the incident shock impingement and the increase in heating leading up to the shear layer attachment peak heating of about 1.8 at  $x/L = 0.43$  in Figure 5-50. The heating below the incident shock at about  $x/L = 0.21$  on the leading edge averaged to a value of  $c_h/c_{h,ref}$  between 1.46 and 1.6, depending on the method used to reduce the data.





**Figure 5-48.** Run 35: IHEAT  $c_h/c_{h,FR}$  contour map for the 0.75 in-radius test article at a 0° AoA.



**Figure 5-49.** Run 48: IHEAT  $c_h/c_{h,FR}$  contour map for the 0.75 in-radius test article at a 0° AoA (zoomed in).

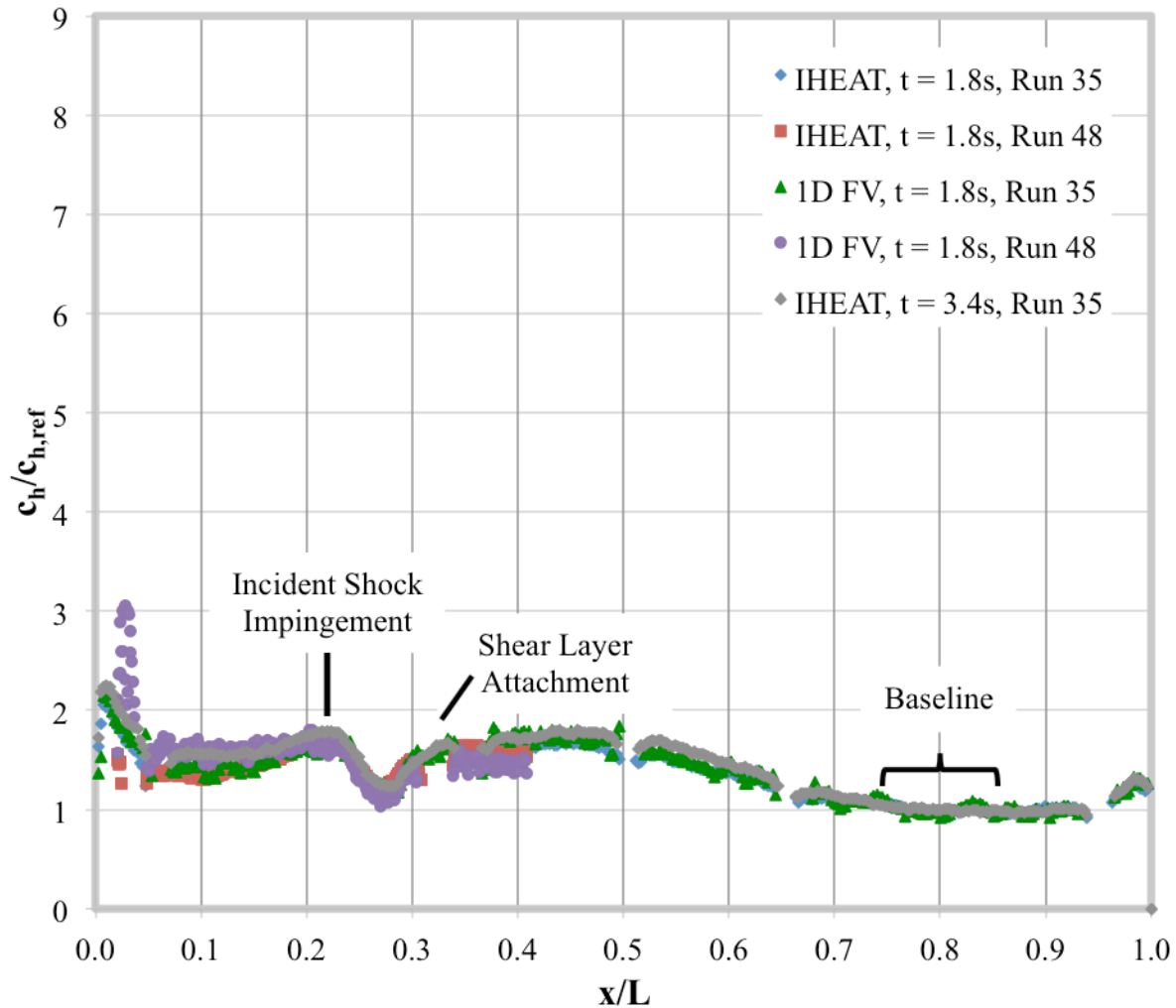


**Figure 5-50.** Non-dimensional heat transfer coefficients from the IHEAT and 1D FV codes for the 0.75 in-radius test article at a 0° AoA.

Temperature data is available along the entire leading edge near the end of the wind tunnel runs for the lower heating cases that correspond to a 0° AoA in this study. For this reason, the 2D FV code is implemented using the temperature data at  $t = 4.6$  s for the 0.75 in-radius test article at 0° AoA to compare to the 1D semi-infinite results from IHEAT. This comparison is shown for non-dimensional heat transfer coefficients in Figure 5-51. In this case the greatest difference between the 1D and 2D results is at the valley between the incident shock and shear layer attachment points. In both the dimensional (not shown) and non-dimensional plots of the heat transfer coefficients, the 2D FV value for the minimum heat transfer coefficient in this valley is about 12% lower than the minimum heat transfer coefficient from IHEAT. Due to time constraints, the other cases with a 0° AoA are not considered in this study. However, the temperature data is available to compare 1D and 2D results for those test configurations at a later time.

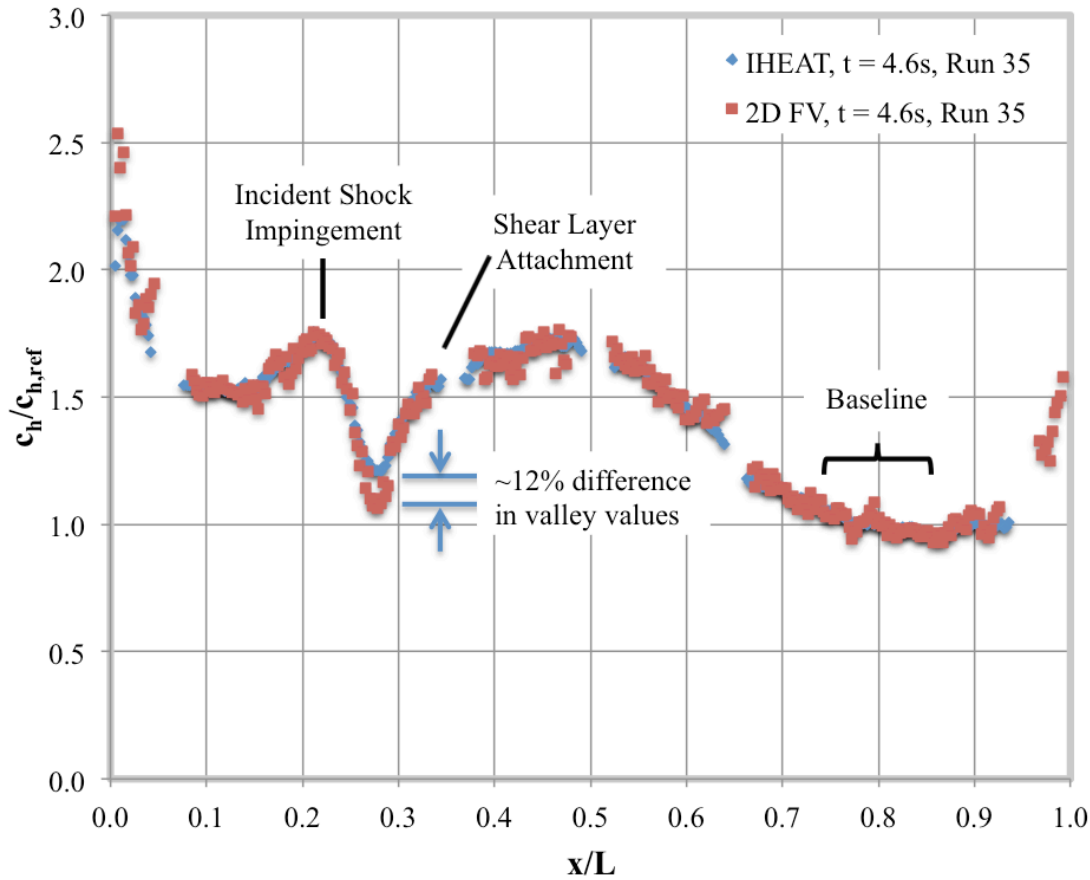


**Figure 5-51.** Non-dimensional heat transfer coefficients at  $t = 4.6$  s from the IHEAT and 2D FV codes for the 0.75 in-radius test article at a  $0^\circ$  AoA.

### 5.2.2. Fin sweep of $-15^\circ$ and a $Re = 2.1 \times 10^6/ft$

The direct Type IV shock-shock interaction created by a  $-15^\circ$  test article AoA produced a large, narrow peak heat transfer coefficient. Two small peaks exist on either side of the peak heat transfer coefficient along the leading edge for this type of interaction.

#### 5.2.2.1. Leading-edge radius of 0.25 in

The contour maps in Figure 5-52 and Figure 5-53 and the line cut data in Figure 5-54 correspond to a Type IV interaction on the 0.25 in-radius test article at a  $-15^\circ$  AoA. The shock interaction wraps around the test article, creating streaks of higher heating coefficients on the side. A sharp narrow peak of about 5 indicates the impingement location of the supersonic jet at approximately  $x/L = 0.24$ . The width of the peak region is approximately 0.025 non-dimensionally or 0.1 in. The maximum temperature in this region exceeds the phosphor limit by  $t = 1.8$  s, so the actual peak heat transfer coefficient cannot be determined. The incident shock impinges on the test article near the base of the sharp peak. The region of varying density above the incident shock in the schlieren videos and images yields a region of increased heating that produces a smaller peak around  $x/L = 0.3$  above the incident shock impingement near  $x/L = 0.26$  on the leading edge.

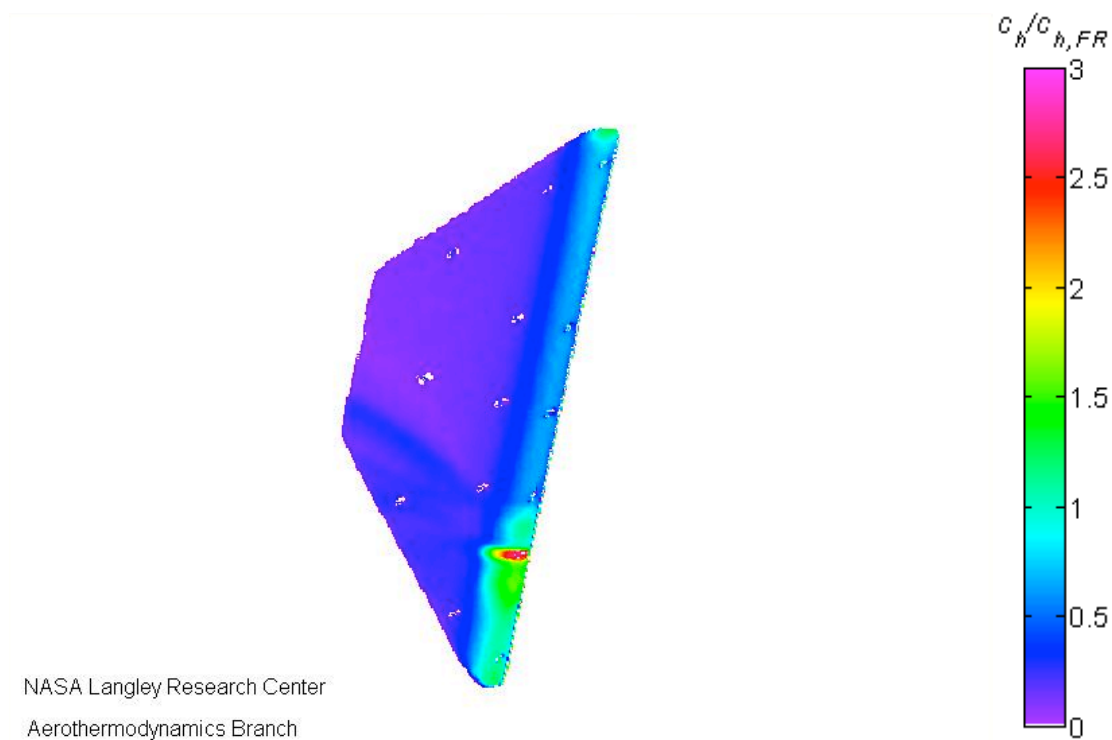


**Figure 5-52.** Run 40: IHEAT  $c_h/c_{h,FR}$  contour map for the 0.25 in-radius test article at a  $-15^\circ$  AoA.

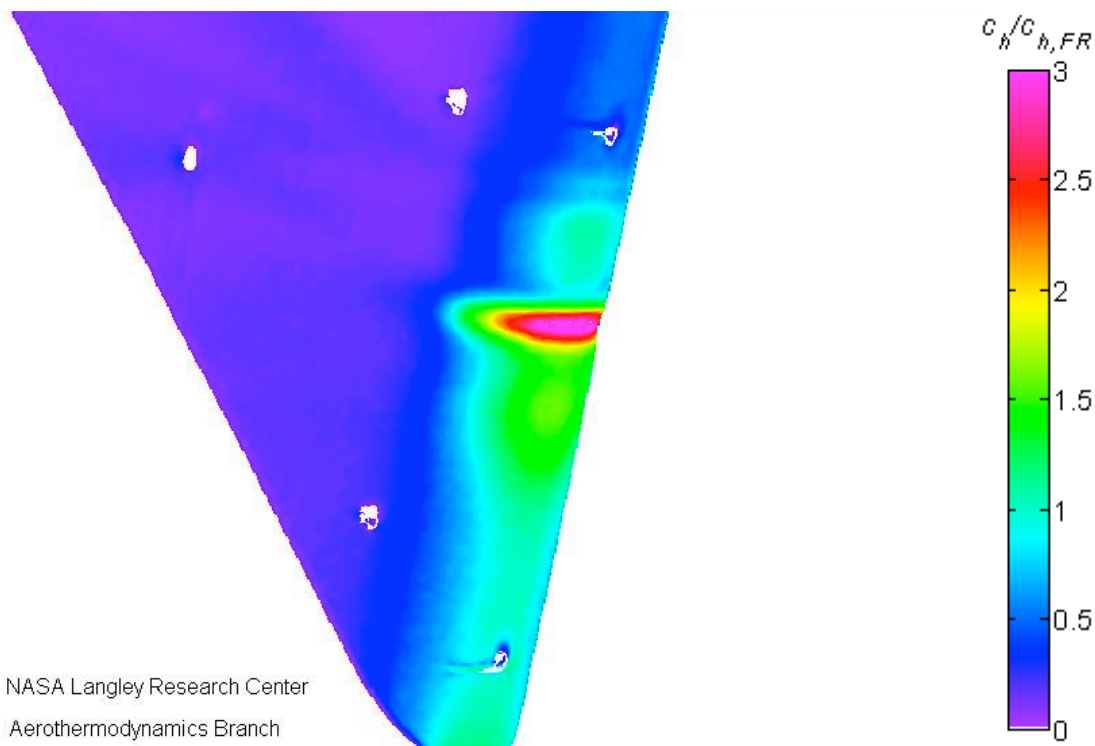


**Figure 5-53.** Run 45: IHEAT  $c_h/c_{h,FR}$  contour map for the 0.25 in-radius test article at a  $-15^\circ$  AoA (zoomed in).

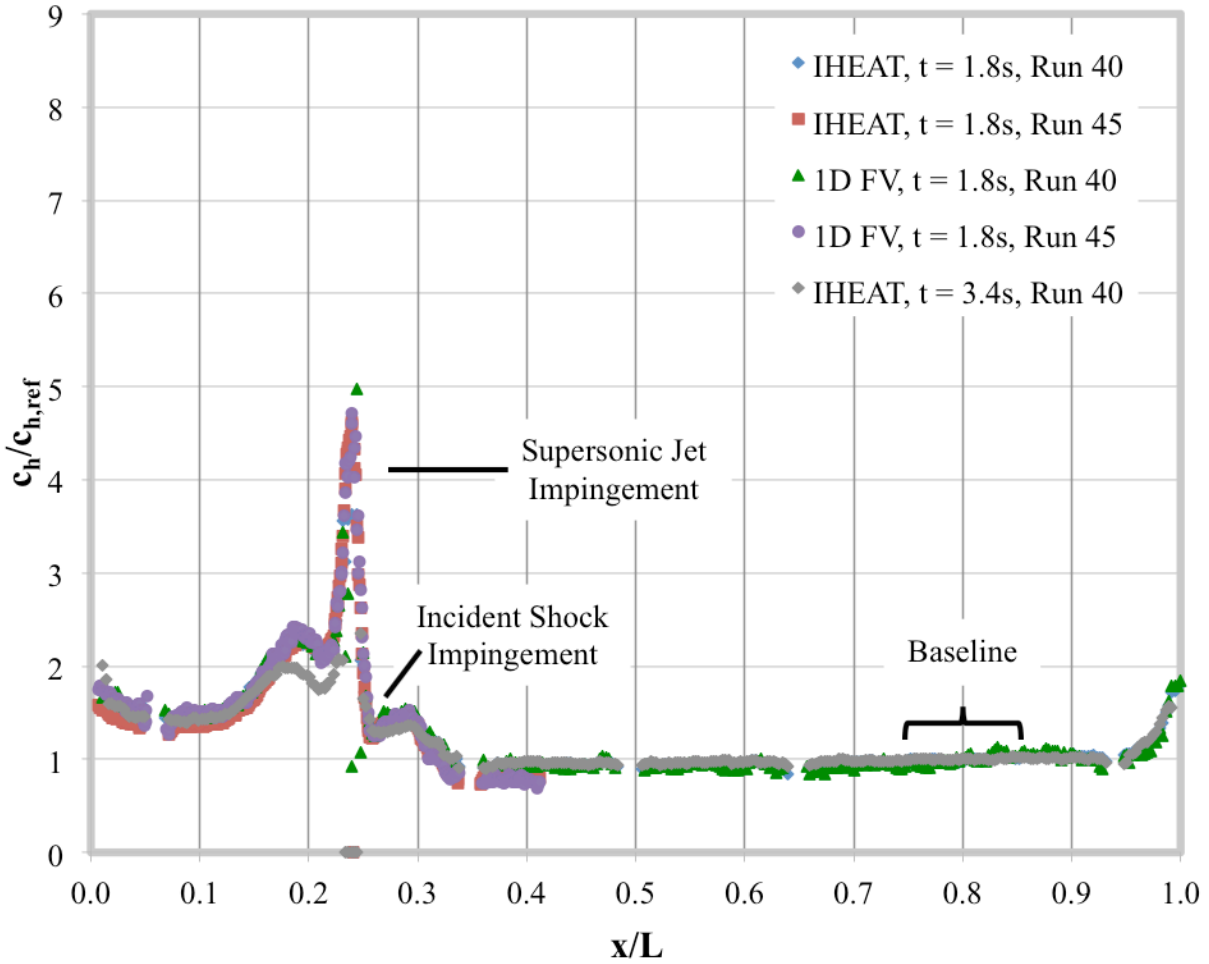


**Figure 5-54.** Non-dimensional heat transfer coefficients from the IHEAT and 1D FV codes for the 0.25 in-radius test article at a  $-15^\circ$  AoA.

The heating results for the direct Type IV shock-shock interaction from Test 6692 are presented in Figure 5-55. The sets of data for the Painted 1 and Upilex® thin-film test articles exhibit the same features of a sharp narrow peak surrounded by two smaller peaks. As in the previous Test 6692 leading edge line cut, the incident shock impingement location is at  $x/L_{Incident Shock} = 0$ .

The magnitude of the heating due to the supersonic jet in this case varies from 6.5 to 7, possibly due to the difference in thermal properties between the fused silica substrate of the phosphor-coated test articles in the current study and the Macor® substrate of the thin-film test articles. Although the heat transfer to the test article due to the shock-shock interaction should not vary depending on which substrate material is implemented in the investigation, the values of the surface heat transfer coefficients depend on the thermal conductivity of the test article material. The peak heat transfer values in the current study are also calculated at different times in the run than for the cases in Test 6692, due to limitations on the available temperature data in Test 6983.

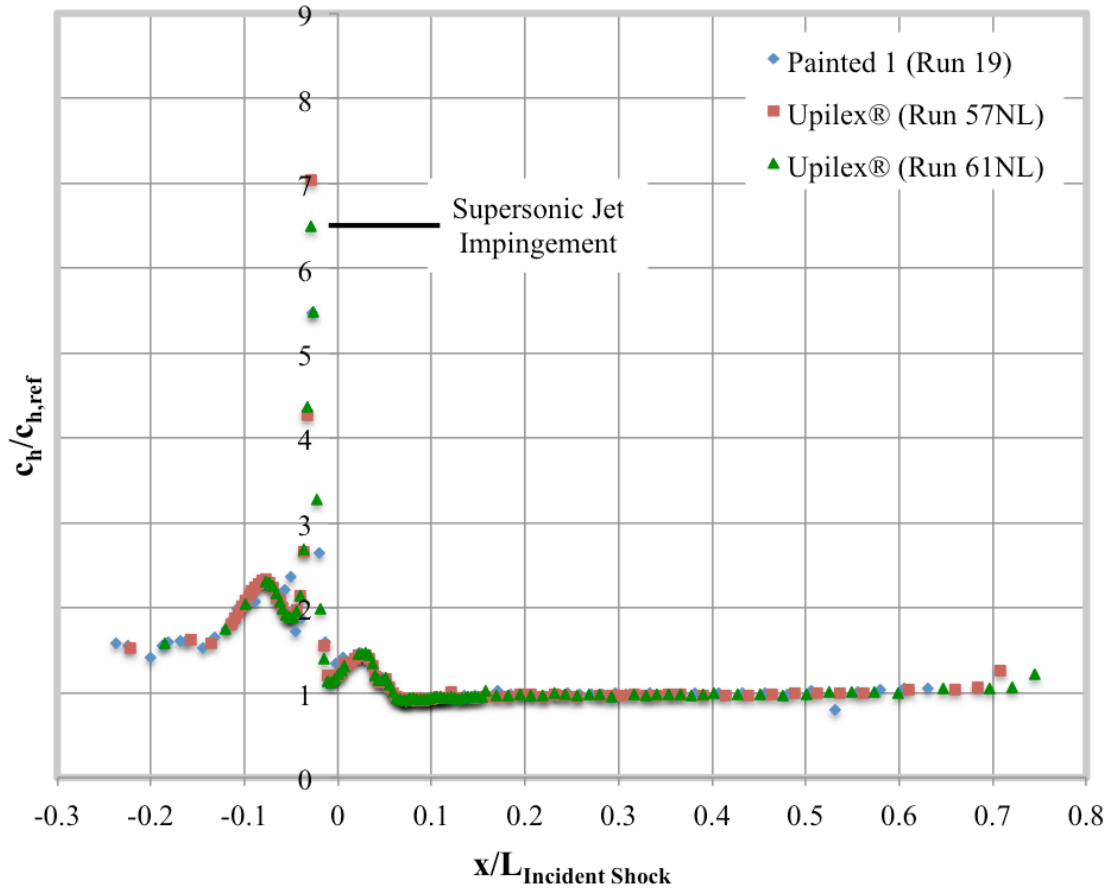
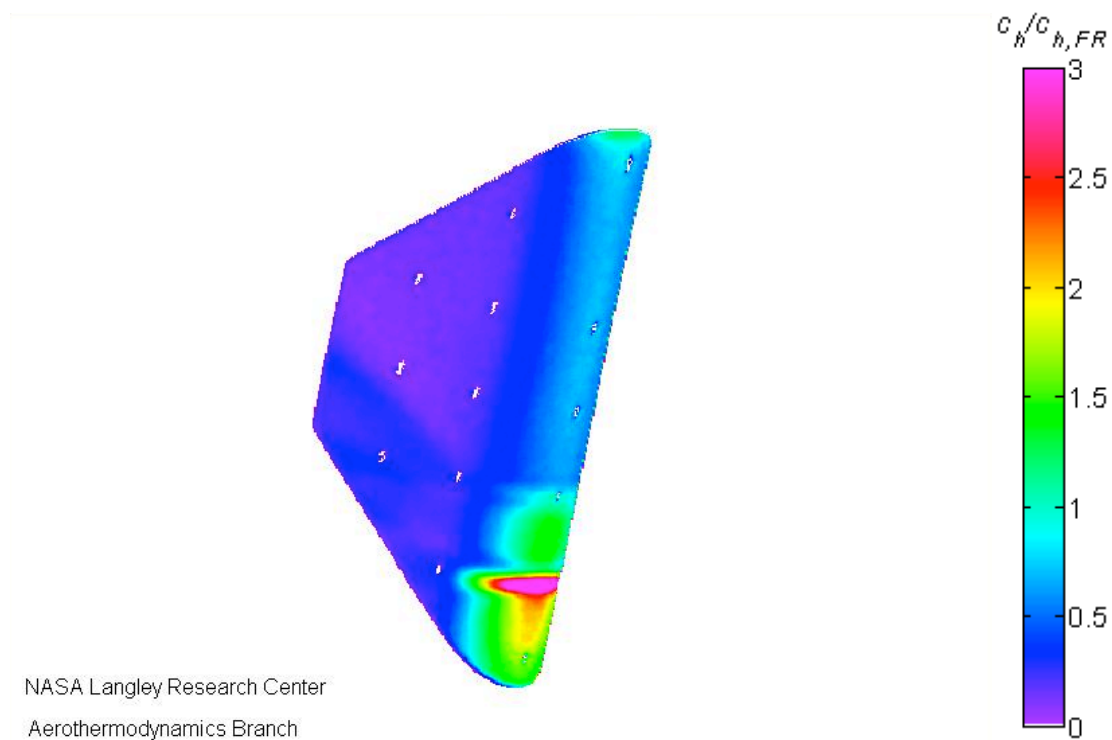


**Figure 5-55.** Non-dimensional heat transfer coefficients from the thin-film gages on the 0.25 in-radius Macor® Painted 1 and Upilex® test articles in Test 6692 at a  $-15^\circ$  AoA (data used with Berry's permission [8]).

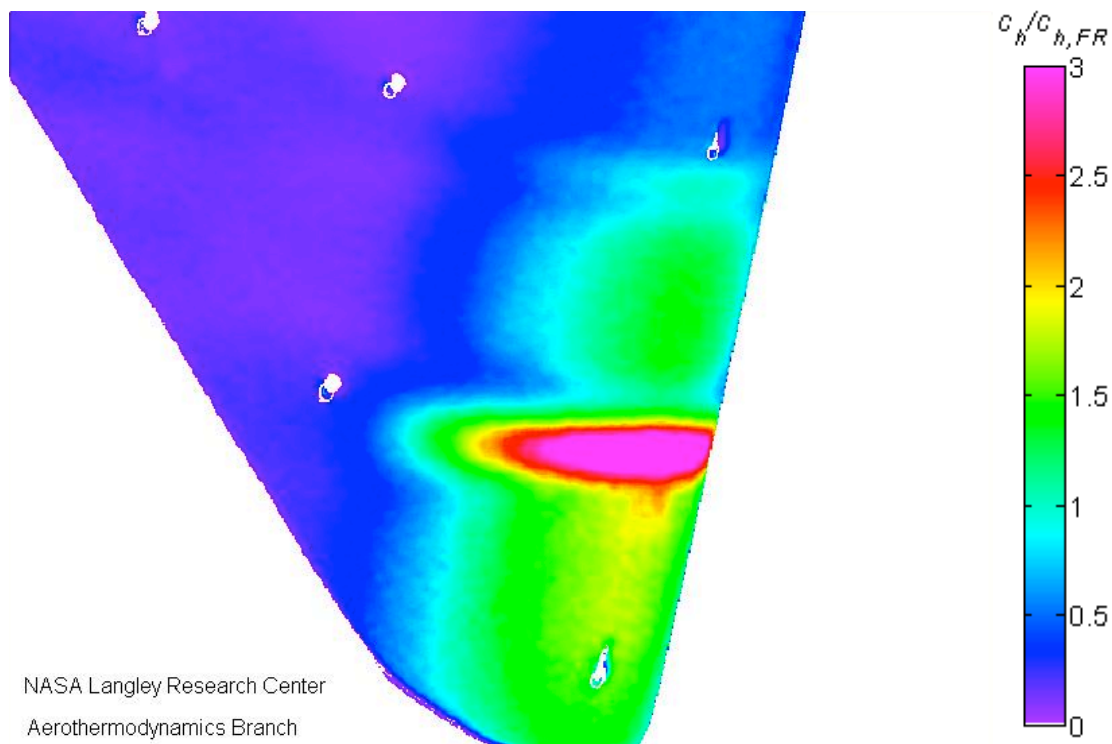
#### 5.2.2.2. Leading-edge radius of 0.50 in

Figure 5-56 and Figure 5-57 display contour maps for the 0.5 in-radius test article at a  $-15^\circ$  AoA. The non-dimensional heating pattern along the leading edge for this Type IV interaction is included in Figure 5-58. In this case the maximum peak heat transfer increases to about 6.7 at  $x/L = 0.18$ , and the width of this peak also increases to about 0.044 non-dimensionally or 0.18 in. The triangular shape seen in the streamlines on the side of the oil flow models for this type of interaction is visible in the heating pattern on the side of this test article in Figure 5-56. The region of heating augmentation above the incident shock impingement at  $x/L = 0.22$  in Figure 5-58 extends farther up the leading edge in this case, corresponding to a broader peak of about  $c_h/c_{h,ref} = 2$  to the right of the heating due to the supersonic jet. The heating to the left of the major peak in this plot is again higher than the average baseline value, but a second small peak is replaced by a small plateau of heat transfer coefficients at a value of around 2.6. The increased heating at the upper tip of the test article is evident in this plot. The shock-shock interaction affects the heat transfer to the lower tip of the test article through lateral conduction since the peak heat transfer location is farther down the leading edge of the test article than for the smaller test article.





**Figure 5-56.** Run 37: IHEAT  $c_h/c_{h,FR}$  contour map for the 0.50 in-radius test article at a -15° AoA.



**Figure 5-57.** Run 52: IHEAT  $c_h/c_{h,FR}$  contour map for the 0.50 in-radius test article at a -15° AoA (zoomed in).

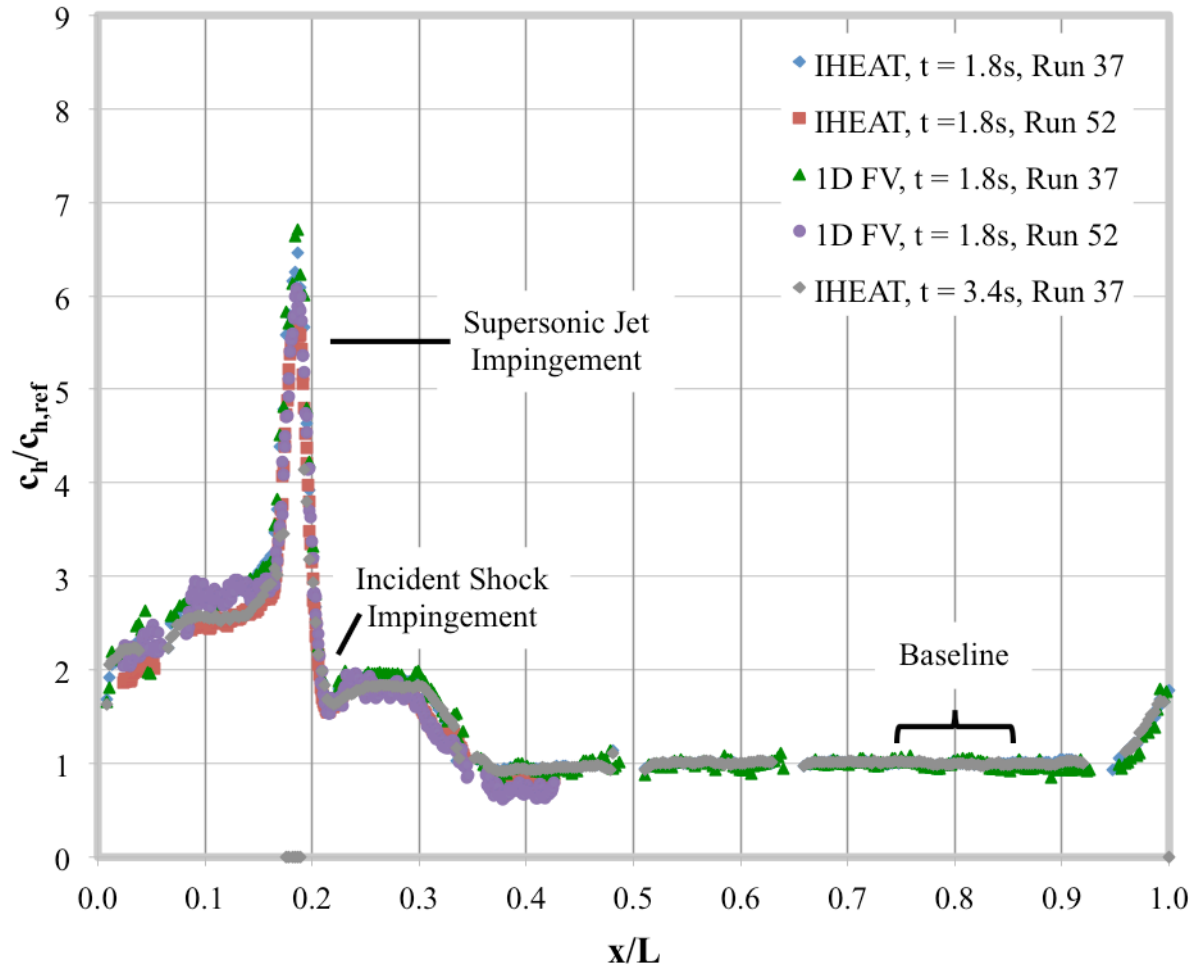


**Figure 5-58.** Non-dimensional heat transfer coefficients from the IHEAT and 1D FV codes for the 0.50 in-radius test article at a  $-15^\circ$  AoA.

### 5.2.2.3. Leading-edge radius of 0.75 in

The contour maps in Figure 5-59 and Figure 5-60 for the 0.75 in-radius test article resemble those for the smaller test articles. The regions of higher heating again spread farther parallel to and around the circumference of the larger leading edge. Figure 5-61 shows the non-dimensional peak heat transfer value is between about 7.0 (IHEAT) and 7.7 (1D FV code) for the supersonic jet at  $x/L = 0.16$ . The width of this peak also increases to approximately 0.06 non-dimensionally or 0.24 in. The separation between the two regions of higher heating in the contour maps correlates to the incident shock location near  $x/L = 0.21$ . This line stretches around the circumference of the cylindrical leading edge just below the lowest fiducial mark in the side column, similar to the incident shock streamline in the oil-flow image in Figure 5-23. The heat transfer coefficients between  $x/L = 0.22$  and  $0.32$  in Figure 5-61 plateau at 2 times the baseline value due to heating from the unsteady, possibly vortical flow above the incident shock. The heating at the upper tip of the leading edge between  $x/L = 0.95$  and  $1$  increases to about 2, while the heat transferred to the lower tip of the test article between  $x/L = 0.1$  and  $0.15$  is nearly uniformly between 2.8 and 3.3 times the baseline value before dropping off near the edge.

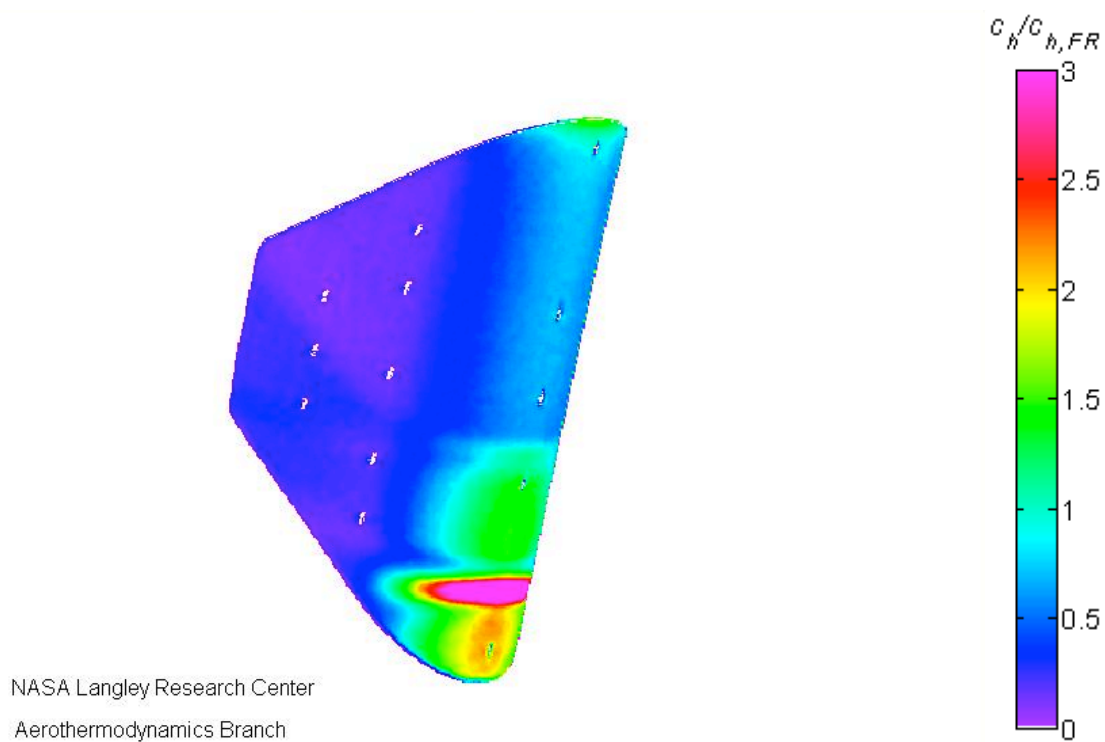


**Figure 5-59.** Run 34: IHEAT  $c_h/c_{h,FR}$  contour map for the 0.75 in-radius test article at a  $-15^\circ$  AoA.

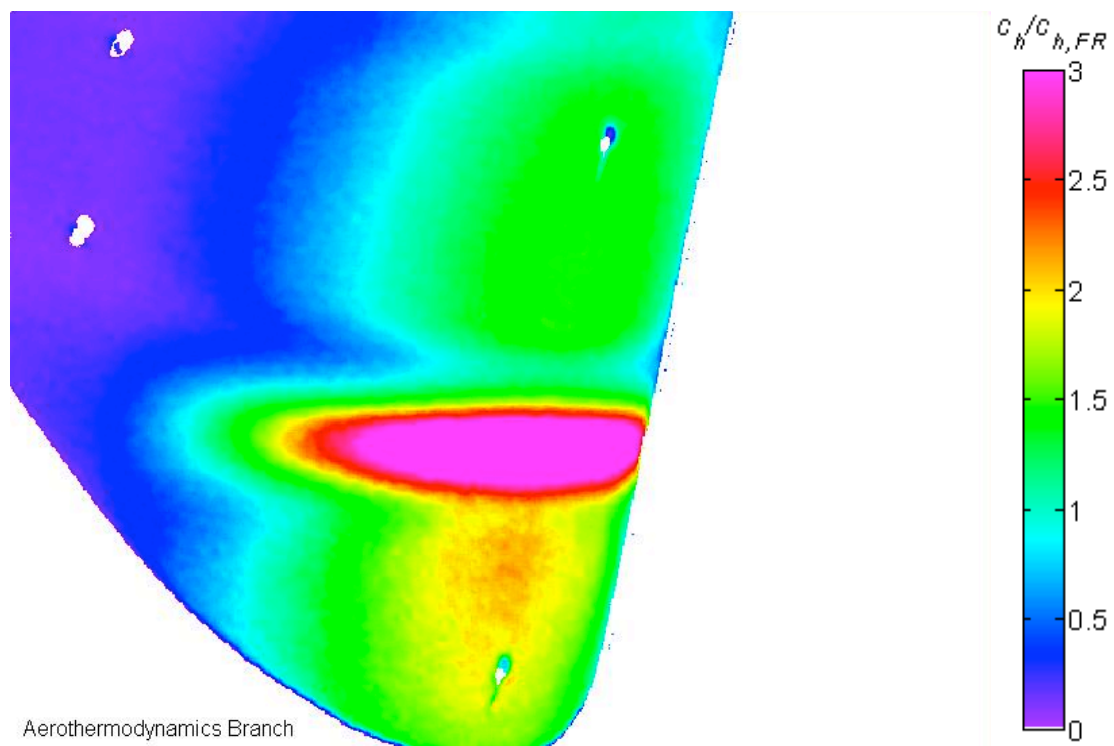


**Figure 5-60.** Run 49: IHEAT  $c_h/c_{h,FR}$  contour map for the 0.75 in-radius test article at a  $-15^\circ$  AoA (zoomed in).

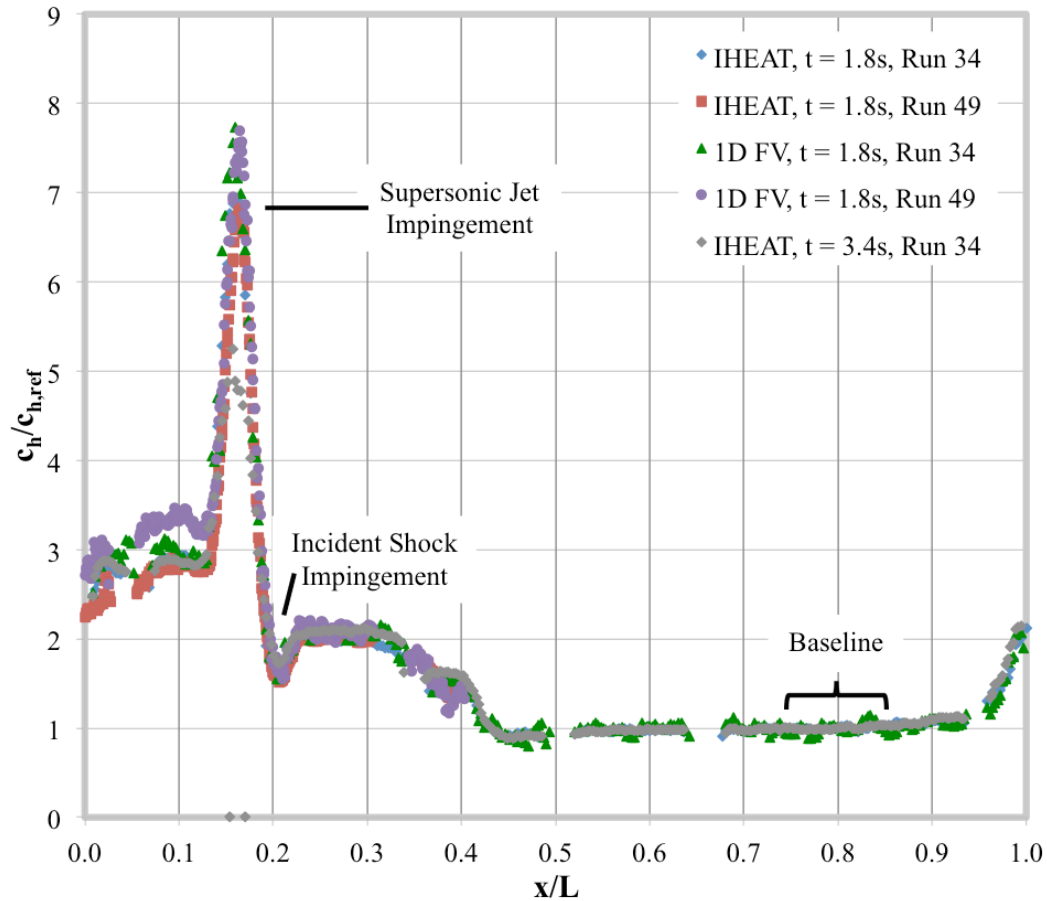


**Figure 5-61.** Non-dimensional heat transfer coefficients from the IHEAT and 1D FV codes for the 0.75 in-radius test article at a  $-15^\circ$  AoA.

### 5.2.3. Fin sweep of $-25^\circ$ and a $Re = 2.1 \times 10^6/ft$

A Type III shock-shock interaction induced by a  $-25^\circ$  test article AoA produces a large, broader peak heat transfer than the Type IV interaction. The heat transfer is nearly uniform to the lower leading edge for this interaction, possibly due to vortices traveling down the leading edge.

#### 5.2.3.1. Leading-edge radius of 0.25 in

Figure 5-62 and Figure 5-63 show contour maps for the 0.25 in-radius test article at a  $-25^\circ$  AoA. Again, the effects of the shock interaction wrap around the test article, creating streaks of higher heating on the side of the test article near the location of the incident shock impingement and shear layer attachment. Figure 5-64 shows a broader peak with a width of 0.065 (0.26 in) with a maximum value of at least 5.2 at  $x/L = 0.22$  at the shear layer attachment point. Again, the actual peak is not calculated for this case because the maximum temperature exceeds the phosphor limit by  $t = 1.8$  s. The incident shock impinges on the test article near  $x/L = 0.3$ , which is seen in Figure 5-63 as a green elliptical region attached to the peak that leads to a blue line of higher heat transfer coefficients around the side of the test article. The heat transfer to the lower portion of the leading edge is about twice the baseline heating.

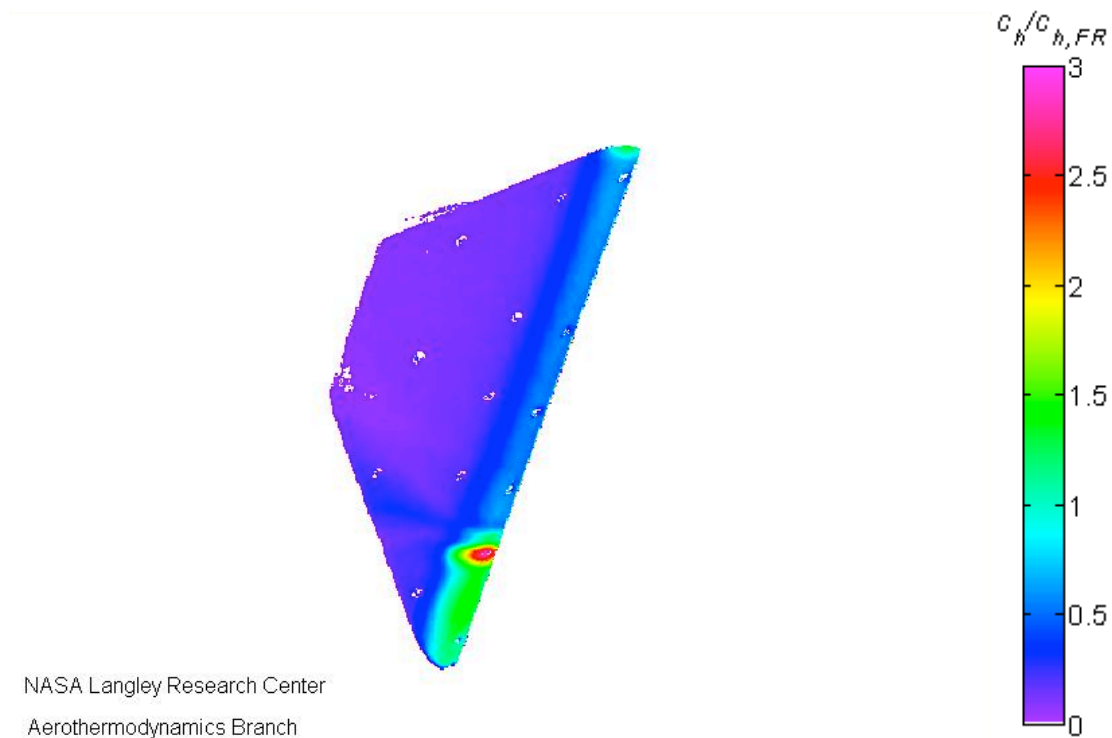


**Figure 5-62.** Run 41: IHEAT  $c_h/c_{h,FR}$  contour map for the 0.25 in-radius test article at a  $-25^\circ$  AoA.

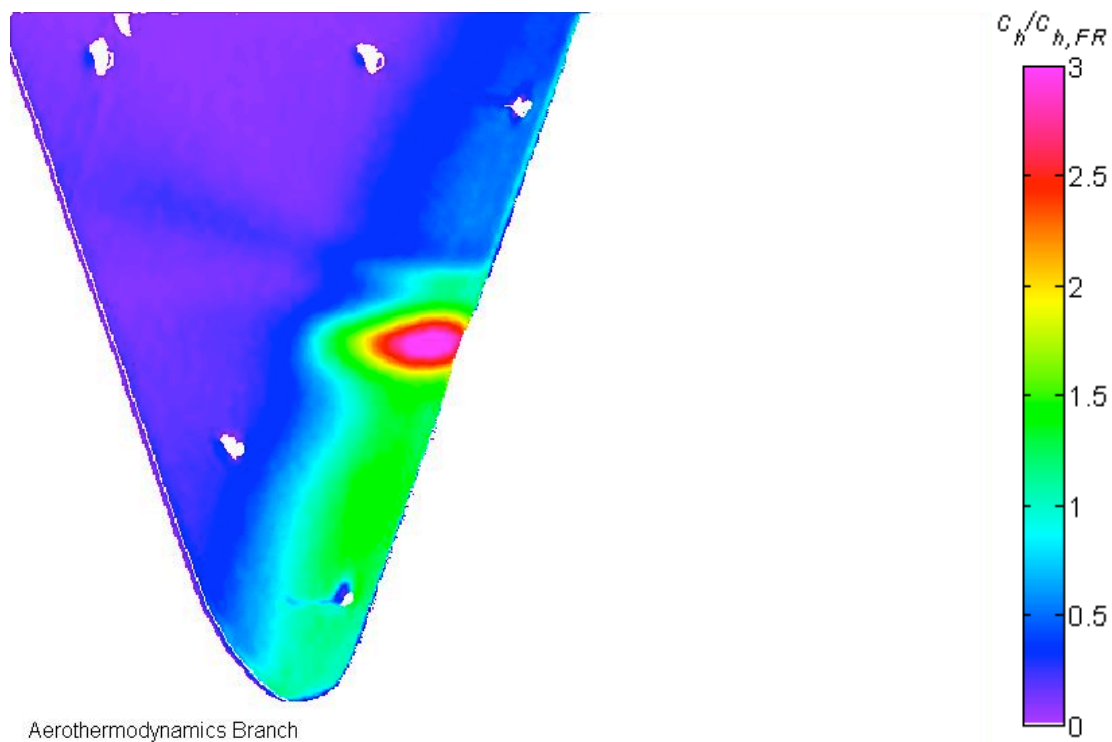


**Figure 5-63.** Run 46: IHEAT  $c_h/c_{h,FR}$  contour map for the 0.25 in-radius test article at a  $-25^\circ$  AoA (zoomed in).

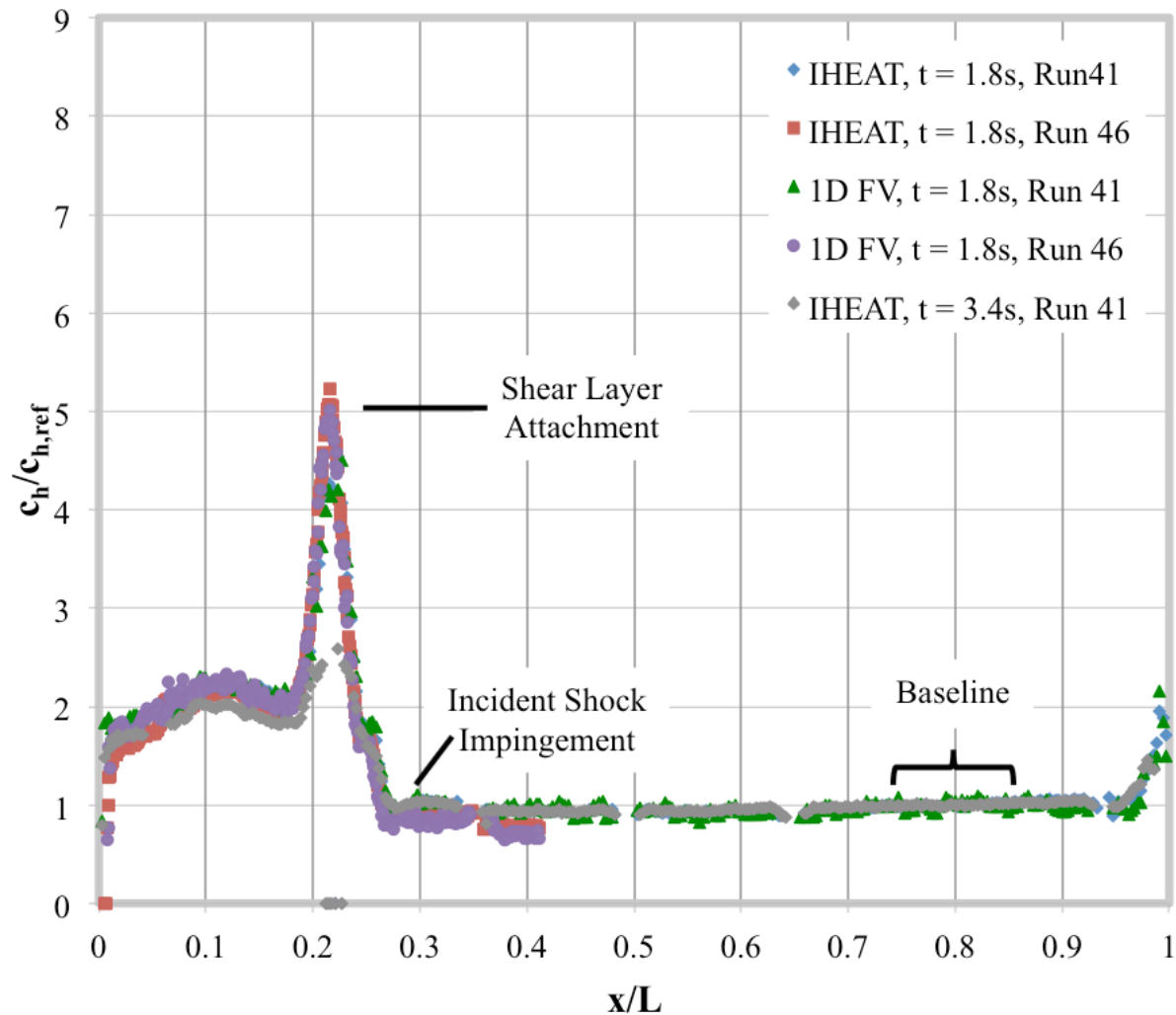


**Figure 5-64.** Non-dimensional heat transfer coefficients from the IHEAT and 1D FV codes for the 0.25 in-radius test article at a  $-25^\circ$  AoA.

Figure 5-65 presents results from the 0.25 in-radius Painted 1 and Upilex® test articles at a  $-25^\circ$  AoA in Test 6692 [8]. The shape of the heat transfer data for Test 6692 is similar to the results from Runs 41 and 46 of Test 6983. Again, the incident shock location in this plot corresponds to the location  $x/L_{Incident Shock} = 0$ . In both plots, a small peak near the incident shock location exists to the right of the large peak due to the shear layer attachment. This peak is not noticeable in this plot or in the non-dimensional coefficients in Figure 5-64, since the maximum value is approximately 1 with lower heat transfer coefficients on either side. However, the peak is visible in the same plots if a smaller y-axis range is implemented. The average value of the non-dimensional heat transfer to the lower portion of the leading edge is approximately 2 before the heat transfer coefficients decrease as in the data from Test 6983.



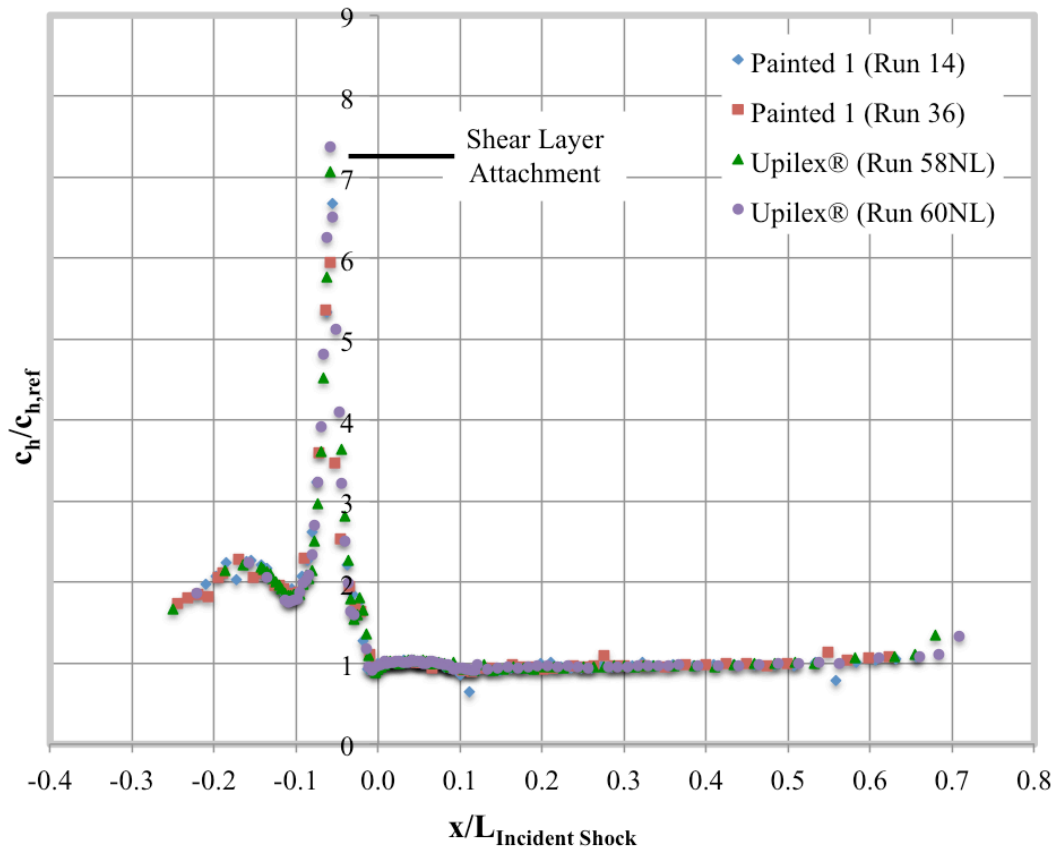


**Figure 5-65.** Non-dimensional heat transfer coefficients from the thin-film gages on the 0.25 in-radius Macor® Painted 1 and Upilex® test articles in Test 6692 at a  $-25^\circ$  AoA (data used with Berry’s permission [8]).

#### 5.2.3.2. Leading-edge radius of 0.50 in

The contour maps in Figure 5-66 and Figure 5-67 show the peak heat transfer at the shear layer attachment point is positioned closer to the lowest leading-edge fiducial mark for the 0.50 in-radius test article. This change in position from the smallest test article geometry is evident in the zoom schlieren images in Figure 5-25 and Figure 5-26. Since the angle of the shear layer relative to the incident shock for a Type III interaction only varies by a few degrees between the three test article geometries, the impingement point moves down the leading edge as the bow shock standoff distance increases and produces a greater distance between the triple point and the surface of the test article. The maximum heat transfer coefficient in this peak region that is 0.089 (0.36 in) wide, provided in the graph in Figure 5-68, is between 6.9 (IHEAT) and 7.4 (1D FV) at  $x/L = 0.15$ . A small peak of about 2.1 exists on the leading edge above the incident shock impingement near  $x/L = 0.22$  before the heat transfer settles down to the baseline value, increasing again only at the tip of the test article. The heat transfer coefficients on the lower tip vary between 2.5 and 3 (depending on the method used to analyze the data) but then drop off at the edge in a manner similar to the smaller test article. Vortices generated by the Type III shock interaction that travel down in the flow parallel to the leading edge may be responsible for this heating near the bottom of the test article.

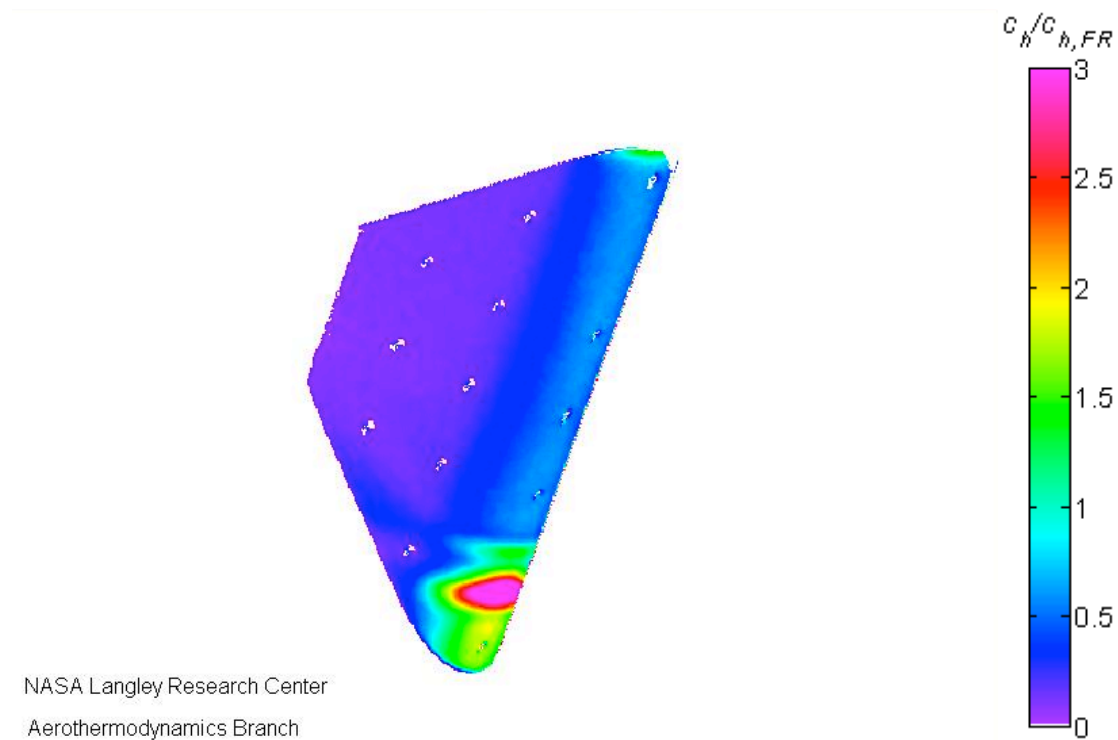


**Figure 5-66.** Run 36: IHEAT  $c_h/c_{h,FR}$  contour map for the 0.50 in-radius test article at a  $-25^\circ$  AoA.

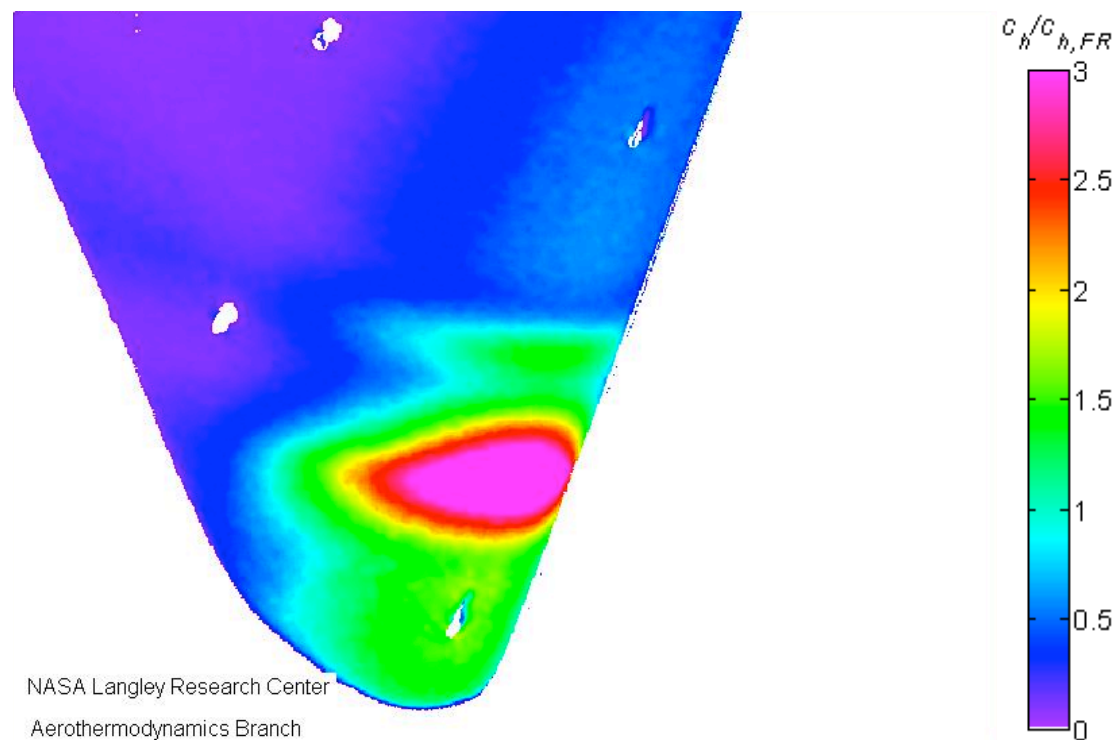


**Figure 5-67.** Run 51: IHEAT  $c_h/c_{h,FR}$  contour map for the 0.75 in-radius test article at a  $-25^\circ$  AoA (zoomed in).

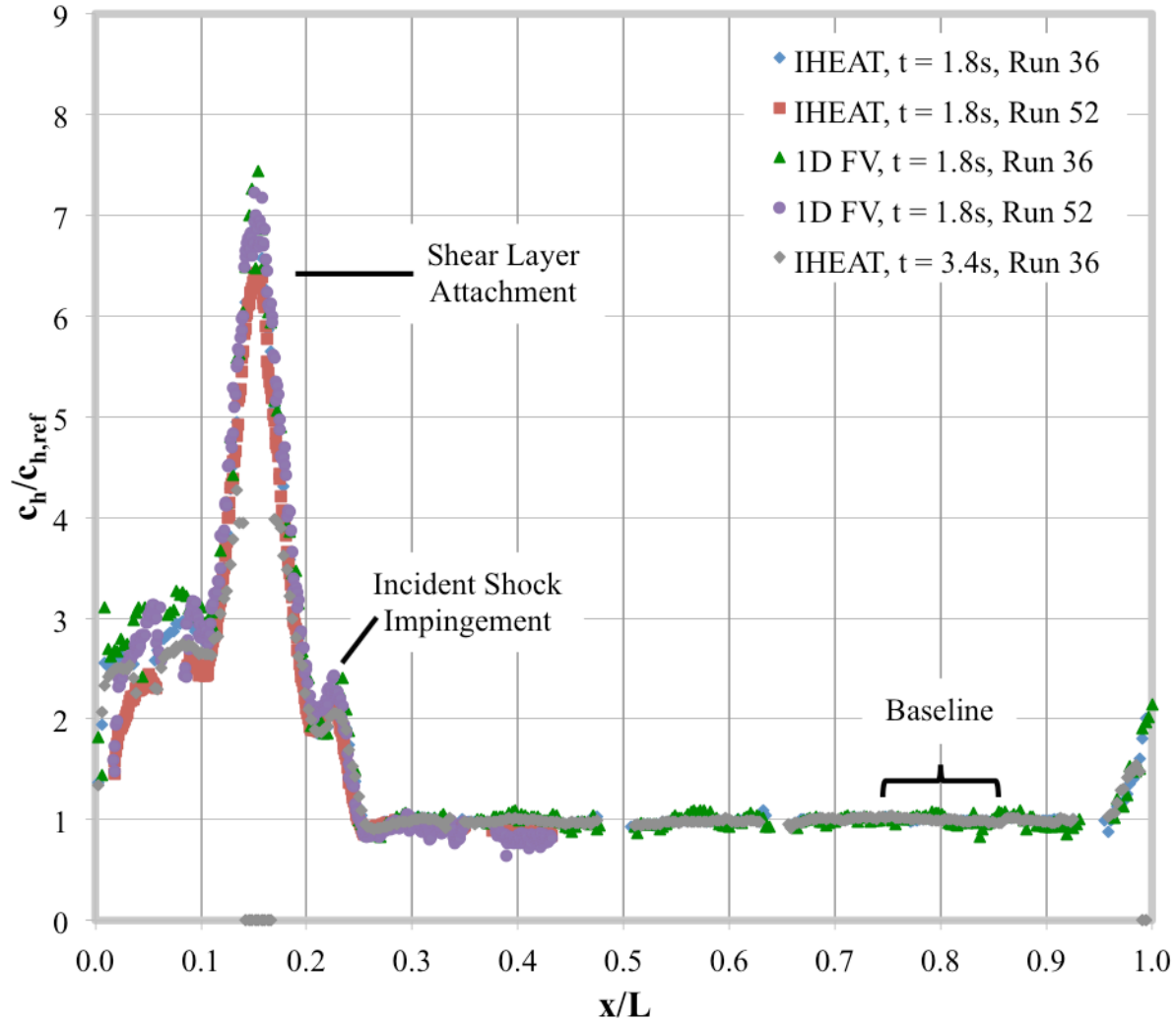


**Figure 5-68.** Non-dimensional heat transfer coefficients from the IHEAT and 1D FV codes for the 0.50 in-radius test article at a  $-25^\circ$  AoA.

### 5.2.3.3. Leading-edge radius of 0.75 in

The contour maps in Figure 5-69 and Figure 5-70 correspond to a Type III interaction on the 0.75 in-radius test article in which the peak heating again moves farther down on the leading edge. The broad peak heat transfer augmentation in Figure 5-71 occurs at  $x/L = 0.13$ , with a maximum value of 7.8 (IHEAT) to 8.5 (1D FV). The width of this peak region, which is 0.14 non-dimensionally or 0.55 in, again exceeds the width of the peak due to the shear layer attachment for the smaller test articles at the same angle of attack. The position of this shock interaction correlates to the schlieren image in Figure 5-27 and the oil-flow image in Figure 5-30 in which the shock-interaction disturbances to the oil occur in the lowest region on the test article leading edge. The heating above the incident shock at about  $x/L = 0.24$  on the leading edge is a slightly broader minor peak of approximately 2.2. The heating near the lower tip of the test article peaks between 2.4 and 3.2 before dropping off near the bottom of the test article.

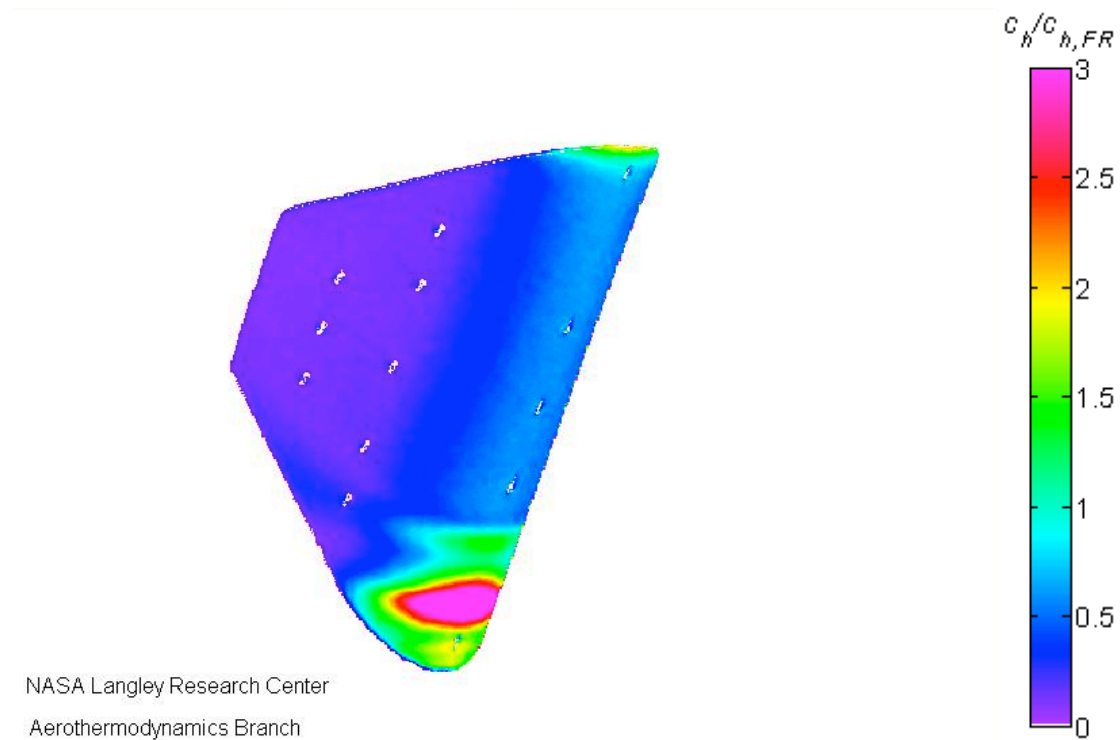


**Figure 5-69.** Run 33: IHEAT  $c_h/c_{h,FR}$  contour map for the 0.75 in-radius test article at a  $-25^\circ$  AoA.

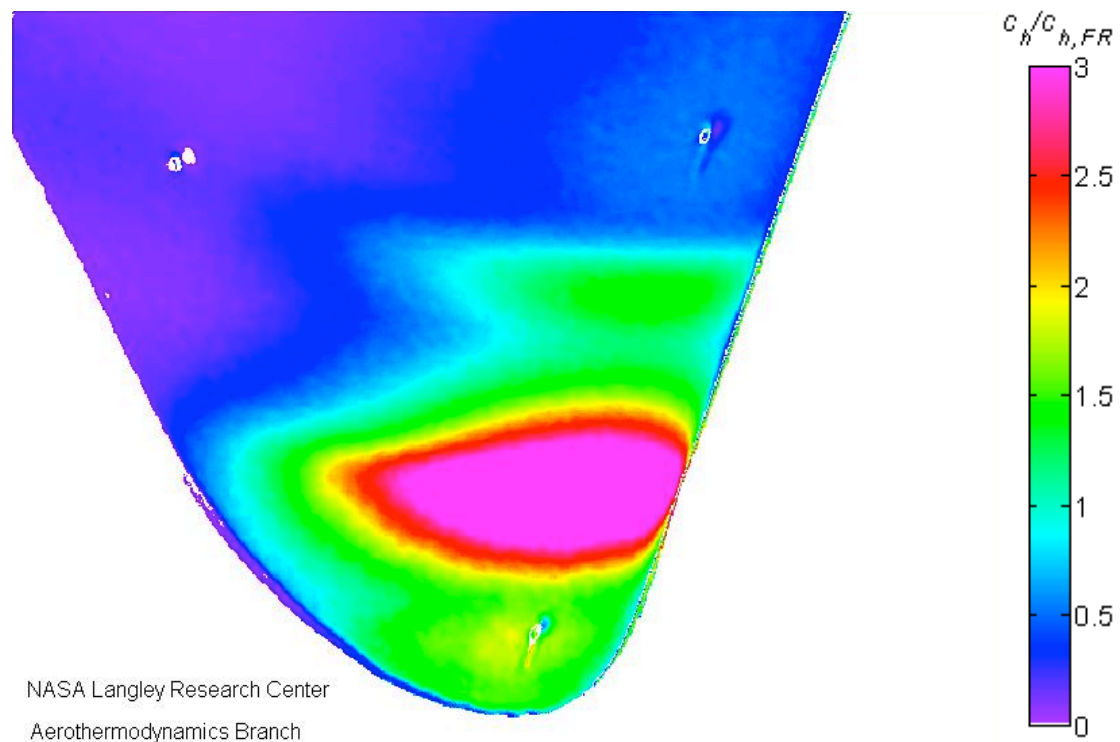


**Figure 5-70.** Run 50: IHEAT  $c_h/c_{h,FR}$  contour map for the 0.75 in-radius test article at a  $-25^\circ$  AoA (zoomed in).

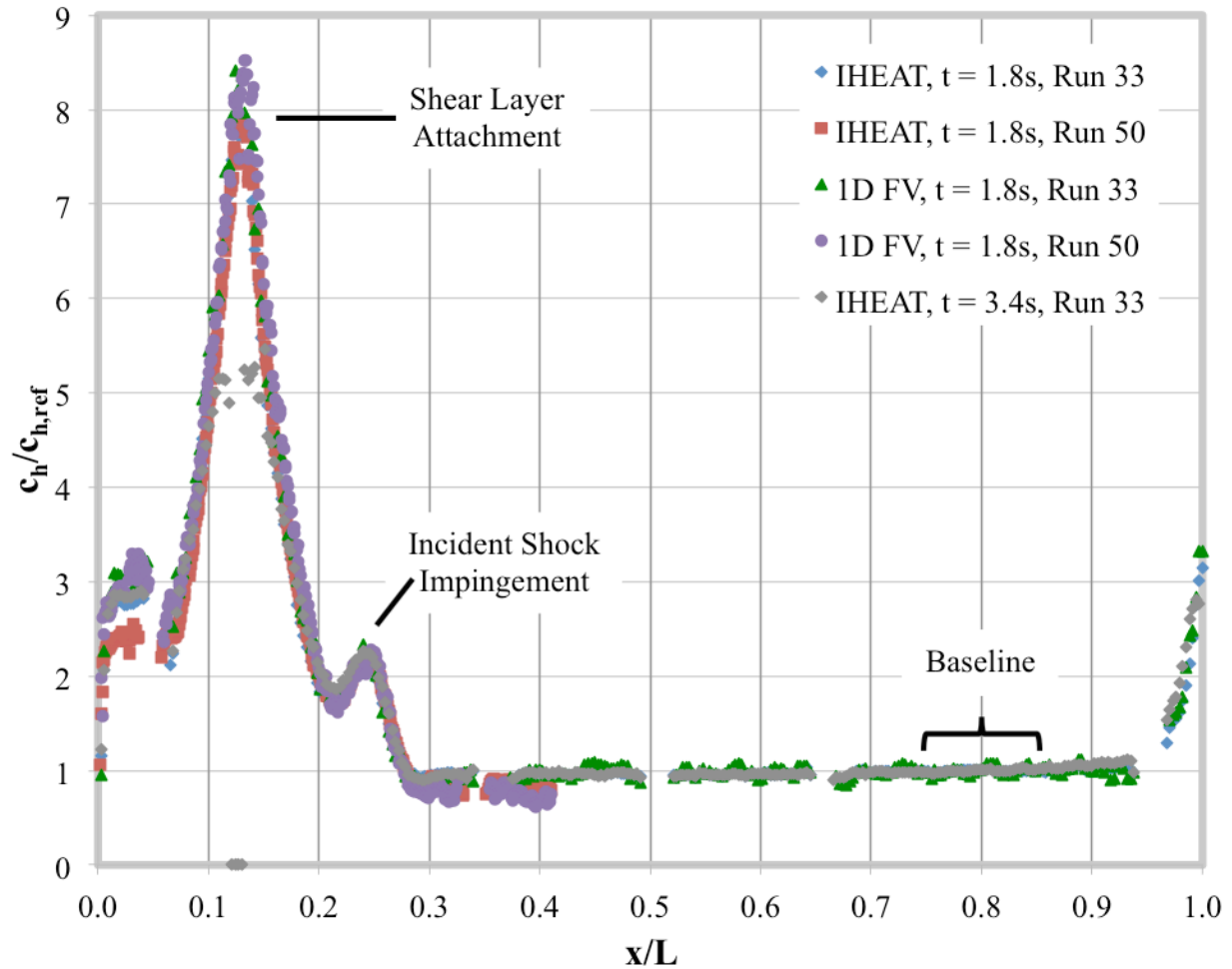


**Figure 5-71.** Non-dimensional heat transfer coefficients from the IHEAT and 1D FV codes for the 0.75 in-radius test article at a  $-25^\circ$  AoA.

#### 5.2.4. Fin sweep of $-15^\circ$ and a Re number sweep

A Re number sweep was conducted to compare the heat transfer results for a Type IV interaction at two additional flow unit Re numbers to the data for the  $Re = 2.1 \times 10^6/\text{ft}$  case. The leading-edge heat transfer line cuts for these three cases are compared in the plot in Figure 5-72. Two runs were conducted with the 0.25 in-radius test article at a  $-15^\circ$  AoA with a  $Re = 1.1 \times 10^6/\text{ft}$ , as shown in the contour maps in Figure 5-73 and Figure 5-74, and one run was conducted at a  $Re = 4.1 \times 10^6/\text{ft}$  as is later shown in the contour map in Figure 5-81. The line cut for the  $Re = 1.1 \times 10^6/\text{ft}$  case was shifted slightly to align the peaks for the three runs in Figure 5-72. This graph shows a peak heat transfer coefficient for the  $Re = 1.1 \times 10^6/\text{ft}$  that appears to exceed the peak values for the other two cases at a higher unit Re number. However, the peaks for those cases are not available because the highest temperatures in the peak region exceeded the maximum limit of the phosphor system by  $t = 1.8$  s into those runs. This result is evident from the heat transfer coefficients that dropped to zero in the peak region for those two cases. The  $Re = 2.1 \times 10^6/\text{ft}$  case was selected for the majority of the wind tunnel runs in the current study because the

peak heat transfer data typically does not exceed the phosphor range prior to  $t = 1.8$  s into a run. Data in the peak region goes off-scale in the first recorded image for the  $Re = 4.1 \times 10^6/\text{ft}$  wind tunnel run, so this flow condition is not suitable for the cases considered during this study. Peak heat transfer data is available later in the run for a  $Re = 1.1 \times 10^6/\text{ft}$  condition, but the required flow total pressure and total temperature to achieve this condition necessitate a significantly longer set-up time for each of these runs, which means fewer wind tunnel runs can be conducted and less data can be collected during the same amount of time in the wind tunnel. For this reason, only two wind tunnel runs at a  $Re = 1.1 \times 10^6/\text{ft}$  were conducted in the current investigation. The data obtained during the  $Re = 1.1 \times 10^6/\text{ft}$  and  $Re = 4.1 \times 10^6/\text{ft}$  wind tunnel runs for the Type IV interaction will be discussed further in this section.

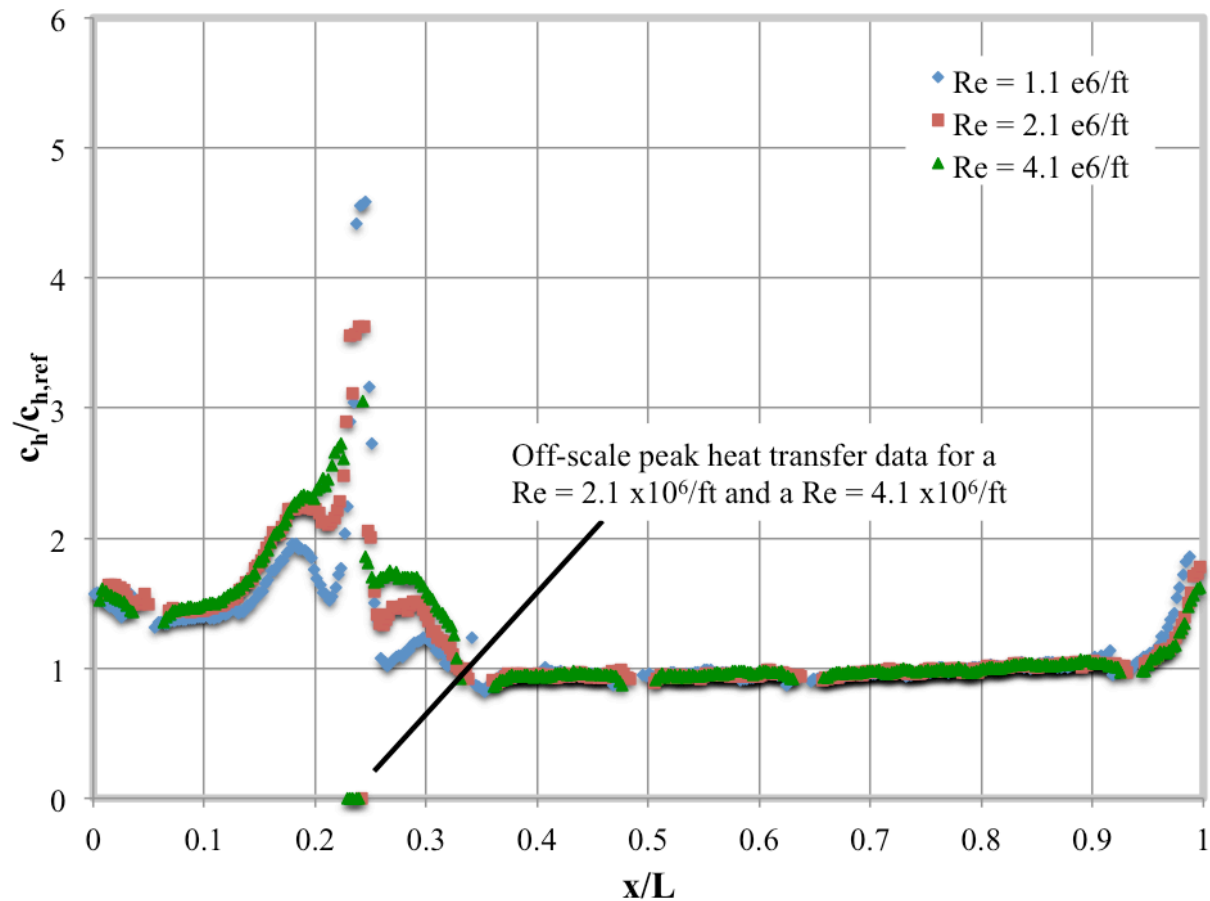


**Figure 5-72.** Non-dimensional heat transfer coefficients from the IHEAT code for the  $Re$  number sweep (considering  $Re = 1.1, 2.1$  and  $4.1 \times 10^6/\text{ft}$ ) for a 0.25 in-radius test article at a  $-15^\circ$  AoA.

Phosphor thermography temperature data is available much later into the run for the  $Re = 1.1 \times 10^6/\text{ft}$  case. Therefore, the leading-edge heat transfer coefficient plots included in Figure 5-75 to Figure 5-82 provide a comparison between 1D and 2D heat transfer analyses at two frames later in this run (Frames 102 and 138). Phosphor thermography data is typically reduced using a 1D semi-infinite analysis (IHEAT) at or near these two frames.



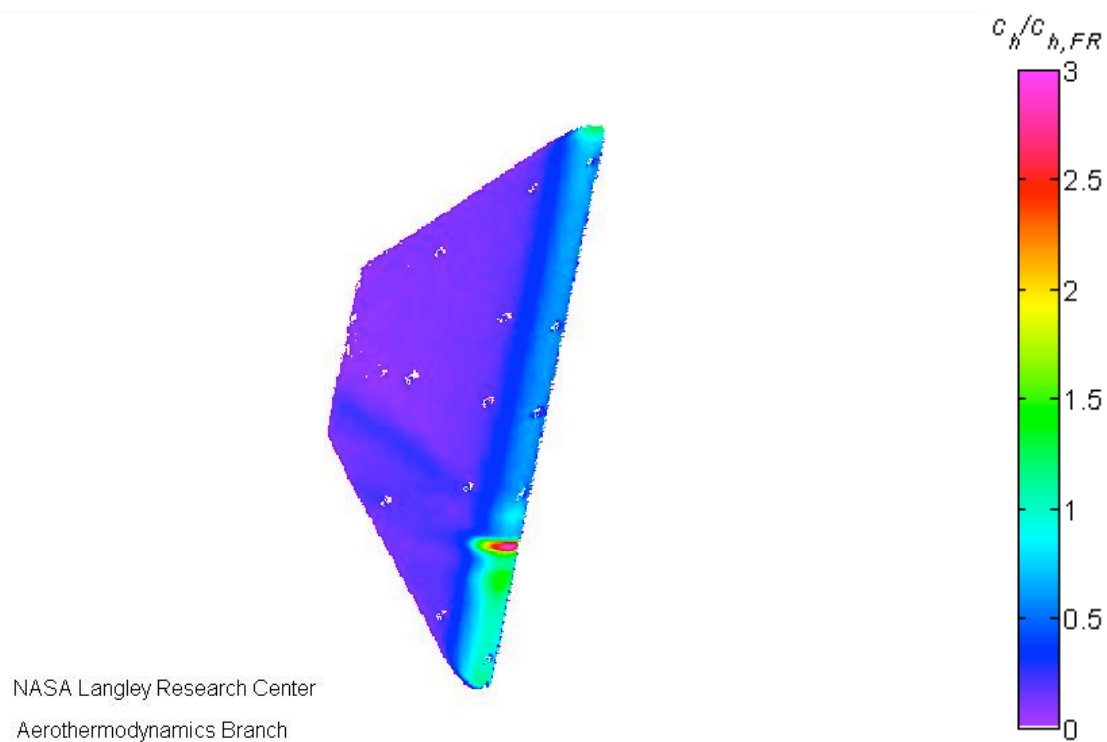


**Figure 5-73.** Run 43: IHEAT  $c_h/c_{h,FR}$  contour map for the 0.25 in-radius test article at a  $-15^\circ$  AoA and a  $Re = 1.1 \times 10^6/ft$ .

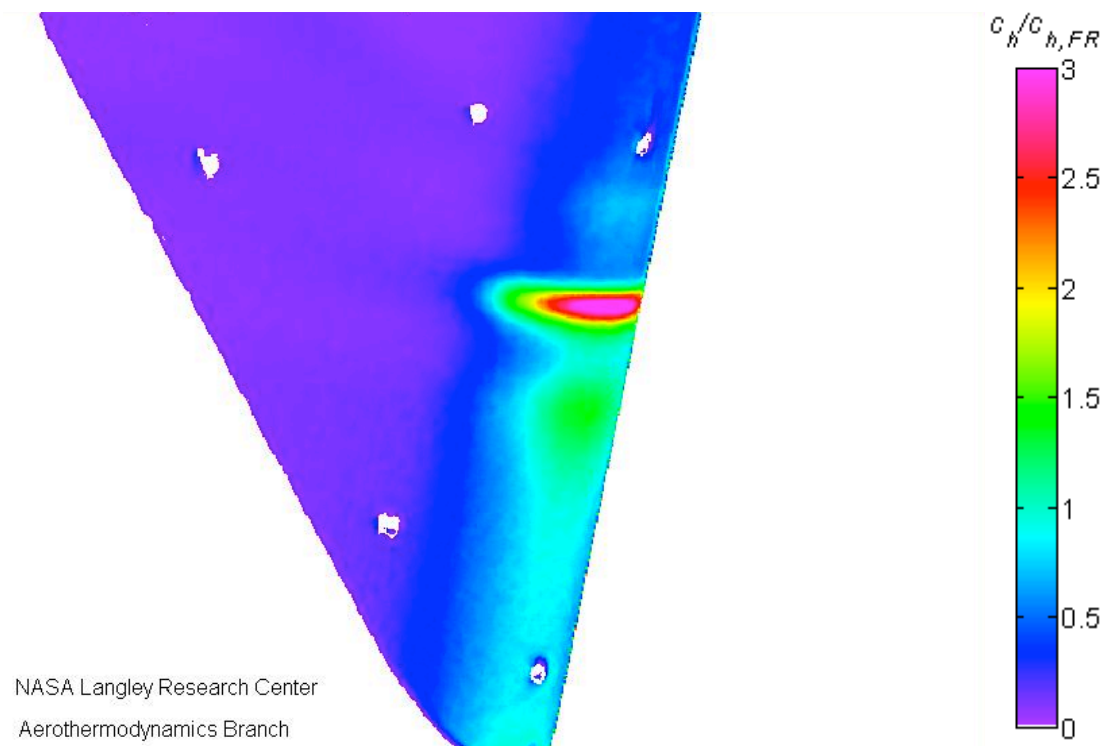


**Figure 5-74.** Run 44: IHEAT  $c_h/c_{h,FR}$  contour map for the 0.25 in-radius test article at a  $-15^\circ$  AoA and a  $Re = 1.1 \times 10^6/ft$  (zoomed in).

The plots in Figure 5-75 and Figure 5-78 show dimensional, enthalpy-based heat transfer coefficients along the leading edge for a 0.25 in-radius test article at a  $-15^\circ$  AoA with a flow unit Re number of  $1.1 \times 10^6/\text{ft}$  at times 3.4 s and 4.6 s into Run 43, respectively. The data in Figure 5-76, Figure 5-77, and Figure 5-79 present non-dimensional heat transfer coefficients for the same sets of data. The input data to the FV codes for this run is changed from every frame to every sixth frame (0.2 s apart) of the recorded surface temperature data obtained during Run 43 since the heat transfer coefficients are analyzed later in the run. Due to the grid convergence study, 1001 volumes are used in the radial direction, yielding a spacing of  $\Delta r = 2.5 \times 10^{-4}$  in. Data is extracted from 358 pixels along the leading edge, so that  $\Delta z = 1.12 \times 10^{-2}$  in.

In both sets of dimensional data, the heat transfer coefficients which are derived using a 2D method and which are away from the shock-interaction region (for  $x/L$  values between 0 and 0.2 and between 0.4 and 1.0, respectively) on the leading edge are lower than those calculated by either 1D method. This trend is reasonable since the 2D code accounts for lateral conduction, thereby reducing the heat assumed to travel in the radial direction since heat also moves to either side of the cell in the lateral direction. The peak heating augmentation due to the supersonic jet impingement for this Type IV interaction is narrower and higher for the 2D case than for the 1D cases. At  $t = 3.4$  s into the run, the 2D FV peak heat transfer is about 16% greater than the peak value from IHEAT.

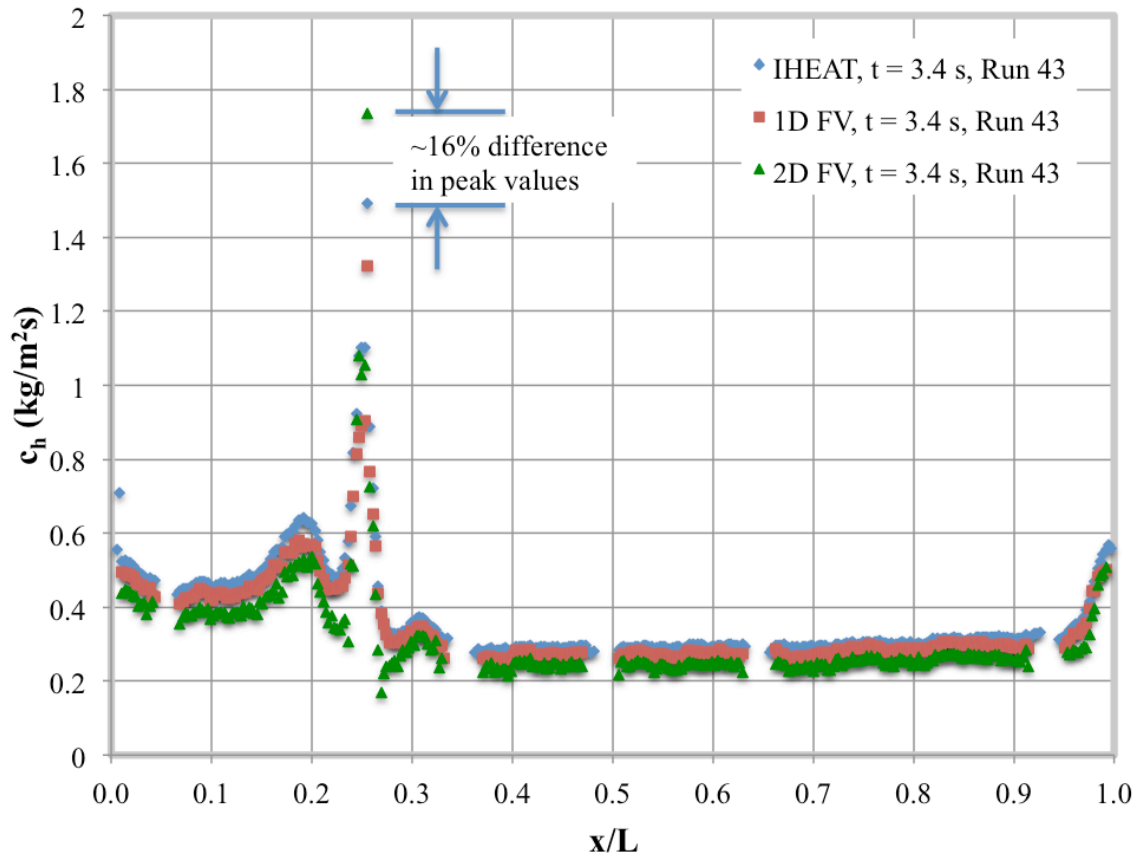


**Figure 5-75.** Enthalpy-based heat transfer coefficients at  $t = 3.4$  s from the IHEAT, 1D, and 2D FV codes for the 0.25 in-radius test article at a  $-15^\circ$  AoA and a  $\text{Re} = 1.1 \times 10^6/\text{ft}$ .

Non-dimensional data at  $t = 3.4$  s in Run 43 is shown in Figure 5-76. The 2D FV peak heat transfer coefficient is approximately 38% higher than the IHEAT peak value. By dividing the heat transfer coefficients by an average baseline value in all three of the methods, the coefficients in the regions away from the peak value collapse on top of each other, suggesting the offset due to the 1D and 2D FV methods is uniform in those regions.

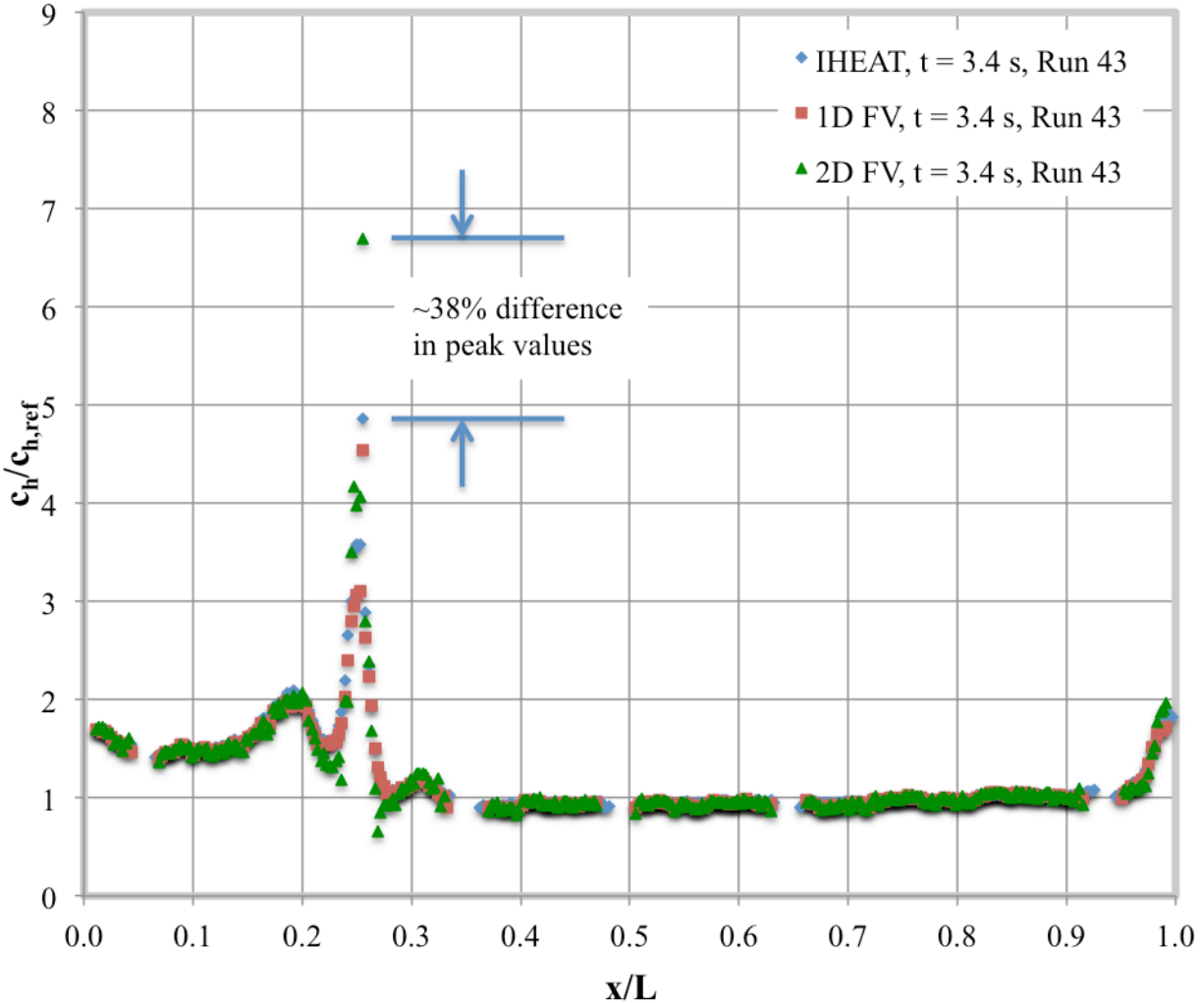


**Figure 5-76.** Non-dimensional heat transfer coefficients at  $t = 3.4$  s from the IHEAT, 1D, and 2D FV codes for the 0.25 in-radius test article at a  $-15^\circ$  AoA and a  $Re = 1.1 \times 10^6/ft$ .

Figure 5-77 to Figure 5-79 provide data at  $t = 4.6$  s. A comparison in Figure 5-77 demonstrates the potential error associated with reducing the zoomed-in data by a reference heat transfer coefficient from a separate wind tunnel run. The ranges for the x- and y-axes are modified in this plot to improve the visibility of the comparison. If an average of the zoomed-in heat transfer data from Run 44 (between  $x/L = 0.38$  and  $x/L = 0.41$ ) is used to obtain non-dimensional heat transfer coefficients, the peak heat transfer coefficient  $c_h/c_{h,ref}$  is 4.33. However, if the reference value from Run 43 (averaged over  $x/L = 0.75$  to  $x/L = 0.85$ ) is used, the peak  $c_h/c_{h,ref}$  is only 3.51.

This discrepancy is likely due to slight differences in the surface temperatures of the test articles in the region away from the peak heat transfer between the runs. If data in Run 44 in the region between  $x/L = 0.75$  and  $x/L = 0.85$  were available to be used for a reference, non-dimensional data from this run would likely lie somewhere between the two curves shown in the plot, since the heat transfer coefficients in the region from  $x/L = 0.38$  to  $x/L = 0.41$  are typically slightly higher than the coefficients farther up the leading edge. Some of the line cuts for the zoomed-in wind tunnel runs did not include heat transfer coefficients away from the peak value to use as a reference value to obtain non-dimensional data. For this reason, the reference values from the corresponding runs with zoomed-out data were used for all the zoomed-in runs to be consistent.

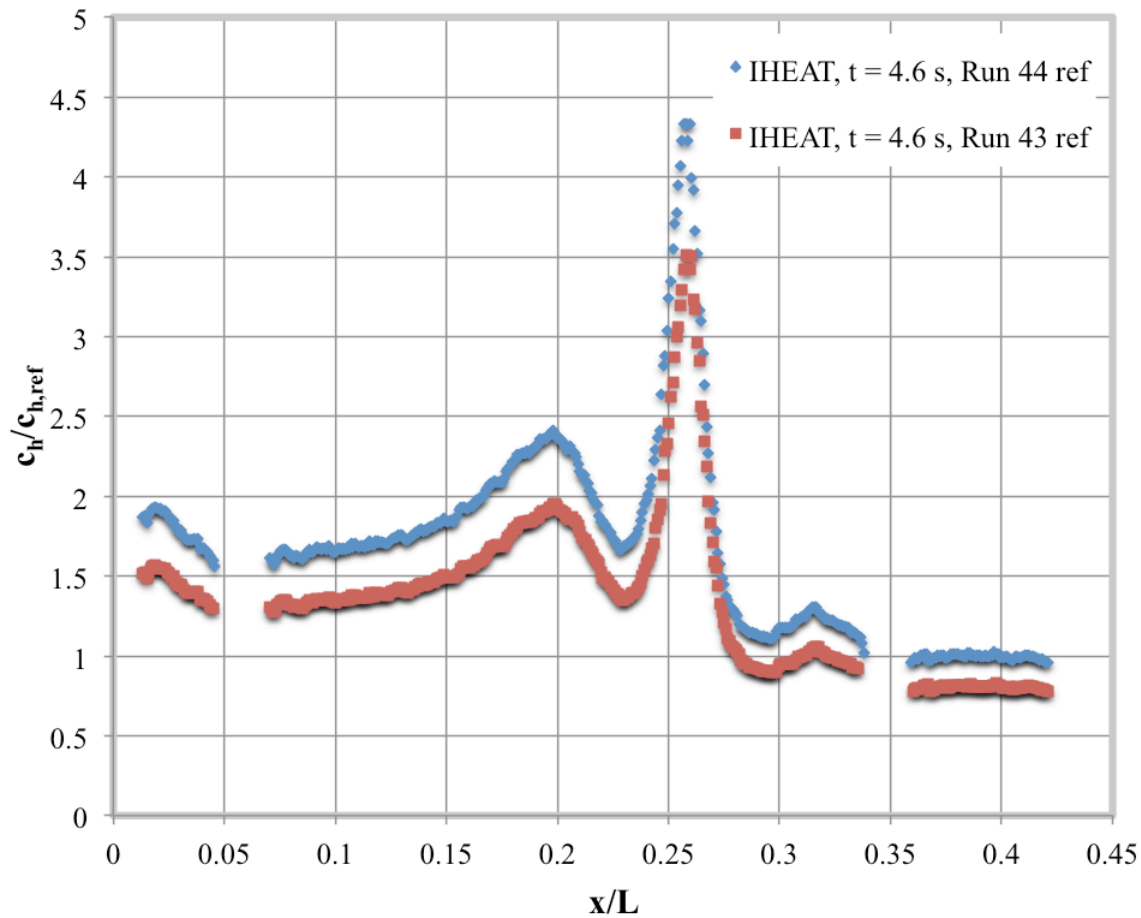


**Figure 5-77.** Heat transfer coefficients for the zoomed-in case at  $t = 4.6$  s from the IHEAT code for the 0.25 in-radius test article at a  $-15^\circ$  AoA and a  $Re = 1.1 \times 10^6/ft$  (using two different reference values).

The plot in Figure 5-78 shows the dimensional heat transfer coefficients at  $t = 4.6$  s for the same case at a  $-15^\circ$  AoA. The maximum value on the y-axis is only 1.4 for this plot to better show the differences between the dimensional line cuts. At this point in the run, the 2D peak heat transfer is about 20% greater than the IHEAT result. As expected, the difference between the IHEAT and 2D outputs increases later in the run due to errors associated with neglecting the lateral conduction and the semi-infinite assumption in IHEAT.

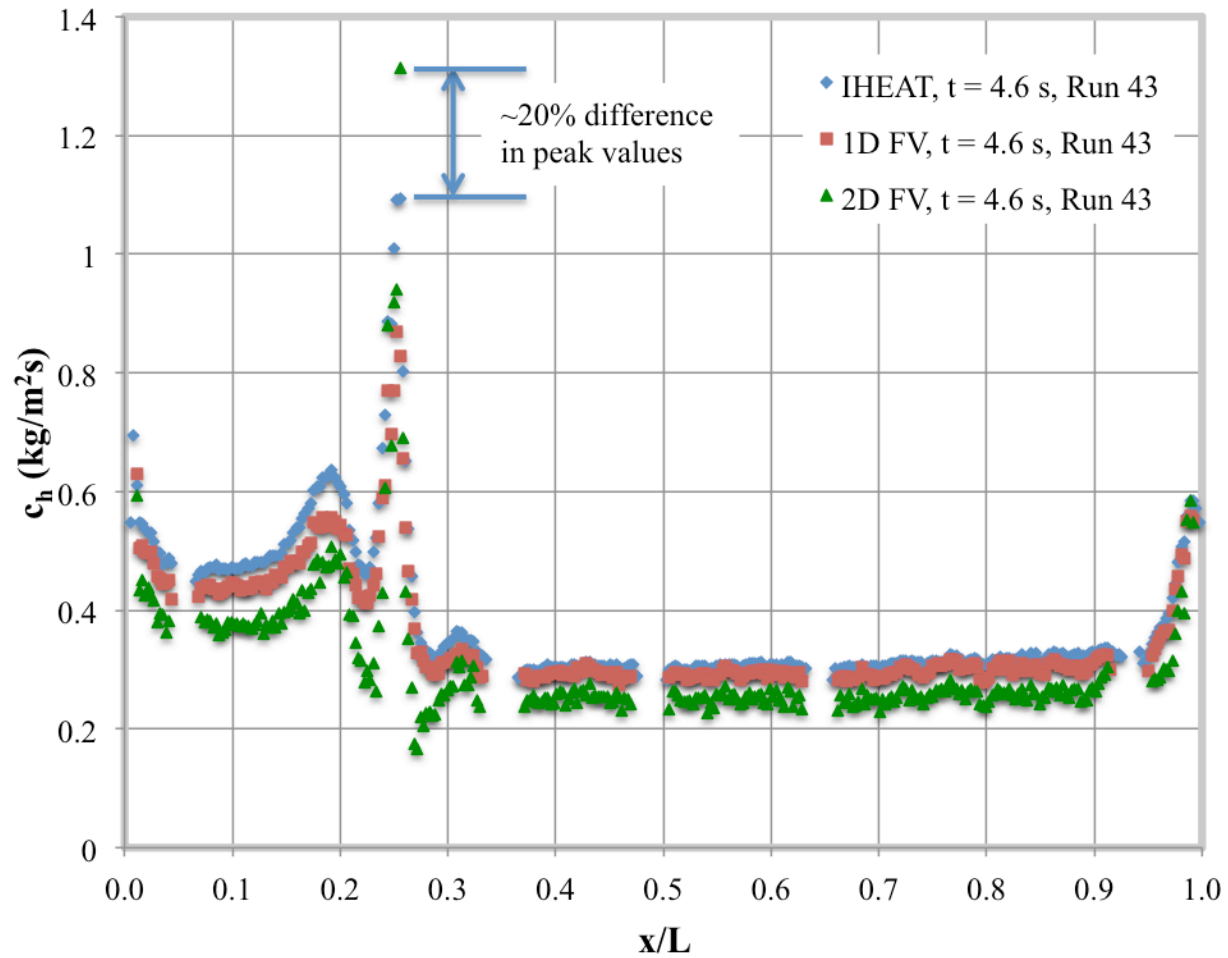


**Figure 5-78.** Enthalpy-based heat transfer coefficients at  $t = 4.6$  s from the IHEAT, 1D, and 2D FV codes for the 0.25 in-radius test article at a  $-15^\circ$  AoA and a  $Re = 1.1 \times 10^6/ft$ .

Again, the difference between the heat transfer peaks for the 2D and IHEAT codes increases when the heat transfer coefficients are divided by a reference value to yield non-dimensional data. In Figure 5-79, the 2D FV peak heat transfer augmentation is about 47% higher than the IHEAT peak value. Berry and Nowak [8] predicted a peak heating augmentation in the Type IV interaction produced by a  $-15^\circ$  AoA for a  $Re = 2.1 \times 10^6/ft$  would increase 43%, from about 7 to 10, if lateral conduction effects were considered in the heat transfer analysis.

The largest differences between the 1D and 2D heat transfer output data occur at the peaks and valleys in these line cuts, as Walker and Scott state in reference [34]. This trend is evident in Figure 5-76 and Figure 5-79 since the non-dimensional heat transfer coefficients derived in the 1D and 2D analyses are very similar in the regions away from the peaks and valleys associated with the shock-shock interaction.

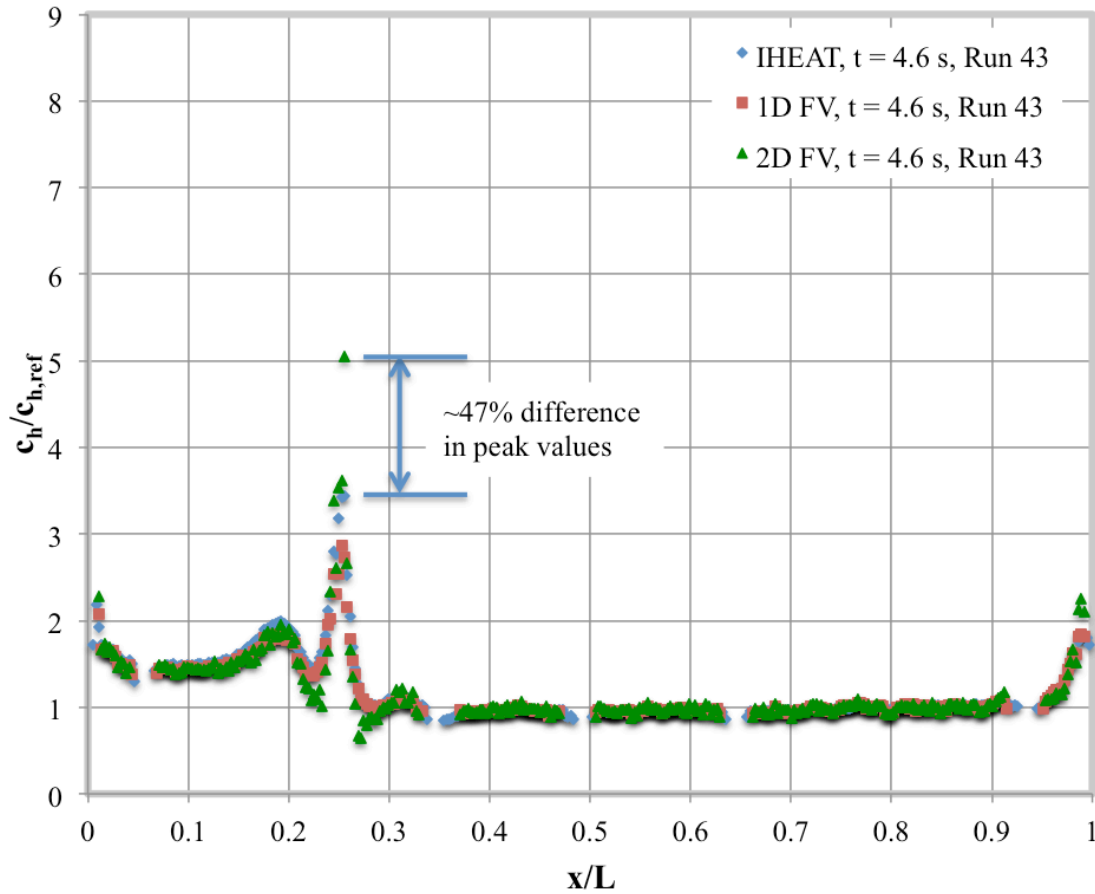


**Figure 5-79.** Non-dimensional heat transfer coefficients at  $t = 4.6$  s from the IHEAT, 1D, and 2D FV codes for the 0.25 in-radius test article at a  $-15^\circ$  AoA and a  $Re = 1.1 \times 10^6/ft$  (zoomed-in and regular).

The plot in Figure 5-80 shows a comparison of the peak region between the non-dimensional heat transfer coefficients output for runs 43 and 44. The x-axis positions for the zoomed-in data from run 44 were manually shifted by a small amount to try to better align the peak location between the two runs. As the data in the plot indicates, the spatial resolution of the zoomed-in data is about 3.8 times greater than the resolution for the zoomed-out or “regular” heat transfer data. As described in section 3.5.2.1, the maximum spacing between consecutive data points in a line cut for the zoomed-out data is 0.015 in, compared to about 0.004 in for the zoomed-in data. In both cases, the spatial resolution of the data from this global thermal imaging technique is sufficient to capture the peak heat transfer due to the shock-shock interaction.

The increased spatial resolution of the zoomed-in data provides additional confidence that the observed trends in the zoomed-out data properly represent the heat transfer behavior in each case. The relative peak values for the zoomed-in cases compared to the zoomed-out cases is affected by how the zoomed-in data is converted to non-dimensional values in the comparisons for the shock-shock interactions in the preceding line cut plots. In absolute heat transfer coefficients, the zoomed-in data more clearly provides a comparison between the results for different spatial resolutions.



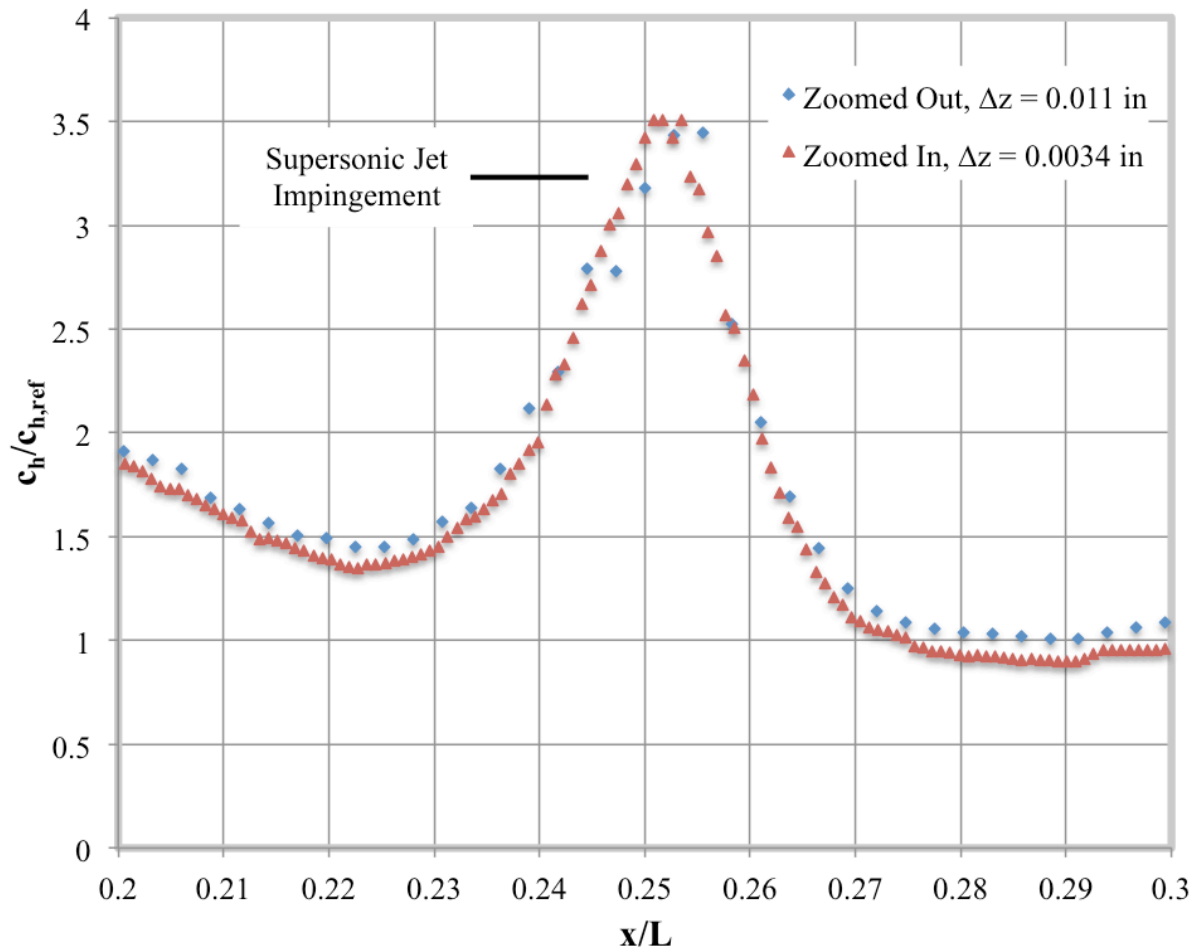


**Figure 5-80.** Spatial resolution of IHEAT zoomed-in versus zoomed-out non-dimensional peak heat transfer coefficients at  $t = 4.6$  s for the 0.25 in-radius test article at a  $-15^\circ$  AoA and a  $Re = 1.1 \times 10^6/\text{ft}$ .

One wind tunnel run was conducted using the 0.25 in-radius test article at a  $-15^\circ$  AoA and a flow unit  $Re$  number of  $4.1 \times 10^6/\text{ft}$ . The contour map for this case in Figure 5-81 demonstrates the difficulty associated with using a higher  $Re$  number. The data in the peak heating region is not available 1.8 s into the run as evidenced by white pixels in the region where the supersonic jet impinges on the test article.

The line cut data in Figure 5-82 confirms this data loss early in the run. The gap in the data near the supersonic jet impingement at  $x/L = 0.23$  indicates the temperatures in this region exceed the maximum limit of the phosphor system so that the peak is not available for this case. The contour map and line cut data are presented at Frame 54 to be consistent with the other runs. However, for this run, an additional line cut was extracted from Frame 48 ( $t = 1.6$  s), which is the first image recorded as the test article reaches the wind tunnel centerline. The gap in data persists for that frame so this line cut is not presented. Since very little data is available in the shock impingement region for this  $Re$  number, a repeat run with these test conditions and the camera zoomed in on the interaction region was not conducted.

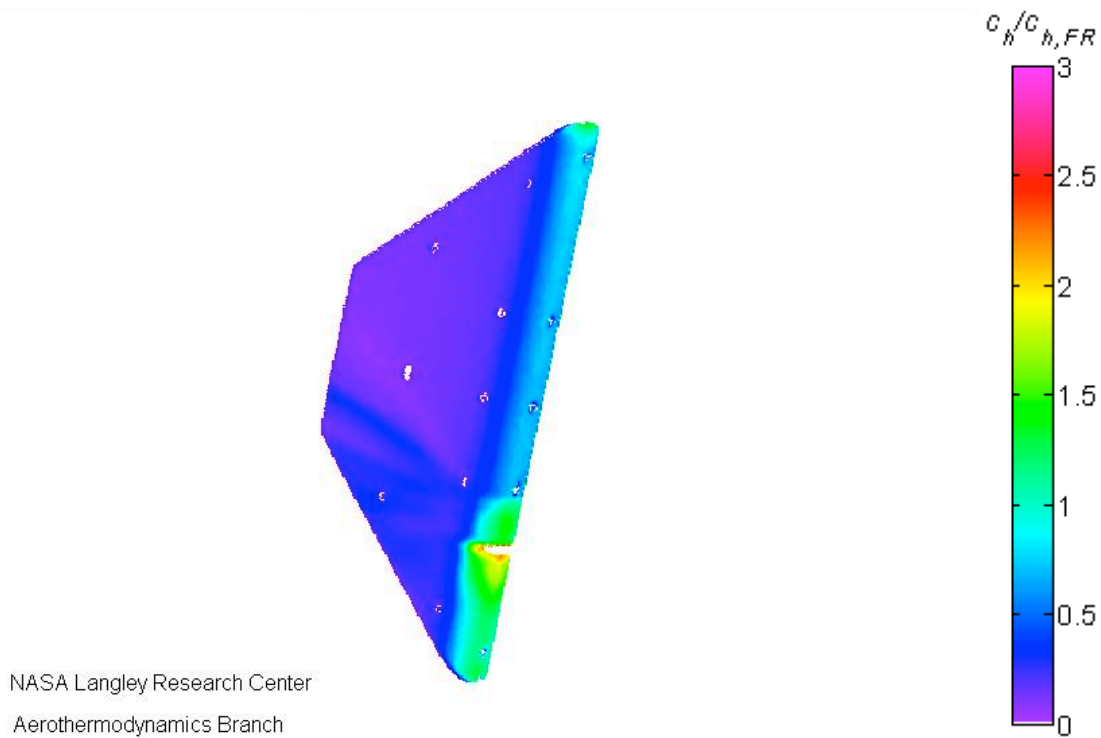


**Figure 5-81.** Run 42: IHEAT  $c_h/c_{h,FR}$  contour map for the 0.25 in-radius test article at a  $-15^\circ$  AoA and a  $Re = 4.1 \times 10^6/ft$ .

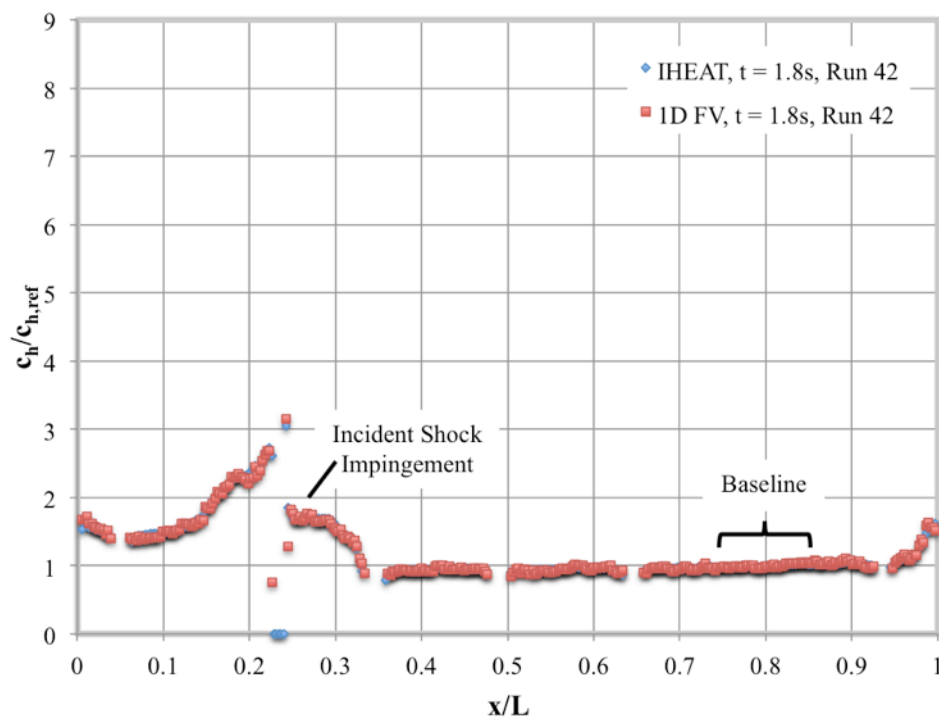


**Figure 5-82.** Non-dimensional heat transfer coefficients from the IHEAT and 1D FV codes for the 0.25 in-radius test article at a  $-15^\circ$  AoA and a  $Re = 4.1 \times 10^6/ft$ .

### 5.3. Preliminary results from the LAURA CFD analysis

A CFD simulation assuming Mach 5.96, laminar flow is conducted in LAURA [51] to approximate the boundary layer thickness over the flat plate shock generator for a  $9^\circ$  SG angle. A grid is generated in Pointwise® to represent the 17 in-long flat plate with a sharp leading edge angled at  $9^\circ$  to the flow. This simulation output is shown in Figure 5-83 and in the contour map in Figure 5-84. The maximum boundary layer thickness at the back of the plate is 2 mm or  $7.9 \times 10^{-2}$  in. Based on this result, a separation of 0.5 in between the lower tip of the test article and the flat plate SG is sufficient to ensure that the flat plate boundary layer does not interact with the flow over the test article.

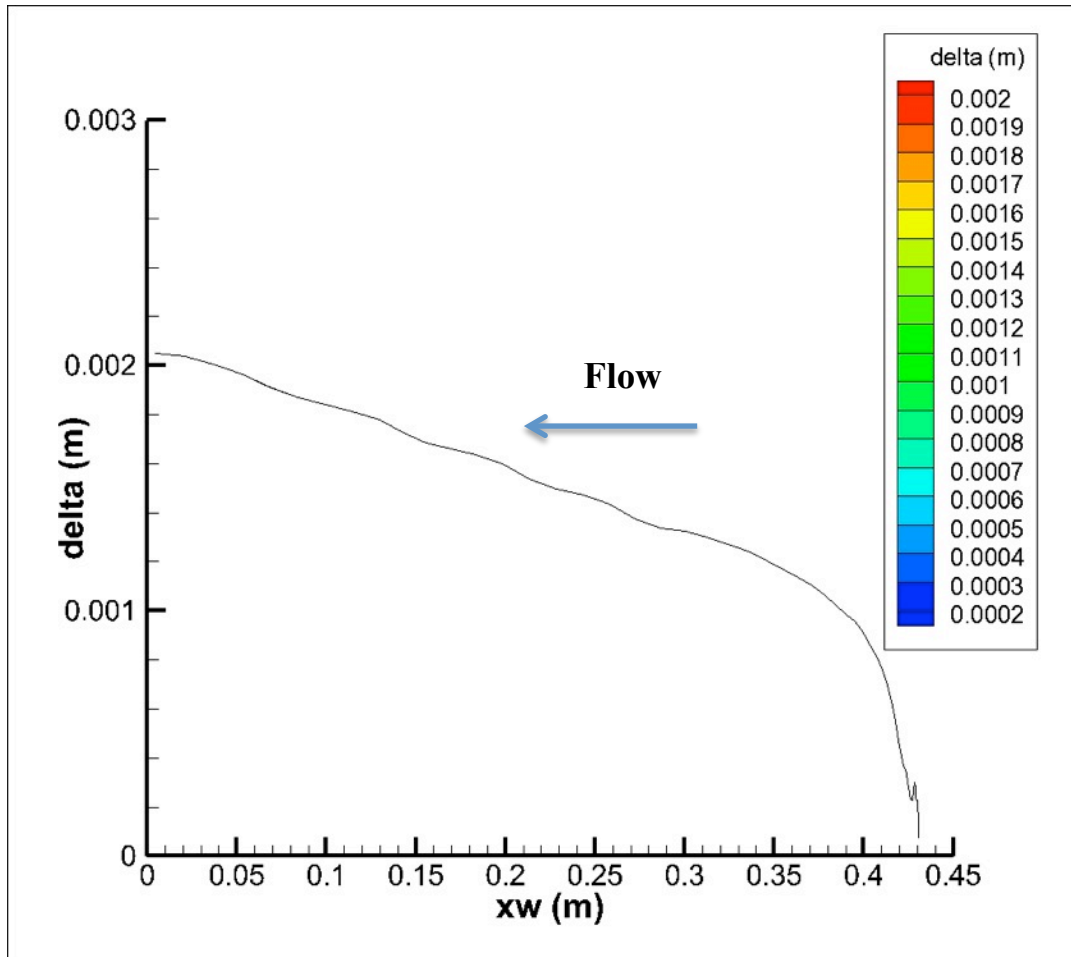


**Figure 5-83.** Flat plate SG boundary layer thickness ( $\Delta$ ) with the leading edge at 0.43 m (17 in) upstream of the Mach 5.96 flow (LAURA simulation).

The LAURA code was modified to simulate shock-shock interactions similar to the experimental configurations. Using the Pointwise® grid generation program and a CAD model of the 0.25 in-radius test article, meshes are created with higher grid resolution in the expected shock-shock interaction region. The grids extend from the stagnation line on the leading edge around the circumference to the centerline of the nose of the test article, and extrude about 0.5 in into the free-stream flow.

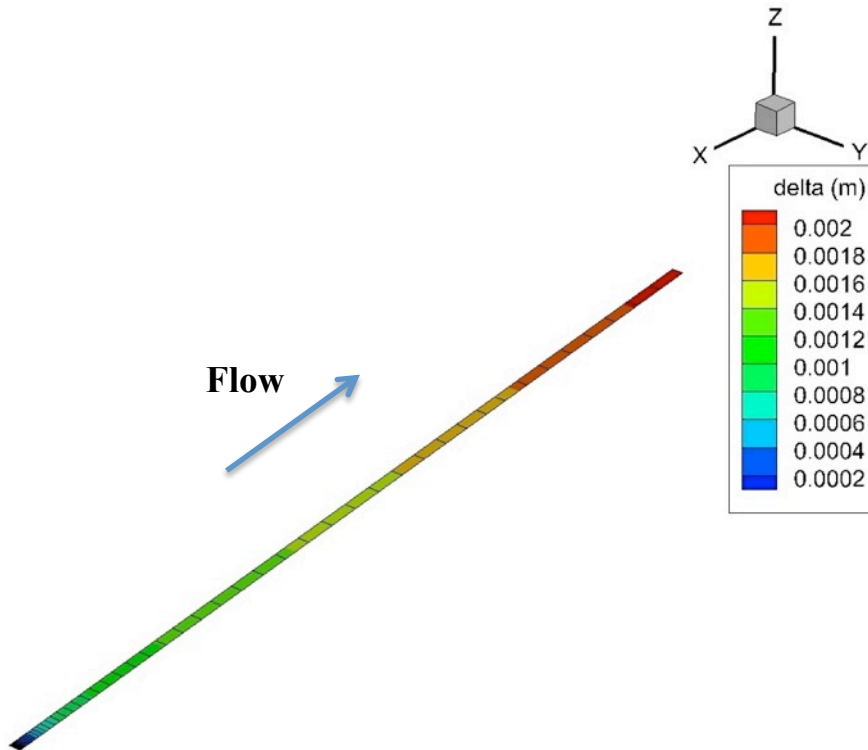


**Figure 5-84.** Contour map of the boundary layer thickness ( $\Delta$ ) over the flat plate SG in Mach 5.96 flow (LAURA simulation).

An initial simulation is run with Mach 5.96, perfect gas flow parameters set in LAURA to obtain a converged solution of the test article bow shock. Then, additional parameters are set to simulate the conditions in the free-stream flow behind an incident shock produced by the flat plate SG (the 2D wedge in the test hardware) with a sharp leading edge [45]. These conditions are specified in the boundary conditions where the impinging shock is expected to intersect the edge of the grid based on oblique shock theory. Due to time constraints, only simulations for two AoA ( $-15^\circ$  and  $-25^\circ$ ) with the smallest test article geometry (0.25 in nose radius) were completed in this study. Numerical schlieren and heat transfer data for these cases are discussed below.

Equation (5-1) is used to calculate the flow density gradients in Tecplot with output data from the LAURA simulations for time-accurate simulations of the two shock-shock interactions. This calculation is called “numerical schlieren” because the changes in the free-stream flow density from a numerical simulation of a given shock-shock interaction are shown as visual density gradients similar to the output for the experimental schlieren technique. This numerical schlieren expression is derived for the case with the test article at a  $-25^\circ$  AoA, and is applied to the  $-15^\circ$  AoA case to obtain reasonably clear density gradients, as given by

$$\text{Numerical schlieren} = \exp\left(\frac{-200 \text{Density Gradient Magnitude}}{189808}\right) \quad (5-1)$$

The numerical schlieren images shown in Figure 5-85 and Figure 5-86 are derived from the output of LAURA simulations for an assumed axisymmetric model of the cylindrical leading edge of the 0.25 in-radius test article. The test articles in these figures are angled at either  $-15^\circ$  or  $-25^\circ$  as appropriate. The density gradients both on the surface of the test articles and in a slice perpendicular to the leading edge (along the stagnation line) are shown in these images.

Although the images are obtained in consecutive order during a time-accurate solution, frames at arbitrary times are included in Figure 5-85 to show the progression of the Type IV simulation over time. The images labeled a through d show an unsteady density gradient circling above the incident shock that resembles the circular density gradient in the experimental zoom schlieren for this type of interaction. Unlike in the experimental schlieren, the later images in this figure show this density gradient eventually diminishes, which suggests the grid resolution in that region may not be sufficiently fine for the CFD simulation to capture that flow phenomenon as time progresses. These images also show small vortices traveling down near the leading edge of the test article, which are not visible in the experimental zoom schlieren, but these flow features also disappear later in the time-accurate simulation. In images g to i, the shock triangles of the supersonic jet are clearly distinguishable.

The images in Figure 5-86 for the Type III interaction are shown in consecutive order from the time-accurate simulation. From this small segment of time, the reflected shock that impinges on the test article surface bounces around as an unsteady rotating density gradient (shown in all the images) interferes with the shear layer from the triple point, causing the shear layer to attach and detach from the surface. Based on a video compiled from these images, the simulated flow in this rotating region moves up the leading edge near the surface, out from the leading edge toward the shear layer, down through the shear layer, and then back toward the test article surface. This motion agrees with the upward direction of the streamlines on the oil flow images above the attachment of the shear layer in the shock interaction region. The flow below the reflected shock moves in vortices down the leading edge. Only in image g does the shear layer attach to the surface of the test article in this segment of frames of the Type III interaction.

Density gradients in both figures for the two types of interactions are seen going around the surface of the test article as well, as indicated by the heat transfer contour maps and oil-flow images from the wind tunnel experiment. Gradients in the flow density behind the test articles in the experimental zoom schlieren suggest these numerical features exist, although changes in flow density on the test article surface cannot be detected by the experimental zoom schlieren method.

The incident shock shown in the stagnation plane does not continue through the bow shock to impinge on the leading edge in either the Type III or Type IV numerical schlieren images. This flow behavior suggests the incident shock intersects the bow shock at the triple point but then wraps around the bow shock to produce a line segment with the same slope as the incident shock that lies between the bow shock and the test article in the experimental zoom schlieren images.

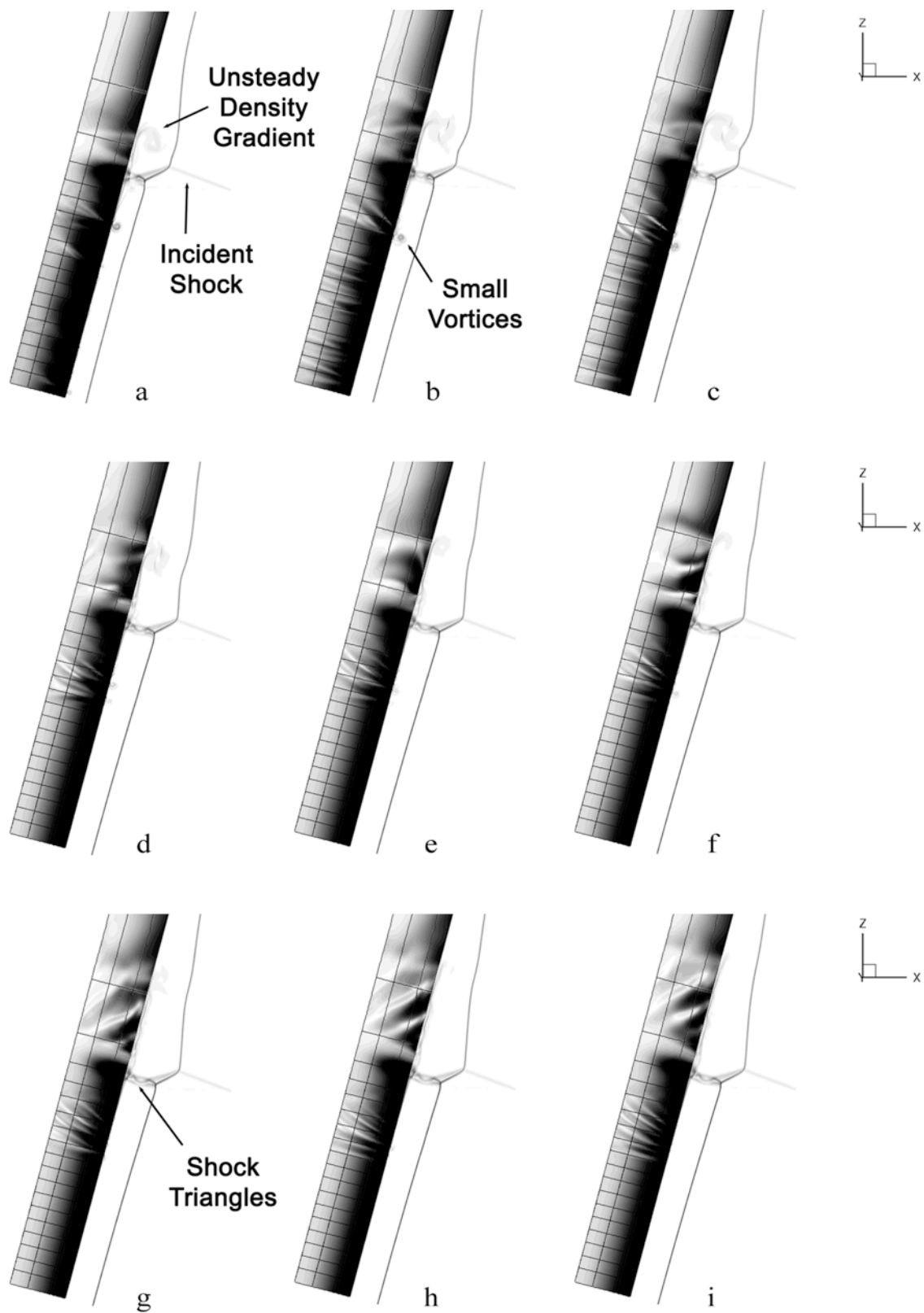


**Figure 5-85.** Numerical schlieren images for the 0.25 in-radius test article at a  $-15^\circ$  AoA with a  $9^\circ$  SG (samples of non-consecutive frames in the time-accurate LAURA simulation).



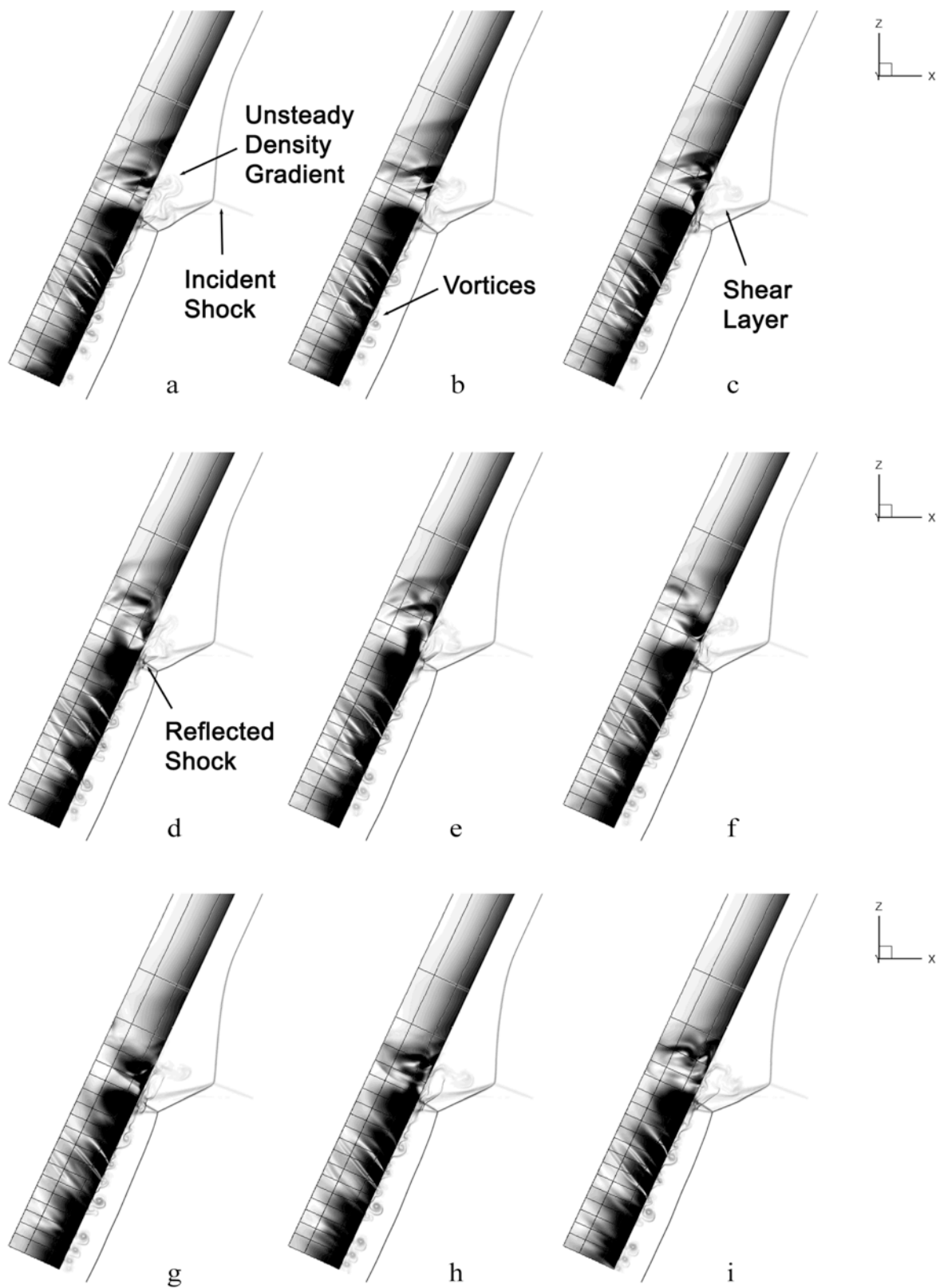


**Figure 5-86.** Numerical schlieren images for the 0.25 in-radius test article at a  $-25^\circ$  AoA with a  $9^\circ$  SG (samples of consecutive frames in the time-accurate LAURA simulation).

Figure 5-87 shows representative snapshots of the heat transfer to the leading edge of the test article obtained in the 3D-axisymmetric LAURA simulations. Heat transfer images from the time-accurate simulations are compiled into videos. Only half of the cylindrical leading edge is included in these simulations, assuming the heat transfer to be similar on either side of the stagnation line (to the right of the two contour maps). The mesh is not shown in these images to avoid obscuring the features of the heat transfer. The leading edges for the two cases have been rotated to view the contour map more clearly. The right image corresponds to the  $-25^\circ$  AoA case, and the left image to the  $-15^\circ$  AoA case. Similar to the experimental data, the peak for the  $-25^\circ$  AoA is broader than the narrow peak for the  $-15^\circ$  case.

The video of the heat transfer from which the  $-25^\circ$  image is captured shows unsteadiness just above the broad peak and along the leading edge below the peak. The peak at times disappears and bounces around in this video, which agrees with the experimental and numerical schlieren evidence of the shear layer attaching and detaching from the test article. Features in the image below the broad peak travel down the leading edge during the video, similar to the vortices seen in the numerical schlieren. Similarly, the unsteadiness above the narrower peak heat transfer for the  $-15^\circ$  case is evident in the right image. This peak is more stable (does not disappear) as expected from the behavior of the supersonic jet in the experimental and numerical schlieren.

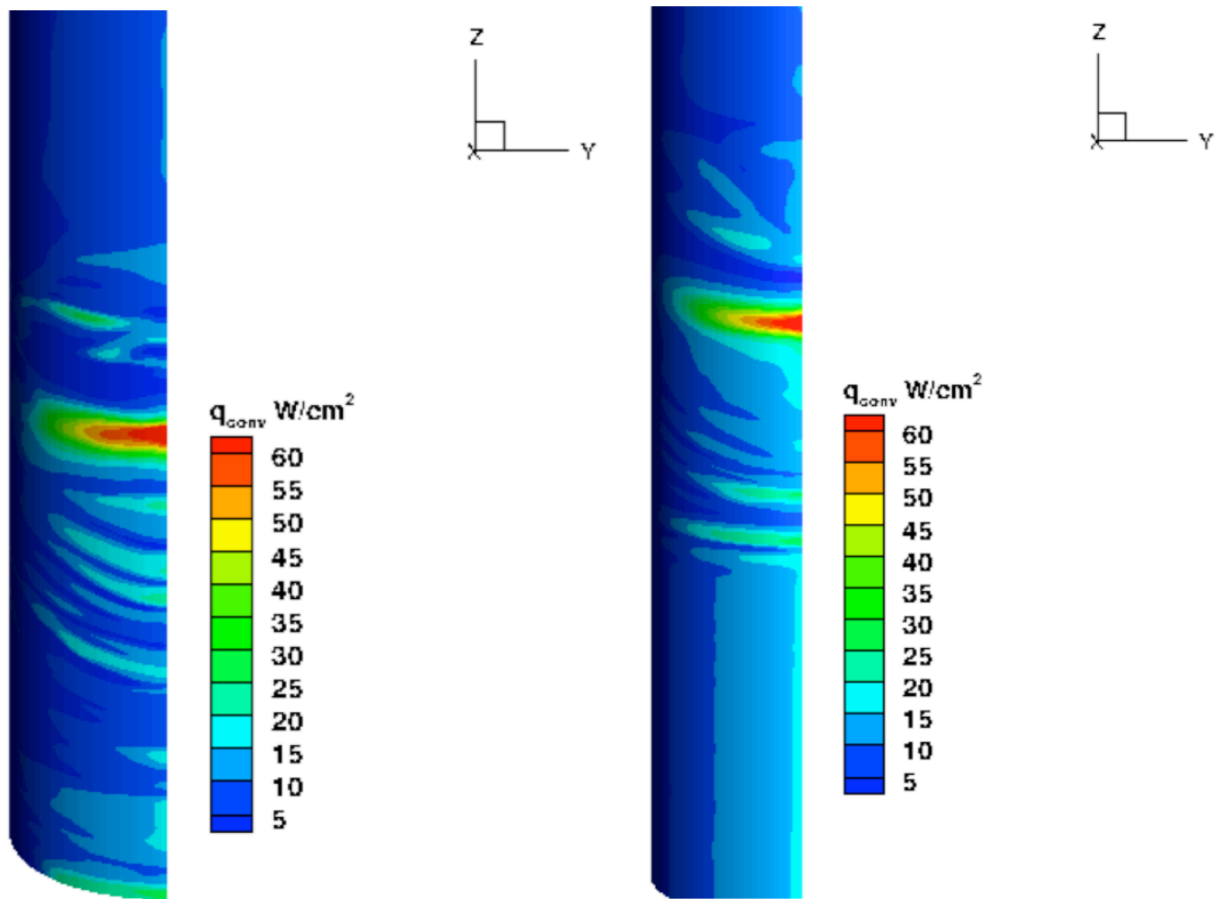


**Figure 5-87.** Heating patterns on the axisymmetric leading edge of the 0.25 in-radius test article at a  $-25^\circ$  AoA (left image) and a  $-15^\circ$  AoA (right image) early in the LAURA simulations.

Figure 5-88 shows contour maps of the density and pressure variables for the  $-15^\circ$  AoA simulated shock interaction. Lines perpendicular to the leading edge in these images represent the blocks of cells in the  $j$  coordinate (the  $z$  direction in the left image) in the Pointwise® grid. Only the surface plane of the mesh is included in both images, with the planes in the free-stream flow above the surface hidden from view. A slice in the  $k$  dimension (perpendicular to the leading edge and parallel to the  $x$ - $z$  plane) is included in the pressure image that is properly oriented at a  $-25^\circ$  AoA. The mesh in the  $k$  dimension is not included in the image due to the high density of equally spaced 511 cells in that direction. The slice included in the numerical schlieren images is also shown the pressure contour map. These images show a few streamlines estimated in the CFD simulation in the free-stream flow and on the surface of the test article.

The streamlines in Figure 5-88 begin at the stagnation line on the leading edge of the test article and travel down and around the cylindrical surface away from the stagnation line. These streamlines match the oil-flow pattern observed near the top of the leading edge on this test article in Figure 5-22. A similar comparison exists between the upper streamlines on the test article leading edge in CFD at a  $-25^\circ$  AoA and the oil flow pattern in Figure 5-30. The fiducial mark locations will be utilized in further comparisons of the experimentally and computationally observed streamlines in a later study.

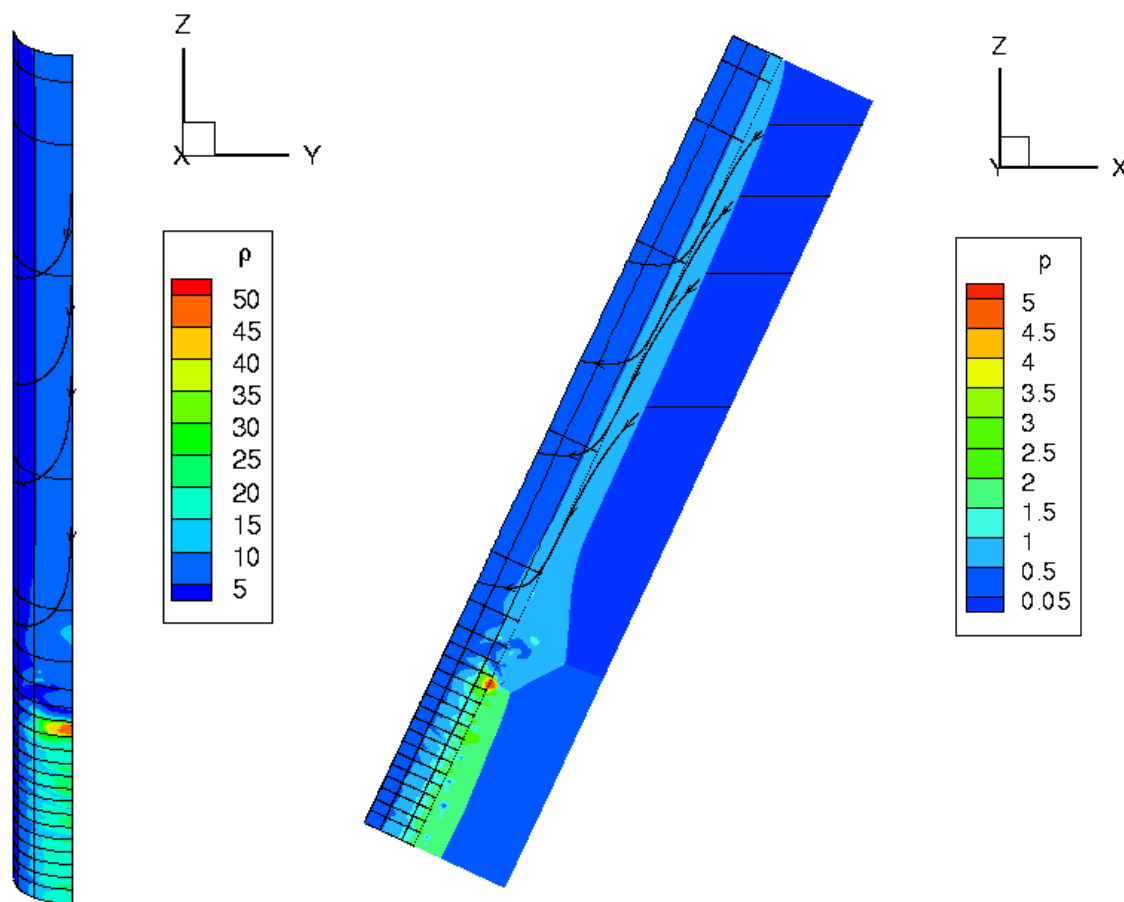


**Figure 5-88.** Density and pressure contour maps with a few streamlines along an axisymmetric leading edge for the 0.25 in-radius test article at a  $-15^\circ$  AoA (from the LAURA simulation).

## 6. Chapter 6: Conclusions

This chapter presents conclusions drawn from the results of the experimental shock-shock interaction study and supplemental computational analysis. A brief discussion of anticipated future work to further investigate the results of this study is included at the end of this chapter.

### 6.1. Characterization of shock-shock interactions

The Type IVa ( $0^\circ$  AoA), direct Type IV ( $-15^\circ$  AoA), and Type III ( $-25^\circ$  AoA) shock-shock interactions were investigated in the current study using three test article geometries with leading edge radii of 0.25 in, 0.50 in, and 0.75 in, respectively. Flow density gradients were observed experimentally using a zoom schlieren technique for these three shock-shock interactions and were modeled computationally through numerical schlieren for the latter two types of shock-shock interactions. The general heating behavior for these three interactions were assessed using 1D IHEAT contour maps generated by phosphor thermography. The leading-edge heat transfer coefficients were analyzed for each run configuration using 1D semi-infinite and FV methods and for two cases using a 2D FV method.

Walker and Scott [34] and Wright et al. [3] recommend a greater spatial resolution than 0.015 in between gages to experimentally resolve the heat transfer peak for the Type IV interaction. The spatial resolution of the temperature and heat transfer data in the phosphor thermography line cuts ranges from 0.004 in to 0.015 in. Therefore, the data resolution in each run is better than or comparable to the discrete temperature gage spacing on test articles utilized in previous shock-shock interaction studies. This improved spatial resolution is significant because the heat transfer data from these line cuts display similar trends to equivalent cases in [8], confirming the assertion in [8] that a 0.015 in gage spacing is sufficient to accurately capture the narrow peak heat transfer augmentation due to a Type IV interaction. The zoomed-in line cut data yielded lower than expected results for the non-dimensional peak heat transfer data in several cases, likely due to the limitation on the reference values used to convert the heat transfer data for these runs to non-dimensional values.

Based on these observations, the Type IVa shock-shock interaction exhibits the smallest peak heating augmentation, with a maximum non-dimensional heat transfer coefficient between 1.4 and 1.8 times higher than the baseline value for the smallest to the largest test articles. The shape of this interaction, with two small peaks separated by a trough, resembles the thin-film data from [8]. The Type IV interaction produces a narrow, steep heat transfer peak due to an impinging supersonic jet. For this type of interaction, the maximum peak heating augmentation over the undisturbed heat transfer is between at least 5 for the smallest test article and 7.7 for the largest test article. The Type III interaction does not include a supersonic jet as in the other two cases, but instead yields a broader peak in the heat transfer coefficients at the shear layer attachment point. The maximum value of these heat transfer coefficients ranged from at least 5.2 for the smallest test article to 8.5 for the largest test article. For both the Type III and IV interactions, the peak heat transfer coefficient for the 0.25 in-radius test article could not be calculated since the maximum temperature in the peak region exceeded the limit of the phosphor thermography system early in the run due to the high localized heat transfer.

The non-dimensional peak heat transfer for a given type of shock-shock interaction increases as the leading-edge radius increases, and the opposite trend occurs for the dimensional heat transfer coefficients. This reversal in the effect of the leading-edge radius occurs because the reference value used to convert the heat transfer coefficients to non-dimensional values changes in each run. As the leading-edge radius increases, the baseline heat transfer coefficients away from the shock-shock interaction region decrease. This trend yields a lower averaged reference value for the larger test articles, which amplifies the non-dimensional peak heat transfer augmentation compared to the smaller test article geometries.

Since the dimensional peak heat transfer coefficient decreases and the width of the peak region increases, the severity of the lateral temperature gradient diminishes with increasing leading-edge radius. Thus, the heat transfer gradient in the lateral direction also decreases so a 2D analysis that considers lateral conduction should be less essential for the test articles with larger leading edges, as was hypothesized. The effect of the leading-edge radius on the errors associated with a 1D heat transfer analysis could not be directly evaluated using the 2D FV code since the temperatures in the peak region for the smallest test article exceeded the phosphor limit for the Type III and IV interactions early in the wind tunnel runs.

## **6.2. Analysis of 1D and 2D heat transfer methods**

As predicted, lateral conduction effects influence heat transfer calculations when a strong temperature gradient in the lateral direction is present. Dimensionally, the peak heat transfer coefficient from a 2D FV analysis was approximately 20% higher than the result from a 1D semi-infinite for a Type IV interaction, which corroborates the findings in [34] for a shock-shock interaction case and in [37] for striation heating due to streams of injected gas. Thus, a multi-dimensional conduction analysis is necessary to account for lateral conduction in cases with large temperature gradients. For the case with a Type IVa interaction and, thus, smaller heating gradients in the lateral direction, the difference between the 1D and 2D results was likewise smaller.

The augmentation in the non-dimensional peak heat transfer predicted for a Type IV interaction at a  $Re = 1.1 \times 10^6/\text{ft}$  using a 2D ADI method is about 38% higher than the value predicted using the 1D semi-infinite IHEAT code at a point 3.4 s into Run 43, and the 2D peak is about 47% higher 4.6 s into the run. Berry and Nowak [8] predicted the non-dimensional peak heating augmentation produced by a Type IV interaction at a  $-15^\circ$  AoA for  $Re = 2.1 \times 10^6/\text{ft}$  would increase 43% from about 7 to 10 if lateral conduction effects were considered in the heat transfer analysis. This difference between 1D and 2D heat transfer results is a reasonable estimate if the results for the  $Re = 1.1 \times 10^6/\text{ft}$  case can be extrapolated to a  $Re = 2.1 \times 10^6/\text{ft}$  case. This difference in the heating profiles suggests a 2D heat transfer analysis is required to ensure conservative heating estimates when the heating profile is not nearly uniform due to impinging shock interference or another source of strong temperature gradients.

## **6.3. Comparison of experimental and computational visualization techniques**

The features exhibited in the experimental zoom schlieren and the simulated numerical schlieren videos (from the LAURA simulations) are similar. For the Type IV interaction, the shock train

(shock triangles formed by reflected shocks within the supersonic jet) and the unsteady density gradient above the incident shock are visible features in the videos acquired with the experimental and computational schlieren techniques. The changes in the position of the shear layer relative to the surface of the test article, as well as the vortices moving down near the leading edge at the bottom of the test article, are visible for the Type III interaction in some of the experimental schlieren videos. These features are more clearly represented in the numerical schlieren for the Type III interaction. The general shape of the streamlines near the top of the leading edge for the cases with the test article inclined at either a  $-15^\circ$  or a  $-25^\circ$  AoA in the LAURA simulations is confirmed by similar streamlines on the oil flow test articles.

#### **6.4. Future work**

The current research can be expanded further and improved in the following ways. Additional comparisons between the 1D and 2D heat transfer analyses in this study require temperature data in the peak interaction region between three and four seconds into the wind tunnel runs. With the current phosphor thermography data, the 2D code can be utilized only for the  $Re = 1.1 \times 10^6/ft$  cases and the wind tunnel runs with a test article at a  $0^\circ$  AoA. In the other runs in the current study, the test article surface temperatures in the shock-interaction region exceed the maximum limit of the current phosphor system early in the run. Therefore, a new phosphor system that can sense higher temperatures is necessary to measure temperatures in the interaction region later in a run that lasts at least six seconds. Currently a higher-temperature phosphor system is being developed, but this phosphor was not available at the time of the test. An IR system with a resolution of at least  $640 \times 480$  pixels, to measure the narrow peaks for the Type IV interactions, also would be sufficient to obtain this temperature data.

One planned improvement to the 2D code is to change the geometry subroutine to accommodate additional shapes beyond a cylindrical leading edge. The 2D code also may be expanded to a 3D analysis method by switching from the ADI method to the Douglas-Gunn algorithm and implementing a 3D mapping program to directly correlate the heat transfer data to the test article geometry. A 3D analysis of shock-shock interactions also includes further work with the updated version of LAURA to run laminar and turbulent simulations for finer, adapted grids for the 0.25 in-radius and additional geometries.



## References

- 1 Andreadis, Dean. *Scramjet Engines Enabling the Seamless Integration of Air & Space Operations*. Pratt & Whitney, West Palm Beach, FL.
- 2 Edney, Barry. *Anomalous Heat Transfer and Pressure Distributions on Blunt Bodies at Hypersonic Speeds in the Presence of an Impinging Shock*. The Aeronautical Research Institute of Sweden, Stockholm, 1968.
- 3 Wright, M. J., Nowak, R. J., Berry, S. A., Glass, C. E., and Candler, G. V. *Numerical/Experimental Investigation of 3-D Swept Fin Shock Interactions*.
- 4 Merski, N. R. Global Aeroheating Wind-Tunnel Measurements Using Improved Two-Color Phosphor Thermography Method. *Journal of Spacecraft and Rockets*, 36, 2 (March-April 1999), 160-170.
- 5 Merski, N. R. Reduction and Analysis of Phosphor Thermography Data with the IHEAT Software Package. ( 1997), AIAA.
- 6 Hollis, Brian R. *User's Manual for the One-Dimensional Hypersonic Experimental Aero-Thermodynamic (1DHEAT) Data Reduction Code*. Hampton, Virginia, August 1995.
- 7 Berger, Karen T., Rufer, Shann J., Kimmel, Roger, and Adamczak, David. Aerothermodynamic Characteristics of Boundary Layer Transition and Trip Effectiveness of the HIFiRE Flight 5 Vehicle. (San Antonio, TX 2009), AIAA. June 22-250.
- 8 Berry, Scott A. and Nowak, Robert J. Fin Leading-Edge Sweep Effect on Shock-Shock Interaction at Mach 6. *Journal of Spacecraft and Rockets*, 34, 4 (July-August 1997), 416-425.
- 9 Watts, Joe D. *Flight Experiment with Shock Impingement and Interference Heating on the X-15-2 Research Airplane*. Washington D.C., 1968.
- 10 Lumpkin, Forrest E., Marichalar, Jeremiah J., and Stewart, Benedicte D. *High Fidelity Simulations of Plume Impingement to the International Space Station*. NASA Johnson Space Center, Houston, TX, 2012.
- 11 McGraw-Hill *Encyclopedia of Science and Technology: "Shock wave"*. The McGraw-Hill Companies, Inc. [online resource]. [updated 2005, cited 13 May 2013]. URL: <http://www.answers.com/topic/shock-wave> (Answers.com).
- 12 Hill, Philip G. and Peterson, Carl R. *Mechanics and Thermodynamics of Propulsion*. Addison-Wesley, Reading, 1992.
- 13 Keyes, J. W. and Hains, F. D. *Analytical and Experimental Studies of Shock Interference Heating in Hypersonic Flows*. Washington D.C., May 1973.
- 14 Burcham, Jr., Frank W. and Nugent, Jack. *Local Flow Field around a Pylon-Mounted Dummy Ramjet Engine on the X-15-2 Airplane for Mach Numbers from 2.0 to 6.7*. NASA, Washington D.C., 1970.
- 15 Harwood, William. *Board Hearing Shows Work to Piece Together Known Data*. Spaceflight Now Inc. [online resource]. [updated Mar 2003, cited Mar 2013]. URL: <http://www.spaceflightrightnow.com/shuttle/sts107/030318hearing/>.
- 16 Bertin, John J. and Cummings, Russell M. Fifty years of hypersonics: where we've been, where we're going. *Progress in Aerospace Sciences*, 39 (2003), 511-536.
- 17 *Great Images in NASA (GRIN): Close-Up STS-107 Launch*. NASA [online resource]. [updated Sep 2009, cited Mar 2013]. URL: <http://grin.hq.nasa.gov/IMAGES/MEDIUM/GPN-2003-00080.jpg>.

- 18 Gehman, Harold W. *Columbia Accident Investigation Board Report, Vol. 3, Appendix E.2*. Government Printing Office, Washington, D. C., Aug 2003. pp. 53-55.
- 19 *Great Images in NASA (GRIN): Grid with Columbia's Debris*. NASA [online resource]. [updated Sep 2009, cited Mar 2013]. URL: <http://grin.hq.nasa.gov/IMAGES/MEDIUM/GPN-2003-00081.jpg>.
- 20 *NASA "Hyper-X" Program Demonstrates Scramjet Technologies*. NASA Dryden Flight Research Center. [updated Dec 2009, cited Mar 2013]. URL: <http://www.nasa.gov/centers/dryden/news/FactSheets/FS-040-DFRC.html>.
- 21 La Rue, Maj. Nori. *NASA X-43A Rockets to Mach 9.8 at Edwards*. Air Force Flight Test Center Public Affairs [online resource], Edwards, CA, [updated Nov 2004, cited Mar 2013]. URL: <http://www.af.mil/news/story.asp?id=123009242>.
- 22 Barnstorff, Kathy. *X-51A Makes Longest Scramjet Flight*. NASA Langley Research Center [online resource], Hampton, VA, [updated May 2010, cited Mar 2013]. URL: <http://www.nasa.gov/topics/aeronautics/features/X-51A.html>.
- 23 Wieting, A. Shock interference heating in scramjet engines. (Orlando, FL October 1990), AIAA.
- 24 Nowak, R., Holden, M., and Wieting, A. Shock/shock interference on a transpiration cooled hemispherical model. (Seattle, WA June 1990), AIAA.
- 25 Stewart, James R., Thareja, Rajiv R., Wieting, Allan R., and Morgan, Ken. Application of Finite Element and Remeshing Technique to Shock Interference on a Cylindrical Leading Edge. (Reno, Nevada 1988), AIAA.
- 26 Vemaganti, G. and Wieting, A. Application of a Finite Element Algorithm for High Speed Viscous Flows Using Structured and Unstructured Meshes. (Seattle, WA June 1990), AIAA.
- 27 Bushnell, Dennis M. *Interference Heating on a Swept Cylinder in Region of Intersection with a Wedge at Mach Number 8*. NASA, Washington, D.C., 1965.
- 28 Bushnell, Dennis M. *Effects of Shock Impingement and Other Factors on Leading-Edge Heat Transfer*. NASA, Washington, D.C., April 1968.
- 29 Beckwith, Ivan E. and Gallagher, James J. *Local Heat Transfer and Recovery Temperatures on a Yawed Cylinder at a Mach Number of 4.15 and High Reynolds Numbers*. NASA, Washington D.C., 1961.
- 30 Carter, Howard S. and Carr, Robert E. *Free-Flight Investigation of Heat Transfer to an Unswept Cylinder Subjected to an Incident Shock and Flow Interference from an Upstream Body at Mach Numbers up to 5.50*. NASA Langley Research Center, Washington, D.C., 1961.
- 31 Hiers, Robert S. and Loubsky, William J. *Effects of Shock-Wave Impingement on the Heat Transfer on a Cylindrical Leading Edge*. NASA, Washington, D.C., 1967.
- 32 Fay, J. A. and Riddell, F. R. Theory of Stagnation Point Heat Transfer in Dissociated Air. *Journal of the Aeronautical Sciences*, 25, 2 (February 1958), 73-85, 121.
- 33 Trumble, Kerry A. and Candler, Graham V. Flow Control of Swept Fin Shock Interactions by Laser-Induced Plasmas. (Reno, Nevada Jan. 2006), AIAA.
- 34 Walker, D. Greg and Scott, Elaine P. The Effects of Lateral Conduction on Heat Flux Estimation from Surface Temperature Measurements. (Albuquerque, NM June 1998), AIAA/ASME.

- 35 Tannehill, John C., Anderson, Dale A., and Pletcher, Richard H. *Computational Fluid Mechanics and Heat Transfer, Second Edition*. Taylor & Francis, Philadelphia, PA, 1997.
- 36 Walker, D. Greg. *Estimation of Unsteady Nonuniform Heating Rates from Surface Temperature Measurements*. Virginia Tech, Blacksburg, VA, 1997.
- 37 Daryabeigi, K., Berry, S. A., Horvath, T. J., and Nowak, R. J. Finite Volume Numerical Methods for Aeroheating Rate Calculations from Infrared Thermographic Data. *Journal of Spacecraft and Rockets*, 43, 1 (January-February 2006), 54-62.
- 38 Rufer, Shann J. Experimental and Computational Study of Underexpanded Jet Impingement Heat Transfer. (San Antonio, TX June 2009), AIAA.
- 39 Coblish, Joseph J., Smith, Michael S., Hand, Terrell, Candler, Graham V., and Nompelis, Ioannis. Double-Cone Experiment and Numerical Analysis at AEDC Hypervelocity Wind Tunnel No. 9. (Reno, NV Jan 2005), AIAA.
- 40 Micol, J. R. Langley Aerothermodynamics Facilities Complex: Enhancements and Testing Capabilities. (Reno, NV Jan. 1998), AIAA.
- 41 Rhode, Matthew N. and DeLoach, Richard. Hypersonic Wind Tunnel Calibration Using the Modern Design of Experiments. (Tucson, AZ 2005), AIAA.
- 42 Rufer, Shann J. and Berridge, Dennis C. Pressure Fluctuation Measurements in the Langley 20-Inch Mach 6 Wind Tunnel. ( 2012), AIAA.
- 43 Hollis, Brian R. and Collier, Arnold S. Turbulent Aeroheating Testing of Mars Science Laboratory Entry Vehicle. *Journal of Spacecraft and Rockets*, 45, 3 (2008), 417-427.
- 44 Hollis, Brian R. *Real-Gas Flow Properties for NASA Langley Research Center Aerothermodynamic Facilities Complex Wind Tunnels*. Raleigh, North Carolina, 1996.
- 45 Devenport, William J. and Ford, Adam. *Compressible Aerodynamics Calculator*. Department of Aerospace and Ocean Engineering, Virginia Tech [online resource], Blacksburg, VA, [updated 2012, cited Mar 2013]. URL: <http://www.dept.aoe.vt.edu/~devenpor/aoe3114/calc.html>.
- 46 Buck, G. M., Powers, M. A., Griffith, M. S., Hopkins, J. W., Veneris, P. H., and Kuykendoll, K. A. *Fabrication of 0.0075-Scale Orbiter Phosphor Thermography Test Models for Shuttle RTF Aeroheating Studies*. Hampton, Virginia, November 2006.
- 47 Patel, Naresh. January 14, 2103. personal communication.
- 48 McBride, Bonnie J., Gordon, Sanford, and Reno, Martin A. *Coefficients for Calculating Thermodynamic and Transport Properties of Individual Species*. NASA, Oct. 1993.
- 49 Burden, Richard L. and Faires, J. Douglas. *Numerical Analysis: Eighth Edition*. Thomson, Brooks/Cole, Belmont, CA, 2005.
- 50 Incropera, Frank P., DeWitt, David P., Bergman, Theodore L., and Lavine, Adrienne S. *Fundamentals of Heat and Mass Transfer, Sixth Ed*. John Wiley & Sons, New York, 2007.
- 51 Mazaheri, A., Gnoffo, P. A., Johnston, C. O., and Kleb, B. *LAURA Users Manual: 5.4-54166*. May 2011.
- 52 Merski, N. R. *An Improved Two-Color Relative-Intensity Phosphor Thermography Method for Hypersonic Wind Tunnel Aeroheating Measurements*. Hampton, Virginia, May 2002.

## A. Appendix A: Thermal properties

Macor® test articles instrumented with thin-film gages were used during Test 6692. Thermophysical Properties Research Laboratory, Inc. (TPRL) measured the thermal conductivity,  $k$ , and specific heat,  $c_p$  of Macor® over a range of temperatures, as shown in Table A-1. IHEAT uses curve fits to account for the changes in these thermal properties with temperature. The 1D and 2D FV codes implement linear interpolation to calculate the thermal properties for a Macor® substrate material.

**Table A-1.** Thermal conductivity ( $k$ ) and specific heat ( $c_p$ ) of Macor®.

$T$ (K)	$k$ (W/m-K)	$c_p$ (J/kg-K)
296.15	1.567	828
323.15	1.570	859
373.15	1.583	911
473.15	1.612	993
573.15	1.637	1064
673.15	1.652	1121
773.15	1.652	1164
873.15	1.641	1203
973.15	1.633	1238
1073.15	1.624	1269

Fused silica was used to make the heat transfer test articles utilized in the current wind tunnel experiment. Similar lists of temperature dependent thermal properties for this substrate material are included in Table A-2 for  $\alpha_d$  and Table A-3 for  $k$ . The columns labeled 1D, 2D and 3D in Table A-2 and 1K, 2K and 3K represent three separate test articles used to measure the respective thermal properties (with “D” for diffusivity measurements and “K” for thermal conductivity measurements).

**Table A-2.** Fused silica thermal diffusivity versus temperature measurements [52].

Temperature (°C)	Thermal Diffusivity, $\alpha_d$ ( $\times 10^{-7} \text{ m}^2/\text{s}$ )		
	1D	2D	3D
Room	6.17	6.16	6.50
60	5.97	5.93	6.32
100	5.75	5.61	6.50
150	5.57	5.42	5.93
200	5.49	5.20	5.69
250	5.40	5.11	5.59
300	5.35	5.06	5.54

**Table A-3.** Fused silica thermal conductivity versus temperature measurements [52].

Temperature (°C)	Thermal Conductivity, $k$ (W/m-K)		
	1K	2K	3K
Room	6.17	6.16	6.50
60	5.97	5.93	6.32
100	5.75	5.61	6.50
150	5.57	5.42	5.93
200	5.49	5.20	5.69
250	5.40	5.11	5.59
300	5.35	5.06	5.54

Curve fits are used in the 1D and 2D FV codes to calculate  $k$ ,  $c_P$ , and the thermal diffusivity,  $\alpha_d$ , for fused silica, as given by

$$k = 6.6817(10^{-1}) - 6.8163(10^{-4})T \quad (\text{A-1})$$

$$\alpha_d = 9.212605264(10^{-7}) - 1.325181821(10^{-9})T + 1.12667(10^{-12})T^2 \quad (\text{A-2})$$

$$c_P = k/\rho\alpha_d \quad (\text{A-3})$$

Thermal properties for the phosphor coating are not included because the coating is assumed to be infinitely thin and, thus, to not affect the thermal properties of the substrate material in the test articles [5].

## **B. Appendix B: Test article measurements**

This appendix includes diagrams with dimensions of the test articles that were either machined or cast for the current study as well as the metal “inserts” that were bonded into the ceramic test articles to provide an interface for the bolts used to attach the test articles to the angle of attack adjuster connected to the sting. These diagrams are shown in Figure B-1 through Figure B-6, which begin on the following pages due to the size of the diagrams. Diagrams of the support hardware are also included in Figure B-7 to Figure B-14.

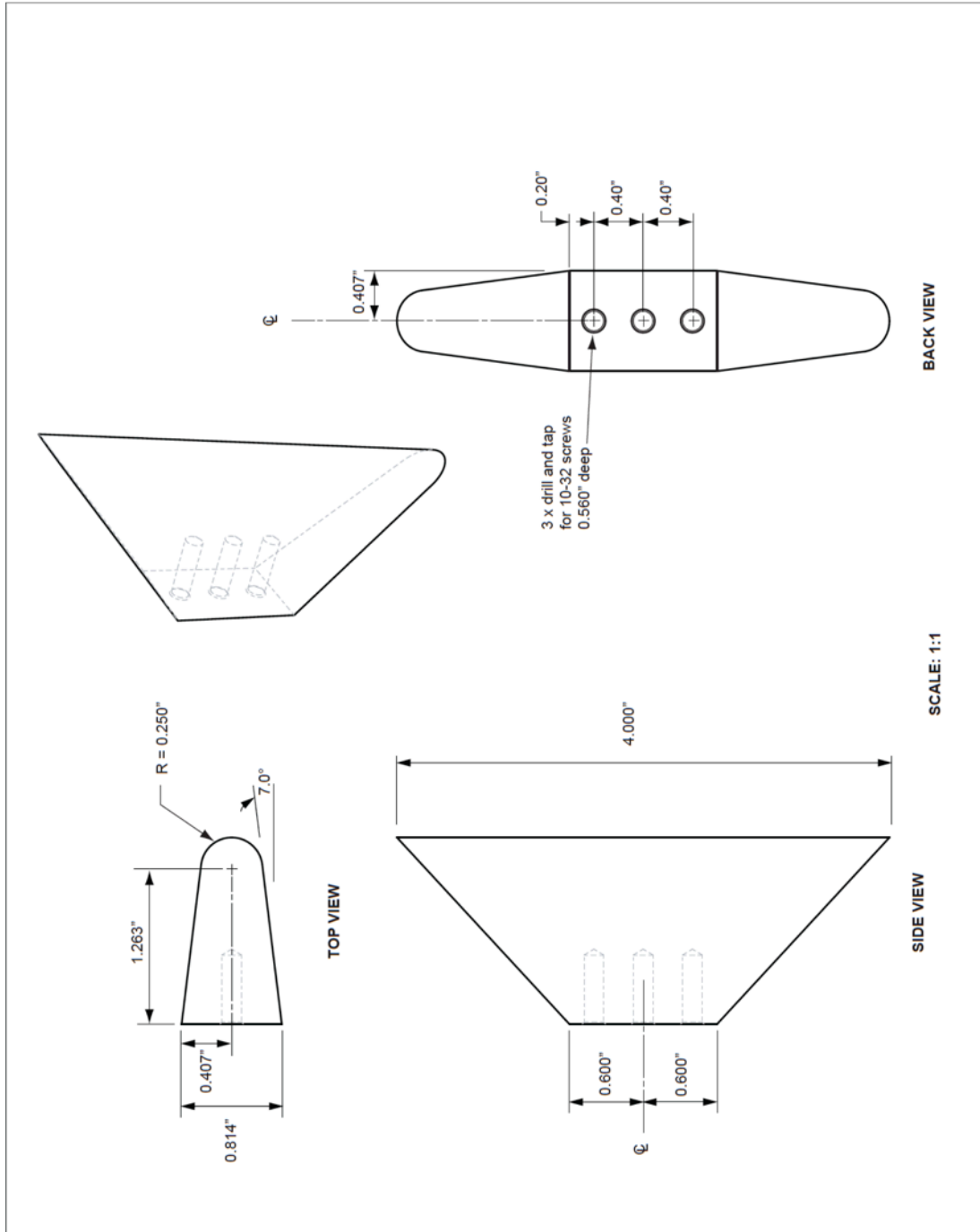


**Figure B-1.** Dimensions of metal oil flow test article with a 0.25 in-radius leading edge, machined from 15-5 stainless steel.



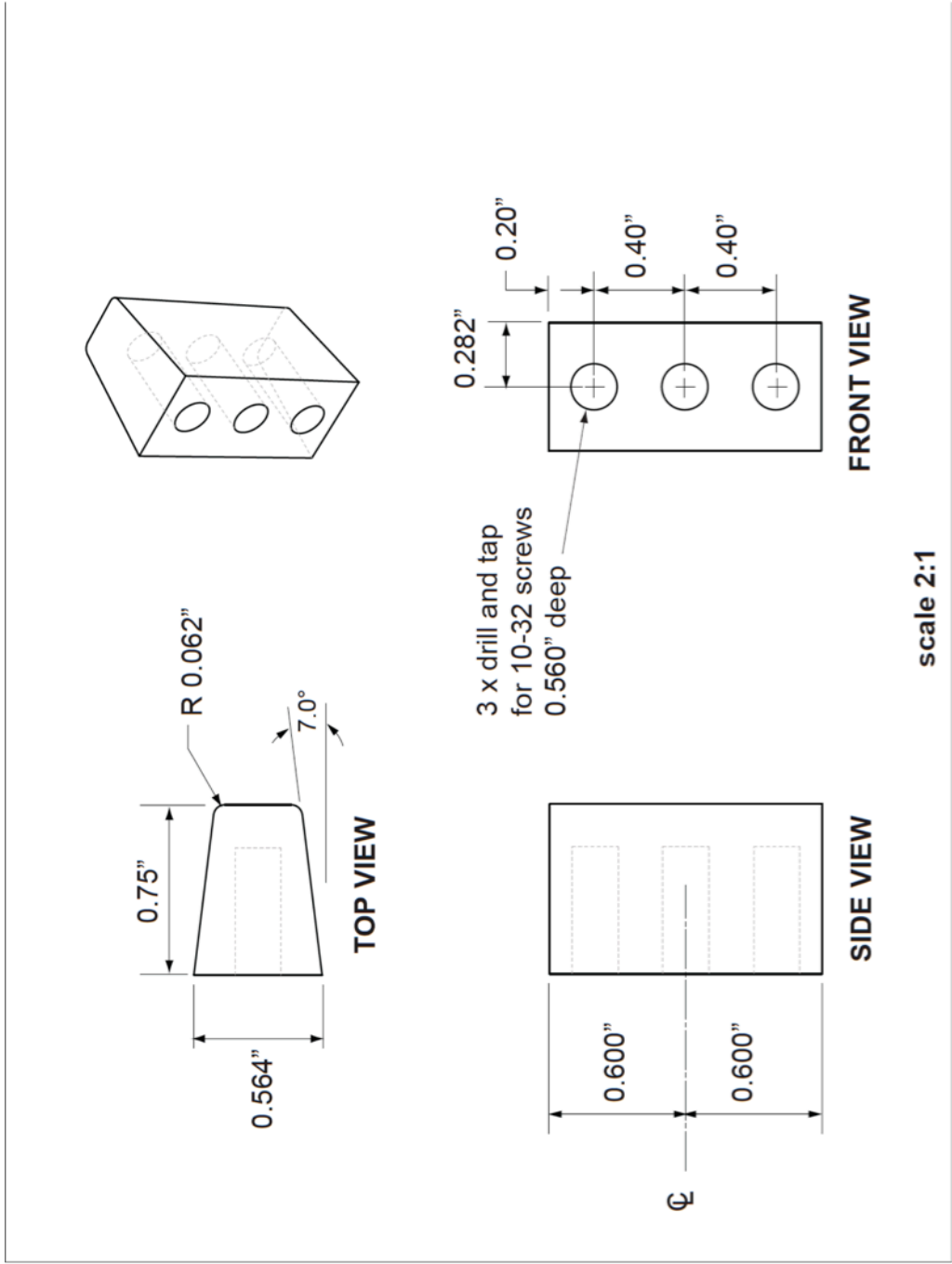


**Figure B-2.** 15-5 stainless steel insert for 0.25 in-radius (leading edge) ceramic test article (used to attach test article with bolts).

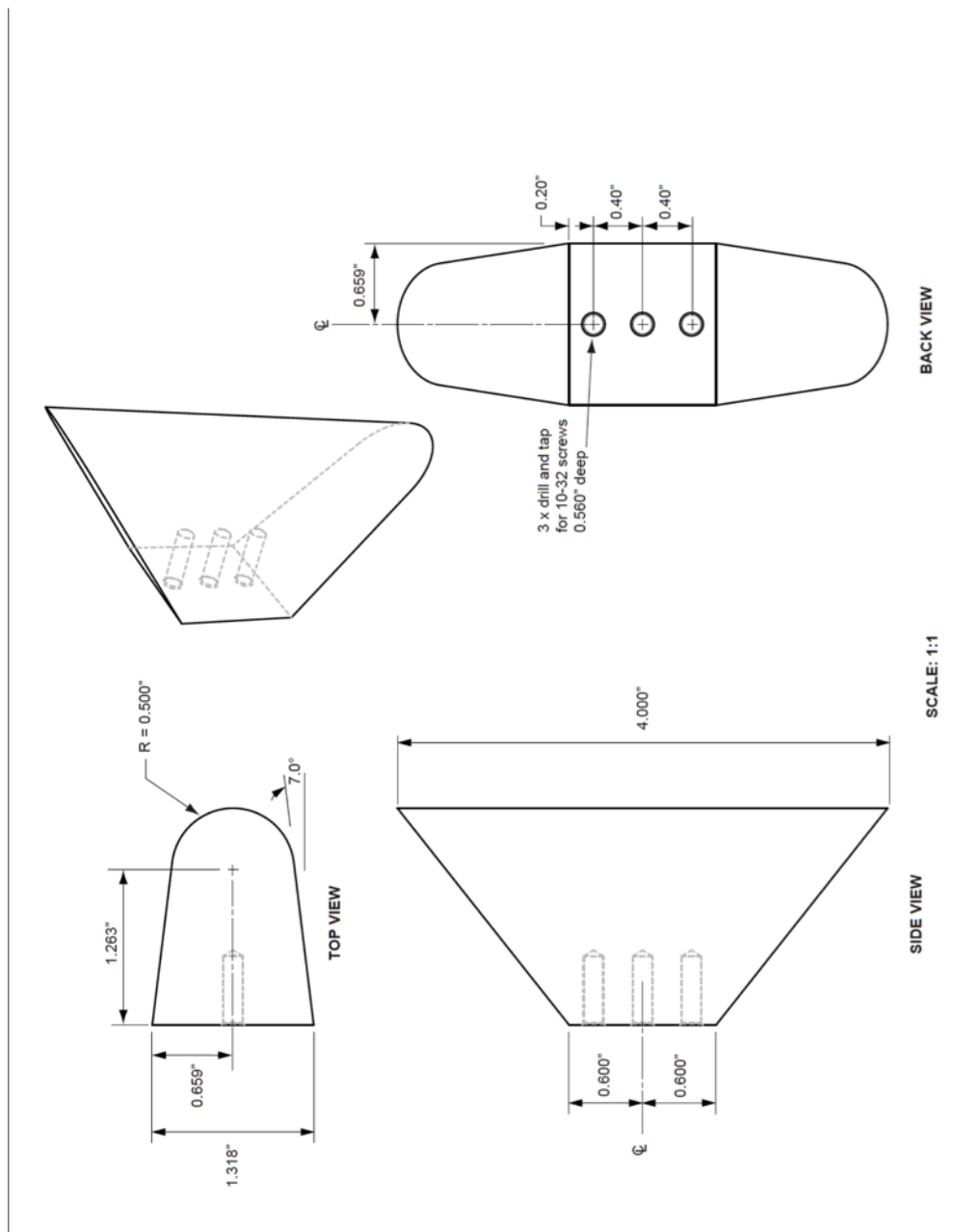


**Figure B-3.** Dimensions of metal oil flow test article with 0.5 in-radius leading edge, machined from 15-5 stainless steel.

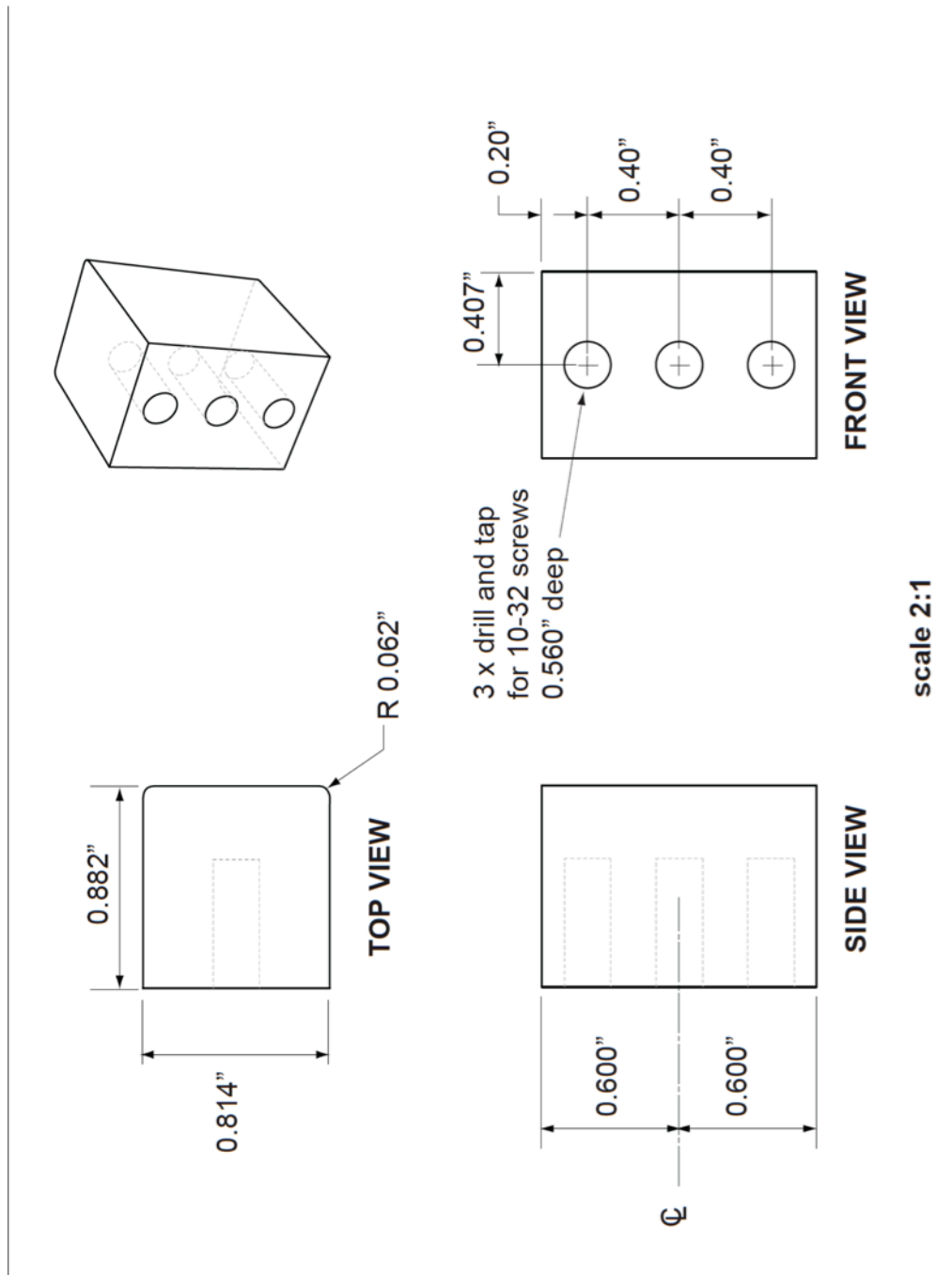


**Figure B-4.** 15-5 stainless steel insert for 0.5 in-radius (leading edge) fused silica test article (used to attach test article with bolts).

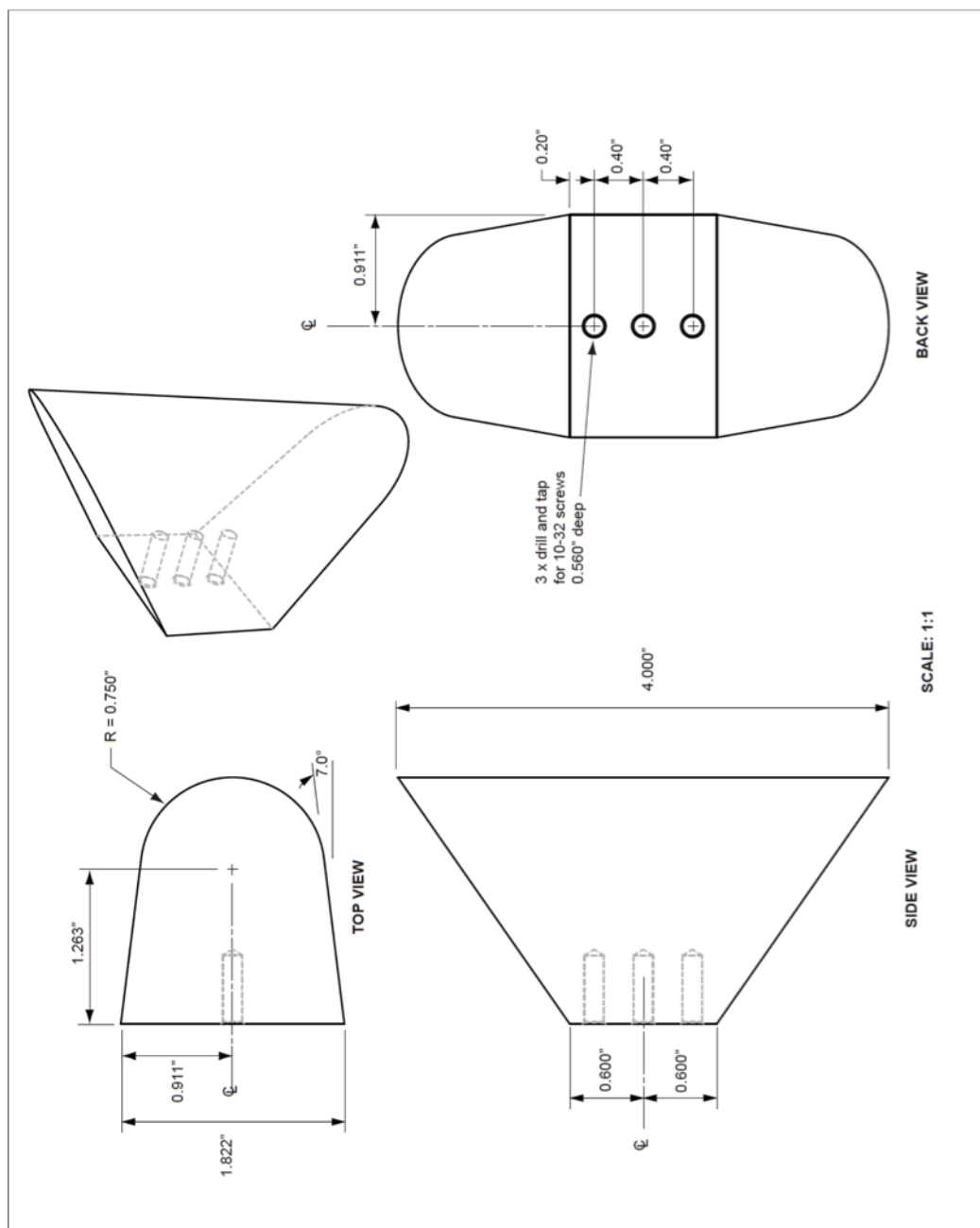


**Figure B-5.** Dimensions of metal oil flow test article with 0.75 in-radius leading edge, machined from 15-5 stainless steel.

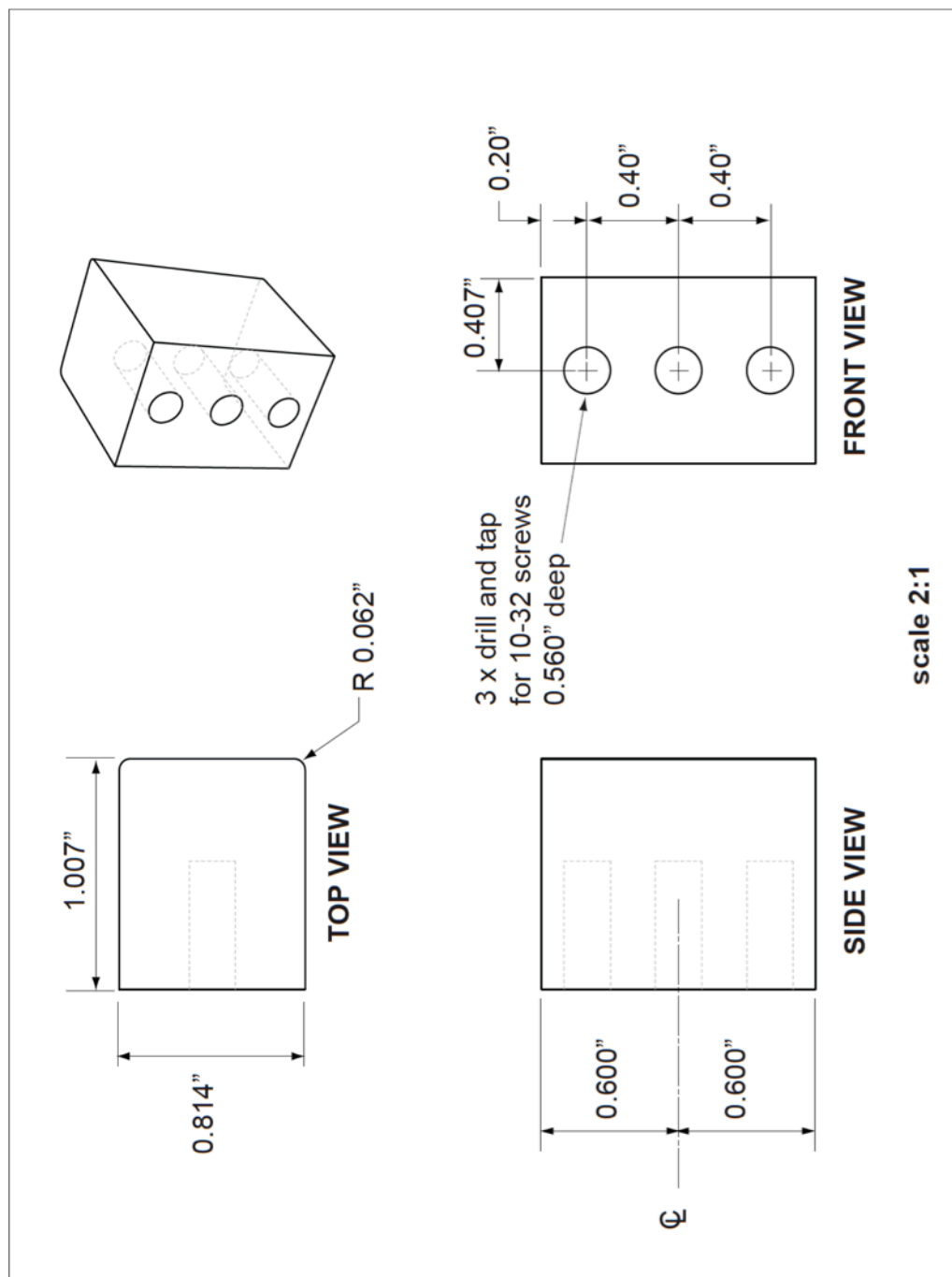


**Figure B-6.** 15-5 stainless steel insert for 0.75 in-radius (leading edge) fused silica test article (used to attach test article with bolts).



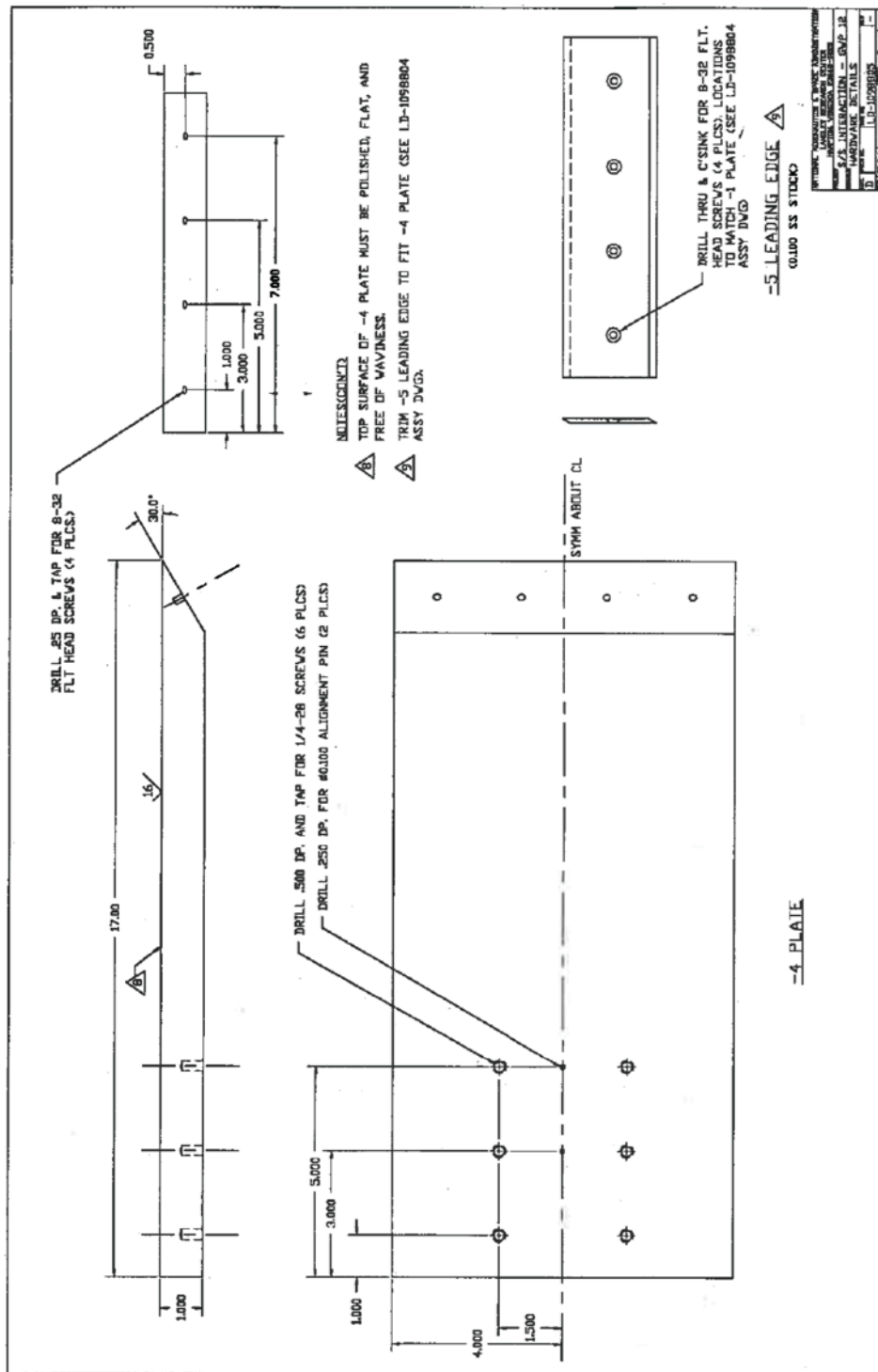


Figure B-8. Diagram of the flat plate with a sharp leading edge used to generate an incident shock (NASA drawing).



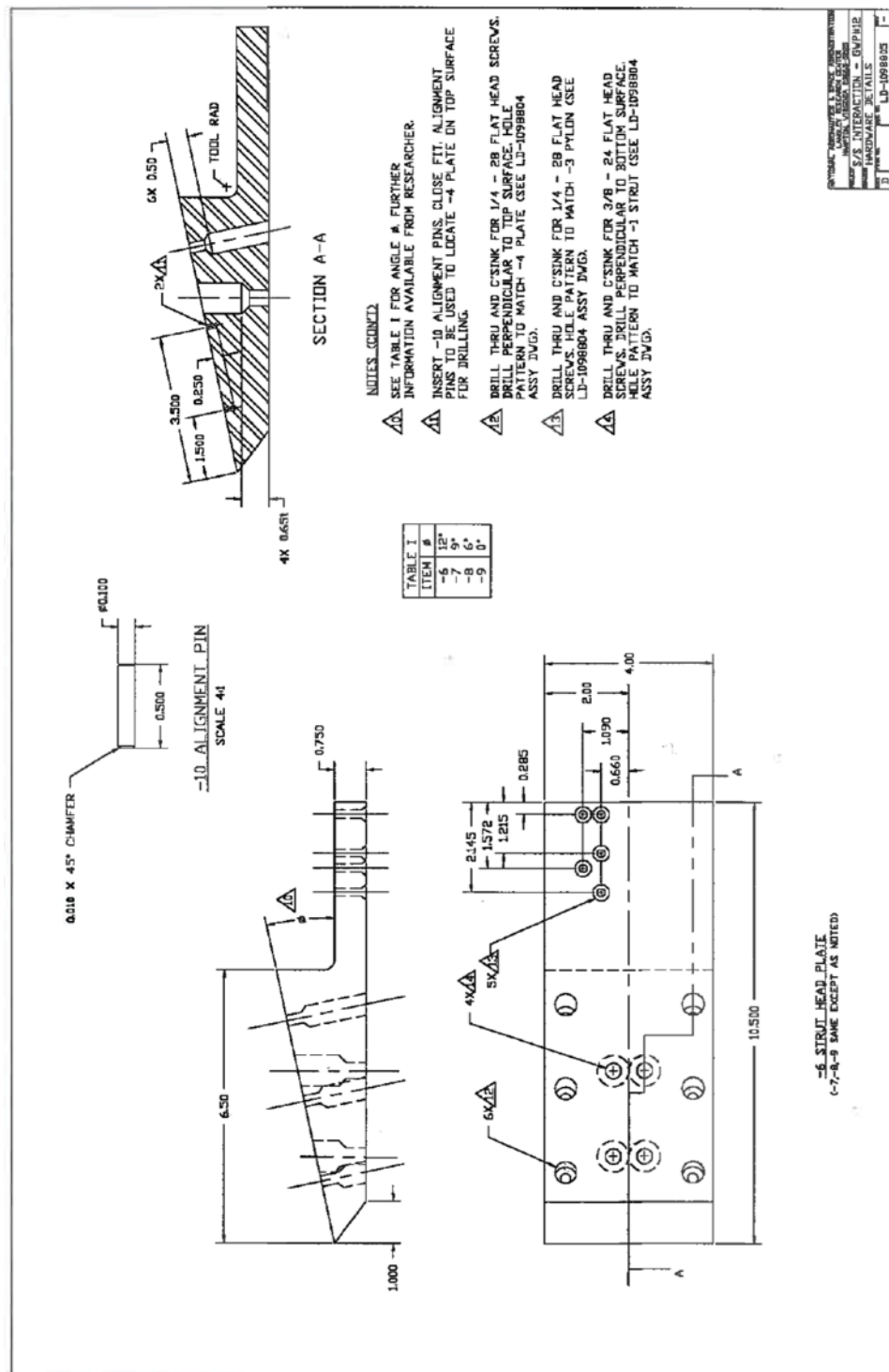
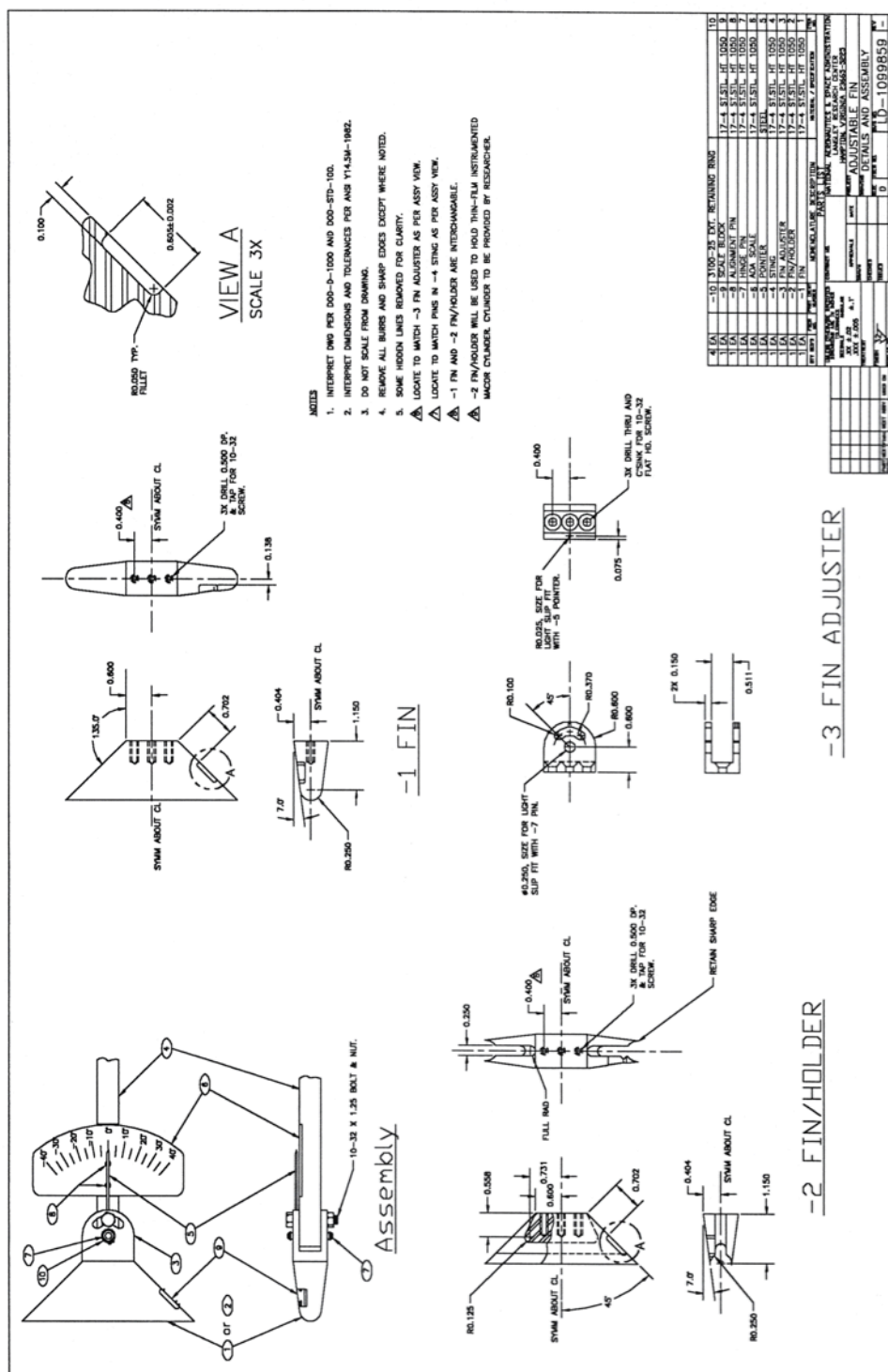
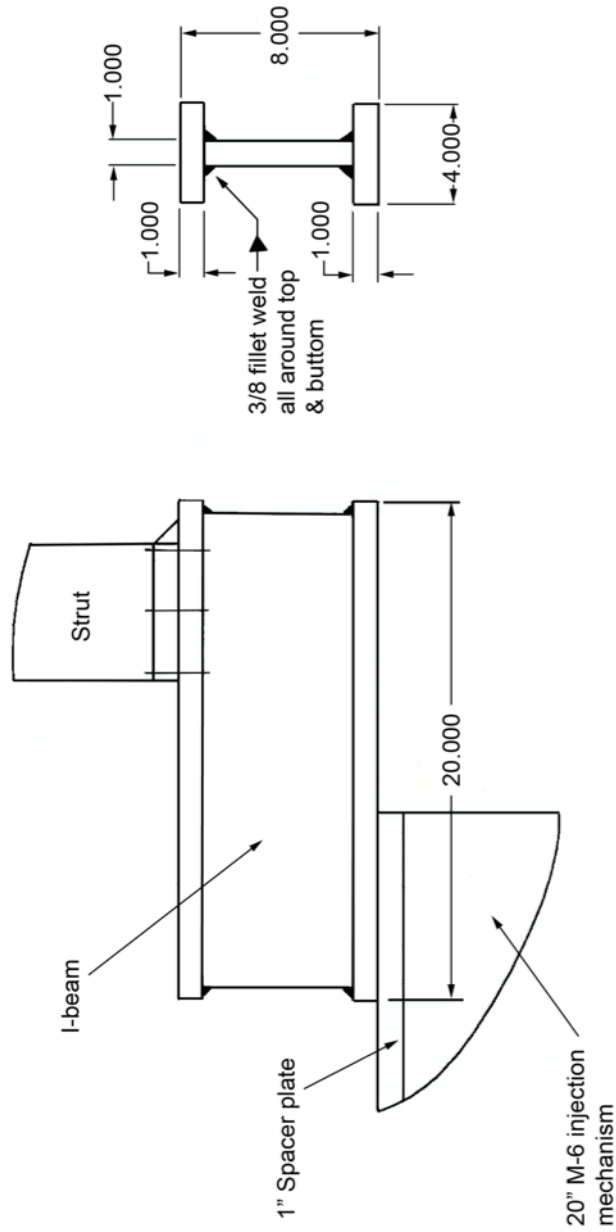


Figure B-9. Diagram of the strut head geometry used to angle the test article at either 6° or 9° (NASA drawing).







**Figure B-12.** Diagram of the legacy I-beam used to raise the test hardware during the wind tunnel runs (NASA drawing).

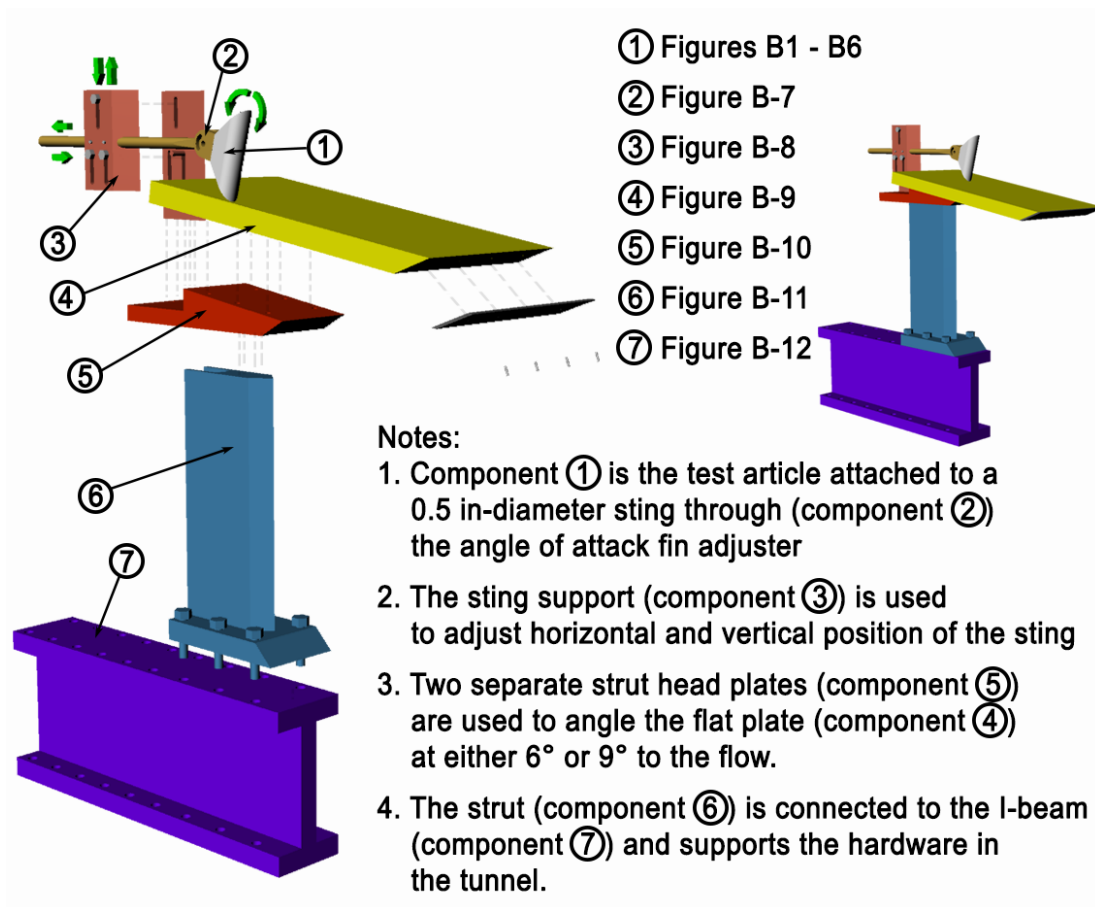


**Figure B-13.** Assembly of hardware components for wind tunnel experiment.

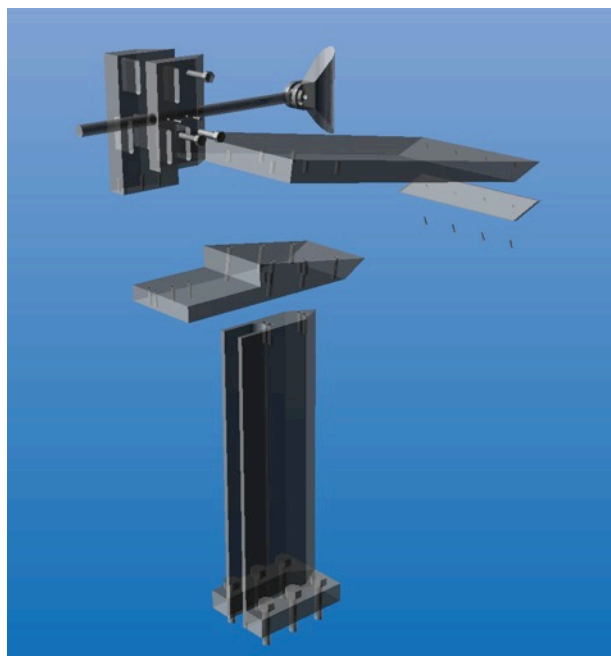


**Figure B-14.** Ghost view of assembly of hardware components for wind tunnel experiment.

Images of the fiducial mark patterns on the three test article geometries are shown in Figure B-15 to Figure B-17. The green dots represent the fiducials on both sides (in the left and right images) and the leading edge (in the center image) of the pink CAD model of the respective test article geometry. Each test article has the same number of fiducial marks (eight on each side and five along the leading edge) though the patterns differ slightly due to the different dimensions among the test articles.

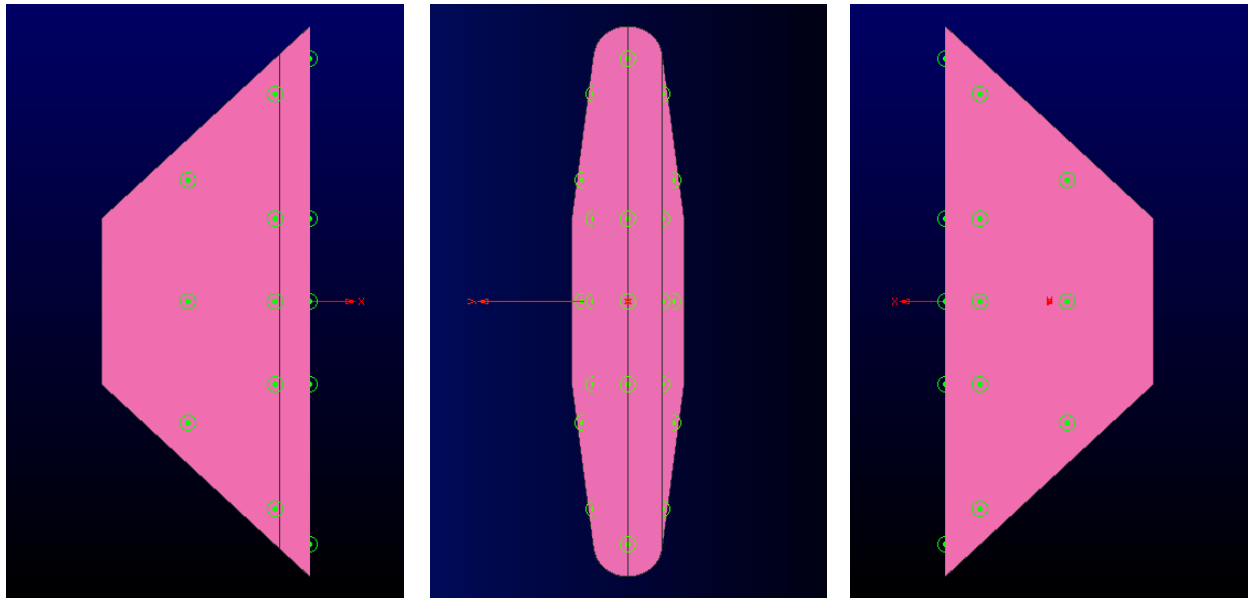


**Figure B-15.** Fiducial mark arrangement for fused silica and metal 0.25 in-radius test articles.

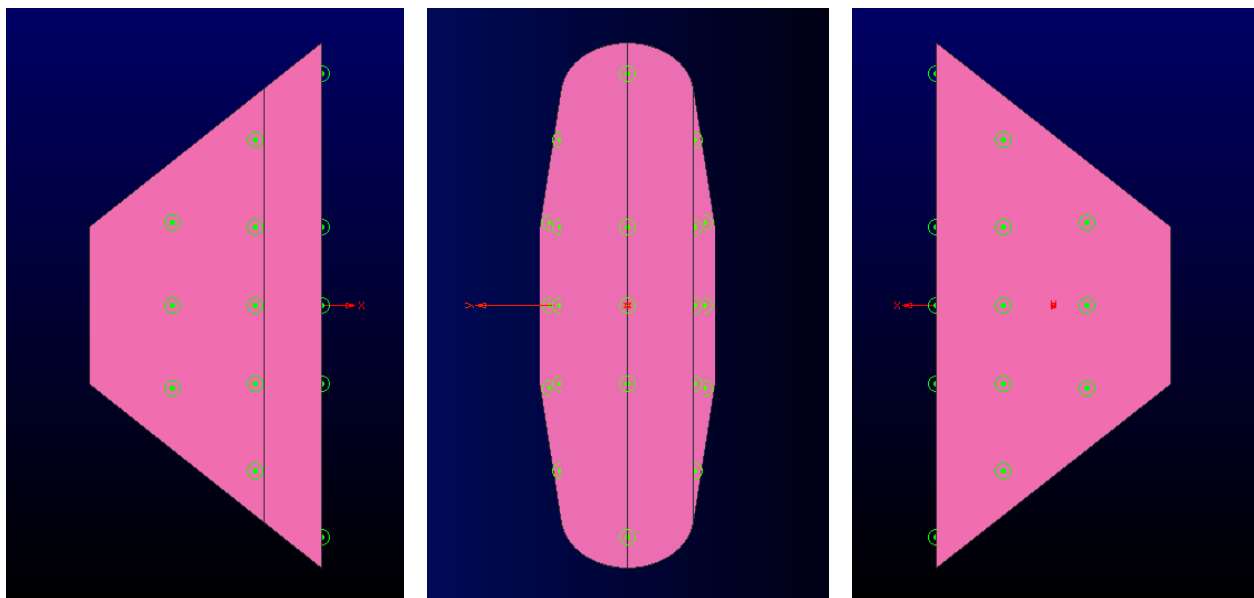


**Figure B-16.** Fiducial mark arrangement for fused silica and metal 0.5 in-radius test articles.

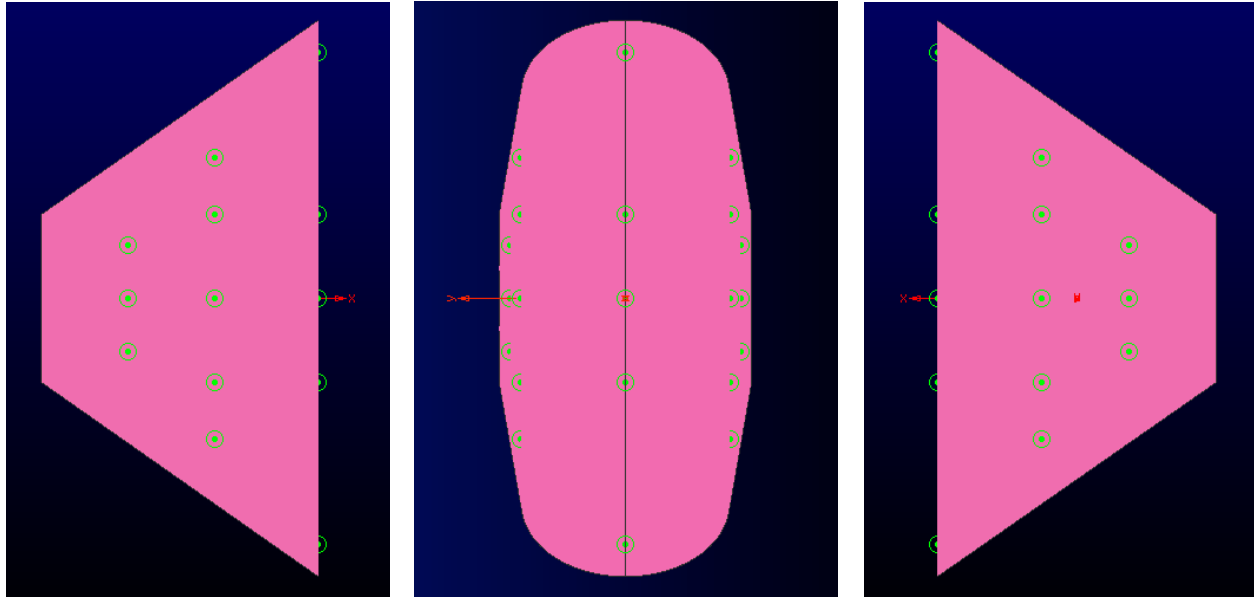


**Figure B-17.** Fiducial mark arrangement for fused silica and metal 0.75 in-radius test articles.

The sketches on the following two pages in Figure B-18 and Figure B-19 show the alignment and specified angles for the fiducial mark patterns for the three test article geometries. The diagram in Figure B-20 shows the numerical order in which the fiducial marks for the fused silica and metal test articles were applied using a CMM. The lists and tables that follow this diagram describe the actual dimensions of the fused silica and oil flow test articles (for a total of nine test articles, including back-up and primary fused silica test articles). The coordinate system used in Table B-1 to Table B-9 matches the coordinate system in the preceding three figures, with x perpendicular to the leading edge pointing out horizontally from the test article (see the red arrow in Figure B-15, for example), y pointing into the paper relative to the left image in each figure, and z pointing up along the leading edge. The measurements for the oil flow test articles are labeled slightly differently than the measurements for the fused silica test articles because the test articles were marked at separate times using slightly different programs. However, the same key dimensions are available for both types of test articles.



6/19/12

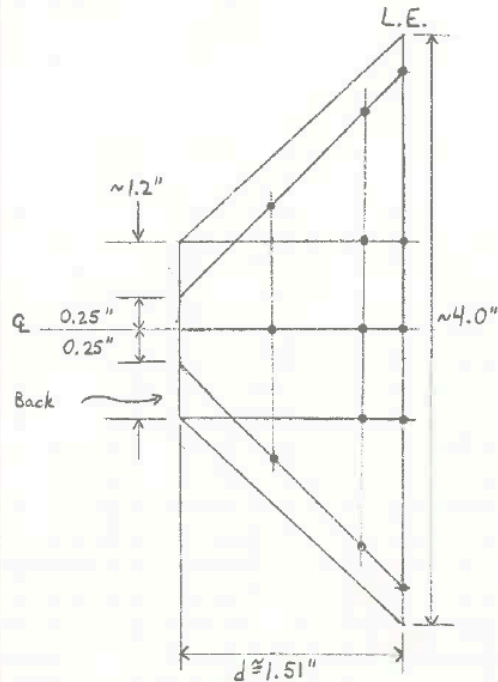
Fiducials on Fin Models

Multidimensional Conduction  
Study

Michelle Jones

1/2

0.5-in. diameter model:



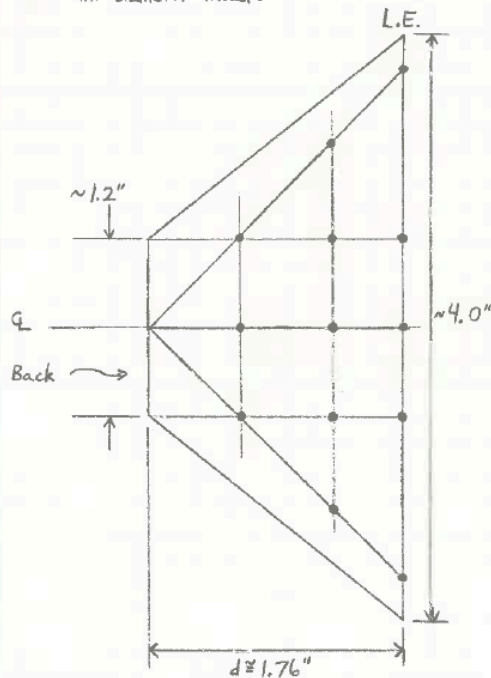
\* Fiducials are in columns approximately 0.63" and 1.26" from flat back surface of model, as well as along the leading edge (L.E.).

\* Fiducials lie on the centerline (CL), on lines angled 45° from horizontal that begin 0.25" from Q, and on horizontal lines ~0.6" above or below Q.

\* Pattern is mirrored on other side of model for a total of 21 fiducial marks.

\* Sketches are only approximately to scale

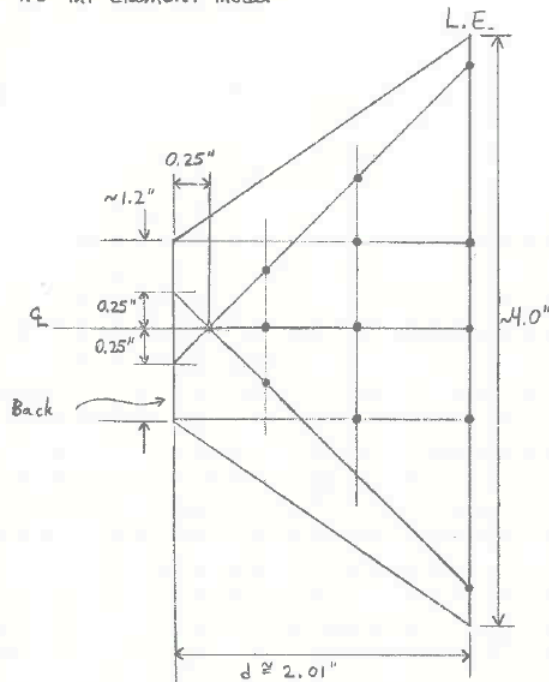
1.0-in. diameter model:



\* Same comments as above, except the 45°-angled lines begin at the centerline.

**Figure B-18.** Sketched locations of the fiducial marks on the 0.25 in-radius and the 0.50 in-radius test articles based on the nominal test article dimensions.

1.5-in. diameter model:



- \* Fiducials lie on the centerline and on lines angled  $45^\circ$  above and below the centerline
- \* The angled lines begin 0.25" horizontally from the back edge or 0.25" on opposite side of Q
- \* Fiducials are positioned in columns approximately 0.63" and 1.26" from back edge of model, and on L.E.
- \* Pattern is mirrored on other side of model for 21 total fiducials

- \* Required measurements:
- 1) Length of leading edge (L.E.)
  - 2) Diameter of leading edge
  - 3) Distance from back surface to leading edge along Q
  - 4) Orientation of metal insert relative to ceramic model
  - 5) Angle between back of model and top/bottom surfaces
  - 6) Angle between back of model and side surfaces
  - 7) Height and width of back surface

**Figure B-19.** Sketched locations of the fiducial marks on the 0.75 in-radius test articles based on the nominal test article dimensions.

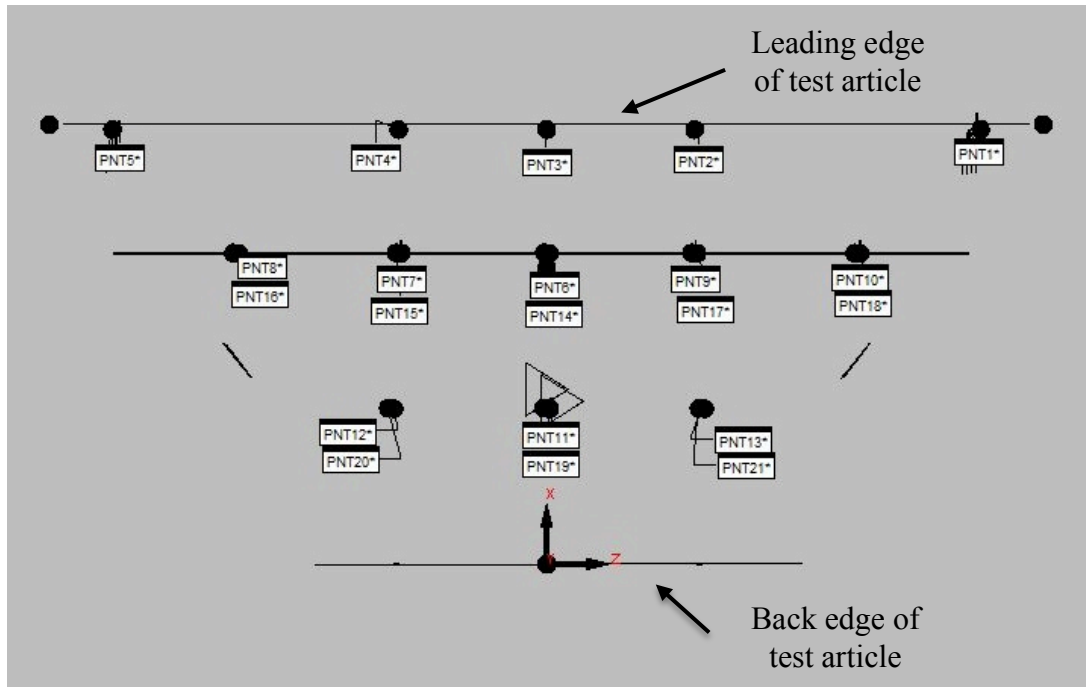


**Figure B-20.** Diagram of fiducial mark numbers for fused silica and metal test articles.

**Measurements for the 0.25 in-radius fused-silica test article with a thermocouple:**

**LEADING EDGE HEIGHT**

AX MEAS  
M 4.0215

**NOSE DIAMETER AND RADIUS**

AX MEAS  
D 0.5159  
R 0.2580

**DISTANCE FROM AFT END TO THE LEADING EDGE**

AX MEAS  
X 1.4907

**LOCATION OF PLANE METAL BASE**

AX MEAS  
X -0.0119  
Y 0.0084  
Z -0.0979  
V 0.9999 0.0007 -0.0145 0.0000

**3D ANGLE FROM PLANE METAL BASE TO X AXIS**

AX MEAS  
A 89.1664

**3D ANGLE FROM PLANE METAL BASE TO Y AXIS**

AX MEAS  
A -0.0401

**3D ANGLE FROM PLANE METAL BASE TO Z AXIS**

AX MEAS  
A -0.8326

**ANGLE Y+, 3D ANGLE FROM PLANE Y+ PLN TO X AXIS**

AX MEAS  
A 7.4937

**ANGLE Y-, 3D ANGLE FROM PLANE Y- PLN TO X AXIS**

AX MEAS  
A -7.2911

**ANGLE Z+, 3D ANGLE FROM PLANE Z+ PLN TO X AXIS**

AX MEAS  
A 42.8538

**ANGLE Z-, 3D ANGLE FROM PLANE Z- PLN TO X AXIS**

AX MEAS  
A -43.8620

**AFT END HEIGHT (Y+)**

AX MEAS  
M 1.1776

**AFT END HEIGHT (Y-)**

AX MEAS  
M 1.1640

**AFT END WIDTH (Z+)**

AX MEAS  
M 0.8328

**AFT END WIDTH (Z-)**

AX MEAS  
M 0.8340

**Table B-1.** Actual fiducial mark locations on the 0.25 in-radius fused silica test article (the primary test article with an embedded thermocouple).

#	X	Y	Z	#	X	Y	Z
1	1.5118	0.0004	1.7590	12	0.6301	-0.3280	-0.8880
2	1.4951	0.0006	0.5992	13	0.6304	-0.3285	0.8880
3	1.4907	0.0005	0.0000	14	1.2586	0.2521	-0.0003
4	1.4871	0.0006	-0.6007	15	1.2587	0.2509	-0.6009
5	1.4831	0.0006	-1.7590	16	1.2585	0.2533	-1.5096
6	1.2599	-0.2449	0.0000	17	1.2587	0.2535	0.6003
7	1.2599	-0.2449	-0.6007	18	1.2587	0.2575	1.5089
8	1.2599	-0.2475	-1.5093	19	0.6288	0.3416	-0.0004
9	1.2601	-0.2473	0.6007	20	0.6286	0.3360	-0.8884
10	1.2601	-0.2501	1.5093	21	0.6289	0.3389	0.8876
11	0.6303	-0.3296	0.0001				

## Measurements for the 0.25 in-radius fused-silica test article without a thermocouple:

### LEADING EDGE HEIGHT

AX MEAS  
M 4.0141

### NOSE DIAMETER AND RADIUS

AX MEAS  
D 0.4794  
R 0.2397

### DISTANCE FROM AFT END TO THE LEADING EDGE

AX MEAS  
X 1.5060

### LOCATION OF PLANE METAL BASE

AX MEAS  
X -0.0094  
Y 0.0085  
Z -0.0981  
V 1.0000 -0.0031 -0.0093 0.0000

### 3D ANGLE PLANE METAL BASE TO X AXIS

AX MEAS  
A 89.4381

### 3D ANGLE PLANE METAL BASE TO Y AXIS

AX MEAS  
A 0.1789

### 3D ANGLE PLANE METAL BASE TO Z AXIS

AX MEAS  
A -0.5327

### ANGLE Y+, 3D ANGLE FROM PLANE Y+ PLN TO X AXIS

AX MEAS  
A 7.3981

### ANGLE Y-, 3D ANGLE FROM PLANE Y- PLN TO X AXIS

AX MEAS  
A -7.1819

### ANGLE Z+, 3D ANGLE FROM PLANE Z+ PLN TO X AXIS

AX MEAS  
A 43.1285

### ANGLE Z-, 3D ANGLE FROM PLANE Z- PLN TO X AXIS

AX MEAS  
A -43.6137

### AFT END HEIGHT (Y+)

AX MEAS  
M 1.1518

**AFT END HEIGHT (Y-)**

AX MEAS  
M 1.1483

**AFT End WIDTH (Z+)**

AX MEAS  
M 0.8275

**AFT End WIDTH (Z-)**

AX MEAS  
M 0.8297

**Table B-2.** Actual fiducial mark locations on the 0.25 in-radius fused silica test article (the back-up test article without an embedded thermocouple).

#	X	Y	Z	#	X	Y	Z
1	1.5078	-0.0001	1.7590	12	0.6302	-0.3255	-0.8879
2	1.5057	0.0003	0.5993	13	0.6303	-0.3263	0.8880
3	1.5060	0.0003	0.0001	14	1.2587	0.2554	-0.0003
4	1.5048	0.0002	-0.6006	15	1.2586	0.2547	-0.6009
5	1.5085	0.0004	-1.7590	16	1.2586	0.2558	-1.5096
6	1.2600	-0.2460	0.0001	17	1.2587	0.2548	0.6003
7	1.2599	-0.2467	-0.6006	18	1.2586	0.2567	1.5089
8	1.2598	-0.2484	-1.5092	19	0.6287	0.3390	-0.0003
9	1.2600	-0.2446	0.6007	20	0.6287	0.3360	-0.8883
10	1.2601	-0.2491	1.5092	21	0.6288	0.3375	0.8876
11	0.6302	-0.3289	0.0000				

**Measurements for the 0.5 in-radius fused-silica test article with a thermocouple:**

**LEADING EDGE HEIGHT**

AX MEAS  
M 4.0349

**NOSE DIAMETER AND RADIUS**

AX MEAS  
D 1.0148  
R 0.5074

**DISTANCE FROM AFT END TO THE LEADING EDGE**

AX MEAS  
X 1.7349

**LOCATION OF PLANE METAL BASE**

AX MEAS  
X -0.0146  
Y -0.0026  
Z -0.0237  
V 0.9999 -0.0009 0.0158 0.0000

**3D ANGLE FROM PLANE METAL BASE TO X AXIS**

AX MEAS  
A -89.0943

**3D ANGLE FROM PLANE METAL BASE TO Y AXIS**

AX MEAS  
A 0.0488

**3D ANGLE FROM PLANE METAL BASE TO Z AXIS**

AX MEAS  
A 0.9044

**ANGLE Y+, 3D ANGLE FROM PLANE Y+ PLN TO X AXIS**

AX MEAS  
A 7.4440

**ANGLE Y-, 3D ANGLE FROM PLANE Y- PLN TO X AXIS**

AX MEAS  
A -7.5651

**ANGLE Z+, 3D ANGLE FROM PLANE Z+ PLN TO X AXIS**

AX MEAS  
A 38.7496

**ANGLE Z-, 3D ANGLE FROM PLANE Z- PLN TO X AXIS**

AX MEAS  
A -39.3710

**AFT END HEIGHT (Y+)**

AX MEAS  
M 1.1977

**AFT END HEIGHT (Y-)**

AX MEAS  
M 1.1904

**AFT END WIDTH (Z+)**

AX MEAS  
M 1.3351

**AFT END WIDTH (Z-)**

AX MEAS  
M 1.3321



**Table B-3.** Actual fiducial mark locations on the 0.50 in-radius fused silica test article (the primary test article with an embedded thermocouple).

#	X	Y	Z	#	X	Y	Z
1	1.7481	-0.0001	1.7587	12	0.6305	-0.5811	-0.6294
2	1.7378	-0.0003	0.6003	13	0.6302	-0.5821	0.6294
3	1.7349	0.0002	-0.0003	14	1.2592	0.4998	-0.0002
4	1.7319	0.0003	-0.5999	15	1.2586	0.5000	-0.5999
5	1.7213	0.0004	-1.7593	16	1.2587	0.5017	-1.2593
6	1.2597	-0.4998	0.0000	17	1.2583	0.4996	0.5992
7	1.2599	-0.4980	-0.5997	18	1.2582	0.5040	1.2587
8	1.2599	-0.4970	-1.2591	19	0.6299	0.5844	-0.0002
9	1.2596	-0.5009	0.5997	20	0.6291	0.5845	-0.6297
10	1.2594	-0.5033	1.2591	21	0.6289	0.5829	0.6290
11	0.6304	-0.5835	0.0000				

**Measurements for the 0.5 in-radius fused-silica test article without a thermocouple:**

**LEADING EDGE HEIGHT**

AX MEAS  
M 4.0021

**NOSE DIAMETER AND RADIUS**

AX MEAS  
D 1.0181  
R 0.5090

**DISTANCE FROM AFT END TO THE LEADING EDGE**

AX MEAS  
X 1.7217

**LOCATION OF PLANE METAL BASE**

AX MEAS  
X -0.0469  
Y -0.0026  
Z -0.0230  
V 1.0000 -0.0032 -0.0044 0.0000

**3D ANGLE PLANE METAL BASE TO X AXIS**

AX MEAS  
A 89.6865

**3D ANGLE PLANE METAL BASE TO Y AXIS**

AX MEAS  
A 0.1834

**3D ANGLE PLANE METAL BASE TO Z AXIS**

AX MEAS  
A -0.2542

ANGLE Y+, 3D ANGLE FROM PLANE Y+ PLN TO X AXIS  
 AX MEAS  
 A 7.3827

ANGLE Y-, 3D ANGLE FROM PLANE Y- PLN TO X AXIS  
 AX MEAS  
 A -7.4957

ANGLE Z+, 3D ANGLE FROM PLANE Z+ PLN TO X AXIS  
 AX MEAS  
 A 38.9541

ANGLE Z-, 3D ANGLE FROM PLANE Z- PLN TO X AXIS  
 AX MEAS  
 A -38.8921

AFT END HEIGHT (Y+)  
 AX MEAS  
 M 1.2084

AFT END HEIGHT (Y-)  
 AX MEAS  
 M 1.2063

AFT END WIDTH (Z+)  
 AX MEAS  
 M 1.3267

AFT END WIDTH (Z-)  
 AX MEAS  
 M 1.3258

**Table B-4.** Actual fiducial mark locations on the 0.50 in-radius fused silica test article (the back-up test article without an embedded thermocouple).

#	X	Y	Z	#	X	Y	Z
1	1.7297	-0.0001	1.7591	12	0.6304	-0.5802	-0.6297
2	1.7206	-0.0007	0.6005	13	0.6305	-0.5816	0.6291
3	1.7217	-0.0002	0.0001	14	1.2594	0.5017	0.0001
4	1.7250	-0.0001	-0.5996	15	1.2586	0.5025	-0.5996
5	1.7370	-0.0002	-1.7591	16	1.2585	0.5012	-1.2591
6	1.2598	-0.4969	-0.0004	17	1.2585	0.5003	0.5996
7	1.2598	-0.4957	-0.6000	18	1.2585	0.4983	1.2592
8	1.2597	-0.4948	-1.2593	19	0.6301	0.5827	0.0000
9	1.2599	-0.4968	0.5993	20	0.6289	0.5841	-0.6294
10	1.2598	-0.4965	1.2587	21	0.6293	0.5809	0.6294
11	0.6304	-0.5808	-0.0001				

## Measurements for the 0.75 in-radius fused-silica test article with a thermocouple:

### LEADING EDGE HEIGHT

AX MEAS  
M 3.9672

### NOSE DIAMETER AND RADIUS

AX MEAS  
D 1.5288  
R 0.7644

### DISTANCE FROM AFT END TO THE LEADING EDGE

AX MEAS  
X 1.9579

### LOCATION OF PLANE METAL BASE

AX MEAS  
X 0.0014  
Y -0.0027  
Z -0.0146  
V 1.0000 0.0027 0.0046 0.0000

### 3D ANGLE FROM PLANE METAL BASE TO X AXIS

AX MEAS  
A -89.6956

### 3D ANGLE FROM PLANE METAL BASE TO Y AXIS

AX MEAS  
A -0.1525

### 3D ANGLE FROM PLANE METAL BASE TO Z AXIS

AX MEAS  
A 0.2634

### ANGLE Y+, 3D ANGLE FROM PLANE Y+ PLN TO X AXIS

AX MEAS  
A 7.4776

### ANGLE Y-, 3D ANGLE FROM PLANE Y- PLN TO X AXIS

AX MEAS  
A -8.0405

### ANGLE Z+, 3D ANGLE FROM PLANE Z+ PLN TO X AXIS

AX MEAS  
A 35.8126

### ANGLE Z-, 3D ANGLE FROM PLANE Z- PLN TO X AXIS

AX MEAS  
A -34.5050

### AFT END HEIGHT (Y+)

AX MEAS  
M 1.2169

**AFT END HEIGHT (Y-)**

AX MEAS  
M 1.2069

**AFT END WIDTH (Z+)**

AX MEAS  
M 1.8385

**AFT END WIDTH (Z-)**

AX MEAS  
M 1.8423

**Table B-5.** Actual fiducial mark locations on the 0.75 in-radius fused silica test article (the primary test article with an embedded thermocouple).

#	X	Y	Z	#	X	Y	Z
1	1.9536	-0.0001	1.7598	12	0.6298	-0.8368	-0.3800
2	1.9518	-0.0007	0.6003	13	0.6295	-0.8360	0.3800
3	1.9579	-0.0002	-0.0001	14	1.2607	0.7585	-0.0001
4	1.9642	-0.0001	-0.5999	15	1.2606	0.7590	-0.6003
5	1.9943	-0.0001	-1.7593	16	1.2601	0.7593	-1.0103
6	1.2595	-0.7500	0.0001	17	1.2601	0.7578	0.5996
7	1.2595	-0.7478	-0.6000	18	1.2605	0.7552	1.0098
8	1.2595	-0.7461	-1.0101	19	0.6311	0.8421	-0.0001
9	1.2594	-0.7481	0.6000	20	0.6311	0.8421	-0.3804
10	1.2594	-0.7456	1.0100	21	0.6306	0.8406	0.3799
11	0.6306	-0.8379	0.0001				

**Measurements for the 0.75 in-radius fused-silica test article without a thermocouple:**

**LEADING EDGE HEIGHT**

AX MEAS  
M 3.9753

**NOSE DIAMETER AND RADIUS**

AX MEAS  
D 1.5295  
R 0.7648

**DISTANCE FROM AFT END TO THE LEADING EDGE**

AX MEAS  
X 1.9522

**LOCATION OF PLANE METAL BASE**

AX MEAS  
X -0.0049  
Y -0.0019  
Z -0.0147  
V 1.0000 -0.0056 0.0052 0.0000

**3D ANGLE FROM PLANE METAL BASE TO X AXIS**

AX MEAS  
A -89.5616

**3D ANGLE FROM PLANE METAL BASE TO Y AXIS**

AX MEAS  
A 0.3224

**3D ANGLE FROM PLANE METAL BASE TO Z AXIS**

AX MEAS  
A 0.2971

**ANGLE Y+, 3D ANGLE FROM PLANE Y+ PLN TO X AXIS**

AX MEAS  
A 7.5514

**ANGLE Y-, 3D ANGLE FROM PLANE Y- PLN TO X AXIS**

AX MEAS  
A -7.5065

**ANGLE Z+, 3D ANGLE FROM PLANE Z+ PLN TO X AXIS**

AX MEAS  
A 35.2323

**ANGLE Z-, 3D ANGLE FROM PLANE Z- PLN TO X AXIS**

AX MEAS  
A -34.9487

**AFT END HEIGHT (Y+)**

AX MEAS  
M 1.1905

**AFT END WIDTH (Y-)**

AX MEAS  
M 1.2106

**AFT END HEIGHT (Z+)**

AX MEAS  
M 1.8319

**AFT END WIDTH (Z-)**

AX MEAS  
M 1.833

**Table B-6.** Actual fiducial mark locations on the 0.75 in-radius fused silica test article (the back-up test article without an embedded thermocouple).

#	X	Y	Z	#	X	Y	Z
1	1.9708	0.0001	1.7596	12	0.6312	-0.8400	-0.3803
2	1.9529	0.0004	0.6003	13	0.6312	-0.8402	0.3796
3	1.9522	0.0003	-0.0002	14	1.2597	0.7515	0.0000
4	1.9611	0.0003	-0.5999	15	1.2597	0.7528	-0.5999
5	1.9802	0.0003	-1.7593	16	1.2597	0.7524	-1.0099
6	1.2610	-0.7607	-0.0004	17	1.2593	0.7481	0.6000
7	1.2609	-0.7598	-0.6003	18	1.2598	0.7440	1.0100
8	1.2610	-0.7562	-1.0103	19	0.6301	0.8334	0.0000
9	1.2607	-0.7599	0.5997	20	0.6301	0.8352	-0.3800
10	1.2605	-0.7593	1.0097	21	0.6295	0.8333	0.3801
11	0.6311	-0.8409	-0.0002				

**Measurements for the 0.25 in-radius oil-flow test article:**

**NOSE RADIUS (Z-)**

AX MEAS  
R 0.2507

**NOSE RADIUS (Z+)**

AX MEAS  
R 0.2495

**LOCATION OF LINE Z AXES CLOCK**

AX MEAS  
X 1.2593

**LOCATION OF LINE Z+ LINE**

AX MEAS  
Z 0.5992

**LOCATION OF LINE Z- LINE**

AX MEAS  
Z -0.6007

**DISTANCE FROM AFT END TO THE LEADING EDGE**

AX MEAS  
X 1.5090

**SURFACE ANGLES:**

**Z+ SIDE SURFACE** 2D ANGLE FROM Z+ PLANE TO XAXIS

AX MEAS  
A 42.6597

**Z- SIDE SURFACE** 2D ANGLE FROM Z- PLANE TO XAXIS

AX MEAS  
A -42.8619

**TOP SURFACE** 2D ANGLE FROM Y+ PLANE TO XAXIS  
 AX MEAS  
 A -7.0870

**BOTTOM SURFACE** 2D ANGLE FROM Y- PLANE TO XAXIS  
 AX MEAS  
 A 6.9432

**AFT END HEIGHT**  
 AX MEAS  
 M 1.1999

**AFT END WIDTH**  
 AX MEAS  
 M 0.8125

**LEADING EDGE HEIGHT**  
 AX MEAS  
 M 3.9955

**Table B-7.** Actual fiducial mark locations on the 0.25 in-radius metal test article (oil flow).

#	X	Y	Z	#	X	Y	Z
1	1.5116	-0.0002	1.7591	12	0.6310	-0.3300	-0.8799
2	1.5100	0.0001	0.5990	13	0.6310	-0.3299	0.8800
3	1.5092	0.0002	0.0001	14	1.2585	0.2508	-0.0004
4	1.5084	0.0002	-0.6008	15	1.2585	0.2503	-0.6011
5	1.5069	0.0003	-1.7589	16	1.2584	0.2503	-1.5096
6	1.2599	-0.2530	0.0000	17	1.2585	0.2503	0.6005
7	1.2596	-0.2532	-0.6009	18	1.2584	0.2503	1.5089
8	1.2592	-0.2530	-1.5092	19	0.6295	0.3286	-0.0003
9	1.2591	-0.2533	0.6007	20	0.6294	0.3284	-0.8804
10	1.2594	-0.2532	1.5093	21	0.6294	0.3287	0.8796
11	0.6310	-0.3297	0.0001				

**Measurements for the 0.5 in-radius oil-flow test article:**

**LOCATION OF CIRCLE Z- CIR**  
 AX MEAS  
 R 0.5021

**LOCATION OF CIRCLE Z+ CIR**  
 AX MEAS  
 R 0.5023

**LOCATION OF LINE Z-AX CLOCK**  
 AX MEAS  
 X 1.2586



**LOCATION OF LINE Z+ LIN**

AX MEAS  
Z 0.6011

**LOCATION OF LINE Z- LIN**

AX MEAS  
Z -0.6005

**DISTANCE FROM AFT END TO THE LEADING EDGE**

AX MEAS  
X 1.7601

**SURFACE ANGLES:**

**Z+ SIDE SURFACE** 2D ANGLE FROM Z+ PLANE TO XAXIS

AX MEAS  
A 38.4286

**Z- SIDE SURFACE** 2D ANGLE FROM Z- PLANE TO XAXIS

AX MEAS  
A -38.4569

**TOP SURFACE** 2D ANGLE FROM Y+ PLANE TO XAXIS

AX MEAS  
A -6.9977

**BOTTOM SURFACE** 2D ANGLE FROM Y- PLANE TO XAXIS

AX MEAS  
A 7.0278

**AFT END HEIGHT**

AX MEAS  
M 1.2016

**AFT END WIDTH**

AX MEAS  
M 1.3177

**LEADING EDGE HEIGHT**

AX MEAS  
M 4.0281

**Table B-8.** Actual fiducial mark locations on the 0.50 in-radius metal test article (oil flow).

#	X	Y	Z	#	X	Y	Z
1	1.7606	0.0004	1.7590	12	0.6305	-0.5808	-0.6297
2	1.7599	-0.0009	0.6004	13	0.6304	-0.5811	0.6292
3	1.7596	-0.0004	0.0001	14	1.2596	0.5037	0.0001
4	1.7597	-0.0002	-0.5996	15	1.2589	0.5038	-0.5996
5	1.7598	-0.0005	-1.7591	16	1.2590	0.5039	-1.2590
6	1.2594	-0.5027	-0.0003	17	1.2587	0.5040	0.5998
7	1.2597	-0.5029	-0.5999	18	1.2586	0.5043	1.2591
8	1.2598	-0.5031	-1.2594	19	0.6303	0.5811	0.0001
9	1.2595	-0.5031	0.5993	20	0.6298	0.5811	-0.6294
10	1.2595	-0.5034	1.2587	21	0.6293	0.5814	0.6295
11	0.6305	-0.5810	-0.0003				

**Measurements for 0.75 in-radius oil-flow test article:**

**NOSE RADIUS (Z-)**

AX MEAS  
R 0.7513

**NOSE RADIUS (Z+)**

AX MEAS  
R 0.7519

**LOCATION OF LINE Z-AX CLOCK**

AX MEAS  
X 1.2603

**LOCATION OF LINE Z+ LIN**

AX MEAS  
Z 0.6000

**LOCATION OF LINE Z- LIN**

AX MEAS  
Z -0.6001

**DISTANCE FROM AFT END TO THE LEADING EDGE**

AX MEAS  
X 2.0114

**SURFACE ANGLES:**

**Z+ SIDE SURFACE** 2D ANGLE FROM Z+ PLANE TO XAXIS

AX MEAS  
A 34.7776

**Z- SIDE SURFACE** 2D ANGLE FROM Z- PLANE TO XAXIS

AX MEAS  
A -34.8707

**TOP SURFACE** 2D ANGLE FROM Y+ PLANE TO XAXIS  
 AX MEAS  
 A -7.0202

**BOTTOM SURFACE** 2D ANGLE FROM Y- PLANE TO XAXIS  
 AX MEAS  
 A 7.0248

**AFT END WIDTH**  
 AX MEAS  
 M 1.2001

**AFT END WIDTH**  
 AX MEAS  
 M 1.8229

**LEADING EDGE HEIGHT**  
 AX MEAS  
 M 4.0014

**Table B-9.** Actual fiducial mark locations on the 0.75 in-radius metal test article (oil flow).

#	X	Y	Z	#	X	Y	Z
1	2.0129	-0.0008	1.7601	12	0.6304	-0.8345	-0.3804
2	2.0117	-0.0010	0.6006	13	0.6298	-0.8348	0.3797
3	2.0113	-0.0010	0.0001	14	1.2605	0.7560	0.0002
4	2.0111	-0.0005	-0.5996	15	1.2601	0.7563	-0.5999
5	2.0108	-0.0009	-1.7590	16	1.2600	0.7565	-1.0101
6	1.2596	-0.7567	-0.0004	17	1.2602	0.7561	0.6000
7	1.2595	-0.7567	-0.6003	18	1.2602	0.7561	1.0100
8	1.2595	-0.7566	-1.0103	19	0.6308	0.8340	0.0001
9	1.2597	-0.7567	0.5997	20	0.6306	0.8340	-0.3800
10	1.2598	-0.7566	1.0098	21	0.6301	0.8340	0.3800

## C. Appendix C: IHEAT heat transfer results at $t = 3.4$ s

This appendix includes contour maps that show the missing data (white pixels on the test article geometry) in the peak region for the cases with the largest peak heat transfer. The contour maps at  $t = 3.4$  s into the run for the Type IVa interaction are included for reference in the following sections.

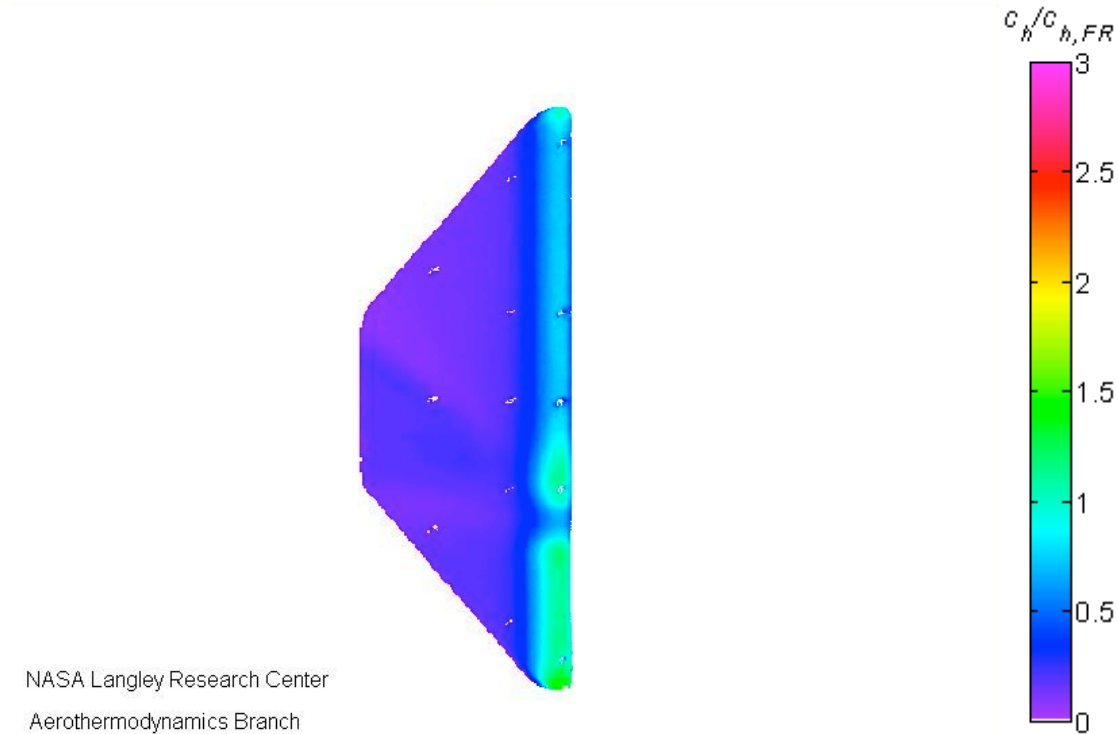


**Figure C-1.** Run 39: IHEAT  $c_h/c_{h,FR}$  contour map for the 0.25 in-radius test article at a  $0^\circ$  AoA.

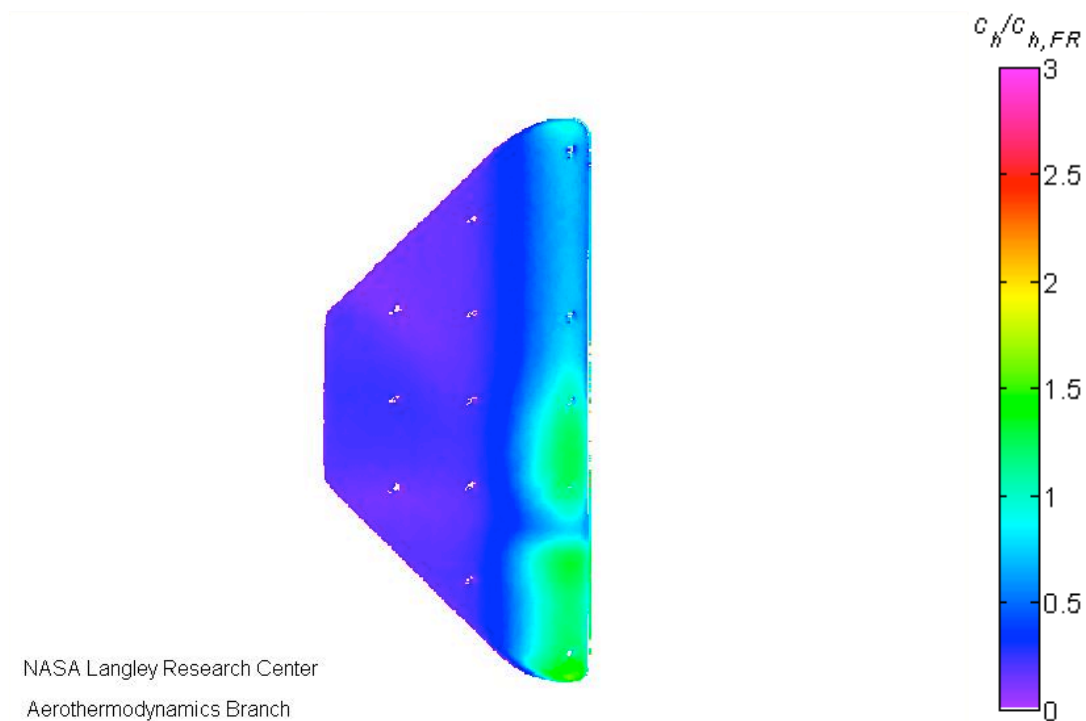


**Figure C-2.** Run 38: IHEAT  $c_h/c_{h,FR}$  contour map for the 0.50 in-radius test article at a 0° AoA.

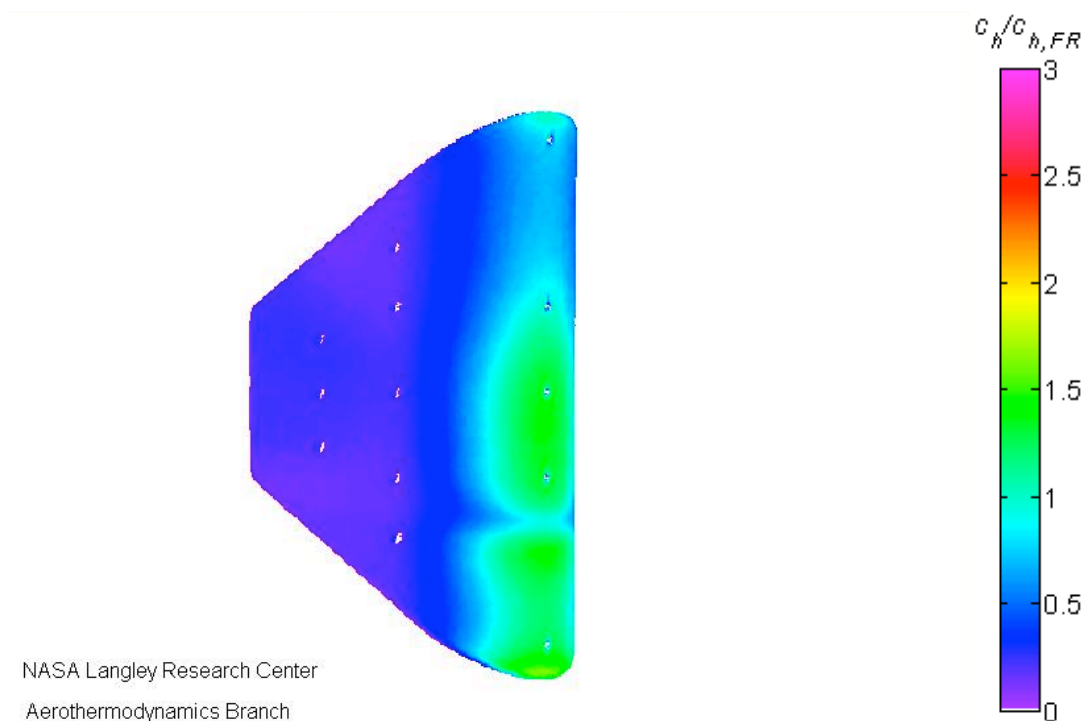


**Figure C-3.** Run 35: IHEAT  $c_h/c_{h,FR}$  contour map for the 0.75 in-radius test article at a 0° AoA.

The contour maps at  $t = 3.4$  s into the run for the Type IV interaction are included for reference in the following sections.

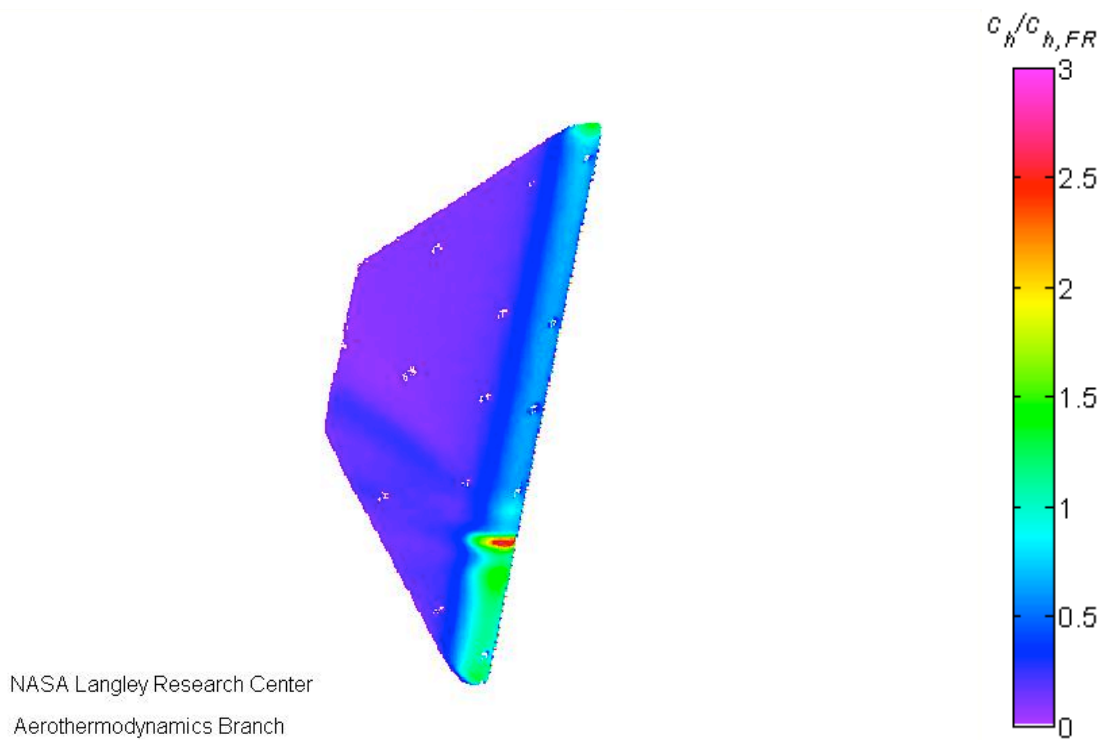


**Figure C-4.** Run 43: IHEAT  $c_h/c_{h,FR}$  contour map for the 0.25 in-radius test article at a  $-15^\circ$  AoA with a  $Re = 1.1 \times 10^6/ft$ .

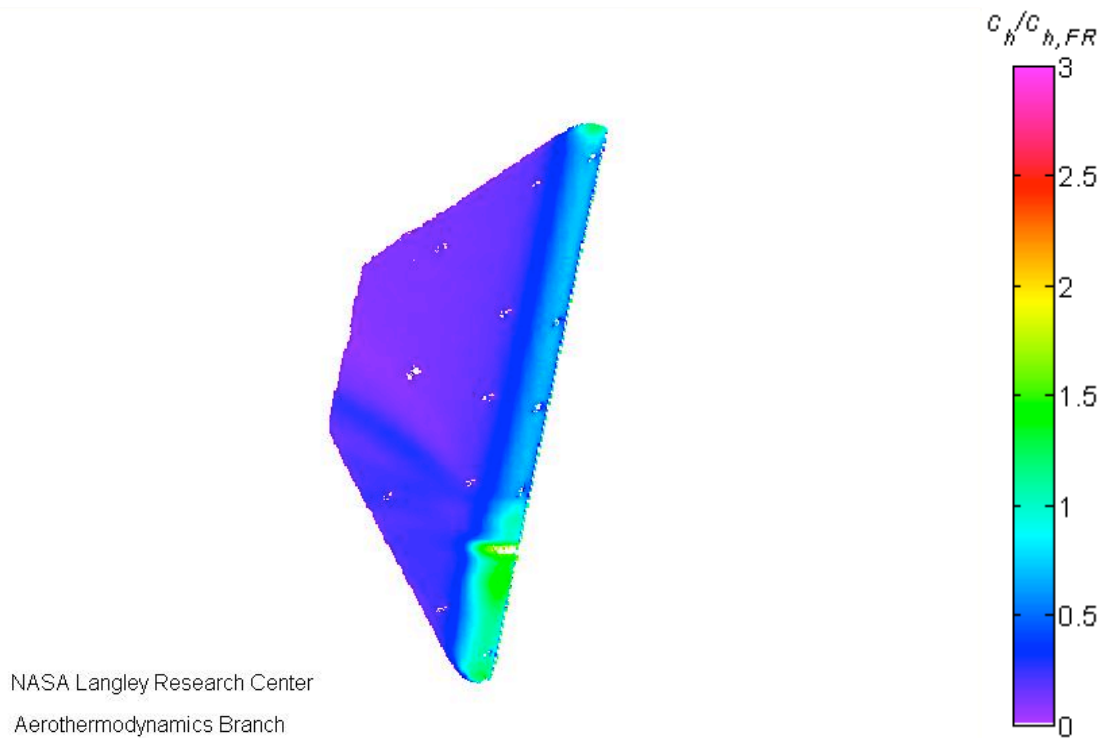


**Figure C-5.** Run 40: IHEAT  $c_h/c_{h,FR}$  contour map for the 0.25 in-radius test article at a  $-15^\circ$  AoA with a  $Re = 2.1 \times 10^6/ft$ .

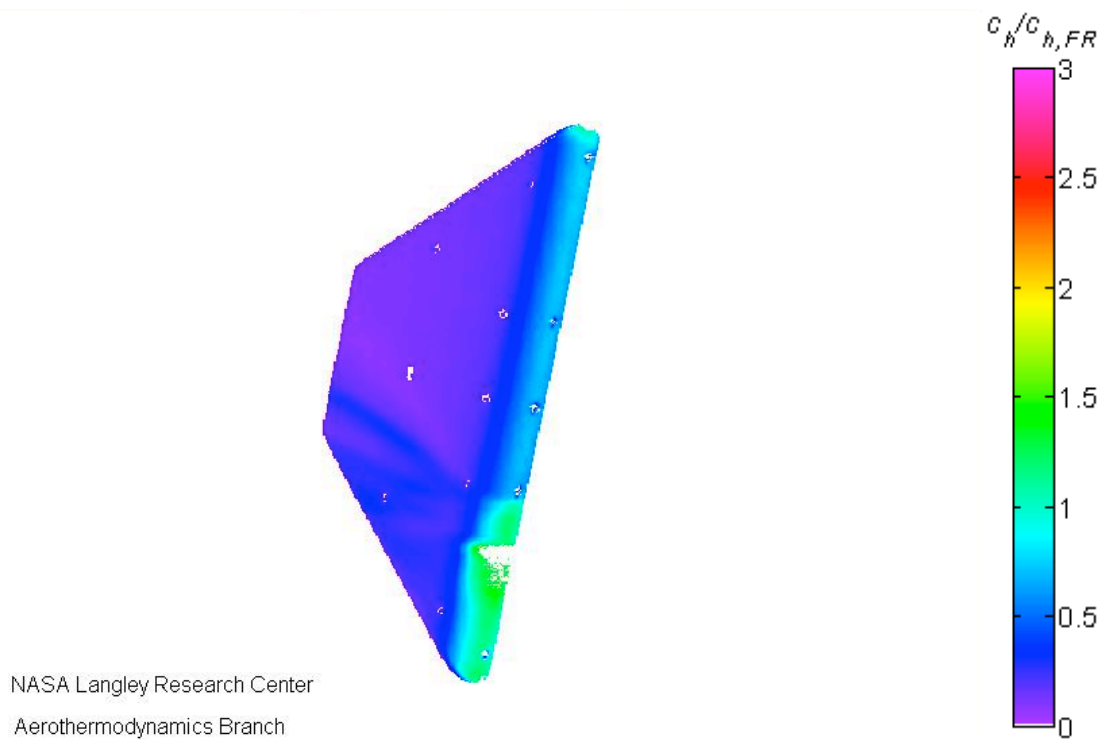


**Figure C-6.** Run 42: IHEAT  $c_h/c_{h,FR}$  contour map for the 0.25 in-radius test article at a 0° AoA with  $Re = 4.1 \times 10^6/ft$ .

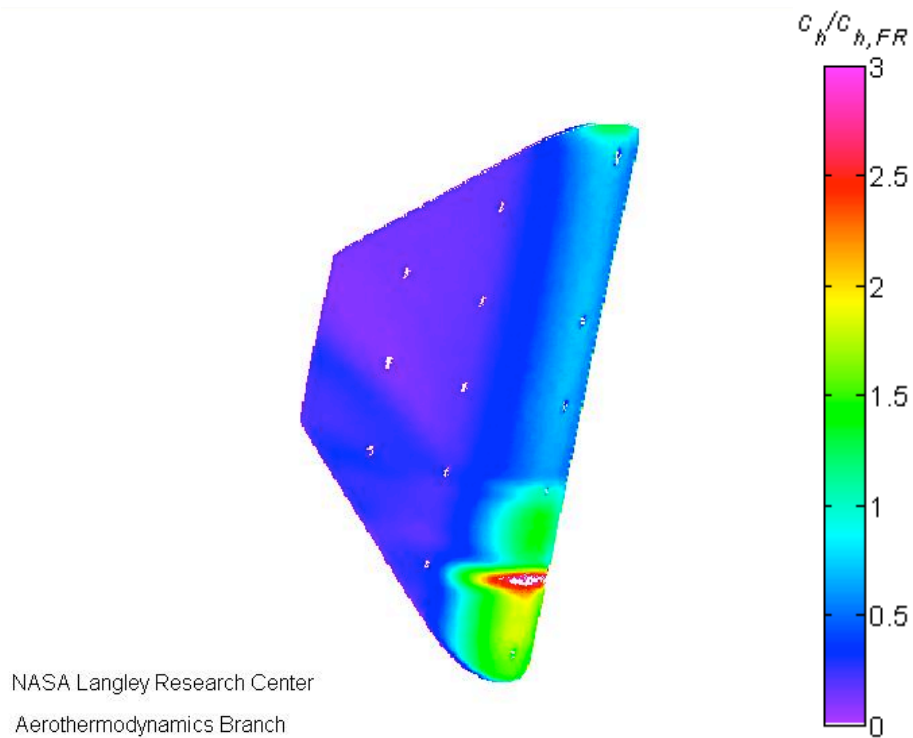


**Figure C-7.** Run 37: IHEAT  $c_h/c_{h,FR}$  contour map for the 0.50 in-radius test article at a -15° AoA.



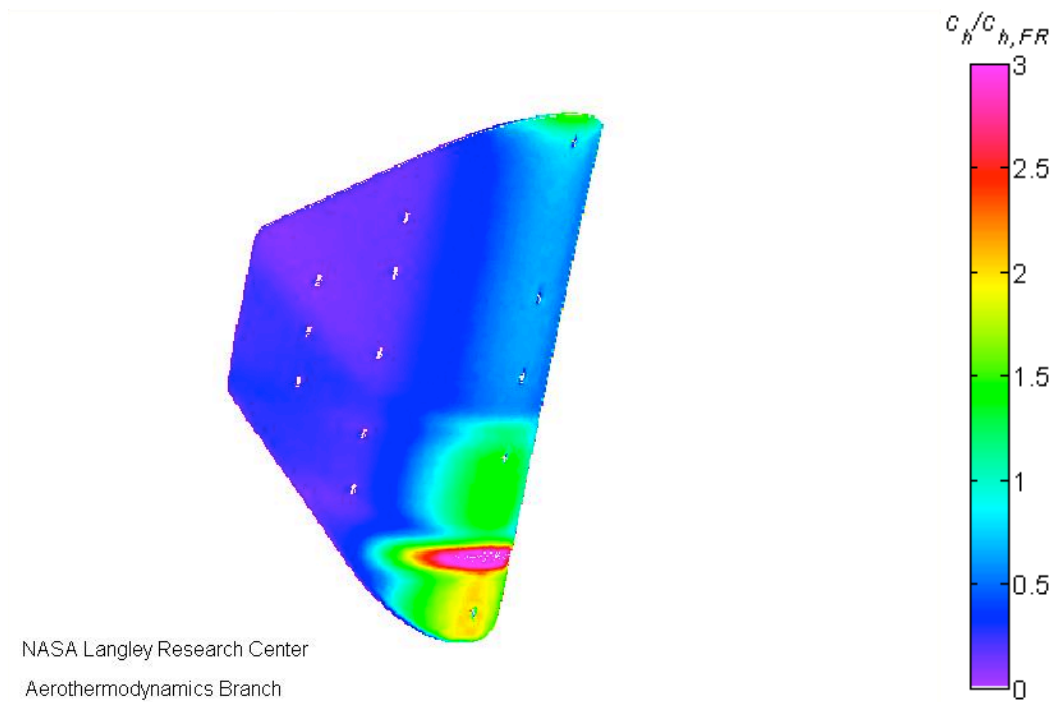


**Figure C-8.** Run 34: IHEAT  $c_h/c_{h,FR}$  contour map for the 0.75 in-radius test article at a  $-15^\circ$  AoA.

The contour maps at  $t = 3.4$  s into the run for the Type III interaction are included for reference in the following sections.

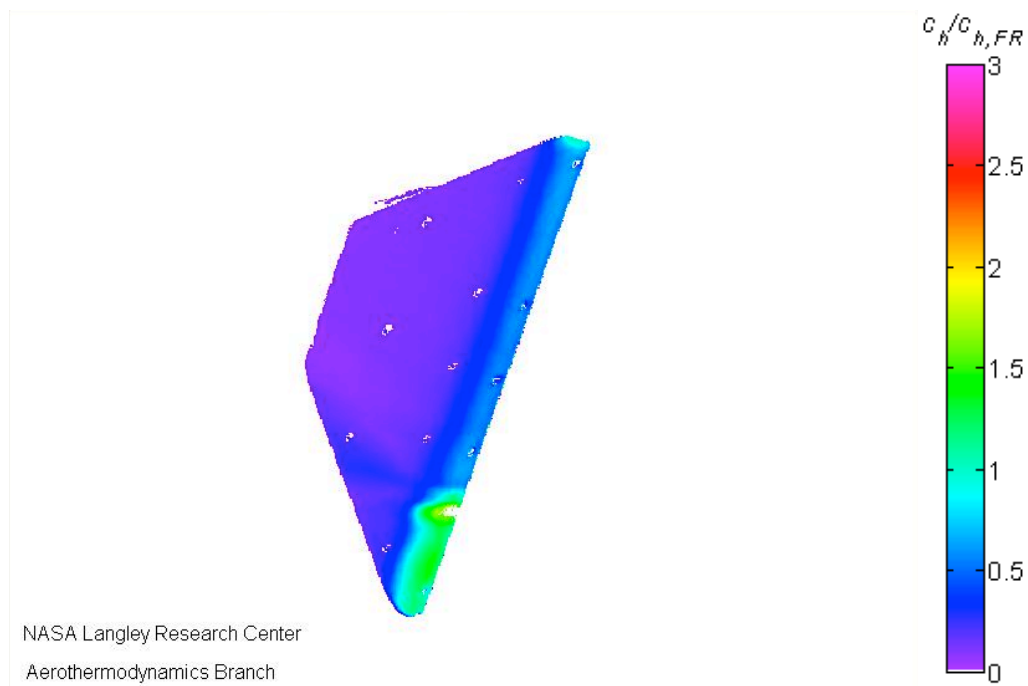


**Figure C-9.** Run 41: IHEAT  $c_h/c_{h,FR}$  contour map for the 0.25 in-radius test article at a  $-25^\circ$  AoA.

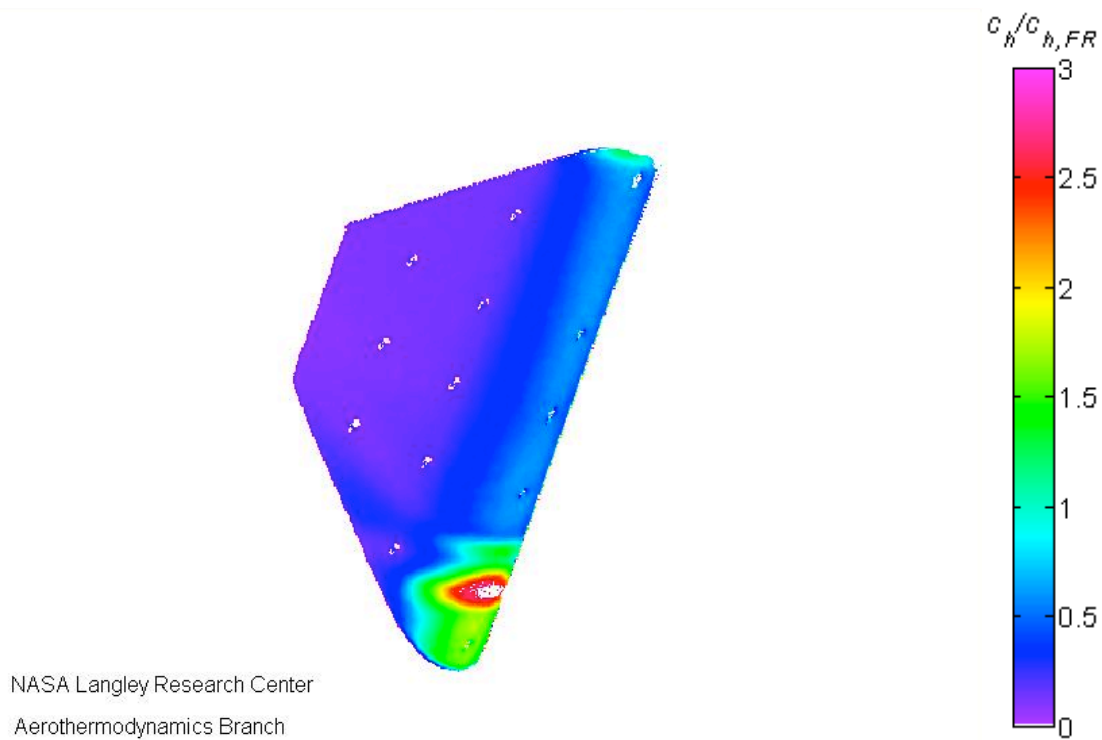


**Figure C-10.** Run 36: IHEAT  $c_h/c_{h,FR}$  contour map for the 0.50 in-radius test article at a -25° AoA.

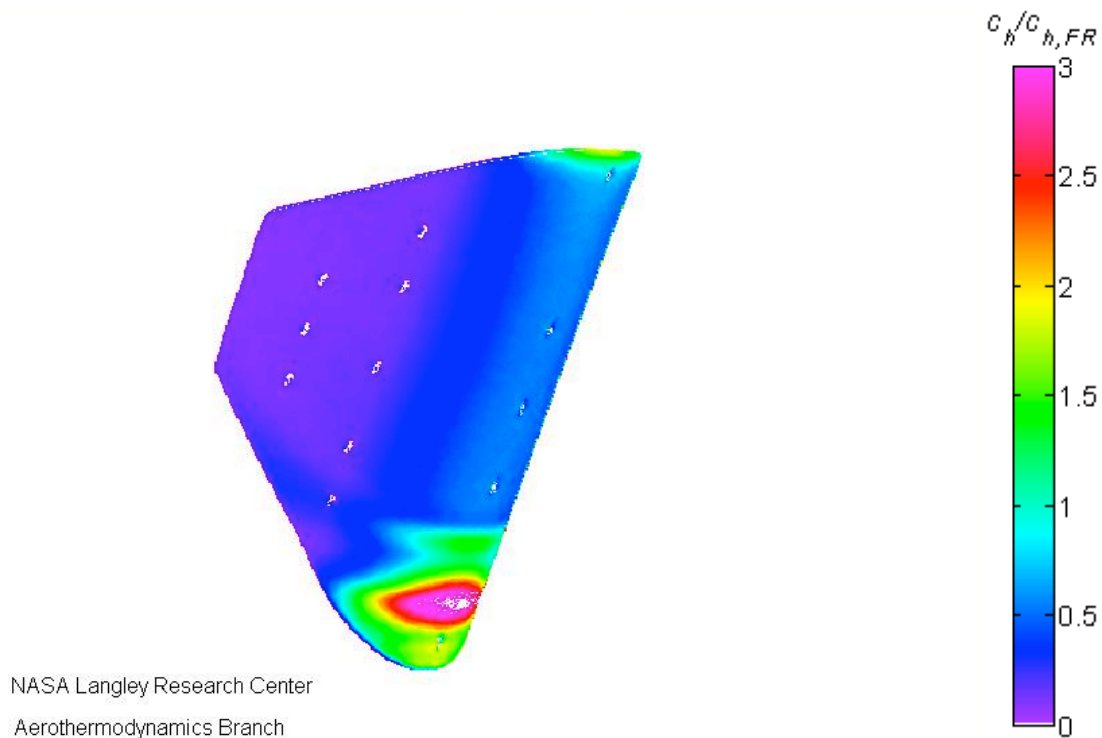


**Figure C-11.** Run 33: IHEAT  $c_h/c_{h,FR}$  contour map for the 0.75 in-radius test article at a -25° AoA.